High-precision nanotools for *in-situ* photo-patterning of biomolecules in 2D and 3D

Dissertation

zur Erlangung des Doktorgrades

der Naturwissenschaften

vorgelegt beim Fachbereich

Biochemie, Chemie und Pharmazie

der Johann Wolfgang Goethe -Universität

in Frankfurt am Main

von

Heike Krüger

aus Mainz

Frankfurt am Main, 2021

(D 30)

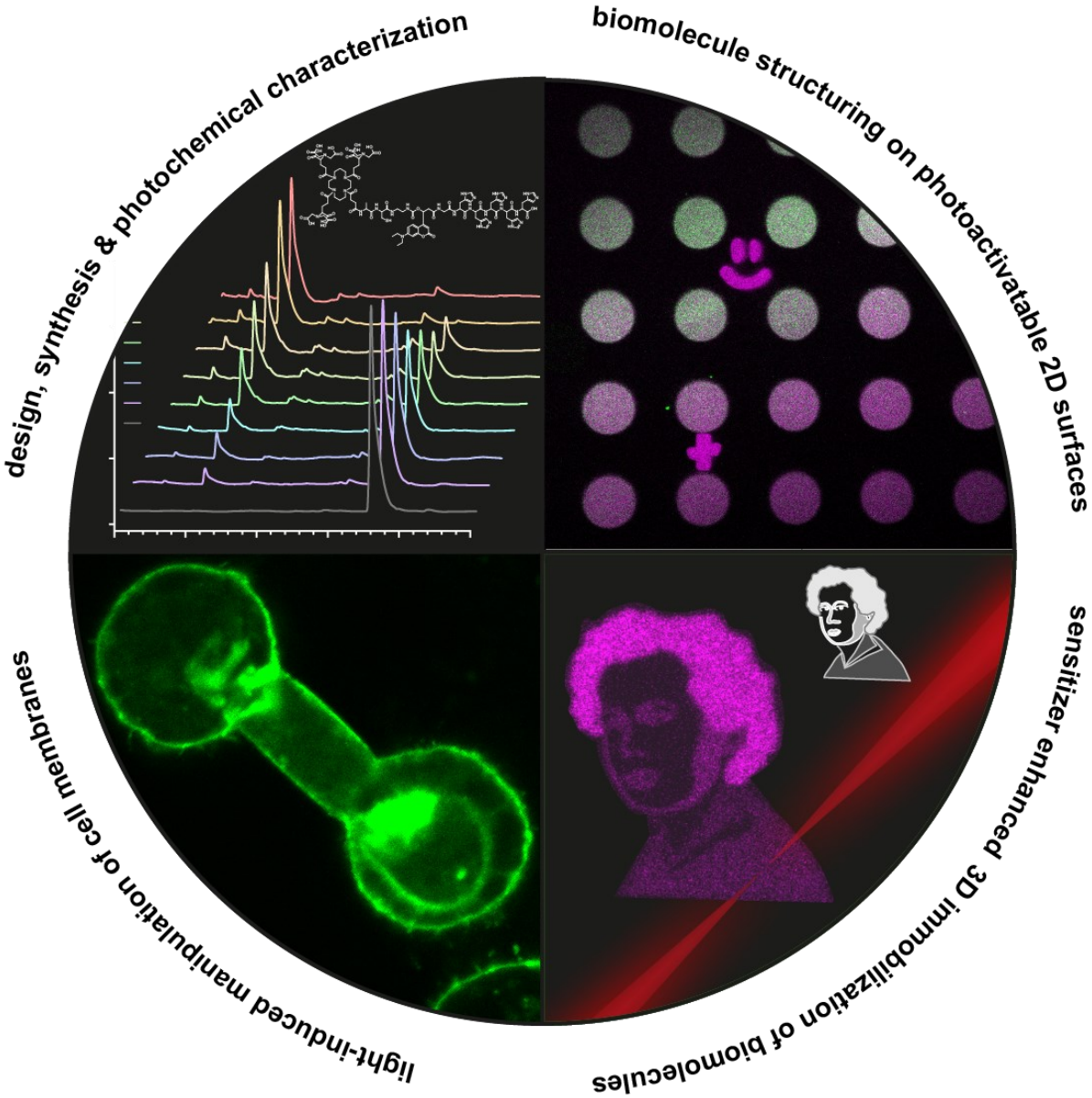
design, synthesis & photochemical characterization
biomolecule structuring on photoactivatable 2D surfaces
sensitizer enhanced 3D immobilization of biomolecules
light-induced manipulation of cell membranes

Vom Fachbereich Biochemie, Chemie und Pharmazie der Johann Wolfgang Goethe-Universität als Dissertation angenommen.

Dekan:	Prof. Dr. Clemens Glaubitz
1. Gutachter	Dr. Ralph Wieneke
2. Gutachter	Prof. Dr. Robert Tampé

Datum der Disputation: 03.03.2022

Dem wahrhaft Neugierigen erschließt sich alles,

was das Leben zu bieten hat.

(William Morris Davis)

Für Alex

Teile der vorliegenden Arbeit wurden veröffentlicht in:

H. Krüger, M. Asido, S. Wachtveitl, R. Tampé, R. Wieneke, Sensitizer-enhanced two-photon patterning of biomolecules in photoinstructive hydrogels, *Commun. Mater*. (in revision)

weitere Publikationen:

J. Brunnberg, V. Herbring, E. G. Castillo, **H. Krüger**, R. Wieneke, R. Tampé, Light control of the peptide-loading complex synchronizes antigen translocations and MHC I trafficking, *Commun. Biol.* **2021**, *4*, 430.

Content

1. Introduction

1.1. Protein labeling

Proteins are tightly controlled in time and in space. To investigate their function and dynamic network, selective labeling of proteins is enormously useful. Specific labeling of the protein of interest (POI) with a fluorescent label can provide valuable insights into their localization, dynamic and role in the cellular network within living cells in real-time. The choice of the labeling method is crucial. The requirements for a good POI-labeling are: (i) high specificity towards its target (ii) no disturbance of the POI´s function (iii) low background labeling for good signal to noise ratio and (iv) small size to allow spatially resolved analysis. In order to fulfill these criteria, plenty of methods have been developed, which can be categorized in four main groups: genetically encoded labeling, enzymatically mediated labeling, chemically conjugated labeling, and affinity-based labeling.

1.1.1. Genetically encoded protein labeling

A very commonly used approach for protein labeling is the expression of the POI fused to a fluorescent protein (FP). Chalfie *et al.*[1] were the first who successfully expressed a genetically encoded FP in an organism of another kingdom. Since they accomplished the expression of green fluorescent protein (GFP) originated from jellyfish *Aequorea Victoria* in *Escherichia coli* (*E. coli*) and *Caenorhabditis elegans* (*C. elegans*) a plethora of FP was developed for protein visualization in cells and animals. Although this was a major milestone, the usage of FPs is restricted due to their large size (> 25 kDa), low photo-stability, long maturation time, pH sensitivity and low fluorescence intensity.[2,3] While their size is likely to cause misplacement and disruption of function in fused proteins, GFP-like proteins also have a tendency to oligomerize, often at very low concentrations (nanomolar).[4] Therefore alternative labeling methods have been developed taking advantage of organic fluorophores with superior photo-physical properties, small size and selectable spectra range. Now that there is a variety of fluorescent probes to choose from, the choice of the best attachment method is a major challenge.

One way to install an attachment side for a fluorescent label into a protein is the incorporation of unnatural amino acids (UAAs). Immense efforts have been made over the last two decades to expand the genetic code, enabling the co-translational and site-specific incorporation of diverse noncanonical “designer” amino acids into proteins synthesized in cells and animals. The first group who achieved the introduction of an UAA in *E. coli* was Wang and Schulz *et. al.*[5] The key for expanding the genetic code is the reassignment of stop codons, most often the amber codon UAG,

by supplementing the cell with necessary components for incorporation of the UAA at the position of the introduced stop codon. Required for this is an ectopic transfer ribonucleic acid (tRNA)/aminoacyl-tRNA synthetase (aaRS) pair, which is able to load an UAA to the tRNA. Most commonly used is the pyrrolysyl-tRNA synthethase (PylS) and the corresponding tRNA ($tRNA^{Pyl}_{CUA}$) derived from *Methanosarcina mazei* or *Methanosarcina barkeri*.[6–8] With this tool kit a variety of structurally and functionally divers UAA (UAA with side chains with biorthogonal reactive handles like tetrazines, alkynes, aldehydes *etc*., crystallographic probes, cross linkers, fluorescent probes) has been introduced into different organism such as yeast, mammalian cells, *Drosophila melanogaster* as well as cell free.[9–11] A detailed overview of the recent developments in this field are summarized by Chin *et al.*[12] and Brown *et. al*.[13]

1.1.2. Enzyme-mediated tags

1.1.2.1. Sortagging

The transpeptidase Sortase A (SrtA), native in the cell envelope of the Gram-positive bacterium *Staphylococcus aureus*, recognizes the *C*-terminal peptide motif LPXTG (X = any aa), an only 5 aa long tag. When SrtA identifies the tag, it cleaves between the Thr and Gly, which results in a covalent intermediate between the Thr and the Cys of the active site.[14] The intermediate is resolved in a transpeptidase reaction with the *N*-terminal amino group of a poly-glycine substrate. This “sortagging” called ligation has been successfully used for installation of single functional handles on fluorescent proteins, enzymes and avidin-mediated structuring of nerve growth factors inside hydrogels.[15,16]

Sortase A tagging becomes more frequent due to the high selectivity and robustness of SrtA as well as the commercially availability of required components and the simple mode of application. The stringent requirement for the LPXTG sequence and the *N*-terminal glycines, lead to an alteration of the *N*-terminus sequence. This can be a drawback of the method because it might influence the POI function.

Furthermore, high enzyme concentrations (µM range) are needed to overcome the low efficiency of the reaction.[17] Quantitative conversion can hardly be obtained, because the reaction product with the sequence (LPXTGGG) is again a substrate for SrtA and furthermore, the reaction is reversible.[18] To overcome these limitations efforts have been made to improve efficiency, yield, and to avoid reverse reactions for example by forming ß-hairpin structures.[19–22]

1.1.2.2. Self-labeling tags

Self-labeling tags are mutated enzymes, which recognize a protein domain or peptide sequence and catalyze the transfer to themselves without the necessity of additives. These enzymes can be fused to a POI for labeling purposes. A leading example of that class is the SNAP-tag, which is derived from the O^6-alkylguanine-DNA alkyltransferase (AGT) a human DNA repair protein. The native function of AGT is the covalent attachment of O^6-alkylguanine-DNA to its cysteine residues. The low substrate specificity of AGT is advantageous in this case because it also reacts with O^6-benzylguanine (BG)- and O^6-benzyl-4-chloropyrrimidine (CP) derivatives bearing different chemical probes.[23,24] Further optimizations promoting faster reaction kinetics, higher affinity for BG derivatives and oxygen stability resulted in the SNAP-tag (Figure 1A), which had been used to install a variety of probes like fluorogenic probes, photoactivatable fluorophores and fluorescent sensors for metal ions.[25–29] Nevertheless, the SNAP-tag has also some drawbacks, for instance the big size of the fusion domain of 20 kDa, which might interfere with the POIs function and potential side reactions with native AGT. The CLIP-tag has been developed as an alternative enzymatic reaction[30], which reacts covalently with O^6-benzylcytosine substrates (Figure 1B). Since the SNAP- and the CLIP-tag are orthogonal to each other, they were used for dual-color labeling in live-cell imaging and super resolution microscopy.[31] Promega modified the bacterial enzyme haloalkane dehalogenase to developed another self-labeling tag, which is orthogonal to the SNAP- and the CLIP-tag, the HALO-tag (Figure 1C).[32] It has been used for localization and trafficking of proteins in living cells by tagging them with chemical probes,[33] quantum dots[34] or cell-permeable ligands.[32] On the one hand this tag has the asset to have no homology to mammalian proteins, so it is less likely to cause side reactions with mammalian proteins. On the other hand, it is likely to distort the POI interaction with substrates because of its size of 33 kDa.

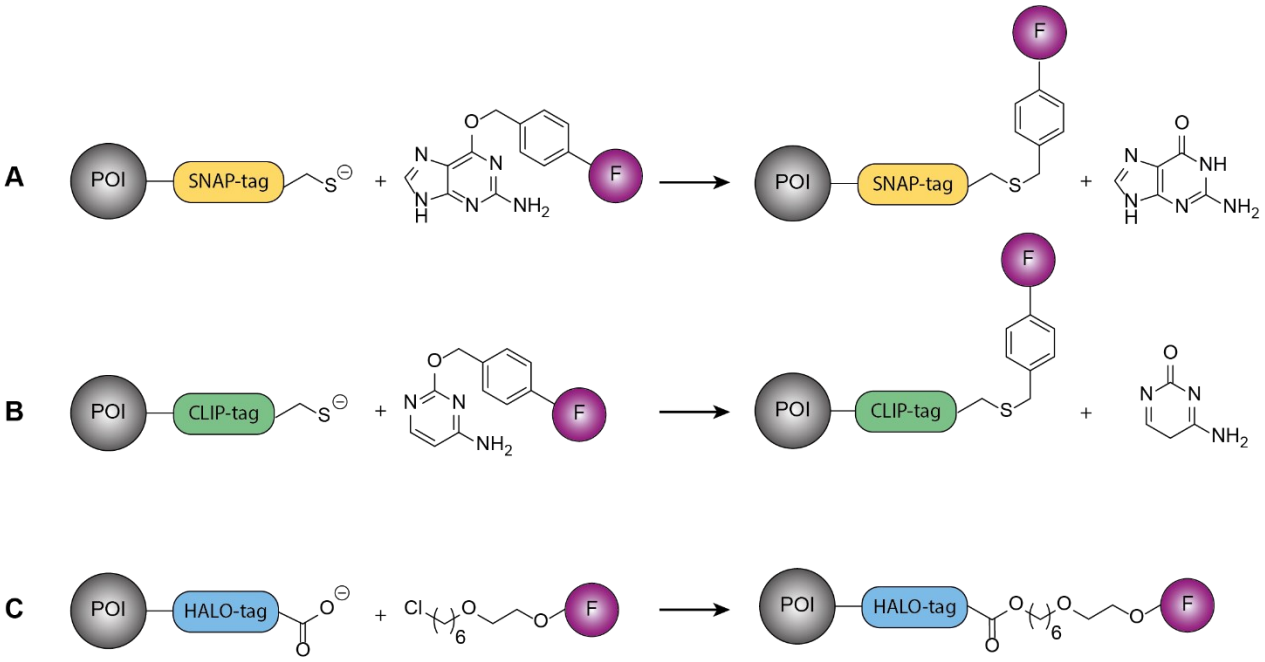

Figure 1: Overview of self-labeling tags. A) SNAP-tagged POIs become labeled *via* a specific reaction with O^6-benzylguanine derivatives, which bear a fluorescent probe. B) The CLIP-tag specifically reacts with O^6-benzylcytosine derivatives, thereby transferring a fluorescent label to the POI. C) HALO-tagged POIs covalently fuse with alkyl halides by nucleophilic substitution.

1.1.3. Direct chemical protein labeling

A classic way of protein labeling *in vitro* is the direct chemical labeling of functionalities in the side chain of proteogenic amino acids. In order to conserve protein functionality, the chemical reaction has to be efficient at physiological conditions (aqueous media, low or ambient temperature, high salt concentrations, neutral pH).[35] The immediate accessibility without the usage of genetic manipulation is favorable but can be accompanied with the problem of multiple labeling in case of a high abundant amino acid.[36] Although lysine has a high natural abundance (e.g. 6% in *E. coli*)[37] it is commonly used for labeling reactions, because of the efficient reactions, which are possible with a nucleophilic, primary amine. If multiple labeling is desired and selectivity is not crucial, lysines can be conjugated with active esters (*N*-hydroxysuccinimide)[38], isothiocyanates[39] or sulfonyl chlorides[40]. When using this labeling technique, it should be noted that the *N*-terminus might also get labeled, because it is also a primary amine. In contrast, if selective modification of the *N*-terminus is intended, this can be realized *via* condensation with 2-pyridinecarboxyaldehydes according to MacDonald *et al.*[41]

The high amount of lysines inside a protein causes less selective labeling. In order to avoid this, cysteines can be used, since they are reactive nucleophiles but less abundant in proteins (<2%).[42]

Covalent attachment of chemical probes can be achieved *via* addition of α-halocarbonyls, iodacetamides or *via* Michael addition to maleimides. In case the POI does not naturally contain a cysteine, it can be introduced by site-directed mutagenesis. Since the specificity of the labeling reactions is low, this labeling technique is used for purified POIs *in vitro* and not *in vivo*.

1.1.4. Affinity-mediated protein labeling

1.1.4.1. Tetracysteine tag

Griffin *et al*.[43] exploited the specificity of trivalent arsenic compounds towards thiols to create fluorogenic, membrane-permeable protein-labels. The tight-binding pair consists of a small tetracysteine motif (CCXXCC, X = any amino acid except cysteine) fused to the POI and Fluorescein Arsenic Helix binder (FlAsH) or Resorufin-based Arsenical Hairpin binder (ReAsH).[43,44] Upon binding of nonfluorescent FlAsH and ReAsH to the closely spaced thiol pairs, they form a tight complex whereupon they become strongly fluorescent. The major drawback of unspecific binding to endogenous cysteine pairs or lipoamide factors causes high background labeling and cellular toxicity, which can be reduced by addition of dithiol ligands such as 1,2-ethandithiol (EDT) in the micromolar range.[45] The increase to millimolar concentrations can outcompete the tetracysteine tag and remove the FlAsH or ReAsH from the protein.[44] Further optimization of the hairpin structured binding sequence, and the flanking region lead to the amino acid sequence HRWCCPGCCKTF and FLNCCPGCCMEP with higher fluorescence quantum yield after complex formation and improved dithiol resistance in comparison to the former version. These improvements resulted in >20-fold increase of the signal-to-noise ratio according to Martin *et al.*[46] Especially the small size of 12 amino acids is an advantage over fluorescent protein (FP) labeling, hence it is less likely to perturb POI function. So far, the tetracysteine tag has been successfully used for correlative fluorescence and electron microscopy (EM),[47] Förster resonance energy transfer (FRET)-based assays[48] and for chromophore assisted light inactivation (CALI) of POIs.[49] Overall, the need for washing with dithiols after staining limits the applicability of the technique in animals.[45]

1.1.4.2. His-tag/NTA-system

The oligohistidine-tag (His-tag) is a very well-known affinity-tag in life science and is routinely used for protein purification.[50] For this purpose, the affinity of histidine clusters to coordinate divalent transition metal ions like Cu(II), Cd(II), Co(II), Zn(II) and Ni(II) is used. In combination with the

chelator *N*-nitrilotriacetic acid (NTA), a octahedral complex is formed, whereby His-tagged proteins can be purified by immobilized metal-ion affinity chromatography (IMAC) under mild conditions.[51] In native proteins consecutive histidines are very rare, which makes it easy to specifically target the POI by encoding a His-tag to its *N*- or *C*-terminus. Since the *mono*NTA/His-tag interaction has a relatively low affinity (K_D ~10 µM), the binding strength during IMAC purifications is reliant on multiple *mono*NTAs creating multivalent attachment sites.[52] Nevertheless, *mono*NTA has been successfully used for incorporation of quantum dots,[53] as biosensor platform[54,55] and for immobilization for proteins on surfaces.[56–58] Meredith and coworkers developed a trifunctional reagent to covalently label proteins.[59] Here the bioreagent consisted of a *mono*NTA group, a phenol-azide and a fluorophore. They used the *mono*NTA moiety to initially selective bind the His-tagged target protein, then an exchanged of the weak *mono*NTA/His-tag complex took place by triggering a photo-crosslinking reaction between the azide and the protein. Other approaches to improve NTA-binding were inspired by the IMAC principle to create multivalency (Figure 2). Attachment of two NTA-groups directly to Cy3, Cy5 or dibromobimane, united elegantly the functional NTA groups with fluorophores, but could not enhance the affinity significantly (dibromobimane-*bis*NTA K_D~40 µM, Cys3/5-*bis*NTA K_D ~0.9 µM).[52,60] Further efforts for improvement have been made by Lata *et. al*.[61–63] and Tinazli *et al*.[64] They designed multivalent chelator heads (MCHs) with *bis*-, *tris*-, and *tetrakis*NTA groups on cyclic or dendritic scaffolds. The best result was achieved with *tris*NTA, displaying a K_D ~20 nM towards *hexa*histidine. Complex stability could not be enhanced with one additional NTA moiety in *tetrakis*NTA, which can be explained by a saturation of the six binding sites of the *hexa*histidine-tag with equally six binding sites in *tris*NTA. The nanomolar affinity, the ultrasmall tag size (*tris*NTA ~1 kDa, *hexa*histidine ~840 Da), but also the reversibility in presence of imidazole, histidine or EDTA, are key advantages of this interaction pair.[61] It has been successfully used for protein binding on various surfaces,[62,63,65,66] super resolution microscopy,[67] single-molecule tracking[68] or protein labeling with different markers like quantum dots,[69] spin probes[70] or streptavidin.[71]

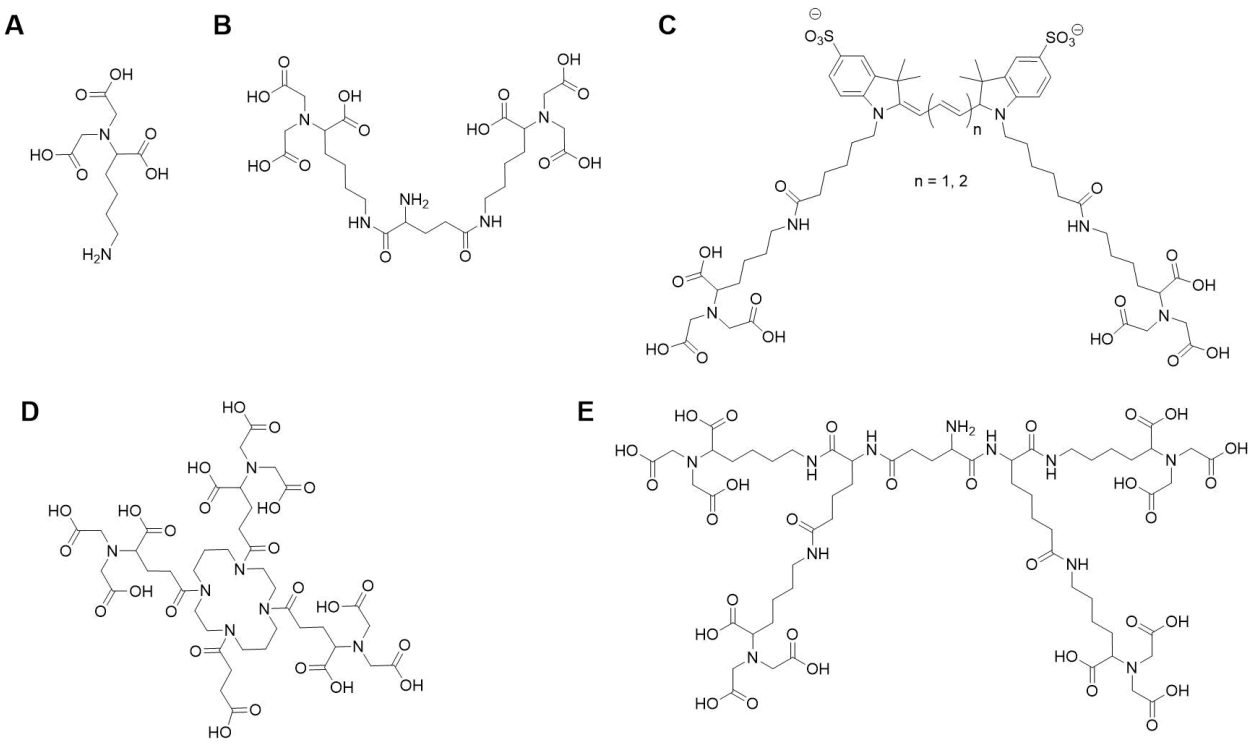

Figure 2: Approaches to optimize NTA-binding affinity and stability with multivalency. A) Structure of basic *mono*NTA. B) Divalent NTA synthesized by Lata *et a*l.[62] C) Divalent NTA with a Cy3 or Cy5 scaffold from Kapanidis *et al*.[52] C) *Tris*NTA moiety with a cyclic skeleton. D) *Tetrakis*NTA developed by Lata *et al*.[61]

In order to add another operation mode, Grunwald *et al*.[72] and Labòria *et al.*[73] designed an interaction molecule, called photoactivatable-*tris*NTA (PA-*tris*NTA), where the POI-binding with *tris*NTA can be remotely controlled by light (Figure 3). Therefore, they connected *tris*NTA *via* a short peptide linker with a hexahistidine tag. The intramolecular His-tag forms a complex with the Ni(II)-loaded *tris*NTA headgroup, whereby the *tris*NTA is autoinhibited. Labòria and coworkers showed that the autoinhibition is due to a high rebinding possibility of the intramolecular His-tag, strong enough to withstand up to 25-fold molar excess of competing His_{10}-tagged protein. Trigger points for remote activation are the two photocleavable amino acids 3-amino-3-(2-nitrophenyl)-propionic acid (Anp), which are incorporated within the His-tag and in front of it. Upon illumination with UV-light, they undergo photo-scission whereby the His-tag is cleaved off and the *tris*NTA groups are free to bind another His-tagged POI or target of interest. Incorporation of two Anp groups causes the His-tag to split into two parts, both containing three histidines, which makes the fragments less likely to rebind to *tris*NTA. If the His-tag fragments would remain bound to *tris*NTA, they would be outcompeted by a His_6-tagged target. This engineered PA-*tris*NTA made it feasible to photo-pattern proteins in functionalized hydrogels *in-situ*[73] and label proteins inside living cells[74] in a spatiotemporal manner.

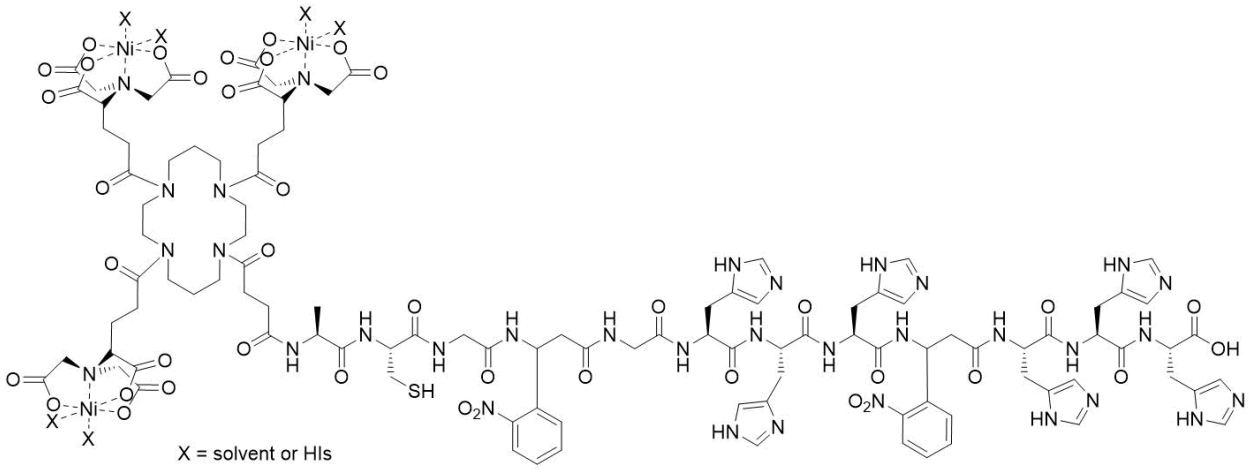

Figure 3: Chemical structure of Ni(II)-loaded photoactivatable-*tris*NTA developed by Labória *et al*.[73] Within and in front of the intramolecular His_6-tag are strategically placed Anp groups, which can be photocleaved to disassemble the His-tag. The Cys inside the peptidic linker enables surface immobilization or fluorophore attachment.

1.2. Protein immobilization on surfaces

For investigation of a proteins function, kinetic or binding mechanism, immobilization can be very beneficial. Moreover, protein functionalized surfaces can be used as protein biosensors in medical, environmental, or technological applications.[75,76] Building a protein biosensor or biochip can be troublesome, because of the high sensitivity of some proteins. It is important that the function and native conformation of the protein remains intact after surface binding. Biochips are usually composed of a solid support, which is suitable for the detection technique used. Common supports are glass or gold surfaces. Gold is used for example for surface plasmon resonance (SPR) spectroscopy and atomic force microscopy (AFM), while glass surfaces are mostly used for fluorescence microscopy. In order to make the surfaces biocompatible and to minimize unspecific binding, the solid supports are typically functionalized with biopolymers like dextran, alginate, or hydrophilic polyethylene glycol (PEG). This layer also contains specific anchor groups to immobilize the POI in a specific and oriented manner, which is very important to avoid impairment of the active side or sterical hindrance that would block ligand binding. Especially for bioanalytic applications, the surface should also enable dense and homogeneous protein distribution for a good signal-to-noise ratio. The composition of biochips and biosensors is highly optimized for each purpose and therefore the protein immobilization methods differ. The most common methods are explained in the following subsections.

1.2.1. Physical immobilization

Physical immobilization is a non-covalent binding constructed by adsorption through Van-der-Waals- or Coulomb interactions. Surfaces of this class are membranes coated with polyaniline or sulfate functionalized dextran.[77,78] Since the interaction is not directed to a specific locus at the protein, the orientation of immobilized proteins is randomly distributed. Thereby, orientations which cause loss of function can occur. Furthermore, the analysis conditions have to be optimal to circumvent unintentional dissociation of the protein from the surface by salt, pH, detergents, or pressure.

1.2.2. Covalent immobilization

A stable binding of proteins to surfaces can be achieved by covalent immobilization if reversibility is not required. The functional group (*e.g.,* amine, thiol, alcohol) of a POI reacts irreversible with the modified surface, whereby a distinction between non-site-specific and site-specific can be made, if the protein orientation can be controlled.[79] If proteins bind to the surface *via* their amine or carboxyl groups, it is a non-directed attachment because proteins have a multitude of reactive groups in their side chains at different positions. This multiple bond formation results in randomly orientated and sometimes non-functional proteins. To evade these problems, site-specific immobilization methods targeting an exclusive surface accessible reactive group, which is usually not present in proteins like the protein labels discussed in chapter 1.1. Exception from that are single-cysteine mutants, which are used for chemisorption on gold surfaces, for thiol-ene photoreactions or Michael-additions on maleimide groups.Bioaffinity immobilization

Bioaffinity-based methods facilitate a mild and reversible immobilization with an oriented structure. Widely used affinity pairs are the streptavidin-biotin, but also immobilized antibodies, which recognize specific epitopes on the protein surface are used.[80,81] In addition, DNA-Chips have been developed for selective immobilization of DNA-protein conjugates through hybridization or as orthogonal systems.[82,83]

1.2.3. Functionalization of two-and three-dimensional scaffolds

1.2.3.1. Functionalization of glass surfaces

Glass is mainly functionalized *via* silanization of the activated surface followed by PEGylation. Therefore, the glass surface is activated with piranha solution (H_2O_2/H_2SO_4) or oxygen plasma to

generate reactive silanol groups. Next, the surfaces are incubated with alkylalkoxysiloxane in organic solvents like methanol or ethanol. Hydrolysis of the siloxanes creates reactive silanol groups, which condensate with the silanol groups of the glass layer, thereby forming a silane-functionalized interface. Silanes are commercially available with functional groups like epoxy, amine, or thiol groups for further modifications such as PEGylation or crosslinking. PEGylation is a common procedure for passivation of biomaterials, hence PEGs are available in different sizes and defined length from few units to thousands of kDa and can be used as biocompatible spacers between the solid support and the anchoring groups for protein immobilization. Conveniently, PEGs are sold homo- or hetero-functionalized with a variety of reactive groups for selective chemical modifications.

Another common approach to build up biochips is the utilization of coatings used in cell culture. Different from silanization, poly-*L*-lysine (PLL) is non-covalently attached to the surface by electrostatic interactions between its positively charged side chain and the negatively charged silica.[84] The cationic nature is advantageous for adhesion of anionic molecules, especially DNA, but also for cell adhesion, since the cell surface is negatively charged. For this reason, PLL coatings are often used for fabrication of DNA[85] or cell microarrays[86,87], but also as biocompatible coating[88] or anchor for further functionalization.[89]

1.2.3.2. Hydrogels as three-dimensional scaffolds

Hydrogels are highly hydrated, three-dimensional polymer networks of either physically or chemically crosslinked polymers. Due to their highly engineerable properties, they are outstanding soft materials with numerous utilizations in regenerative medicine, tissue engineering and dynamic cell culture.[90] Hydrogel fabrication has developed from static to smart materials, whose structure and properties are dynamically tunable by external stimuli like temperature,[91] pH,[92] enzymes,[93,94] light,[95,96] electric[97,98] or magnetic[99,100] field and ion concentration. This unique level of control over material attributes and the excellent biocompatibility gave rise to a plethora of application in the medical and industrial field like wound healing[101], drug delivery[102], ligand presentation[103], cell-guidance[104], 3D cell culture[105], chemical sensors[106,107] and soft actuators.[108]

Hydrogels can be assembled from a variety of natural or synthetic monomers. Typical used naturally components are gelatin, collagen, alginate, hyaluronic acid (HA), fibrin and Matrigel whereas synthetic materials for hydrogels are based on polyacrylamide (PA), polyethylene glycol (PEG) and polyvinyl alcohol (PVA).[109] The hydrogel fabrication process varies from component

to component. Collagen for example forms gels by self-assembly into collagen fibrils at 37 °C. Alginate gelates, when monovalent cations are exchanged with divalent cations, and fibrin hydrogel formation is based on the natural polymerization reaction catalyzed by thrombin.[110] Hydrogels based on HA, gelatin, PEG, PVA can be modified with functional groups, which offer the possibility for crosslinking, host-guest interaction, thiol-ene reaction, Michael addition, tetrazine-ligation, photodimerization or click reactions.[111] Based on the crosslinking strategy, the fabrication process may involve harsh solvents, toxic reactants or can be mild, reversible and possible to form *in vivo* in the presence of cells and tissue. Therefore, the fabrication concept is crucial for the overall responsiveness of the hydrogel and has to be well planned for the specific application.

The extracellular matrix (ECM) is a non-cellular compartment, which is present in all tissues with vital structural and biological function.[112] Cells are embedded within the complex meshwork of synergistic collagens, proteoglycans and adhesion proteins. The ECM is not only a physical framework for the cells, which offers adhesion sites but also influences cell morphogenesis, proliferation and differentiation.[109] Since hydrogels offer many possibilities to fine-tune their topography, composition, stiffness and shape as well as incorporate bioactive cues, current approaches seek to mimic the ECM. An emerging focus is on dynamically tunable hydrogels containing photolabile functional groups, which allow for on-demand, *in-situ* control over hydrogel properties at any position of interest.

1.3. Photolithography

Biological processes are tightly controlled in time and in space. In order to understand protein relationships and their down/upstream processes, tools are required to investigate these pathways in a spatiotemporal manner. An emerging option, which has developed rapidly over the past years is light as an external trigger. Light has several advantages over processes triggered by small molecules, temperature, enzymes, ultrasound or pH shifts.[113] For instance, light can be delivered with a high spatiotemporal accuracy, it does not cause sample contamination or dilution and if applied carefully it is non-invasive. Furthermore, dosage and wavelength can be adjusted for selective control over different biological processes. Photochemistry opens up the possibility not only to observe but also to direct cellular processes. Techniques for photolithography differ in spacial and temporal resolution. In **mask-based photolithography** light comes through translucent parts of a photomask, which is placed between the light source and the sample. Thereby, designed 2D shapes can be applied on the sample. Typical light sources are for example

mercury lamps or LED lamps. On one hand it is beneficial that this method is fast and inexpensive, on the other hand it is limited to predefined patterns without control over the z-depth. When using **single-photon laser-scanning lithography,** defined regions are illuminated with laser light to initiate photoreactions at the focal point. Hereby, the x,y-resolution is in the micrometer range while the z-resolution is usually about >20 µm, because of the unavoidable light exposition above and beneath the focal point. This approach offers good control over x,y-direction, but only limited control in z-direction. Laser scanning has a longer processing time but is feasible on commercial confocal laser scanning microscopes. Drawbacks of single-photon lithography can be overcome by **multiphoton laser-scanning lithography**. Multiphoton lasers create femtosecond (fs) pulsed near-infrared (NIR) photons, which are almost simultaneously absorbed by molecules in the focal plane. The photoreaction only occurs at the focal point and thus z-resolution (~2-3 µm) is tremendously improved compared to single photon lithography. Additionally, the usage of NIR light enables deeper tissue penetrations and causes less photodamage than ultraviolet (UV) light but the technique is time consuming and needs expensive lasers.

Since the last few decades, a plethora of approaches utilizing light responsive reactions like isomerization, rearrangement, addition, dimerization and bond cleavage have been developed.[90,114] Giving rise to investigations of cellular processes from outside, but also within the cell and furthermore to create photo-responsive materials to direct cell fate. The toolbox of light-driven approaches is continuously increasing. For more detailed information see Ruskowitz *et al*.[90] or Weinstain *et al*.[115]

1.3.1. Photo-labile protecting groups

In 1978 Hoffmann and co-workers were the first who introduced the term “caged” for biologically active substances, which have been inactivated by an photolabile group called “cage” or also “caging group”.[116] Since the term “cage” can be misleading, alternative naming like photoremovable, photoreleasable photocleavable, photoactivatable or photolabile protecting group (PPG) arose. For inactivation of a biomolecule the PPG should be covalently installed at a functional relevant position, which leads to its biological inactivation. Upon illumination with light of a certain energy, the PPG undergoes bond photolysis and thereby releasing the so called “uncaged” biological active molecule.

The first description of photo-mediated bond cleavage can be dated back to 1962, when Baltrop and Schofield[117] observed that glycine was formed after UV irradiation of benzylcarbonylglycine. Thereafter, a vast amount of photolabile protecting groups were developed for many different

applications: release of peptides[118], oligonucleotides[119], proteins[120], neurotransmitters[121], fluorophores[122] and for gene regulation[123], drug-delivery systems[124]. Dependending on the desired application, the PPG has to match certain requirements. First of all, the photo-mediated cleavage reaction should have a high efficiency. The photolysis efficiency is characterized by the product $\phi\varepsilon_{(\lambda)}$ of the quantum yield ϕ and the molar decadic extinction coefficient at a certain wavelength $\varepsilon_{(\lambda)}$, which is proportional to the amount of photolysis.[125] Second, the caged molecule should be stable under the experimental conditions and soluble in the medium, which is used. Third, for biological applications the activation wavelength for photolysis should be above 300 nm but ideally red-shifted into the therapeutic-window (ca. 650-950 nm) to reduce photodamage and absorption of activation light by sample components. If a very fast biological process is being investigated, the reaction must be even faster than the process under investigation. Furthermore, the cleavage product of the PPG should be non-toxic. PPGs not always fulfill all these characteristics. Despite the formation of cell toxic nitrosobenzaldehyde as a cleavage product and quite low uncaging yield, the *o*-nitrobenzyl group is the most often used PPG, because it is synthetically well accessible, and a variety of derivatives are commercially available. Favorable alternatives are coumarin compounds which became increasingly popular since their demonstration as PPG by Givens *et al.* in 1984.[126] *o*-Nitrobenzyl and coumarin cages have been used in this work and therefore they are described in more detail in the next subchapters.

1.3.1.1. *o*-Nitrobenzyl derivative-based photolabile protecting groups

The *o*-nitrobenzyl (*o*-NB) group is one of the most often used PPGs so far. Since Patchornik and Amit[127] proposed it as a promising PPG in 1970, the *o*-nitrobenzyl group has been explored as a scaffold for PPG development. The uncaging mechanism has been vastly investigated[128–130]. The simplified photolysis mechanism is shown in Figure 4 on the example of *o*-nitrobenzylmethylether **1**, where methanol is caged by *o*-nitrobenzyl.[125] First UV-excitation of **1** in the ground state initiates hydrogen abstraction by the nitro group, whereupon *aci*-nitro intermediate **2** is formed. *Aci*-nitro component **2** is in equilibrium with the deprotonated state **3**, but only *aci*-nitro form **2** irreversible reacts by cyclization to 1,3-dihydrobenz[c]isoxazole-1-ol **4.** *Via* ring-opening, **4** transforms into a hemiacetal intermediate **5**, which finally hydrolyzes to *o*-nitroso-benzaldehyde **6** under release of the leaving group (LG) methanol. The rate-determining step of the reaction is the transformation of *aci*-nitro **2** to **4**. Whereas, the reaction kinetic is strongly depended on the substitution pattern, the solvent and in aqueous solution the pH.[125]

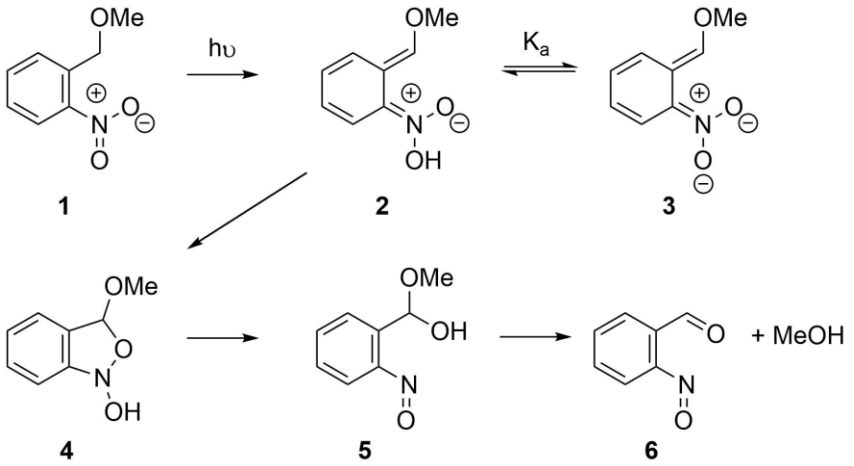

Figure 4: Uncaging mechanism of *o*-nitrobenzyl cages on the example of *o*-nitrobenzylmethylether. UV-excitation initiates hydrogen abstraction, whereupon *aci*-nitro intermediate **2** is formed, which is in an equilibrium with the deprotonated state **3**. A*ci*-nitro **2** reacts by cyclization to **4**, which transforms *via* ring opening to **5**. Finally, **5** hydrolyzes to *o*-nitroso-benzaldehyde **6**. Adapted from Klán *et al*.[125]

The formation of toxic benzaldehyde, which can react with cell components due to its reactivity is one of the major disadvantages of this protective group, especially for cell applications. Because of the low quantum yield of the photoreaction, intensive irradiation with UV light is necessary for a sufficient photolysis reaction. This in turn increases the cytotoxic influence of the irradiation. To improve the *o*-NB group´s properties, a variety of photolabile protecting groups based on the *o*-NB backbone have been prepared, which are grouped under *o*-NB derivate family. Commonly used examples are 6-nitroveratryl (NV), 6-nitropiperonyloxycarbonyl (NP) or nitrodibenzofuran (NDBF). In case of NP, the insertion of a benzylic methyl group, results in a ketone as a less reactive photolysis product instead of an aldehyde. The methoxy groups of the NV group and the acetal structure as well as the extended Π-system of the NDBF group serve to shift the absorption wavelength towards the visible range (bathochromic shift). The NDBF group, which was developed by Ellis-Davis and Barsotti[131], has a high single-photon photolysis efficiency and the property of two-photon absorption, which will be discussed in more detail in chapter 1.3.2. The photophysical properties of the *o*-NB derivatives compared to their basic structure are listed in Table 1. It should be noted that comparisons have to be taken with caution, because experimental execution, compound concentration and solvent may vary and can have significant influence on photophysical parameters.

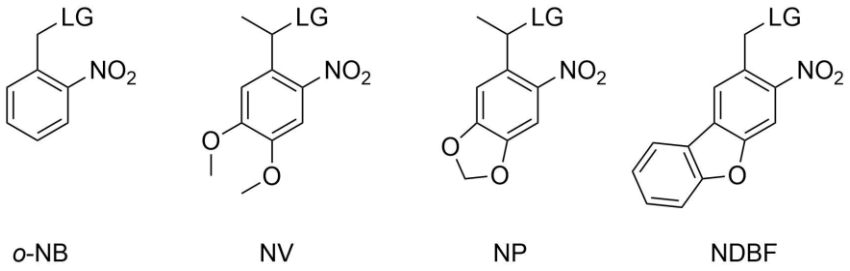

Figure 5: Overview of common *ortho*-nitrobenzyl PPGs. Derived from the *ortho*-nitrobenzyl (*o*-NB) PPG 6-nitroveratryl (NV), 6-nitropiperonyloxycarbonyl (NP) or nitrodibenzofuran (NDBF) were developed to improve the quantum yield of the photoreaction and to bathochromic shift the absorption wavelength.

Table 1: Photophysical characteristics of o-NB, NV, NP and NDBF photolabile protecting groups. Adapted from Klán *et al*.[125] and Brieke *et al*.[114]

PPG	LG	Solvent, ratio	λ_{irr}/nm	ϕ	ε/$M^{-1}cm^{-1}$	ref
o-NB	thymidine-OCO_2	MeOH/H_2O, 1:1	365	0.033	5,200	[132]
NV	1-threo-ß-benzyloxyaspartate	PBS buffer pH 7.4	355	0.005	3,900	[133]
NP	thymidine-OCO_2	MeOH/H_2O, 1:1	365	0.0075	3,500	[134]
NDBF	EGTA (Ca^{2+})	HEPES buffer pH 7.2	350	0.7	18,400	[131]

1.3.1.2. Coumarin-based PPGs

Coumarin is an herbal substance that was first extracted from the tonka bean in 1822. The aromatic substance and its derivatives are used as fragrances, flavoring agents in edibles, but also as fluorescent dyes (*e.g.*, Alexa Fluor350, Alexa Fluor430, coumarin343) in research and as anticoagulants (warfarin) in medicine. After Givens *et al*.[126] reported the light-induced release of a diethyl phosphate protected with 7-methoxycoumarin in 1984 (Figure 6), scientists interest in coumarin derivatives as photocages rose quickly.

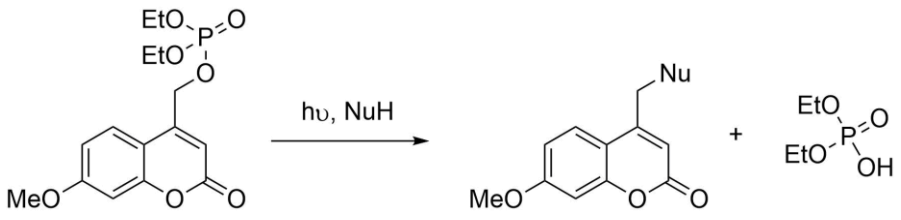

Figure 6: First reported application of coumarin as photo-cage. Givens *et al*.[126] observed light-induced release of diethyl phosphate from 7-methoxycoumarin.

The increasing use of coumarins is due to their high absorption coefficient, fast cleavage rate, the red shift of the absorption spectrum by substituents and the possibility of multiphoton induced reactions. According to Schade *et al*.[135] the mechanism of the photocleavage of coumarin compounds is a solvent-assisted photoheterolysis (Figure 7).

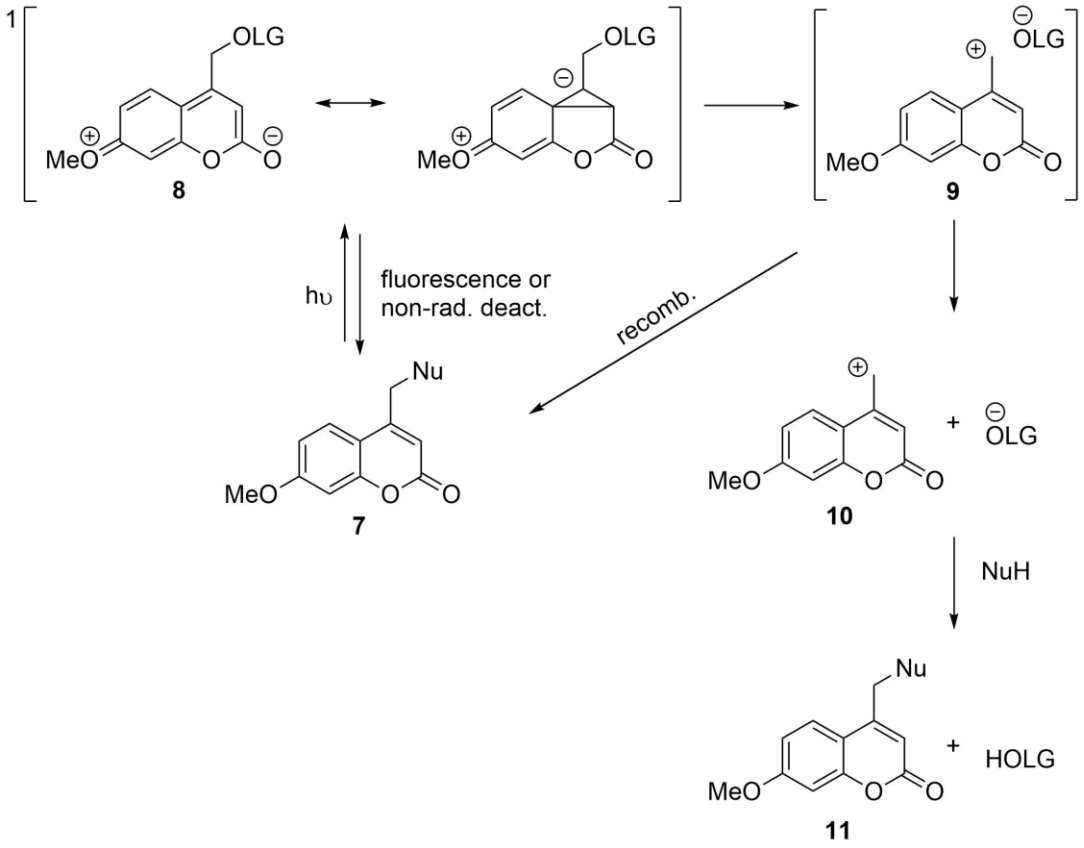

Figure 7: Photolysis mechanism of coumarin caging groups. After excitation of coumarin **7** to the lowest excited state **8**, heterolytic cleavage takes place between the leaving group (LG) and the ethylene group. The resulting tight-ion pair (TIP) can either recombine to **7** or split to the coumarin product **11** and the released LG by nucleophilic addition. Adapted from Klán *et al*.[125]

After initial absorption of light, coumarin **7** relaxes to the lowest excited S^1-state **8** in concurrence with non-radiative decay and fluorescence. In the S^1-state, electron-donating substituents in the 7-position shift electron density into the aromatic ring. This stabilizes the carbocation **9** formed during the subsequent heterolytic cleavage between the leaving group (LG) and the methylene group. The resulting tight ion pair (TIP) is the crucial intermediate in the cleavage process. The TIP surrounded by a solvent shell can now either recombine, in which case the caged compound **7** is recovered, or the TIP gets separated by the solvent (**10**). When a nucleophile adds to the

coumarin methyl cation **10** formation of the coumarin product **11** and the release of the caged LG occurs.

This illustrates that the solvent has a strong influence on the cleavage efficiency of coumarins. In nonpolar solvents, the radiationless relaxation is predominant. The more polar the solvent, the better the TIP is stabilized, so that the quantum yield of photolysis increases. Since aqueous media are therefore particularly suitable solvents, coumarins are a very good choice for cell biology applications. LG such as alcohols, phenols, thiols, and amines have been proven to be poor leaving groups for coumarins because they prevent heterolysis. In this case, linkage *via* a carbonate or thiocarbonate, carbamate structure is very effective (Figure 8). In this case, the uncaging mechanism proceeds *via* decarboxylation.

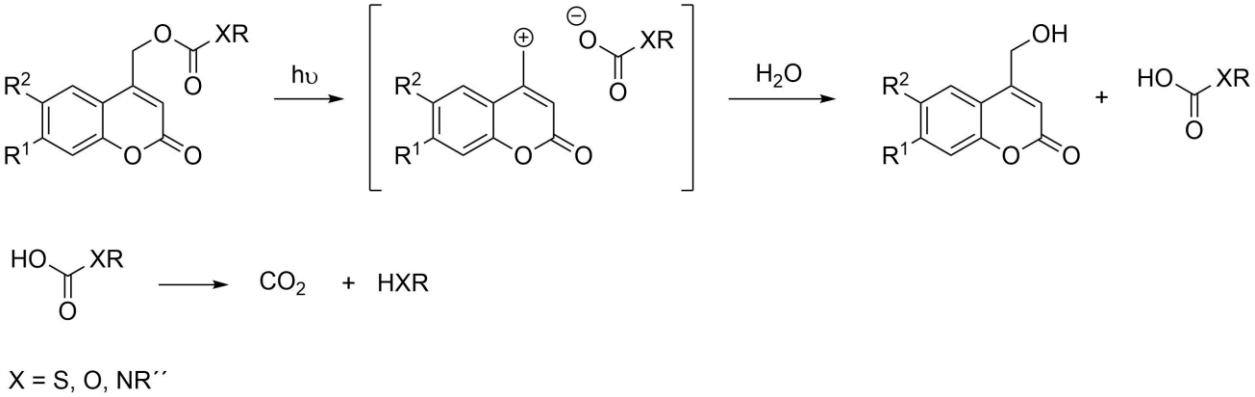

Figure 8: Release of alcohols, phenols, thiols or amines *via* decarboxylation. By light-excitation and subsequent heterolytic cleavage a tight ion pair (TIP) of coumarin methyl cation and carboxylic anion is formed. Addition of water to the TIP results in the coumarin alcohol and a carbonate/carbamate or thiocarbonate, which decomposes to carbon dioxide and an alcohol/amine or thiol. Adapted from Klán *et al*.[125]

The initially used 7-alkoxycoumarin derivatives to which coumarin-4-ylmethyl (CM) and 7-hydroxycoumarin-4-yl-methyl (HCM) belong, possess absorption maxima between 310 nm and 330 nm and have low water solubility. Therefore, efforts have been dedicated towards the development of water-soluble coumarin compounds with high photolysis-rates in the red-shifted absorption region. By substituting the C6-position with bromine, its inductive effect significantly increased the acidity of the hydroxy group in C7-position so that it deprotonates under physiological conditions. Therefore, the developed (6-bromo-7-hydroxycoumarin-4-yl)methyl (Bhc) group has an improved water solubility and a bathochromic shift to 370-376 nm. Hagen *et. al*.[136] enhanced the electron-donating effect in C7-position by introducing a diethylamino group (DEAC group), which shifted the absorption maximum of DEAC to 390-402 nm and increased the water solubility. Bhc as well as DEAC groups have the ability to be cleaved by two-photon

excitation, making them suitable for multiphoton lithography. The chemical structure of coumarin, Bhc and DEAC is depicted in Figure 9.

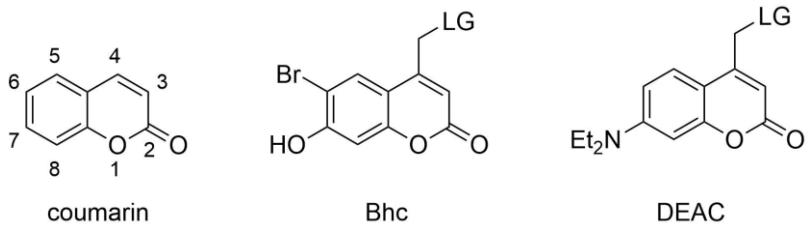

Figure 9: Chemical structure of the coumarin core moiety with atom labels and 6-bromo-7-hydroxycoumarin-4-yl)methyl (Bhc) and 7-diethylaminocoumarin (DEAC) photo-cages.

1.3.2. Two-photon absorption for uncaging

In 1931, Maria Göppert-Mayer used theoretical calculations in her dissertation to describe the possibility of a molecule to absorb two photons quasi-simultaneously and thus entering the excited state. Maria Göppert-Mayer was ahead of her time, since the experimental proof could not be provided until 1961, after the development of sub-picosecond pulsed lasers in 1960.[137] Kaiser and Garret proved the two-photon absorption by fluorescent radiation of a $CaF_2:Eu^{2+}$-crystal after irradiation at 694 nm.[138] Research on two-photon absorption received a boost with the availability of high pulsed Ti:Sa lasers in the 1990s, and the development of two-photon laser scanning microscopes by Webb and colleagues.[139]

Thereafter, the precision of the two-photon technique was exploited to improve microscopy,[140,141] microfabrication,[142] photodynamic therapy,[143] photolithography[144] and data storage.[145,146] The key difference of two-photon absorption (2PA) is that the required transition energy to bring the molecule from the ground state to the excited state is the sum of two photons of approximately half the energy (or approximately twice the wavelength) in comparison to one-photon absorption (1PA) (Figure 10A). Therefore, the transition probability for 2PA depends on the square of the local intensity of the excitation light, while for 1PA it is linear to the intensity. To generate the necessary intensity, the high pulsed lasers are needed. The intensity dependence is also the reason for the 3D resolution of 2PA, since above and below the focal plane the photon density is not high enough for molecular excitation (Figure 10B). The excitation volume can be as small as 1 fL.[147] Since higher wavelengths can be used, it allows two- to three times deeper penetration into tissue. In addition, photodamage, autofluorescence, self-absorption in the sample as well as light scattering are significantly reduced. However, the application of the two-photon technique

depends not only on the laser setup, but also on the suitability of the photolabile protecting group to absorb 2P. Analogous to the photolysis efficiency $\phi\varepsilon(\lambda)$ in the one-photon case, the two-photon effect can be quantified with the two-photon action cross section $\delta_u = \sigma_2 \cdot \Phi_u$, where σ_2 is the absorption cross section and Φ_u is the uncaging quantum yield . The unit of σ_2 and accordingly also δ_u is Goeppert-Mayer (GM), where 1 GM = 10^{-50}cm^4/photon.

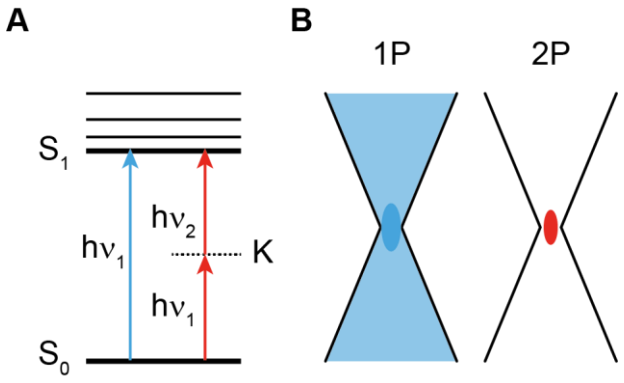

Figure 10: Two-photon absorption (2PA) in comparison to one-photon absorption (1PA). **A)** Simplified Jablonski diagram of 1PA (blue) and 2PA (red), with the virtual state K. B) Schematic illustration of the excitation volume in case of 1P or 2P excitation.

1.3.2.1. Sensitized two-photon uncaging

The probability of synchronous absorption of two photons is intrinsically lower than the absorption of one photon, hence 2PA is less efficient than 1PA.[148] Therefore the interest to address this weakness of the method is great. A variety of studies have investigated the structural requirements for high 2PA efficiency.[149–151] A popular strategy to increase the two-photon absorption cross section is to enlarge the π- system or to add electron drawing and electron donating substituents to create a di-, quadru-, or even octapolar structure.[151] However, according to the gap law, the frequency of a non-radiative transition increases exponentially as the associated energy gap decreases, so photoreactions of PPGs with large π- systems are often very inefficient. [115,152,153] As a result, some PPGs have a very small uncaging quantum yield but a very large two-photon absorption cross section σ_2, making the two-photon action cross section δ_u large enough for practical use. But in some studies, modifications of the substitution pattern of the cage rendered them light-insensitive.[154,155] In addition to the electronic influences of the substituents, the molecular symmetry also has a major effect on the photochemical reaction.[156,157] Increasing the 2P action cross section by changing the molecular structure can be very challenging.

In common PPG applications, the light absorption and bond cleavage are inherently connected in the same molecule, but another strategy is to decouple the two processes using a bimolecular system. This approach involves a chromophore for efficient two-photon absorption, which triggers a PPG *via* energy transfer to undergo cleavage. The first demonstration of such a sensitizing or "tandem" system came from Zhao *et al*.,[158] who used a NPE group to cage a coumarin fluorophore. They found that the coumarin, which has a bigger $\sigma_2$value acted as a sensitizer and transferred energy to NPE, leading to bond cleavage (Figure 11). Thereafter, more synergistic systems between chromophores and cages were developed, like the benzophenone sensitizer and a 4-methoxy-7-nitroindolinyl (MNI) cage, 9H-thioxanthen-9-one sensitizer and a (2-nitrophenylpropoxycarbonyl (NPPOC) cage and a fluorene derivative sensitizer and a nitroveratryl (NV) cage.[159–161]

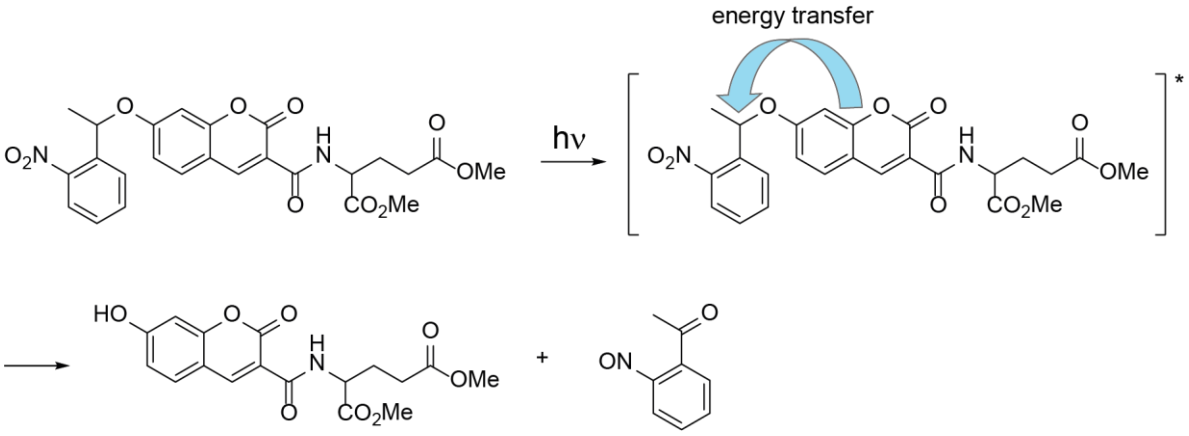

Figure 11: First reported sensitized uncaging reaction by Zhao *et al*.[158] Coumarin-glutamate caged by a NPE moiety was efficiently released after illumination, due to an energy transfers from coumarin to the NPE group.

The mechanisms of sensitization vary between the sensitization systems. Figure 12 shows a comparative overview between direct release after illumination (Figure 12A), release after formation of a reactive intermediate and different sensitization pathways (Figure 12C-F). Besides the energy transfer between the sensitizer (sens) and the PPG (Figure 12C), it is also possible that electrons are transferred (Figure 12D). The excited chromophore can also be the PPG and react in its excited state with a solvent or other auxiliary molecule by electron transfer (Figure 12E). An alternative route is sensitization by the photodynamic effect. Here, upon irradiation the sensitizer generates singlet oxygen or other reactive oxygen species (ROS), which then causes oxidative bond cleavage of the PPG (Figure 12F).

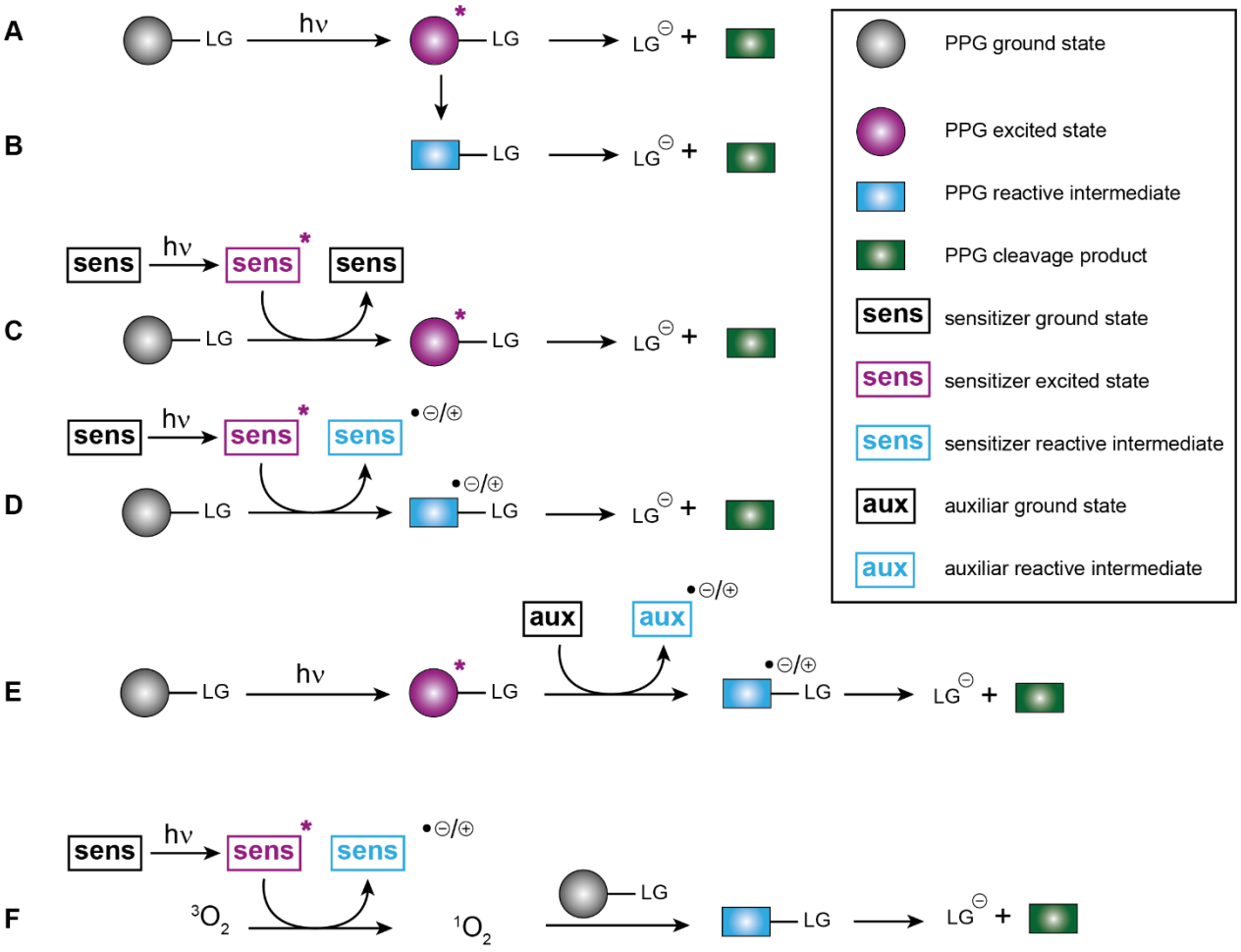

Figure 12: Schematic overview of photo-induced, sensitized uncaging pathways. After one- or two-photon absorption, the excited PPG either A) immediately cleaves into leaving group (LG) and photo product or B) forms a reactive intermediate, which than cleaves into the cleavage product and the LG. C) Light irradiation excites a sensitizing agent (sens), which transfers its energy to a PPG. The PPG in the excited state than disassembles into the cleavage product and the LG. D) The sensitizing agent in the excited state reacts with the PPG as electron donor or acceptor. The resulting PPG radical cleaves into cleavage product and LG. E) By photon absorption the PPG goes into the excited state and relaxes to the ground state by electron transfer with an auxiliar. The resulting PPG radical cleaves into the reaction product and LG. F) Upon irradiation a sensitizing agent goes into the excited state, which than generates from triplett oxygen singlet oxygen (photodynamic effect), which than reacts with the PPG. Adapted from Klán *et al.*[115]

2. Aim of this thesis

Spatial and temporal control over chemical and biological processes plays a key role to understand relationships in cellular systems. However, dense, and oriented tethering of proteins and protein-complexes to biomaterials still pose a considerable challenge. Furthermore, many existing methods lack the possibility for reversible, user defined control over protein organization. Tools are required, which allow *in-situ* actuation with no offset-time, accurate localization, and selective mode of action. Light-activatable compounds fulfill these demands.

Labòria *et al*.[73] designed a photo-activatable *tris*NTA (PA-*tris*NTA), which has been shown to bind proteins upon one-photon excitement. The activation of this affinity tool cannot be achieved by two-photon (2P) excitation, but only by UV light, because of the very low two-photon (2P) absorption cross section of the incorporated photolabile protecting group (PPG). Both are disadvantageous for cell applications. To extend the application possibilities, the aim of this work was to develop a two-photon activatable *tris*NTA (TPA-*tris*NTA) to precisely pattern biomolecules in 2D and in 3D as well as for cell studies. For this purpose, the work was divided into five sections:

I.Design and synthesis of TPA-*tris*NTA

Based on the preliminary work of Labòria *et al*.[73] the goal was to redesign and synthesize PA-*tris*NTA that i) it is two-photon cleavable, ii) it has a bathochrome shifted absorption maximum, iii) it is self-inactivated and light-activatable, and iv) it is water soluble. For this purpose, several photocleavable groups should be synthesized as carbaldehydes. Based on these building blocks, the corresponding ß-hydroxy acids and amino acid derivatives should be prepared and tested for incorporation into TPA-*tris*NTA by solid phase peptide synthesis (SPPS).

II. Photophysical characterization of TPA-*tris*NTA

The photocleavage efficiency of PPG should be tested depending on exposure intensity in solution before incorporation into TPA-*tris*NTA. Furthermore, the 1P and 2P properties of TPA-*tris*NTA should be investigated. For this purpose, the UV-Vis spectrum, the 2P absorption spectrum as well as the power dependence of the two-photon effect should be determined.

III. Photo-patterning of proteins of interest (POIs) in 2D

TPA-*tris*NTA and PA-*tris*NTA functionalized glass surfaces should be prepared to verify autoinhibition and light activability by immobilizing POIs *in vitro*. In addition, several functionalization strategies for glass surfaces should be tested to achieve highest specificity of protein patterning. The optimized surfaces should be used to write *in-situ* protein patterns.

IV. Two-photon lithography of TPA-*tris*NTA functionalized hydrogels

The exposure conditions tested on 2D surfaces will be used to specifically immobilize proteins in TPA-*tris*NTA functionalized hydrogels. Two-photon activation should be systematically investigated and optimized depending on the laser intensity and exposure time used to obtain the highest possible activation at the lowest possible light dose. To achieve this, the use of photosensitizers should also be tested.

V.TPA-*tris*NTA functionalized hydrogels for cell studies

Ultimately, the objective is to prepare TPA-*tris*NTA functionalized hydrogels to investigate on demand protein and membrane protein confinement of living cells. This application requires both precise and efficient photoreaction and biocompatibility of the TPA-*tris*NTA. Therefore, the viability of the embedded cells in the hydrogel has to be tested. Then, the *in-situ* patterning of His-tagged membrane proteins by a light trigger should be investigated. The particular complexity lies in monitoring the proteins assembly process with confocal microscopy in 3D.

3. Experimental section

3.1. Materials

All reagents and solvents were purchased in highest grade available and were used without further purification. If not stated otherwise *tris*NTA moieties were always Ni(II)-loaded. His_{10}-MBP^{OG488}, His_6-GFP were gratefully provided by Dr. Karl Gatterdam (Tampé lab), His_{10}-mVenus was kindly supplied by Dr. Valentina Herbring (Tampé lab), *tris*NTA headgroup and thio-*tris*NTA was synthesized by Katrin Schanner (Tampé lab). *tris*NTA^{AF647}, His_6-SGGGSGGG-C^{AF647}-A-NH_2 was generously contributed by Dr. Ralph Wieneke (Wieneke lab) and His_6-mCherry was kindly provided by Dr. Simon Trowitzsch (Trowitzsch lab). HeLa Kyoto Flp-In T-Rex cells stably containing the His_6-Y_2R^{mEGFP} plasmid were produced and kindly provided by Dr. Florencia Maria Sanchez (Tampé lab).

Table 2: List of chemicals used in this study

Substance	Supplier
(1-Cyano-2-ethoxy-2-oxoethylideneaminooxy) dimethylamino-morpholino-uronium hexafluorophosphate (COMU)	Iris Biotech
(*R*)-*tert*-Butanesulfinamide	Alfa Aesar
1-(Trimethylsiloxy)-1-ethoxycyclopropane	Sigma-Aldrich
1,2-Ethanedithiol (EDT)	Sigma-Aldrich
1,4-Dithiothreitol (DTT)	Carl Roth
1-Hydroxybenzotriazol (HOBt · H_2O)	Sigma-Aldrich
2-(4-(2-Hydroxyethyl)-1-piperazinyl)-ethane sulfonic acid (HEPES)	Carl Roth
2-Iodophenol (**13**)	Sigma-Aldrich
2-Methyl-2-propanol (^{t}BuOH)	Carl Roth
3-(Maleimido)propionic acid *N*-hydroxysuccinimide ester	Sigma-Aldrich
3-Ethoxy-3-oxopropylzinc bromide	Sigma-Aldrich
3-Glycidyloxypropyl-trimethoxysilane (GOPTS)	TCI chemicals
4-Bromoresorcinol (**18**)	Acros Organics
4-Fluoro-2-nitrobenzaldehyde (**12**)	VWR
4-Nitrophenyl chloroformate	TCI Chemicals
Acetic acid (AcOH)	VWR

Acetic anhydride (Ac_2O)	Carl Roth
Acetonitrile (MeCN)	VWR
Annexin V AF647 conjugate	Invitrogen
Blasticidin S HCl	Thermo Fisher
Bovine serum albumin (BSA)	Carl Roth
$CaCl_2 \cdot 2\ H_2O$	Carl Roth
Celite 545	Fluka
Cesium carbonate	Sigma-Aldrich
Chloromethyl methyl ether	Carbolution
Copper(I)bromide	Sigma-Aldrich
Dess-Martin periodinane (DMP)	Sigma-Aldrich
Diamino-PEG (2000 kDa)	Rapp Polymere
Dichloromethane (DCM)	VWR
Diethyl ether (Et_2O)	VWR
Dimethyl sulfoxide (DMSO)	Acros Organics
Dulbecco´s Modified Eagle Medium (DMEM)	Gibco
Dulbecco´s Phosphate Buffered saline (PBS)	Gibco
Ethanol (EtOH)	Sigma-Aldrich
Ethyl 4-chloroacetoacetate (**19**)	Sigma-Aldrich
Ethyl acetate (EA)	Sigma-Aldrich
Ethylacetoacetate (**23**)	Sigma-Aldrich
Ethylene glycol	VWR
Ethylenediaminetetraacetic acid disodium salt dihydrate (EDTA $\cdot 2\ H_2O$)	Carl Roth
Fetal calf serum (FCS)	Sigma-Aldrich
Fmoc-ethylenediamine $\cdot$ HCl (Fmoc-EDA)	VWR
GlutaMAX	Gibco
Halt protease inhibitor cocktail EDTA-free	Thermo Fisher
HCl, 37%	VWR
Hellmanex	Hellman
Hygromycin	Merck

Imidazole	Carl Roth
Isopropanol (*i*PrOH)	VWR
Live cell imaging solution (LCIS)	Invitrogen
Manganese(IV) oxide	Acros Organics
Methanol (MeOH)	VWR
Methyl-PEG_4-NHS ester (MS-PEG_4)	Thermo Fisher
$MgCl_2$	Carl Roth
$MgSO_4$	Carl Roth
MTT Assay Kit	abcam
N,*N*-Diisopropylethylamine (DIPEA)	VWR
N,N-Dimethylacetamide (DMA)	Carl Roth
N,*N*-Dimethylformamide (DMF)	Sigma-Aldrich
N,N-Dimethylformamide dimethyl acetal	Sigma-Aldrich
Na_2SO_4	VWR
NaCl	Sigma-Aldrich
$NaHCO_3$	Carl Roth
NaOH	Carl Roth
N-Ethyl-*N*'-(3-dimethylaminopropyl)carbodiimide · HCl (EDC · HCl)	Iris Biotech
N-Hydroxysuccinimide (NHS)	Fluka
$NiCl_2 \cdot 6\ H_2O$	Sigma-Aldrich
N-Methylpyrolidone (NMP)	Sigma-Aldrich
NucBlue live ready probes reagent (Hoechst33342)	Invitrogen
Palladium(II) acetate	Sigma-Aldrich
para-Toluolsulfonic acid (PTSA)	Carl Roth
2-Amino-2-(hydroxymethyl)propane-1,3-diol (Tris)	VWR
Phenol	Sigma-Aldrich
Phenylsilane	Sigma-Aldrich
Piperidine	Alfa Aesar
Poly-L-lysine (PLL)	Sigma-Aldrich
Potassium carbonate	Carl Roth

Pyridin	Sigma-Aldrich
Slow gelling 3-D life PVA-PEG hydrogel kit	Cellendes
tert-Butylbromoactetate	Carbolution
Thioanisole	Sigma-Aldrich
Thioglycerol	Cellendes
Titanium(IV) ethoxide	Alfa Aesar
Toluene	Acros Organics
Triethylamine (TEA)	Sigma-Aldrich
Triethylsilane (Et_3SiH)	Sigma-Aldrich
Trifluoroacetic acid (TFA)	Carl Roth
Triisopropylsilane (TIPS)	Sigma-Aldrich
Triphosgene	Sigma-Aldrich
Tris(2-carboxyethyl)phosphine · HCl (TCEP)	Sigma-Aldrich
Tween-20	Carl Roth
Zinc iodide	VWR
Zinc powder	Sigma-Aldrich
3-Aminopropyl-trimethoxysilan	Sigma-Aldrich

Table 3: Fluorophores used in this study

Fluorophore	Supplier
Alexa Fluor 647 maleimide (AF647)	Thermo Fisher
ATTO390 carboxylic acid (ATTO390)	ATTO-Tec
Oregon Green488 NHS (OG488)	Thermo Fisher
Rhodamine B carboxylic acid (RB)	Santa Cruz

Table 4: Building blocks and resin used for SPPS

Building block	Supplier
Fmoc-*L*-Ala-OH	Carbolution
Fmoc-*L*-Cys(Trt)-OH	Carbolution
Fmoc-*L*-Gly-OH	Carbolution
Fmoc-*L*-His(Trt)-OH	Carbolution
Fmoc-*R*-Anp-OH	Alfa Aesar
Fmoc Wang resin	Sigma-Aldrich

Table 5: Buffers used in this study

Buffer	Composition
10x HBS buffer pH 7.2 (hydrogel kit)	0.5 M HEPES/NaOH pH 7.2, 1.1 M NaCl, 0.05 M KCl, 10 mg/mL glucose, 0.2 M NaH_2PO_4, 0.2 mg/mL phenol red
Annexin binding buffer	10 mM HEPES/NaOH pH 7.4, 140 mM NaCl, 2.5 mM $CaCl_2$
Borate buffer	50 mM borate pH 8.4, 1 mM EDTA,
Dulbecco´s phosphate buffer saline (PBS buffer)	8 mM Na_2HPO_4, 1.5 mM KH_2PO_4 pH 7.4, 2.7 mM KCl, 138 mM NaCl
TBS-T	50 mM Tris/HCl pH 7.5, 150 mM NaCl, 0.5% Tween-20, v/v
HBS	20 mM HEPES/NaOH pH 7.2, 150 mM NaCl

Table 6: List of instruments and equipment used in this study

Instrument/Equipment	Company
µ-Dish 35 mm, high grid-500 glass bottom	Ibidi
365 nm LED	Thorlabs
405 nm power LED	Thorlabs
Cell culture plates, 6 well	Greiner
Clariostar plate reader	BMG Labtech
Confocal laser scanning microscope LSM880 NLO	Zeiss
CS2010 curing System	Thorlabs
DC2200 LED Driver	Thorlabs
Digital handheld optical power meter console + photometer	Thorlabs
Surveyor MSQ ESI-MS	ThermoFisher
Voyager-DE-STR MADI-TOF-MS	Applied Biosystems
Femto low-pressure plasma system	Diener Electronics
Glass slides (24 mm ø, 160-190 mm)	Menzel
Jasco HPLC 2000 with MD-2010	Jasco Deutschland
Jasco HPLC 2000 with MD-2018 and AS-2057	Jasco Deutschland
Liberty blue	CEM
Nanodrop 1000	PEQLab
ILF-835 integrative sphere	Jasco Deutschland
FP-8500 fluorescence spectrometer	Jasco Deutschland
SpectraPro 300i spectrograph	Acton Research
EEV 400_1340F CCD-camera	Roper Scientific
NMR spectrometer AV250/AV400/AV500/AV600	Bruker
PerfectSil C_{18} column 250 x 10 mm 300 ODS, 5 µm analytical	MZ Analysentechnik
PerfectSil C_{18} column 250 x 22 mm 300 ODS, 5 µm semi-preparative	MZ Analysentechnik

3.2. Methods

3.2.1. Chemical methods

3.2.1.1. Microwave-assisted solid phase peptide synthesis of TPA-*tris*NTA peptide backbone

TPA-*tris*NTA peptide backbone was synthesized *via* Fmoc-based SPPS on a pre-loaded Fmoc-His(Trt)-Wang resin as a solid support with a Liberty 2 microwave peptide synthesizer using the method described in Table 7. Individually customized coupling method for each aa is listed in Table 7. Prior to synthesis additional swelling of the resin for 15 min in DMF took place. All coupling reactions except coupling of **43** (single coupling) were done twice with 0.2 M of Fmoc-protected aa, 0.5 M DIC, and 0.5 M HOBt monohydrate in DMF.

Table 7: Protocol of microwave assisted SPPS of TPA-*tris*NTA peptide backbone. Coupling conditions of each aa are listed in Table 8. In case of photoactivatable aa derivative **43** steps 7 and 8 were not carried out.

Step	Process	Reagent	t (min)	T (°C)	V (mL)
1	Swelling	DMF	5.0		10.0
2	Initial deprotection	20% (v/v) piperidine/DMF, 0.1 M HOBt	0.5	60	3.0
3	Washing	DMF	-	25	2.0
4	Deprotection	20% (v/v) piperidine/DMF, 0.1 M HOBt	3.0	60	3.0
5	Washing x3	DMF	-	25	3.0
6	Coupling	0.2 M aa, 0.5 M DIC, 0.5 M HOBt, DMF	see Table 8		2.5
7	Washing x3	DMF	-	25	3.0
8	Coupling	0.2 M aa, 0.5 M DIC, 0.5 M HOBt, DMF	see Table 8		2.5
9	Washing x3	DMF	-	25	3.0

Table 8: Coupling conditions for each aa used for SPPS of the TPA-*tris*NTA backbone.

aa	Microwave power (W)	t (min)	T (°C)
Fmoc-His(Trt)-COOH	34	6.5	50
Fmoc-Gly-COOH	30	5.5	60
43	10	42	30
Fmoc-Cys(Trt)-COOH	30	5.5	60
Fmoc-Ala-COOH	30	5.5	60

3.2.1.2. Manual solid phase peptide synthesis of PA-*tris*NTA peptide backbone

The PA-*tris*NTA peptide backbone was manually synthesized on a pre-loaded Fmoc-His(Trt)-Wang resin as a solid using the method described in Table 9. Prior to synthesis swelling of the resin for 30 min in DMF took place. All coupling reactions were done twice with 0.6 mM of Fmoc-protected aa, 0.6 mM COMU, and 1.2 mM DIPEA in DMF. Fmoc-aa, COMU and DIPEA in DMF were preincubated for 5 min before addition to the resin.

Table 9: Procedure of manual peptide backbone synthesis of PA-*tris*NTA.

Step	Process	Reagent	t [min]	V [mL]
1	Deprotection	20% (v/v) piperidine/DMF	15	3.0
2	Washing x3	DMF	-	3.0
3	Coupling	Fmoc-aa (3 eq.), COMU (3 eq.), DIPEA (6 eq.), DMF	30	2.0
4	Washing x3	DMF	-	3.0
5	Coupling	Fmoc-aa (3 eq.), COMU (3 eq.), DIPEA (6 eq.), DMF	30	2.0
6	Washing x3	DMF	-	3.0

3.2.1.3. Manual coupling of carboxy-*tris*NTA to peptide backbone

A solution of O^{t}Bu-protected carboxy-*tris*NTA (3 eq.) in 1 mL DMF was prepared as well as a solution of COMU (3 eq.) and DIPEA (6 eq.) in 1 mL DMF. Both solutions were combined and incubated at RT for 5 min before addition to the deprotected resin. Coupling proceeded for 2 h at RT under gentle shaking. Successful coupling was controlled by TNBS test (section 3.2.1.5). In case coupling was incomplete the procedure was repeated.

3.2.1.4. TFA-mediated cleavage of peptides from resin

The resin was washed three times with each DMF, DCM, MeOH, Et_2O respectively before dried under vacuum for 3 h. Following, the cleavage mixture containing 95% (v/v) TFA and 5% of scavengers (water, EDT 2.5% v/v each) was added to the dry resin and incubated for 2 h at RT under gentle shaking. Afterwards the peptide was precipitated in ice-cold Et_2O, pelleted, and washed with ice-cold Et_2O. This was repeated five times. Finally, the pellet was dissolved in $^tBuOH/H_2O$ (4:1, v/v) and lyophilized.

3.2.1.5. Deprotection control or coupling control *via* TNBS test

The status of deprotection or coupling was checked *via* 2,4,6-Trinitrobenzene-1-sulfonic acid (TNBS) test by detection of a primary amine at the *N*-terminus. Therefore, some resin beats were placed in an Eppendorf tube and washed by careful addition and removal of DMF (500 µL). After removal of most of the DMF, three drops of 1% (v/v) TNBS in DMF and three drops of 10% (v/v) DIPEA in DMF were added and incubated for 5 min at RT under gentle shaking. Then the beads were washed as before and transferred to a coverslip for analysis under an optical light-microscope. Orange to red colored beads indicate primary amine, whereas colorless beads mean no free primary amine.

3.2.1.6. Nuclear magnetic resonance spectroscopy

^1H and ^{13}C NMR spectra were recorded on Bruker AV250, AV400, AV500 or AV600. NMR signals were calibrated on solvent signals. ^1H-NMR: $CDCl_3$: 7.26 ppm; DMSO-d_6: 2.50 ppm; ^{13}C-NMR: $CDCl_3$: 77.16 ppm; DMSO-d_6: 39.52 ppm. ^1H-NMR data are presented as chemical shift in ppm (multiplicity, coupling constant, integration). The following abbreviations are used in reporting NMR-Data: s, singlet; d, doublet; t, triplet; q, quartet; dd, doublet of doublets; m, multiplet.

3.2.1.7. Reverse-phase C_{18}-high performance liquid chromatography

Lyophilized raw product was purified by semipreparative RP-C_{18}-HPLC on a Jasco HPLC 2000 equipped with a PerfectSil C_{18} column (250 x 10 mm 300 ODS, 5 µm) with a constant flowrate of 4 mL/min. The mobile phase consisted of solution A: 0.1% (v/v) TFA (aq.) and solution B: MeCN + 0.1% (v/v) TFA. The purity of the compounds was controlled by analytical RP-C_{18}-HPLC with a PerfectSil C_{18} column (250 x 4 mm 300 ODS, 5 µm) with a constant flowrate of 1 mL/min.

Chromatograms were examined at 220 nm, 280 nm, and optionally at 400 nm. Elution gradients are listed in Table 10.

Table 10: RP-C_{18}-HPLC gradients for purification and for analysis.

Method 1		
t (min)	Solution A (%)	Solution B (%)
0	95	5
20	0	100
25	0	100
26	95	5
30	95	5

Method 2		
t (min)	Solution A (%)	Solution B (%)
0	95	5
30	30	70
31	0	100
35	0	100
36	95	5
40	95	5

3.2.1.8. Preparation of functionalized glass surfaces

3.2.1.8.1. GOPTS-functionalized glass surfaces

In order to distinguish between functionalized and non-functionalized surface, an “R” was scratched on one side of glass slides (round, 24 mm ø, 160-190 mm thick, Menzel) with a diamond pencil. Next, the glass slides were placed in custom made Teflon® holders and cleaned by consecutive sonication for 20 min in 1% (v/v) Hellmanex, acetone, ethanol, 1 M KOH (aq.) with thoroughly washing with MQ water between each step. Thereafter, the glass surface was activated by treatment with peroxymonosulfuric acid (H_2O_2:H_2SO_4, 1:2 v/v) for 30 min. The slides were washed with MQ water, dried in a nitrogen stream, followed by addition of 10 µL

3-glycidyloxypropyl-trimethoxysilane (GOPTS) and the slides were sandwiched. The stacked slides were incubated for 90 min at 75 °C in an oven. Subsequently the slides were separated and sonicated twice in acetone for 3 min before drying with a nitrogen stream. A small amount of solid diamino-PEG (2 kDa) was placed on the functionalized side of one glass slide and placed in the oven at 75 °C until the PEG melted, then the second glass slide was placed on top. The stack was incubated on a metal block in an oven at 75 °C overnight. After the PEGylation reaction, the slides were separated and washed several times with MQ water before drying with nitrogen. For variable anchoring of thiol-containing compounds the surface was modified with a maleimide head group. Therefore, 15 µL of 3-maleimidopropionic acid *N*-hydroxysuccinimide ester solution (saturated in anhydrous DMF) was placed between two slides and incubated for 2 h at RT. The slides were washed with chloroform and dried with nitrogen. Functionalization of the surface with PA-*tris*NTA or TPA-*tris*NTA was achieved by incubation with 20 µL of the respective compound (2.4 mM in HBS buffer) between two slides in the sandwich arrangement for 1 h at RT in the dark. Finally, the surfaces were washed with HBS buffer and remaining maleimide-groups were blocked by incubation with 50 mM cysteine solution (in HBS buffer) for 30 min. After washing with HBS buffer and drying with nitrogen the slides were ready for photo-patterning.

3.2.1.8.2. PLL-functionalized glass surfaces

The preparation of poly-*L*-lysin (PLL) functionalized was till the plasma cleaning analogous to section 3.2.1.8.3. 100 µL of PA-*tris*NTA (100 mM in HBS buffer) were combined with 50 µL of 3-maleimido-PEG-*N*-hydroxysuccinimide ester (Mal-PEG-NHS) (200 mM in HBS buffer, 3 kDa, Rapp Polymere) and preincubated for 15 min before addition of 250 µL PLL (15-30 kDa, 1.5 mM in borate buffer). The combined mixture was incubated overnight at RT. The next day, 15 µL of the PLL-PEG-PA-*tris*NTA solution was added between to glass slides and incubated for 2 h in a humidity chamber. Remaining PLL-PEG-PA-*tris*NTA solution can be stored at -80 °C. Subsequently, the slides were carefully separated and extensively washed with HBS buffer.

3.2.1.8.3. APTES-functionalized glass surfaces

Similar to functionalization with GOPTS (section 3.2.1.8.1) glass slides (round, 24 mm ø, 160-190 mm thick, Menzel) were washed with MQ water, sonicated for 20 min in acetone, dried by a nitrogen stream, followed by plasma cleaning (0.3 mbar, 80%, Diener Electronics) with oxygen for 10 min. Subsequently, the slides were incubated in a Teflon holder with a solution consisting of

25 mL methanol, 1.25 mL acetic acid and 0.75 mL 3-aminopropyl-triethoxysilane (APTES) for 20 min at RT, sonicated for 1 min and again incubated for 20 min. A mixture consisting of 10 µL PA-*tris*NTA or TPA-*tris*NTA (800 µM in MQ water), 10 µL 3-maleimidopropionic acid *N*-hydroxysuccinimide ester (400 µM in MQ water) and 10 µL of sodium hydrocarbonate (0.1 M in MQ water) were preincubated for 15 min at RT, before placing it between two functionalized glass slides in a sandwich like manner. The reaction was allowed to proceed overnight in a humidity chamber protected from light. The next day, the glass slides were extensively washed with TBS-T buffer and dried with a nitrogen stream. Thereafter, the surfaces were consecutively incubated with imidazole (1 M in MQ water, 3 min), EDTA (100 mM in MQ water, 3 min), $NiCl_2$ (10 mM in MQ water, 5 min) with washing steps using TBS-T buffer between each treatment. If not state otherwise, surfaces were used for photopatterning without further processing.

Two strategies were tested to prevent non-specific binding to the glass slides. Either surfaces were incubated for 30 min with a MS-PEG_4 solution (25 mM in 0.1 M $NaHCO_3$ aq., 3 kDa) or in 5% BSA in HBS buffer for 10 min. Finally, the surfaces were washed with TBS-T and dried in a nitrogen stream.

3.2.1.9. Ni(II)-loading of *tris*NTA moieties on functionalized glass surfaces

(T)PA-*tris*NTA functionalized glass slides were placed in a Teflon holder and consecutive incubated with imidazole (1 M in MQ water, 1 min), EDTA (100 mM in MQ water, 1 min) and $NiCl_2$ (10 mM in MQ water, 5 min) with extensive washing with TBS-T buffer between each step. After final washing with TBS-T buffer the surfaces were dried with in a nitrogen stream.

3.2.1.10. Preparation of (T)PA-*tris*NTA functionalized hydrogels

Hydrogels were prepared from commercially available slow gelling 3-D Life PVA-PEG hydrogel Kit (Cellendes) in gridded imaging dishes (µ-Dish 35 mm, high Grid-500, ibidi). Gel formation was performed according Figure 13 and Table 12. First, 10x HBS buffer, water and maleimide-PVA were mixed, then secondly PA-*tris*NTA or TPA-*tris*NTA solution (aq.) was added and immediately mixed *via* pipetting. The mixture was incubated for 5 min at RT in the dark. After a quick spin down (700 g, 10 s), the reaction mixture was added to the dithiol-linker placed in the middle of the imaging dish and quickly homogenized by pipetting. The network formation was allowed to proceed for 10 min in the dark. Successful solidification was verified by careful touching with a pipet tip. Finally, the hydrogel was equilibrated with 1 mL HBS buffer.

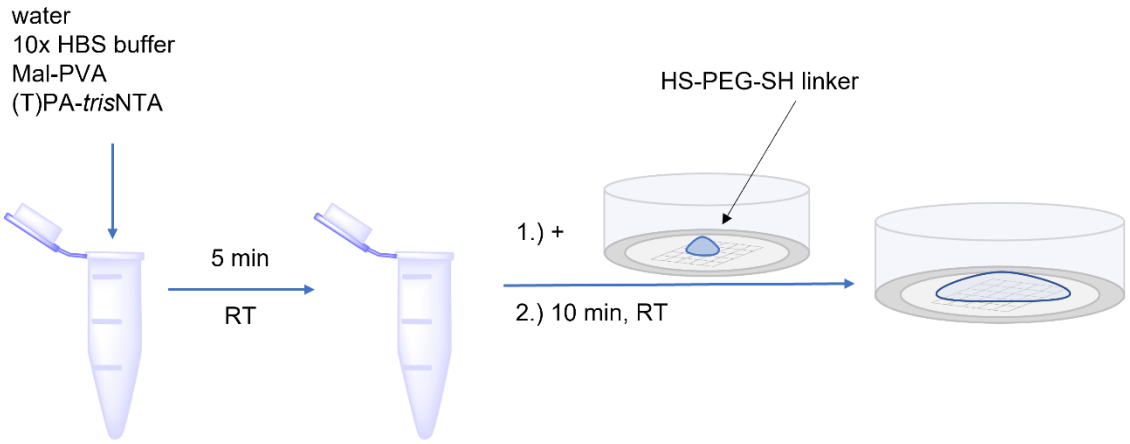

Figure 13: Schematic illustration of workflow for preparation of functionalized hydrogels. Water, 10x HBS buffer pH 7.2, maleimide-polyvinylalcohole (Mal-PVA) and TPA-*tris*NTA or PA-*tris*NTA were preincubated. Following the mixture was combined with the dithiol-linker in a gritted, glass bottom microscope dish.

Table 11: Hydrogel composition for functionalized hydrogels used for POI-tethering

Component	c (mM)	V (µL)
10x HBS buffer		0.60
Mal-PVA SG	30.00	1.20
(T)PA-*tris*NTA	0.79	1.52
dithiol linker	20.00	1.74
water		0.98
total volume		6.04

3.2.1.11. Ni(II)-loading of *tris*NTA moieties inside hydrogels

Solidified hydrogels were covered with $NiCl_2$ (1 mL, 10 mM in MQ water) and incubated for 30 min under gentle shaking. Thereafter the hydrogel was washed five times with HBS buffer (2 mL).

3.2.1.12. POI immobilization inside PA-*tris*NTA or TPA-*tris*NTA functionalized hydrogels

After photo-patterning and Ni(II)-loading, written structures inside the hydrogel were visualized by incubation with POI-His_6 (1 mL, 300 nM in HBS buffer). After 30 min evolution in the dark with gentle shaking, the POI-His_6 solution was removed. For following removal of unbound POI, the

hydrogel was washed in a beaker with HBS buffer (50 mL) with gentle agitation. After 30 min under gentle shaking, the dish was taken out and dried externally with a paper towel. Finally, the hydrogel was covered with 1 mL of fresh HBS buffer and subsequently imaged *via* confocal laser-scanning microscopy (LSM 880 AxioObserver).

3.2.1.13. Activation of zinc powder

The activation of zinc powder was conducted as reported.[162] Zinc powder (0.13 g, 2.00 mmol) was suspended in MQ water (468 µL) and concentrated HCl (52 µL) and pivoted for 20 min at RT. The aqueous phase was decanted, and zinc was washed with MQ water (3x 450 µL), acetone (3x 450 µL), Et_2O (3x 450 µL) consecutive. Following the zinc was dried *in vacuo* for 1 h before it was used for further reactions.

3.2.1.14. Synthesis of (4-(2-iodophenoxy)-2-nitrobenzaldehyde (14)

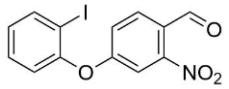

14

The synthesis was conducted as described by Friedrich *et al.*[163] Briefly, 4-fluoro-2-nitro-benzaldehyde (3.52 g, 15.90 mmol, 1 eq.) was dissolved in pyridine (50 mL). 2-Iodophenol (2.68 g, 15.90 mmol, 1 eq.), copper(I) bromide (2.28 g, 15.9 mmol, 1 eq.), and K_2CO_3 (4.39 g 31.8 mmol, 2 eq.) were added, and the reaction was heated to 60 °C under an argon atmosphere. After 24 h the reaction was cooled to RT and the pyridine was evaporated under reduced pressure. The residue was dissolved in Et_2O (100 mL), insoluble solid was filtered off, and the organic phase was washed successively with NaOH (50 mL, 1M), H_2O (200 mL), and brine (100 mL). The organic phase was dried with Na_2SO_4 and evaporated under reduced pressure. The residue was separated by column chromatography (CH:EA 20:1, v/v). **14** was obtained as a yellow solid (46% yield, 2.7 g, 7.31 mmol).

^{1}H-NMR (400 MHz, $CDCl_3$) δ[ppm] = 10.25 (s, 1H), 7.92 (d, *J* = 8,6, 1H), 7.88 (dd, *J* = 7.9, *J* = 1.5, 1H), 7,43 (d, J = 2.4 Hz,1 H), 7.39 (td, *J* = 8.1, 1.5 Hz, 1H), 7.19 (s, 1H), 7.14 (dd, *J* = 8.6, 2.4, Hz, 1H), 7.08 – 6.97 (m, 2H).

ESI-MS MW calculated for $C_{13}H_7INO_4$ $[M-H]^-$ 367.95 Da, found 367.89 Da.

3.2.1.15. Synthesis of 2-(4-(2-iodophenoxy)-2-nitrophenyl)-1,3-dioxolane (15)

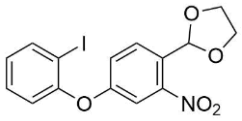

15

2-(4-(2-Iodophenoxy)-2-nitrophenyl)-1,3-dioxolane was synthesized as described before.[163] Briefly, 4-(2-Iodophenoxy)-2-nitrobenzaldehyde **14** (2.32 g, 6.29 mmol, 1 eq.) was dissolved in toluene (30 mL). Ethylene glycol (2.10 mL, 2.34 g, 37.70 mmol, 6 eq.) and *p*-toluenesulfonic acid (0.19 g, 1.00 mmol, 0.6 eq.) were added and the reaction was then heated to reflux under argon atmosphere. After 24 h the reaction mixture was diluted with DCM (10 mL) and washed with saturated $NaHCO_3$ (50 mL). The aqueous phase was extracted with DCM (3x 40 mL) and the combined organic phase was then dried with Na_2SO_4 and evaporated under reduced pressure. The residue was purified by column chromatography (CH:EA 5:1, v/v) to afford **15** as a yellow solid (97% yield, 2.52 g, 6.10 mmol)

^{1}H-NMR (400 MHz, $CDCl_3$) δ[ppm] = 7.84 (dd, *J* = 7.9, 1.5 Hz, 1H), 7.68 (d, *J* = 8.7 Hz, 1H), 7.36 – 7.28 (m, 2H), 7.19 (s, 1H), 7.08 (dd, *J* = 8.7, 2.5 Hz, 1H), 6.99 – 6.88 (m, 2H), 6.33 (s, 1H).

3.2.1.16. Synthesis of 2-(1,3-dioxolan-2-yl)-3-nitrodibenzofuran (16)

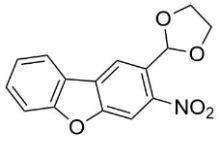

16

2-(1,3-Dioxolan-2-yl)-3-nitrodibenzofuran **16** was synthesized as reported.[163] **15** (0.26 g, 0.63 mmol, 1 eq.) was solved in dimethylacetamide (1.50 mL). After addition of Cs_2CO_3 (0.41 g, 1.26 mmol, 2 eq.), $Pd(OAc)_2$ (43 mg, 0.19 mmol, 0.3 eq.), and H_2O (30 µL) the reaction was heated to 80 °C and allowed to proceed for one week. Following the reaction mixture was filtrated over Celite. The filtrate was diluted with EA (3 mL) and the organic phase was washed with water and brine (3x 5 mL). The organic phase was then dried with Na_2SO_4 and evaporated under reduced pressure. The residue was purified by column chromatography (CH:EA 5:1, v/v) to afford **16** as a yellow solid (81% yield, 150 mg, 0.5 mmol)

^{1}H-NMR (400 MHz, $CDCl_3$) δ[ppm] = 8.37 (s, 1H), 8.17 (s, 1H), 8.03 (d, *J* = 7.8 Hz, 1H), 7.66 – 7.55 (m, 2H), 7.43 (m, 1H), 6.62 (s, 1H), 4.12 (s, 4H).

3.2.1.17. Synthesis of 3-nitrodibenzofuran-2-carbaldehyde (17)

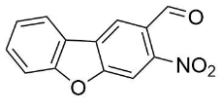

17

3-Nitrodibenzofuran-2-carbaldehyde was prepared as described by Friedrich *et al.* except of the purification step.[163] Therefore **16** (0.54 g, 1.89 mmol) was stirred in THF (5 mL) and HCl (4 mL, 1 M) at RT. The reaction progress was monitored by TLC analysis (CH:EA, 5:1, v/v). After one week the reaction was completed and the reaction mixture was extracted with EA (3x10 mL). The organic phase was dried with $MgSO_4$ and evaporated under reduced pressure. The residue was purified by column chromatography (CH:EA, 10:1, v/v) to obtain **17** as a yellow solid (85% yield, 0.38 g, 1.61 mmol)

^{1}H-NMR (250 MHz, $CDCl_3$) δ[ppm] = 10.50 (s, 1H), 8.56 (s, 1H), 8.32 (s, 1H), 8.08 (d, *J* = 7.8 Hz, 1H), 7.74 – 7.59 (m, 2H), 7.56 – 7.42 (m, 1H).

^{13}C-NMR (101 MHz, $CDCl_3$) δ[ppm] = 187.75, 158.64, 157.05, 131.21, 130.30, 129.36, 127.22, 124.58, 122.20, 122.13, 122.09, 112.54, 108.89.

ESI-MS MW calculated for $C_{13}H_6NO_4$ $[M-H]^-$ 240.04 Da, found 240.06 Da.

3.2.1.18. Synthesis of 6-bromo-4-(chloromethyl)-7-hydroxy-2*H*-chromen-2-one (20)

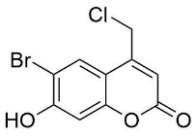

20

6-Bromo-4-(chloromethyl)-7-hydroxy-2H-chromen-2-one **20** was synthesized as described by Hagen *et al.*[164] Briefly, 4-bromoresorcinol **18** (4.28 g, 22.77 mmol, 1 eq.) was dissolved in methanesulfonic acid (34 mL) and supplemented with ethyl 4-chloroacetoactetate **19** (4.50 mL, 5.49 g, 33.5 mmol, 1.5 eq.). The reaction was stirred for 3 h at RT, then poured into ice-cold water (50 mL) and stirred for 1 h. The precipitate was filtered off and washed with ice-cold water. After lyophilization the solid was purified by column chromatography (CH:EA:HOAc, 50:50:1, v/v) to obtain **20** as a colorless solid (90% yield, 5.88 g, 20.49 mmol).

^{1}H-NMR (400 MHz, DMSO-d_6) δ[ppm] = 11.58 (s, 1H), 8.01 (s, 1H), 6.93 (s, 1H), 6.49 (s, 1H), 5.01 (s, 2H).

^{13}C-NMR (126 MHz, DMSO-d_6) δ[ppm] = 160.15, 157.98, 154.52, 150.59, 129.49, 112.57, 111.14, 106.64, 103.73, 41.68.

ESI-MS MW calculated for $C_{10}H_5BrClO_3$ $[M-H]^-$ 286.92 Da, found 286.87 Da.

3.2.1.19. Synthesis of 6-bromo-7-hydroxy-4-(hydroxymethyl)-2*H*-chromen-2-one (21)

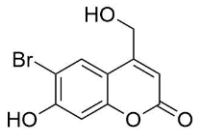

21

20 (2.50 g, 8.68 mmol) was suspended in MQ water (500 mL) and heated to reflux for 48 h. The resulting solution was allowed to cool to RT. The precipitate was filtered off and washed with ice-cold water. After lyophilization to dryness the product **21** was maintained as an off-white solid in quantitative amounts (2.50 g, 8.68 mmol).

^{1}H-NMR (400 MHz, DMSO-d_6) δ[ppm] = 11.39 (s, 1H), 7.83 (s, 1H), 6.90 (s, 1H), 6.28 (s, 1H), 4.70 (s, 2H).

^{13}C-NMR (101 MHz, DMSO-d_6) δ[ppm] = 160.12, 157.02, 155.92, 153.64, 128.12, 110.97, 107.67, 105.93, 103.04, 59.04.

ESI-MS MW calculated for $C_{10}H_6BrO_4$ $[M-H]^-$ 268.95 Da, found 269.03 Da.

3.2.1.20. Synthesis of 6-bromo-7-hydroxy-4-methyl-2*H*-chromen-2-one (24)

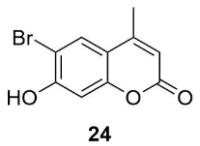

24

6-bromo-7-hydroxy-4-methyl-2H-chromen-2-one **24** was prepared analogous to **20**. To a solution of 4-bromoresorcinol **18** (3.0 g, 15.87 mmol, 1 eq.) in methanesulfonic acid (32 mL) was added ethyl ethylacetoacetate **23** (3.03 mL, 3.10 g, 23.81 mmol, 1.5 eq.). The reaction was stirred for 3 h

at RT, then poured into ice-cold water (50 mL) and stirred for 1 h. The precipitate was filtered off and washed with ice-cold water. After lyophilization the solid was purified by column chromatography (CH:EA, 1:1, v/v) to obtain **24** as a colorless solid (92% yield, 3.71 g, 14.6 mmol).

^{1}H-NMR (400 MHz, DMSO-d_6) δ[ppm] = 11.43 (s, 1H), 7.89 (s, 1H), 6.89 (s, 1H), 6.20 (s, 1H), 2.39 (s, 3H).

^{13}C-NMR (101 MHz, DMSO-d_6) δ[ppm] = 159.79, 157.17, 153.58, 152.76, 129.07, 113.42, 111.21, 105.92, 102.96, 18.05.

ESI-MS MW calculated for $C_{10}H_6BrO_3$ $[M-H]^-$ 252.96 Da, found 252.96 Da.

3.2.1.21. Synthesis of 6-bromo-7-hydroxy-2-oxo-2*H*-chromene-4-carbaldehyde (26)

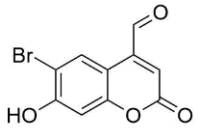

26

Synthesis of 6-bromo-7-hydroxy-2-oxo-2H-chromene-4-carbaldehyde 26 was adapted from Ito *et al.*[165] **24** (0.50 g, 1.97 mmol, 1 eq.) was added to a suspension of SeO_2 powder (0.35 g, 3.15 mmol, 1.5 eq.) in anhydrous 1,4-dioxane (10 mL). The reaction mixture was stirred for 24 h at 120 °C. Following the reaction mixture was filtered and the solvent was evaporated *in vacuo.* The remainings were purified *via* column chromatography (CH:EA, 2:1, v/v). The desired product **26** was received as a yellow solid (51% yield, 0.27 g, 1.00 mmol).

^{1}H-NMR (400 MHz, DMSO-d_6) δ[ppm] = 10.06 (s, 1H), 8.59 (s, 1H), 6.98 (s, 1H), 6.94 (s, 1H).

ESI-MS MW calculated for $C_{10}H_4BrO_3$ $[M-H]^-$ 266.94 Da, found 266.94 Da.

3.2.1.22. Synthesis of (*E*)-7-(diethylamino)-4-[2-(dimethylamino)vinyl]-2*H*-chromen-2-one (28)

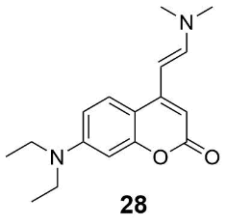

28

To commercially available 7-diethylamino-4-methyl-2-oxo-2H-chromen (1.0 g, 4.32 mmol, 1 eq.) DMF-DMA (862 µL, 0.77 g, 6.49 mmol, 1.5 eq.) was added in anhydrous DMF (3 mL). The reaction mixture was stirred at 160 °C for 24 h, cooled to RT, and poured in ice-cold MQ water (10 mL). The resulting suspension was filtrated, and the precipitate was washed three times with ice-cold MQ water (10 mL). The precipitate was lyophilized to dryness to obtain the product as a yellow solid (98% yield, 1.22 g, 4.26 mmol).

^{1}H-NMR (400 MHz, $CDCl_3$) δ[ppm] = 7.63 (d, *J* = 8.2 Hz, 1H), 7.29 (s, 1H), 6.83 – 6.49 (m, 2H), 5.95 (s, 1H), 5.22 (d, *J* = 12.9 Hz, 1H), 3.42 (q, *J* = 7.0 Hz, 4H), 3.02 (s, 6H), 1.22 (t, *J* = 7.1 Hz, 6H).

ESI-MS MW calculated for $C_{17}H_{23}N_2O_2$ $[M+H]^+$ 287.18 Da, found 287.18 Da.

3.2.1.23. Synthesis of 7-(diethylamino)-2-oxo-2*H*-chromene-4-carbaldehyde (29)

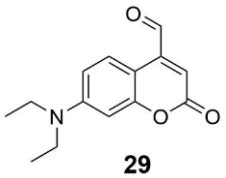

29

To a stirred suspension of **28** (1.2 g, 4.19 mmol, 1 eq.) in water:THF (1:1, v/v, 90 mL) was added sodium periodate (2.69 g, 12.5 mmol, 3 eq.) and stirred for 24 h at RT. Subsequently, the suspension was filtered over silica gel and washed with EA until the silica gel stayed colorless. The organic solvents were evaporated under reduced pressure. The residue was washed with DCM (3x 50 mL) and the combined organic layers were dried over Na_2SO_4, filtrated, and evaporated under reduced pressure. The crude product was purified by column chromatography (CH:EA 3:1, v/v). **29** was obtained as a red solid (85% yield, 0.87 g, 3.55 mmol).

^{1}H-NMR (400 MHz, $CDCl_3$) δ[ppm] = 10.03 (s, 1H), 8.32 (d, *J* = 9.2 Hz, 1H), 6.67 (dd, *J* = 9.2, 2.4 Hz, 1H), 6.57 (d, *J* = 2.4 Hz, 1H), 6.47 (s, 1H), 3.43 (q, *J* = 7.1 Hz, 4H), 1.22 (t, *J* = 7.1 Hz, 6H).

^{13}C-NMR (126 MHz, $CDCl_3$) δ[ppm] = 192.41, 161.52, 157.17, 149.59, 143.83, 127.47, 119.00, 111.29, 100.25, 46.30, 12.26.

ESI-MS MW calculated for $C_{14}H_{16}NO_3$ $[M+H]^+$ 246.11 Da, found 246.13 Da.

3.2.1.24. Synthesis of (*R*)-*N*-(4,5-dimethoxy-2-nitrobenzylidene)-2-methylpropane-2-sulfinamide (31)

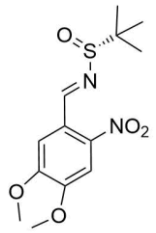

31

(*R*)-*N*-(4,5-Dimethoxy-2-nitrobenzylidene)-2-methylpropane-2-sulfinamide **31** was synthesized as described by Liu *et al*.[166] NV carbaldehyde **30** (0.25 g, 1.2 mmol, 1 eq.) was added into a flame-dried flask and solved in anhydrous THF (3 mL) under argon atmosphere. To this solution (*R*)-*tert*-butylsulfinamide (0.12 g, 1.0 mmol, 0.83 eq.) and $Ti(OEt)_2$ (0.55 g, 2.4 mmol, 2 eq.) was added and stirred at RT. After 24 h brine (3 mL) was added under vigorous stirring. The suspension was filtered over Celite and the filter cake was washed with EA. The filtrate was washed with brine (3x6 mL). The combined organic phases were dried with Na_2SO_4, filtered and the solvent was evaporated under reduced pressure. The remaining solids were purified by column chromatography (CH:EA 2:1, v/v). **31** was retained as a yellow solid (88% yield, 0.33 g, 1.06 mmol).

^{1}H-NMR (400 MHz, $CDCl_3$) δ[ppm] = 9.10 (s, 1H), 7.62 (s, 1H), 7.48 (s, 1H), 4.02 (s, 6H), 1.29 (s, 9H).

ESI-MS MW calculated for $C_{13}H_{18}N_2O_5S$ $[M+H]^+$ 315.09 Da, found 314.87 Da.

3.2.1.25. Synthesis of (*R*)-2-methyl-*N*-((3-nitrodibenzofuran-2-yl)methylene) propane-2-sulfinamide (33)

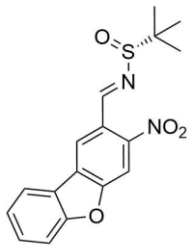

33

(R)-2-methyl-*N*-((3-nitrodibenzofuran-2-yl)methylene)propane-2-sulfinamide **33** was synthesized as reported previously.[166] A solution of NDBF carbaldehyde **17** (0.25 g, 1.05 mmol, 1 eq.) in anhydrous THF (3 mL) was stirred in a flame dried flask under argon atmosphere. Following (*R*)-*tert*-butylsulfinamide (0.11 g, 0.87 mmol, 0.83 eq.) and $Ti(OEt)_2$ (0.48 g, 2.1 mmol, 2 eq.) was added and stirred at RT. After 24 h, brine (3 mL) was added under vigorous stirring. The suspension was filtered over Celite and the filter cake was washed with EA. The filtrate was washed with brine (3x6 mL). The combined organic phases were dried with Na_2SO_4, filtered and the solvent was evaporated under reduced pressure. The remainings were purified by column chromatography (CH:EA 3:1, v/v). **31** was retained as a yellow solid (29% yield, 0.10 g, 0.30 mmol).

^{1}H-NMR (250 MHz, $CDCl_3$) δ[ppm] = 9.09 (s, 1H), 8.53 (s, 1H), 8.24 (s, 1H), 8.07 (d, *J* = 7.7 Hz, 1H), 7.71 – 7.58 (m, 2H), 7.52 – 7.42 (m, 2H), 1.34 (s, 9H).

^{13}C-NMR (101 MHz, $CDCl_3$) δ[ppm] = 159.93, 158.62, 156.36, 147.81, 130.17, 129.17, 124.86, 124.42, 122.32, 122.31, 122.12, 112.59, 109.01, 100.12, 58.54, 27.04, 22.87.

ESI-MS MW calculated for $C_{17}H_{17}N_2O_4S$ $[M+H]^+$ 345.08 Da, found 344.83 Da.

3.2.1.26. Synthesis of 6-bromo-7-(methoxymethoxy)-2-oxo-2*H*-chromene-4-carbaldehyde (38)

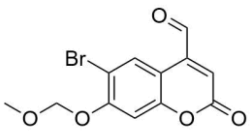

38

Bhc carbaldehyde **22** (0.25 g, 1.0 mmol, 1 eq.) was dissolved in anhydrous 1,4-dioxane (30 mL) and DMF (15 mL) and cooled to 0 °C. Following DIPEA (0.87 mL, 1.29 g, 10.0 mmol, 10 eq.) and

MOMCl (0.61 mL, 0.64 g, 8.0 mmol, 8 eq.) were added. The reaction mixture was stirred for 24 h at RT. Subsequently the solvents were removed *in vacuo* and the residue was dissolved in EA (30 mL). The solution was washed with $NaHCO_3$, MQ water and brine (30 mL each). The organic phase was dried with Na_2SO_4 and the solvent was evaporated under reduced pressure. The residue was purified by column chromatography (CH:EA 3:1, v/v) to obtain **38** as a yellow solid (89% yield, 0.28 g, 0.89 mmol).

^{1}H-NMR (250 MHz, DMSO-d_6) δ[ppm] = 10.09 (s, 1H), 8.67 (s, 1H), 7.32 (s, 1H), 7.10 (s, 1H), 5.45 (s, 2H), 3.43 (s, 3H).

^{13}C-NMR (101 MHz, DMSO-d_6) δ[ppm] = 193.42, 159.88, 155.49, 154.55, 142.29, 129.34, 123.03, 110.17, 107.98, 103.69, 94.84, 56.28.

MALDI-TOF MS MW calculated for $C_{12}H_{10Br}O_5$ $[M+H]^+$ 312.96 Da, found 313.96 Da.

3.2.1.27. Synthesis of *tert*-butyl 3-(6-bromo-7-(methoxymethoxy)-2-oxo-2H-chromen-4-yl)-3-hydroxypropanoate (39)

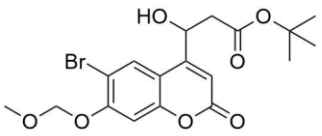

39

Tert-butyl 3-(6-bromo-7-(methoxymethoxy)-2-oxo-2H-chromen-4-yl)-3-hydroxy-propanoate **39** was synthesized analog to Seyfried *et al*.[162] To a suspension of activated zinc powder (0.26 g, 4.0 mmol, 4 eq.) in anhydrous DMF (3 mL) t*ert*-butyl bromoactetate (0.59 mL, 4.0 mmol, 4 eq.) was added and stirred at 0 °C. After 1 h, **38** (0.31 g, 1.0 mmol, 1 eq.) was added and stirred for 1 h at 0 °C. Following the reaction was quenched by addition of saturated NH_4Cl solution (10 mL). The rection mixture was filtered through silica and extracted with Et_2O (3x10 mL). The combined organic phases were dried over Na_2SO_4, filtrated, and the solvent was removed under reduced pressure. The raw product was purified by column chromatography (CH:EA:HOAc, 50:50:1, v/v). The product was obtained as a yellow solid (98% yield, 0.42 g, 0.98 mmol).

^{1}H-NMR (250 MHz, DMSO-d_6) δ[ppm] = 8.02 (s, 1H), 7.28 (s, 1H), 6.39 (s, 1H), 6.00 (d, *J* = 5.2 Hz, 1H), 5.43 (s, 2H), 4.01 (s, 1H), 3.42 (s, 3H), 2.39 (s, 2H), 1.39 (s, 9H).

ESI-MS MW calculated for $C_{18}H_{22}BrO_7$ $[M+H]^+$ 429.05 Da, found 429.00 Da.

3.2.1.28. Synthesis of *tert*-butyl-3-(7-(diethylamino)-2-oxo-2*H*-chromen-4-yl)-3-hydroxypropanoate (40)

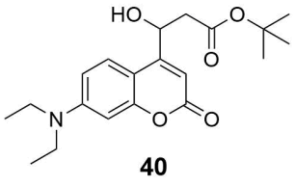

40

Preparation of *tert*-butyl-3-(7-(diethylamino)-2-oxo-2H-chromen-4-yl)-3-hydroxypropanoate was adapted from Seyfried *et al.*[162] *Tert*-butyl bromoactetate (221 µL, 1.5 mmol, 1.5 eq.) was added to a suspension of activated zinc powder (0.131 g, 2.0 mmol, 2 eq.) in 3 mL dry DMF at 0 °C. The mixture was stirred at 0 °C for 1 h followed by supplementation of **29** (0.245 g, 1.0 mmol, 1 eq.). After 1 h, the reaction was quenched by addition of saturated NH_4Cl solution (10 mL). The suspension was filtered through silica gel to remove unreacted zinc. Afterwards, the filtrate was extracted three times with Et_2O (3x10 mL). The combined organic layers were dried over Na_2SO_4 and after filtration the solvent was removed under reduced pressure. The raw product was purified by column chromatography (DCM:acetone, 20:1, v/v). The product was obtained as a yellow solid (75% yield, 270 mg, 0.75 mmol).

^{1}H-NMR (250 MHz, $CDCl_3$) δ[ppm] = 7.38 (d, *J* = 9.0 Hz, 1H), 6.58 (dd, *J* = 9.0, 2.6 Hz, 1H), 6.52 (d, *J* = 2.6 Hz, 1H), 6.30 (s, 1H), 5.34 (d, *J* = 9.6 Hz, 1H), 3.56 (d, J = 3.5 Hz, 1H), 3.41 (q, J = 7.1 Hz, 4H), 2.76 (dd, J = 16.8, 2.9 Hz, 1H), 2.60 (dd, J = 16.8, 9.4 Hz, 1H), 1.49 (s, 9H), 1.20 (t, *J* = 7.1 Hz, 6H).

^{13}C-NMR (101 MHz, $CDCl_3$) δ[ppm] = 171.40, 162.22, 156.53, 155.64, 150.30, 124.72, 108.69, 105.88, 100.00, 98.18, 82.33, 66.21, 44.81, 42.24, 28.12, 12.43.

ESI-MS MW calculated for $C_{20}H_{28}NO_5$ $[M+H]^+$ 362.19 Da, found 362.18 Da.

3.2.1.29. Synthesis of *tert*-butyl 10-(7-(diethylamino)-2-oxo-2*H*-chromen-4-yl)-1-(9*H*-fluoren-9-yl)-3,8-dioxo-2,9-dioxa-4,7-diazadodecan-12-oate (42)

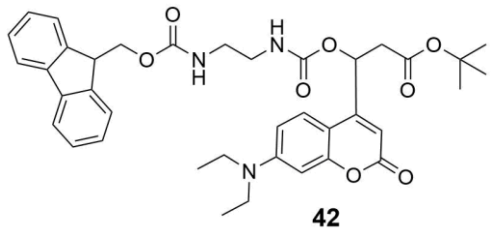

42

DIPEA (225 µL, 1.32 mmol, 4 eq.) was titrated dropwise in a solution of **40** (119 mg, 0.33 mmol, 1 eq.) in anhydrous THF (1.5 mL) at 0 °C. After 5 min incubation time, triphosgene (118 mg, 0.39 mmol, 1.2 eq.) was added and the reaction mixture was stirred at RT for 90 min. The solvent was evaporated to receive **40** chloroformate as a pale-yellow solid, which was used without additional purifications. Quantitative conversion was assumed for further reactions.

Mono-Fmoc ethylenediamine hydrochloride (210 mg, 0.66 mmol, 2 eq.) and DIPEA (225 µL, 1.32 mmol, 4 eq.) were added to a solution of the chloroformate (139 mg, 0.33 mmol, 1 eq.) in anhydrous 1,4-dioxane (2 mL). The reaction mixture was stirred for 1 d at RT, thereafter the solvent was evaporated. The remainings were dissolved in water:EA (4 mL, 1:1, v/v) and the organic layer was washed with water (2 mL) and brine (2 mL). The organic layer was dried over Na_2SO_4. After filtration, the solvent was removed under reduced pressure. The raw product was purified by column chromatography (CH:EA, 1:1, v/v). The product **42** was obtained as a pale-yellow solid (56% yield, 127 mg, 0.19 mmol).

^{1}H-NMR (600 MHz, DMSO-d_6) δ[ppm] =7.88 (d, *J* = 7.4 Hz, 2H), 7.67 (d, *J* = 7.5 Hz, 2H), 7.52 (s, 1H), 7.47 (d, *J* = 9.1 Hz, 1H), 7.40 (t, *J* = 7.3 Hz, 2H), 7.31 (t, *J* = 7.3 Hz, 2H), 7.28 (s, 1H), 6.74 (d, *J* = 9.1 Hz, 1H), 6.55 (s, 1H), 6.11 (dd, *J* = 9.0, 3.5 Hz, 1H), 5.96 (s, 1H), 4.33 – 4.24 (m, 2H), 4.19 (t, *J* = 6.9 Hz, 1H), 3.42 (q, *J* = 7.0 Hz, 4H), 3.09-3.01 (m, 4H), 2.86-2.83 (m, 1H), 2.69 – 2.58 (m, 1H), 1.38 (s, 9H), 1.11 (t, *J* = 7.0 Hz, 6H).

^{13}C-NMR (101 MHz, DMSO-d_6) δ[ppm] =168.58, 161.07, 156.48, 156.39, 155.16, 154.68, 150.75, 144.24, 144.18, 141.05, 141.04, 129.25, 127.91, 127.37, 125.47, 125.45, 125.39, 121.70, 120.42, 109.39, 105.10, 104.62, 99.86, 97.42, 90.81, 81.10, 76.67, 70.13, 67.76, 65.68, 65.66, 47.04, 44.33, 27.93, 12.62.

ESI-MS MW calculated for $C_{38}H_{44}N_3O_8$ $[M+H]^+$ 670.31 Da, found 670.19 Da.

3.2.1.30. Synthesis of 10-(7-(diethylamino)-2-oxo-2*H*-chromen-4-yl)-1-(9*H*-fluoren-9-yl)-3,8-dioxo-2,9-dioxa-4,7-diazadodecan-12-oic acid (43)

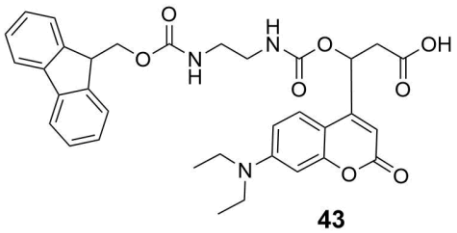

43

A solution of **42** (500 mg, 0.75 mmol) in ice-cold DCM:TFA (1:1, v/v, 8 mL) was stirred for 1 h, before it was concentrated under reduced pressure. The crude product was purified by column chromatography using RP-C_{18} silica (water: MeCN, 1:1, 1% TFA v/v%). The product **43** was obtained as a pale-yellow solid (73% yield, 337 mg, 0.55 mmol).

^{1}H-NMR (500 MHz, DMSO-d_6) δ[ppm] = 7.88 (d, *J* = 7.5 Hz, 2H), 7.67 (d, *J* = 7.4 Hz, 2H), 7.54 (s, 1H), 7.47 (d, *J* = 9.1 Hz, 1H), 7.40 (t, *J* = 7.4 Hz, 2H), 7.33-7.30 (m, 3H), 6.73 (dd, *J* = 9.1, 2.4 Hz, 1H), 6.54 (d, *J* = 2.3 Hz, 1H), 6.11 (dd, *J* = 9.3, 3.1 Hz, 1H), 5.95 (s, 1H), 4.34 – 4.25 (m, 2H), 4.20 (t, *J* = 6.8 Hz, 1H), 3.42 (q, *J* = 6.9 Hz, 4H), 3.09-3.02 (m, 4H), 2.85 (dd, *J* = 16.4, 3.3 Hz, 1H), 2.72 – 2.62 (m, 1H), 1.11 (t, *J* = 7.0 Hz, 6H).

^{13}C-NMR (126 MHz, DMSO-d_6) δ[ppm] = 171.23, 161.24, 156.61, 156.54, 155.34, 155.31, 150.88, 144.40, 144.34, 141.19, 128.06, 127.53, 125.63, 125.50, 120.57, 109.54, 105.24, 104.43, 97.56, 68.00, 65.83, 47.17, 44.47, 12.78.

ESI-MS MW calculated for $C_{34}H_{36}N_3O_8$ $[M+H]^+$ 614.25 Da, found 614.25 Da.

3.2.2. Biophysical methods

3.2.2.1. Mass spectrometry analysis

Mass spectrometry analysis was carried out by the mass spectrometry service unit of the Goethe University Frankfurt, department 14. MALDI-TOF-MS were recorded with a Voyager-DE STR Applied Biosystems spectrometer using 2.5-dihidroxybenzoic acid as calibration matrix. ESI-MS were measured on a ThermoFisher Surveyor MSQ.

3.2.2.2. UV-Vis absorption and fluorescence emission spectra

Absorption spectra were recorded from 250 to 800 nm at 25 °C with 1 nm interval on an Agilent Cary 100 UV/Vis instrument. Fluorescence emission spectra were obtained from 400 to 800 nm with excitation at 380 nm at a Varian Cary Eclipse spectrometer. Samples were freshly prepared (50-100 µM, in HBS buffer:MeCN, 1:1, v/v). Path length of the cuvette was 1 cm. All spectra were corrected for HBS buffer/MeCN (1:1, v/v) and subsequently normalized.

3.2.2.3. Photometric quantification of compound concentrations

Photometric quantification was performed by measuring the absorbance of the compound on a Nanodrop 1000 spectrometer. Absorbance was measured for proteins at 280 nm, coumarin-containing compounds at 400 nm (ε=18 600 $M^{-1}cm^{-1}$)[167], fluorophores or fluorophore labeled compounds at the absorbance maximum of the fluorophore. Concentrations were calculated based on the Lambert-Beer-Law (equation 1):

$$A = \varepsilon \cdot c \cdot d \qquad \text{Equation 1}$$

A = absorbance, ε = molar extinction coefficient, d = optical path length

3.2.2.4. Fluorescence quantum yield of TPA-*tris*NTA

The fluorescence quantum yield ϕ_F was assessed by Marvin Asido (Wachtveitl lab). ϕ_F was determined by using a Jasco ILF-835 integrative sphere attached to a fluorescence spectrometer (FP-8500, Jasco). Spectra were recorded from 250 nm to 900 nm with a spectral resolution of 2 nm. The PMT voltage was adjusted to 440 V to achieve the maximum fluorescence signal without saturation of the detector. For all measurements a 4x10 mm quartz cuvette was used. The OD of TPA-*tris*NTA in HBS buffer was adjusted to ~0.1 (10 mm optical path length) to circumvent reabsorption effects. The reference signal of HBS buffer was subtracted from the sample signal. ϕ_F was calculated by the ratio between the residual fluorescence and the excitation integrals. Processing and quantum yield calculation were performed with the Jasco software package (Spectra Manager Suite).

3.2.2.5. Photolysis analysis of Fmoc-EDA-DEAC amino acid (43) in solution

A stock solution of Fmoc-EDA-DEAC amino acid **43** in HBS buffer was illuminated at 405 nm (185 mW/cm^2, Thorlabs LED system). To study the photolysis kinetics, 50 µL aliquots were taken at different time points (0, 5, 10, 15, 30, 45, 60, 300 and 900 s) and analyzed by analytical RP-C_{18}-HPLC (Method 1). The elution signal of Fmoc-EDA-DEAC amino acid **43** and the photolysis product were integrated and monoexponentially fitted to extract the decay kinetic.

3.2.2.6. Two-photon absorption spectrum of TPA-*tris*NTA

The two-photon absorption spectrum were detected by Marvin Asido (Wachtveitl lab) using the method of two-photon excitation fluorescence (TPEF). The one-photon fluorescence quantum yield was assumed to equal the two-photon fluorescence quantum yield. The experiment was performed with a tunable Ti:Sa laser (Tsunami) with a pulse duration of 150 fs and a repetition rate of 80 MHz. The TPEF-signal was coupled into a spectrograph (SpectraPro 300i) equipped with a CCD-camera (EEV 400_1340F).

The average energy of each wavelength was adjusted to 100 mW and the pulses were tightly focused on the sample. Coumarin 307 was used as reference, and values for calculation were taken from Xu et *al*.[168] Concentrations of the TPA-*tris*NTA and coumarin 307 were adjusted to 100 µM in a final volume of 300 µL. Fluorescence spectra in the range of 770-870 nm were recorded. After baseline and detector correction of the fluorescence spectra, the integrals were calculated to obtain the fluorescence intensity of TPA-*tris*NTA ($I_F(X)$) and coumarin 307 as a reference ($I_F(R)$). For calculation of the two-photon absorption cross section (σ_2) the following equation 2 was used. The refractive indices of the samples (at 20 °C, Vis-NIR range) were determined to be $\eta(R)$ = 1.33 (in MeOH) and $\eta(R)$ = 1.33 (in H_2O).

$$\phi_F(X)\,\sigma_2(X) = \sigma_2(R) \cdot \phi_F(R) \frac{I_F(X) \cdot c(R) \cdot \eta(R)}{I_F(R) \cdot c(X) \cdot \eta(X)} \qquad \text{Equation 2}$$

σ_2 = two-photon absorption cross section, ϕ_F = fluorescence quantum yield, X = TPA-*tris*NTA, R = coumarin 307, I_F = fluorescence intensity, c = concentration, η = refractive index of the solvent

3.2.2.7. Two-photon power dependence of TPA-*tris*NTA

Measurements and calculations were carried out by Marvin Asido (Wachtveitl lab). To certify the two-photon absorption effect of TPA-*tris*NTA, a scan of the fluorescence intensity over a series of excitation energies (20-100 mW) was performed at a specific wavelength (800 nm). The count rate of the fluorescence response was logarithmically plotted against the logarithm of the excitation energy.

3.2.2.8. Mask-patterning of functionalized glass/hydrogel surfaces

For photo-patterning of large areas, functionalized hydrogels or glass slides were exposed to UV light (405 nm or 365 nm LED lamp, 185 mW/cm^2) for the specified time period through a quartz mask with various sized chrome patterns on top. After illumination, the hydrogels/glass slides were washed five times with HBS buffer.

3.2.2.9. Laser-supported photo-patterning of functionalized glass surfaces

In-situ photo-patterning of functionalized glass surfaces was performed using a confocal laser scanning microscope (TCS SP5 microscope, Leica) equipped with a Plan Apochromat 63xOil (NA 1.4) objective. For precise and spatial controlled pattering, the 405 nm laser (maximum output power 25 mW) with a scan speed of 1.54 µs/pixel was exploited. The illumination process was controlled with the Leica Suite software.

3.2.2.10. Laser-supported photo-patterning of functionalized hydrogels

For photo-patterning by one- or two-photon excitation, a confocal laser-scanning microscope (LSM 880 AxioObserver) equipped with a Plan-Apochromat 63x/Oil (NA 1.4) objective, a 405 nm LED diode, and an ultrafast Ti:Sa laser (Chameleon) was used for spatial-defined illumination. The 405 nm laser has a maximal output of 4.5 mW and the Ti:Sa laser has a pulse duration of 140 fs, 80 MHz repetition rate and maximal output of 2.5 W. Custom-defined ROI scanning mode and bleaching setting were used to precisely write patterns in 3D. The output power of the two-photon laser was measured each time after a warm-up time of at least 1 h at the sample location with a photometer (Thorlabs) for the wavelengths intended to be used. For two-photon patterning the applied power was adjusted before each experiment to match 0.5, 1.5, 3.1 and 5.5 mW (corresponding to 0.3, 0.7, 1.2, 2.2% of maximal laser power). Photo-activation of hydrogels was

performed in HBS buffer. Hydrogels with incorporated living cells were illuminated with the 405 nm laser at maximal power (4.5 mW) for 600 iterations covered in live cell imaging solution (LCIS) at 37 °C. If not stated otherwise the scan speed was fixed at 1.54 µs/pixel. The patterning process was controlled with the Zeiss Zen Black software.

3.2.2.11. Reversibility of POI trapping

POI release was induced by incubating the hydrogel or glass surface with 1 mL of 500 mM imidazole in HBS buffer at RT. For POI reattachment, the gel was washed five times with HBS buffer and immersed to 300 nM fluorescently labeled POI His_6-AF647, followed by washing with HBS buffer. Visualization of POI binding, release and reattachment was monitored by confocal laser scanning microscopy.

3.2.2.12. Confocal imaging

Confocal imaging was performed using a confocal laser-scanning microscope LSM 880 AxioObserver (Zeiss) or TCS SP5 microscope (Leica), and images were taken with the Plan-Apochromat 20x (NA 0.8) and/or the Plan-Apochromat 63x/Oil (NA 1.4) objective. Laser lines used for excitation were: 405 nm (diode laser) for DAPI, Hoechst33342; 488 nm (argon laser) for green fluorescent protein (His_6-GFP); and 633 nm (helium-neon laser) for His_6-AF647 and Annexing V-AF647 conjugate. The imaging process was controlled with the Zeiss Zen Black software. Image processing and evaluation was done with Fiji.[169]

3.2.2.13. Long-term stability and persistence of photo-patterns

A custom-designed (bird) photo-pattern was generated by two-photon excitation at 800 nm within a hydrogel and visualized by incubation with 300 nM His_6-AF647 in HBS buffer. After removal of access His_6-AF647 by washing with HBS buffer the pattern was imaged within the hydrogel (day 0). After 10 days the HBS buffer on top of the hydrogel was exchange and imaging with the same settings (laser power, detector amplification and pinhole) was repeated. To investigate long-term stability, fluorescence intensity was analyzed at four different sites within the photo-pattern using Fiji software.[169]

3.2.2.14. Z-axis profile analysis

Depths of photo-patterned ROIs along the z-axis were analyzed by recording z-stacks (35 slices, z-step width 1 µm) through the entire photo-activated area at a CLSM. Following, orthogonal cross-sections (x/z-plane) of the ROI were created and the fluorescence intensity within the voxel was measured with Fiji sofware.[169] Additionally, a line scan profile along the z-axis of the ROI was generated.

3.2.2.15. Full width at half maximum determination

On basis of a line scan profile along the z-axis of a ROI (see 3.2.2.14) the Full width at half maximum (FWHM) in z-direction was determined by fitting a Gaussian (equation 3) to the line scan profile. All analyses were performed with OriginLab and Fiji software.[169]

$$y = y_0 + \frac{A}{w\sqrt{\frac{\pi}{2}}} \cdot e^{-2\frac{(x-x_c)^2}{w^2}} \qquad \text{Equation 3}$$

y_0 = baseline offset, x_c = center of peak, w = 0.849 the width of the peak at half height, A = area under the peak

3.2.2.16. Enhancement effect of two-photon sensitizers in hydrogels

20 square ROIs (15x15 µm) were written into TPA-*tris*NTA functionalized hydrogel by two-photon-excitation at 800 nm with a Plan-Apochromat 63x/Oil (NA 1.4) objective. Laser power (0.5, 1.5, 3.1 and 5.5 mW) as well as illumination time (6, 12, 18, 24, 30 s) were stepwise increased to vary light dosage for each ROI. Photo-activation was performed in HBS buffer, in presence of ATTO390 (50, 100, 500 µM in HBS buffer) or of rhodamine B (50, 100 µM in HBS buffer). After washing with HBS buffer, Ni(II)-loading and again washing with HBS buffer, His_6-AF647 (300 nM in HBS buffer) immobilization was conducted. Z-stacks (35 slices, z-step width 1 µm) of the written ROIs were recorded *via* CLSM. Imaging conditions (laser power, detector amplification, pinhole, and imaging speed.) were kept constant. After background subtraction, z-slices of each ROI were summed up and quantified by determining the total integrated fluorescence density of each voxel. The total integrated fluorescence densities obtained in different replicates, photopatterned under equal conditions were averaged for comparison. Each experiment was performed in triplicate or quadruplicate, and error bars indicate the s.d. Quantification was performed using Zeiss Zen Black and Fiji software.[169]

3.2.2.17. Enhanced three-dimensional POI-tethering in functionalized hydrogels

For precise POI recruitment by two-photon illumination at 800 nm the Ti:Sa Chameleon laser tuned to 800 nm and a Plan-Apochromat 63x/Oil (NA 1.4) were employed. Photo-patterning was realized in 50 µM rhodamine B in HBS buffer. The bleaching mode of the Zeiss Zen Black software was used to write custom-designed ROIs in different z-layers into the hydrogel. If not stated otherwise 3.1 mW (1.2%; max output 2.5 W), a scan speed of 1.54 µs/pixel was applied. The written patterns were visualized by washing with HBS buffer followed by Ni(II)-loading and subsequent POI binding *via* incubation with 300 nM His_6-AF647 in HBS buffer at RT. The POI assembly was recorded *via* z-stack with optimal sectioning of images (z-stack slices 0.7 µm separated) on a confocal laser-scanning microscope (Zeiss LSM880).

3.2.3. Cell culture

3.2.3.1. Cell culture and receptor induction

HeLa Flp-In T-Rex cells stably expressing the hormone neuropeptide Y_2 receptor modify with a *C*-terminal mEGFP and a *N*-terminal His_6-tag (His_6-Y_2R^{mEGFP}) were produced by Florencia Maria Sanchez (Tampé lab).[170] The cells were cultured in Dulbecco´s Modified Eagle Medium (DMEM) containing 4.5 g/L glucose (Gibco), supplied with 10% (v/v) tetracycline free fetal calf serum (FCS, Gibco), 1 µg/mL blasticidine S (ThermoFisher), 50 µg/mL hygromycin B (Sigma Aldrich) and 436 µg/mL GlutaMAX (Gibco). Passaging of the cells was achieved by washing with PBS buffer followed by detachment from the culture dish T75 (Greiner) using 0.05% trypsin/0.02% EDTA/PBS (GE Healthcare). For maintenance a humidified tissue culture incubator at 37 °C and 5% CO_2 was used. For receptor expression 0.1 µg/mL tetracycline (Fluka) was added to the medium 16 h before the experiment. Mycoplasma contamination tests were implemented regularly, following the guidelines described.[171]

3.2.3.2. Cell encapsulation in hydrogels

Cells were detached with 0.05% trypsin/0.02% EDTA/PBS (GE Healthcare) 16 h post receptor induction, centrifuged and solubilized in 200 µL Life Cell Imaging Solution (LCIS, Invitrogen). For hydrogel formation all components listed in Table 12 except the dithiol-linker and the cells were merged and homogenized *via* vortexer. Either TPA-*tris*NTA or PA-*tris*NTA or thioglycerol were used is specified in the experiment. The cells were added after vortexing. The dithiol-linker was placed in the center of an µ-dish (35 mm, high grid-500 glass bottom; Ibidi) and quickly mixed *via*

pipetting with the other precombined components. Hydrogel network formation was allowed to proceed for 10 min at RT. Subsequently the hydrogel was covered with 1 mL LCIS (Invitrogen).

Table 12: Hydrogel composition for life-cell encapsulation.

Component	c (mM)	V (µL)
10x CB buffer pH 7.2		3.0
Mal-PVA SG	30.0	2.5
PA-*tris*NTA/ TPA-*tris*NTA/ thioglycerol	20.0	0.8
dithiol linker	20.0	3.0
water		11.3
cells		10.0
total volume		30.6

3.2.3.3. Viability test of cells encapsulated in hydrogels

To study eventual cytotoxic effects through encapsulation of the cells into hydrogels, a live-cell annexin V staining was performed to report on apoptotic cells. Therefore, HeLa Flp-In T-Rex cells ($1x10^6$ cells/mL) were washed and suspended in 100 µL annexin V binding buffer. After addition of 25 µL of annexin V-AF647 conjugate (Invitrogen) and one drop of NucBlue Live Ready Probes (Thermo Fisher), cells were incubated for 15 min at RT and then washed again with annexin V binding buffer. Subsequently, the cells were incorporated in a TPA-*tris*NTA functionalized hydrogel. Analysis of cell viability was conducted by CLSM. Cell nuclei stained with Hoechst33342 were visualized by excitation with a 405 nm diode laser and the membrane of cells which are in an early apoptosis state were displayed *via* excitation of AF647 of the annexin V-AF647 conjugate with the 633 nm laser. 708.5 µm x 708.5 µm images were taken with the 20x fold objective (NA 0.8). To determine the total amount of cells indicated by the Hoechst33342 signal and the number of AF647-stained cells, stained cells were separately counted with Fiji multipoint tool[169] in the Hoechst33342 and AF647 channel. Cell vitality was calculated by the ratio of Hoechst33342 and AF647-stained cells. All experiments were performed in triplicates.

3.2.3.4. *tris*NTA labeling of living cells expressing Y_2 receptor inside hydrogels

HeLa Flp-In T-rex cells expressing His_6-Y_2R^{mEGFP} were embedded according to Table 12 into hydrogels, using thioglycerol (20 mM, Cellendes Hydrogel Kit). After solidification, the hydrogel was covered with 1 mL of 200 nM *tris*NTA^{AF647} solved in Live Cell Imaging Solution (LCIS, Invitrogen) equilibrated to 37 °C and incubated for 30 min in a humidified tissue culture incubator at 37 °C and 5% CO_2. Subsequently, the hydrogel was washed by addition of 2 mL LCIS and incubation for 5 min, which was repeated 5 times, before analysis by CLSM.

3.2.3.5. Cytotoxicity test of photosensitizers

200 µL HeLa Flp-In T-rex cells ($5x10^6$ cells/mL) were seeded per well into two 96-well cell culture microplates (Greiner Bio-One) in DMEM supplemented with 4.5 g/L glucose and without Phenol Red (Gibco), supplied with 10% (v/v) FCS. For cell adhesion the plates were incubated for 24 h at 37 °C in a fully humidified atmosphere of 5% CO_2. Subsequently, the medium was carefully exchanged with 100 µL photo-sensitizer solution at different concentrations (ATTO390: 50, 100, 500 µM; rhodamine B: 50, 100 µM) in HBS buffer. One 96-well plate was kept under ambient light whereas the second plate was illuminated for 1 min at 365 nm by 185 mW/cm^2 with a custom made 96-well LED setup. After illumination both plates were incubated at 37 °C and 5% CO_2 for 2 h before the photo-enhancer solutions were carefully aspirated and fresh culture medium was added. The next day, the culture medium was removed and 50 µL serum-free media and 50 µL 3-(4,5-dimethylthiazol-2yl)-2,5-dipehnyltetrazolium bromide (MTT) solution (5 mg/mL in DPBS, sterile filtrated; Abcam) were added to each well. The plates were incubated for 3 h under standard cell culture conditions, before 150 µL MTT Solvent (Abcam) were added and pipetted thoroughly up and down to dissolve precipitated MTT formazan. Absorbance was measured at 590 nm with 20 readings per well using a ClarioStar microplate reader (BMG Labtech). Background absorbance (from wells treated as above but without cells) was subtracted and the untreated control cells were assumed as 100%. Cell viability was calculated using equation 4. All conditions were tested as triplicates per sample and control.

$$rel.cell\ viability = \frac{experim.value - background\ value}{untreated\ control - background\ value} \cdot 100\% \qquad \text{Equation 4}$$

4. Results and Discussion

The precise structuring of proteins and biomolecules in artificial tissue is an important prerequisite for the study of cell migration and cellular signal transduction. Many immobilization strategies often rely on the addition of small molecules, a pH shift or involves harsh conditions like free radicals. Light on the other hand, is an ideal external trigger for immobilization strategies. Light offers control in time, space and intensity and is orthogonal to other experimental manipulations.

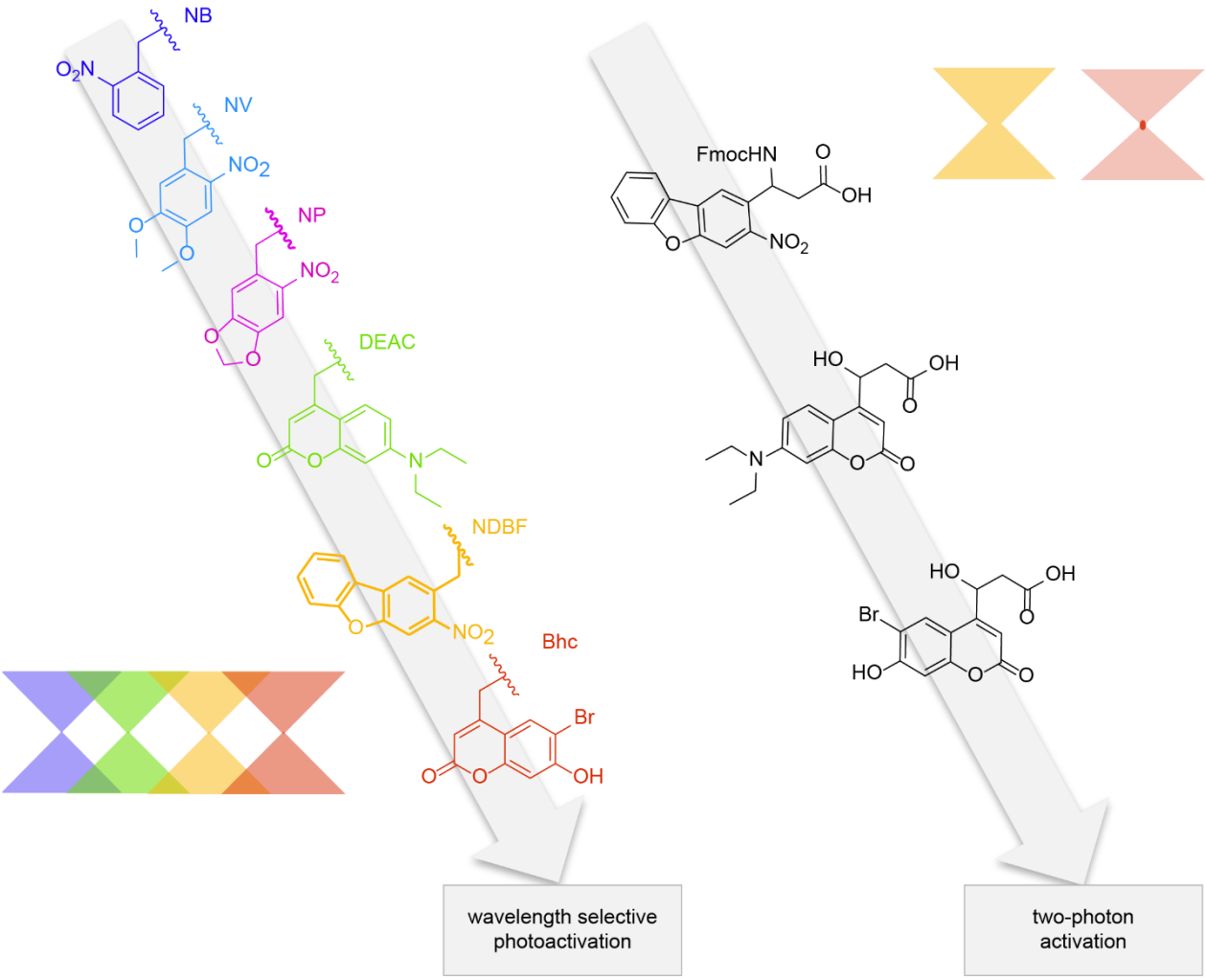

Figure 14: Multi-wavelength photo-activation of new amino acid analog. For orthogonal activation of interaction molecules amino acid analogs bearing different photo-activatable moieties in the side chain *e.g.* NB, NV, NP, DEAC, NDBF or Bhc, can be used (left side). NDBF, DEAC and Bhc also have the advantage to be two-photon activatable. Therefore, they shall be used to build amino acids or ß-hydroxy acids for incorporation into the interaction tools.

The goal is to build new light-responsive interaction molecules that have superior photoactivation properties in terms of wavelength selectivity and two-photon uncaging efficiency. The use of PPGs

with different absorption maxima allows to orthogonally address different biochemical cues within a system (Figure 14). In addition to PA-*tris*NTA, which contains Anp as a photocleavable group, a derivative with improved photo-physical properties should be produced and used to build light-structurable interfaces.

The project was focused on the PPGs nitro-dibenzofuran (NDBF), diethylamino-coumarin (DEAC) and bromo-hydroxycoumarin (Bhc) (Figure 15). Because of their bathochrome red-shifted absorption spectra, they were of particular interest for biological applications. In addition, the ability of two-photon excitation of these groups allow a spatially defined activation with axial precision. The UV-absorbing PPGs nitroveratryl (NV) and nitropiperonyl NP are interesting alternatives for nitrobenzyl (NB) as they have already been successfully applied in biological systems.[147,172,173]

To enable the incorporation of the photocages into the peptide linker *via* solid phase peptide synthesis, Fmoc-protected amino acid derivatives of the PPGs should be prepared. Important intermediates for the synthesis strategy are aldehydes of the respective PPGs, since both ß-amino acids and ß-hydroxy acids can be produced from these building blocks.

NV and NP are commercially available as aldehydes, so that they were ideal test compounds for the preparation of amino acid derivatives. NB is already available as ß-amino acid in the form of 3-amino-3-3(2-nitrophenyl)-propionic acid (Anp) and could be directly incorporated by solid-phase peptide synthesis in the PA-*tris*NTA developed by Grunwald *et. al.*[72] and Labòria *et al*.[73]

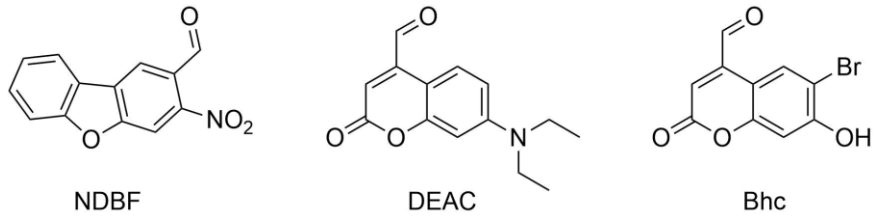

Figure 15: Target structures of NDBF, DEAC and Bhc building blocks with a carbaldehyde moiety. The carbaldehyde functionality can used for the construction of photocleavable amino acid derivatives.

4.1. Synthesis of PPG carbaldehyde building blocks

The synthesis of the NDBF carbaldehyde was performed as described by Friedrich *et al*.[163] In the first step, 4-fluoro-2-nitro-benzaldehyde **12** and 2-iodophenol **13** were coupled *via* Ullmann reaction to yield compound **14**. To avoid in the following Heck coupling the coordination of the palladium(II) acetate catalyst to the carbaldehyde moiety, the carbaldehyde was protected as an acetal by addition of glycol in *para*-toluenesulfonic acid (PTSA). The cyclization of compound **15** to **16** by Heck coupling using palladium(II) acetate as catalyst and Cs_2CO_3 as base, resulted with 81% yield in the desired product **16**. The acetal **16** was deprotected under acidic conditions in THF to obtain final compound **17**. The NDBF carbaldehyde **17** was subsequently used for reactions to build photocleavable amino acid derivatives.

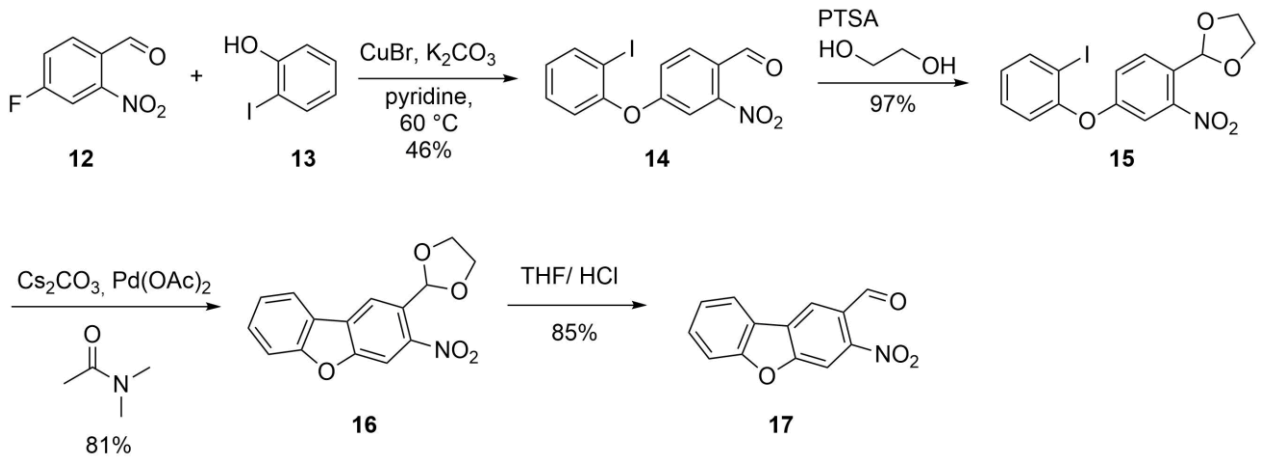

Figure 16: Synthesis of NDBF carbaldehyde according to Friedrich *et al*.[163] In four steps the NDBF carbaldehyde could be obtained. The synthesis started with an Ullman coupling of 4-fluoro-2-nitro-benzaldehyde **12** and 2-iodophenol **13**. Following an acetal functionality was introduced to protect the carbaldehyde for the following Heck coupling. After the cyclization the carbaldehyde functionality was recovered from the acetal to obtain the desired structure **17**.

For the preparation of the Bhc carbaldehyde, the Bhc alcohol **21** had to be synthesized first. **21** should then lead to the desired Bhc carbaldehyde **22** by oxidation. For this purpose, the Bhc backbone was first prepared as described by Hagen *et al*.[164] 4-Bromoresorcinol **18** was reacted in methane sulfonic acid and ethyl 4-chloroacetoacetate **19** in a Pechmann condensation to give chloromethyl-Bhc **20**. The reaction proceeded with high yield (90%). Subsequently, the chloromethyl group was hydrolyzed in refluxing water.[174] This resulted in Bhc alcohol **21** in quantitative yield. Oxidation of the alcohol functionality by manganese(IV) oxide was carried out according to Lin and Lawrence *et al*.[175] However, no conversion was detected even after 4 days.

As an alternative, oxidation with Dess-Martin periodinane (DMP) was tested following the procedure described by Kitamura *et al*.[176] None of the reaction products could be assigned to the desired product **22** by NMR spectroscopy or mass spectrometry. The compound which was obtained could be identified as the hydrolyzed reaction product of DMP.

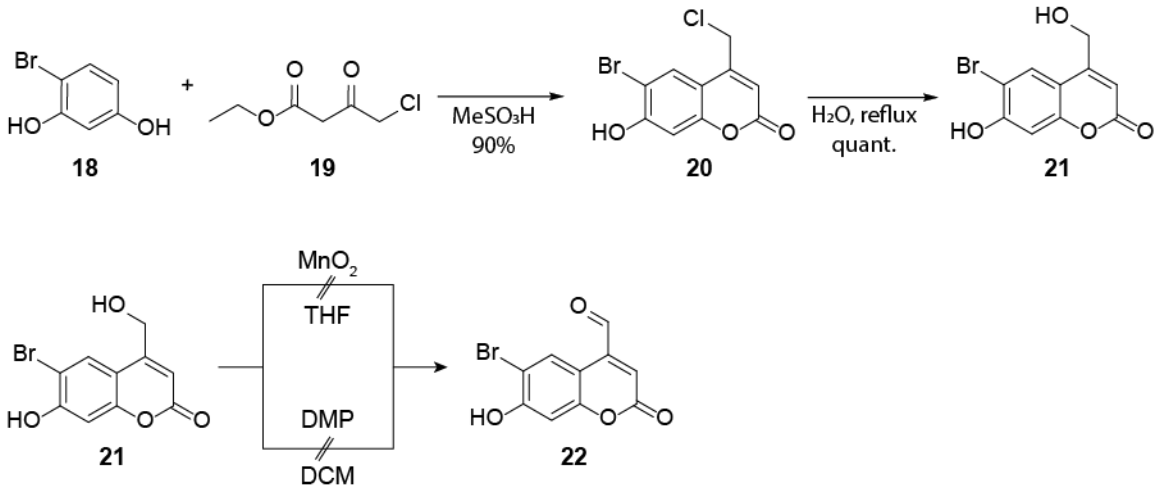

Figure 17: Synthesis scheme for Bhc carbaldehyde *via* oxidation of the Bhc alcohol. Chloromethyl Bhc **20** was obtained by Pechmann condensation of 4-bromoresorcinol **18** and ethyl 4-chloroacetoacetate **19**. Subsequently Bhc alcohol **21** was generated by hydrolysis in refluxing water. Oxidation to the desired Bhc carbaldehyde **22** was unsuccessful for the approach with manganese(IV) oxide and with Dess-Martin periodinane (DMP).

Since the previous attempts to obtain Bhc carbaldehyde **22** *via* oxidation of the corresponding alcohol were not successful, alternative synthetic routes were developed. Both reaction paths started from the preparation of 4-methyl Bhc **24**. The first possibility would be to produce the corresponding enamine **25**, which should then be oxidized to the carbaldehyde **26**. In the second variant, 4-methyl Bhc **24** could be converted directly to the carbaldehyde using selenium dioxide.

For this purpose, 4-methyl Bhc **24** was first prepared *via* a Pechmann condensation of 4-bromoresorcinol **18** and ethyl acetoacetate **23**. Unfortunately, the conversion of **24** to the enamine **25** analog to the prescription of Weinrich *et al*.[177] was not successful. Besides several by-products, mainly the starting material was recovered. Therefore, the oxidation to carbaldehyde using sodium periodate was not carried out.

The reaction of 4-methyl Bhc **24** with selenium dioxide was first carried out in p-xylol according to the description of Ito and Maruyama *et al*.[165] In addition to a low yield of 29%, the reaction also exhibited several side products. In order to improve the reaction, the slightly more polar solvent 1,4-dioxane was tested. The solubility of **24** was significantly improved, in addition, fewer by-products appeared, and the yield was increased to 51%.

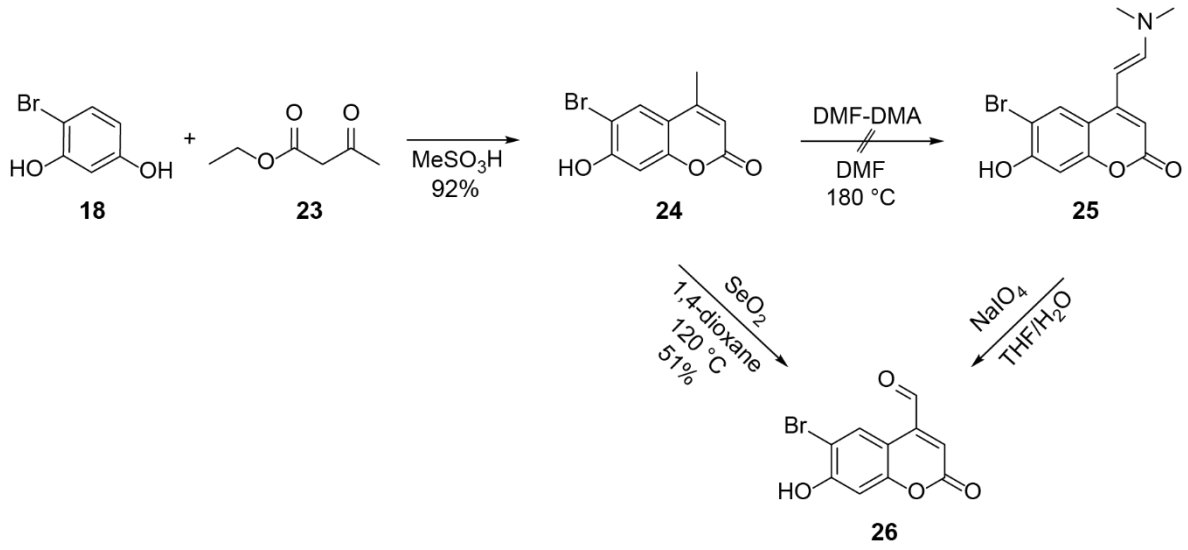

Figure 18: Synthesis scheme for Bhc carbaldehyde starting from 4-methyl Bhc **24**. The conversion of **24** to enamine **25** did not take place, therefore the oxidation with sodium periodate was not carried out. Instead, **24** was directly oxidized by selenium dioxide to form carbaldehyde **26**. First attempts in *p*-xylol were low yielding and produced a lot of byproducts. Exchanging the solvent to 1,4-dioxane increased the solubility of **24**, decreased the number of byproducts and increased the yield to 51%.

For the last building block, the carbaldehyde of DEAC, the same synthetic routes as for Bhc were tested. Since the oxidation with selenium dioxide was successful for Bhc, it was also tested for DEAC. Selen dioxide was added to commercially available 4-methyl DEAC **27** in 1,4-dioxane. However, in the case of **27**, the reaction was not successful. A large number of by-products were obtained. Despite multiple column chromatographic purifications, no product could be isolated. Therefore, the reaction pathway *via* the enamine intermediate was tested. Condensation of **27** with dimethylformamide dimethylacetal (DMF-DMA) led to the formation of DEAC-enamine **28** in 98% yield, which could then be converted to the desired building block **29** by oxidative cleavage with sodium periodate with 85% yield.

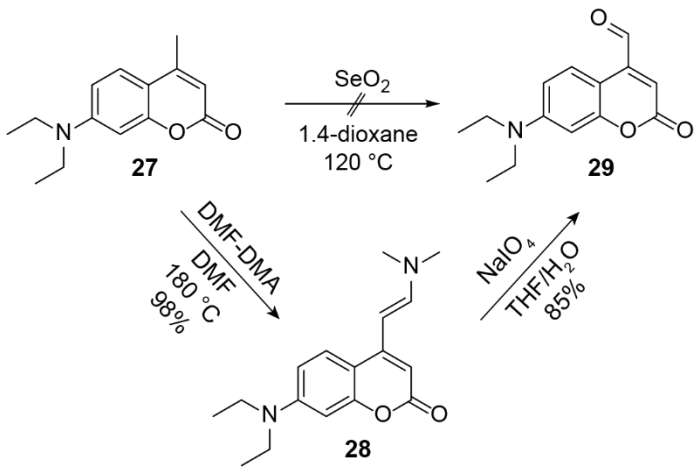

Figure 19: Synthesis routes for DEAC carbaldehyde. Oxidation of commercial available 4-methyl DEAC **27** with selendium (IV)dioxide was not successful. As alternative, a two step route with DEAC-enamine **28** was carried out. The enamine was obtained *via* condensation of **27** with dimethylformamide dimethylacetat. Follwing oxidative cleavage with sodium periodate yielded the desired product **29**.

It is worth noting that 4-methy Bhc **24** and 4-methyl DEAC **27** behave very differently in the reaction with selenium dioxide and DMF-DMA. The reaction of **24** with selenium dioxide caused fewer by-products and higher yields, whereas the reaction with DMF-DMA resulted in no product. For **27**, the behavior is the opposite. Since the backbone and the methyl group in position 4 are identical, the difference in reaction behavior could be due to the substituents in positions 6 and 7. Bhc has a bromine substituent in position 6 and a hydroxy substituent in position 7. The bromine substituent increases the acidity of the hydroxy group so that it deprotonates more easily, and thereby a positive inductive effect occurs in addition to the bromine. The negative inductive effect of the lactam moiety in the coumarin skeleton results in a push-pull system. In compound **27** the diethylamino group in position 7 has a positive inductive effect, while the lactam moiety has a negative inductive effect, thereby also creating a push-pull system. Since in both coumarin compounds the reaction should occur at position 4, it is possible that the different reactivity is due to the symmetry and arrangement of the push-pull system. Also, the different polarity of the solvent during the reaction probably plays a role. DEAC **27** is better soluble in more polar solvents (*e.g.*, EA, acetone, DMF) than in less polar ones (*e.g.*, 1,4-dioxane, THF, diethylether). The hydroxyl group in Bhc **24** is protonated in 1,4-dioxane and therefore has a lower solubility in polar solvents. Since the solubility and polarity of the solvent play an important role in the course of the reaction, it can be assumed that the different reaction courses of **24** and **27** are partially due to this.

4.2. Synthesis of Fmoc-protected PPG amino acids

The photolabile amino acid derivatives should to be incorporated into the linker of TPA-*tris*NTA using solid phase peptide synthesis (SPPS). For this purpose, building blocks with an Fmoc-protected primary amino group and a carboxylic acid group should be prepared following the synthesis scheme depicted in Figure 20. To realize this, first the amino group should be introduced into the molecule. Therefore, *N*-*tert*-butanesulfinyl imines were produced *via* condensation reaction between the carbaldehyde building blocks and *tert*-butanesulfinamide using the $Ti(OEt)_4$ as dehydrating agent. Due to its Lewis acidity and water scavenging ability the Ti(IV) salt is described to condense amines with ketones and alehydes.[166] Following, ethyl (*R*)-4-((*tert*-propylsulfinyl)amino)-butanoate should be prepared by nucleophilic addition of a Reformatsky reagent or a zinc homoenolate to the imine. Since the preparation of a Reformatsky reagent is often laborious and proceeds in low yield, the commercially available 3-ethoxy-3-oxopropylzinc bromide was used analog to the procedure of Brinner *et al*.[178] An alternative synthetic route is the Reformatsky reaction with 1-(trimethylsiloxy)-1-ethoxycyclopropane with the use of catalytic amounts of zinc iodide, described by Nakamura *et al.*[179] Zinc iodide opens the cyclopropane ring to give the zinc homoenolate, releasing iodotrimethylsilane, which then acts as a Lewis acid activating the imine group. The subsequent nucleophilic addition of the zinc homoenolate to the imine releases the zinc iodide again.

The sulfinyl group can then be removed under acidic conditions (HCl, 1 M in Et_2O/EtOH) to give the amino group. Subsequently, the primary amine should be Fmoc-protected and the carboxylic acid group should be released by basic ester cleavage to give the desired target structure.

The preparation of Fmoc-protected gamma amino acids was tested with the nitrobenzyl-based PPG carbaldehydes NDBF and NV. The preparation of gamma amino acids with a coumarin side chain (DEAC or Bhc) did not appear to be useful since light-induced bond cleavage of N-C bonds in coumarins is reported in the literature to be unsuccessful or very slow.[125,180,181]

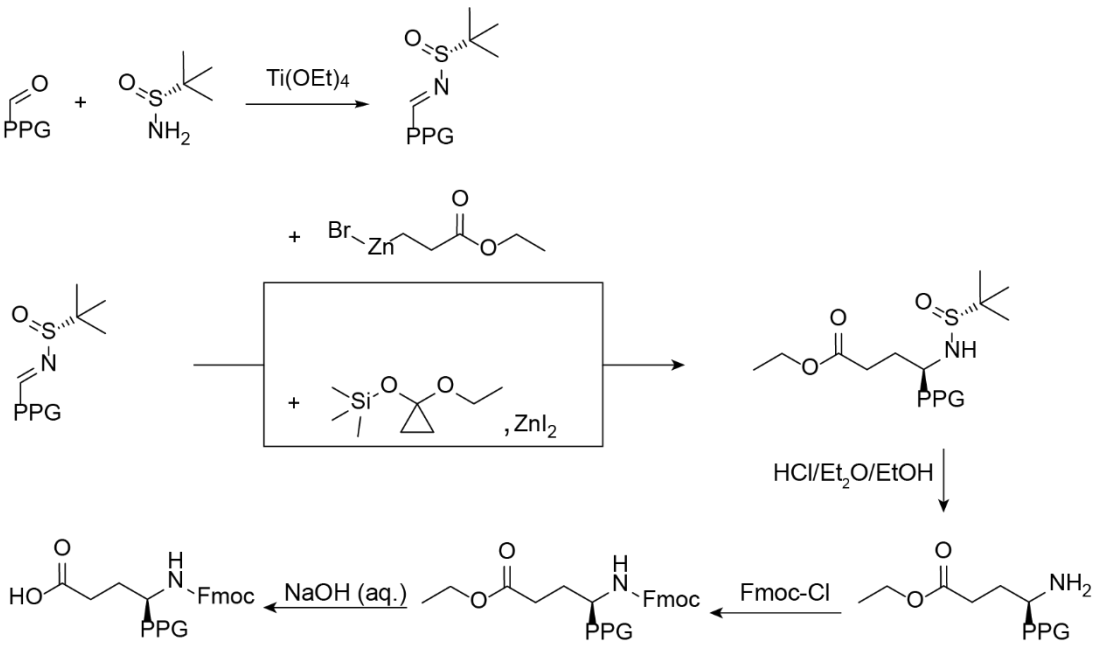

Figure 20: Synthesis strategy for the production of PPG based Fmoc-protected amino acids. Based on the PPG carbaldehydes sulfinylimines shall be produced, which than will be tranformed to ethyl (*R*)-4-((*tert*-butylsulfinyl)-amino)-butanoate by nucleophilic addition of a Reformatsky reagent or homoenolate. Subsequently the sulfinyl group should be removed by HCl in Et_2O, whereafter the free amino group will be Fmoc-protected. Finally basic ester cleavage shall take place to obtain the carboxylic acid.

The synthesis strategy was carried out with NV carbaldehyde **30** (Figure 21). The preparation of NV *N*-sulfinyl amine **31** proceeded in 88% yield. In addition to the desired product, an unidentified by-product and the starting material were obtained. That some starting material would be retained was expected, because an excess of the carbaldehyde was used according to the procedure of Liu *et al*.[166] Subsequently, the reaction of **31** was tested both with 1-(trimethylsiloxy)-1-ethoxycyclopropane under zinc iodide catalysis and with 3-ethoxy-3-oxopropylzinc bromide. Unfortunately, the desired compound **32** could not be obtained by either reaction pathway. In the case of the homoenolate reaction, numerous by-products were obtained, none of which could be identified as the desired molecule by mass spectrometry or NMR spectroscopy. In contrast, fewer side-products were obtained in the reaction of imine **31** with the Reformatsky reagent. The major component identified by thin layer chromatography (TLC) and mass spectrometry was the starting material imine **31**. Further addition of the Reformatsky reagent, extenting the reaction time and increasing the temperature to room temperature showed no effect. It is hypothesized that 3-ethoxy-3-oxopropylzinc bromide is not reactive enough for nucleophilic addition to the imine.

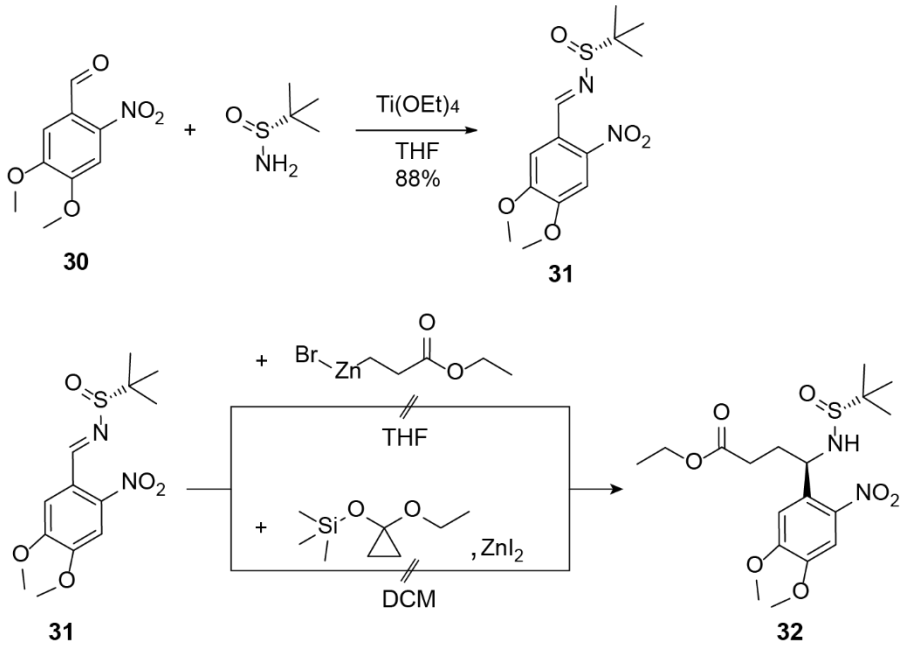

Figure 21: NV carbaldehyde based reactions to obtain photolabile amino acide with NV side chain. In the first step sulfinyl imine **32** was obtained with 88% yield by condensation with *tert*-butanesulfinamide. The follwing reactions of **31** with 3-ethoxy-3-oxopropylzinc bromide or 1-(trimethylsiloxy)-1-ethoxycyclopropane were not successful.

In an analogous manner, the preparation of photolabile amino acids with a NDBF side chain was tested (Figure 22). Therefore, sulfinyl imine **33** was first synthesized with NBDF carbaldehyde **17** in the manner described above. The reaction proceeded with few by-products but only 29% yield. Compared to the synthesis of **31**, more starting material was recovered, indicating that the conversion of the reaction was lower with NDBF. In the following, the reaction of **33** was carried out with the Reformatsky reagent 3-ethoxy-3-oxopropylzinc bromide. Unfortunately, the desired product **34** could not be obtained. The TLC as well as the mass spectrometry analysis showed the starting material **33** as the main component of the reaction mixture.

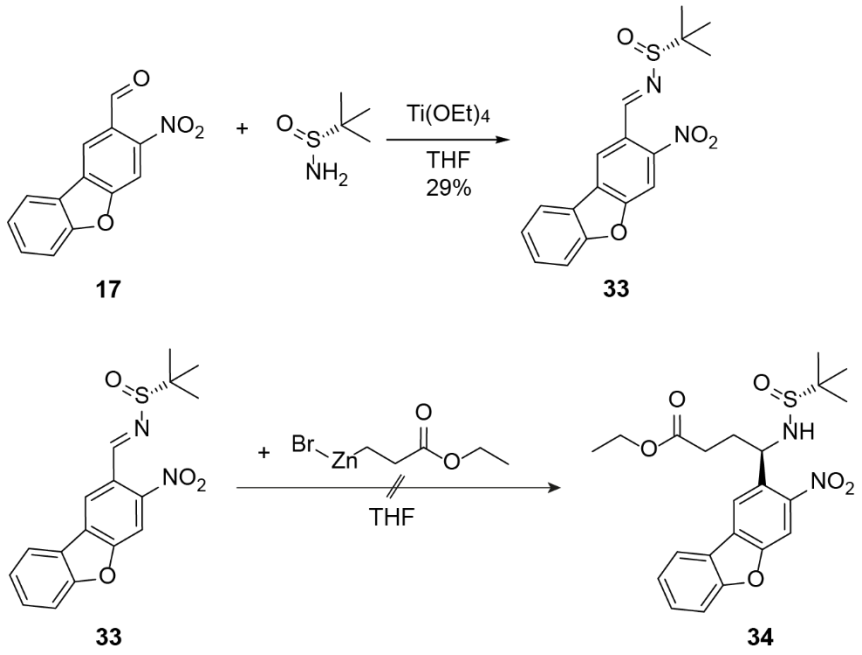

Figure 22: Syntheis of photolabile amino acid with NDBF side chain. In the first step sulfinyl imine **33** was obtained with 29% yield by condensation with *tert*-butanesulfinamide. The follwing reactions of **33** with 3-ethoxy-3-oxopropylzinc bromide was not successful.

4.3. Synthesis of ß-hydroxy acids containing PPGs

In addition to the construction of photolabile amino acid analogs, the production of hydroxy acids with PPG side chains was tested. These can be incorporated into the peptide backbone with a carbamate linkage. For this purpose, carbaldehydes NV **30**, DEAC **29**, and NDBF **17** were used for Reformatsky reaction with 3-ethoxy-3-oxopropylzinc bromide (Figure 23). The reactions were carried out in the same way for all three building blocks in order to analyze the reaction process, *i.e.*, the number and type of by-products and yields.

Before adding the Reformatsky reagent, the solution of carbaldehyde in THF was cooled to 0 °C in an ice bath and then 3-ethoxy-3-oxopropylzinc bromide was slowly added under argon atmosphere. In case of **17**, the yellow starting material precipitated out under cooling. This is probably due to low solubility in THF. Therefore, the solution was allowed to warm to room temperature, which caused the yellow precipitate to completely dissolve again. Zinc organyl was then added to the solution. Unfortunately, the reaction with NDBF carbaldehyde **17** showed no conversion. After the work up, **17** was recovered. Repetition of the reaction with increased amounts of Reformatsky reagent also did not result in a conversion. In contrast, the reactions with DEAC carbaldehyde **29** and NV carbaldehyde **30** led to a large number of side products.

Therefore, a lack of reactivity of 3-ethoxy-3-oxopropylzinc bromide does not seem to be the case. From both reactions of **29** and **30**, no compound could be isolated that had the desired mass or structural features in the NMR spectrum.

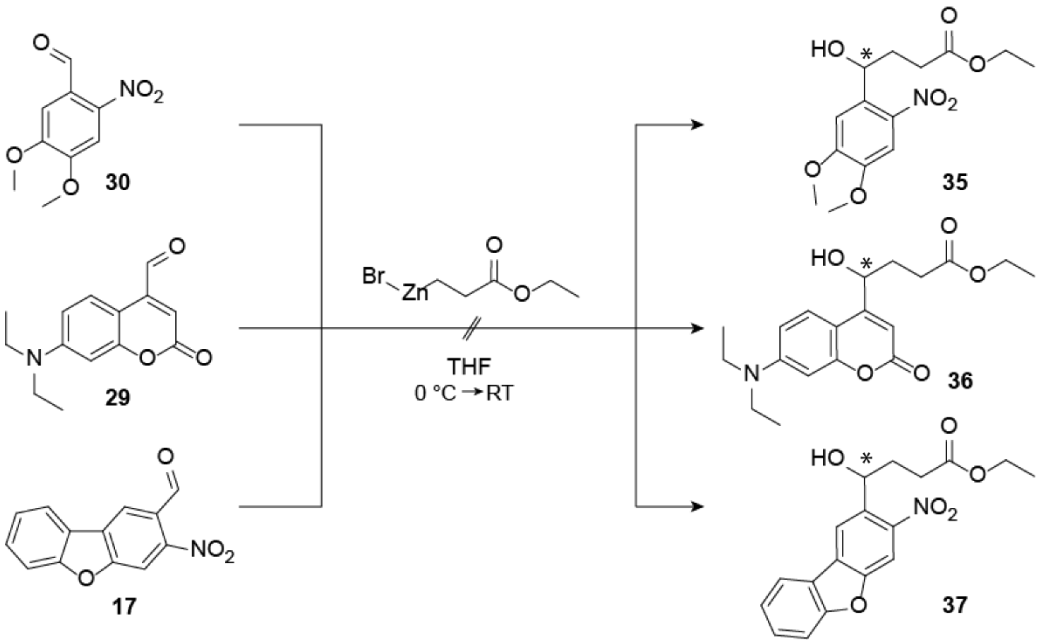

Figure 23: Reformatsky reactions of 3-ethoxy-3-oxopropylzinc bromide with carbaldehydes of NV **30**, DEAC **29** and NDBF **17**. Reactions were performed in the same way for all three components. The intended products could not be obtained for all of them.

Since the desired product could not be isolated with 3-ethoxy-3-oxopropylzinc bromide and the carbaldehydes, the *in-situ* preparation of the Reformatsky reagent (2-(*tert*-butoxy)-2-oxoethyl)zinc bromide was carried out alternatively as described by Seyfried *et al* (Figure 24).[162] For this purpose, zinc powder was etched with diluted hydrochloric acid and supplemented with *tert*-butyl bromoacetate. By oxidative addition, zinc inserts into the halogen-carbon bond to form the Reformatsky reagent, which then reacts with the carbaldehyde to give the desired ß-hydroxy *tert*-butyl ester.

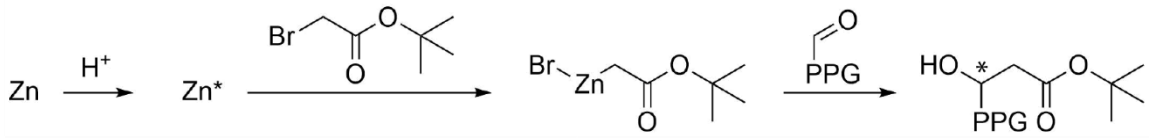

Figure 24: Reaction scheme of *in-situ* Reformatsky reaction of (2-(*tert*-butoxy)-2-oxoethyl)zinc bromide with PPG carbaldehydes. First zinc powder is activated by acid to react with *tert*-butylbromoacetate *via* oxidative addition to (2-(*tert*-butoxy)-2-oxoethyl)zinc bromide. Second the PPG carbaldehyde is added to form the intended *tert*-butyl protected ß-hydroxy acid.

The described reaction was tested with the carbaldehydes of Bhc **22**, DEAC **29** and NDBF **17.** For the *in-situ* reaction of Bhc **22** with 2-(*tert*-butoxy)-2-oxoethyl)zinc bromide, the hydroxy group in position 7 was previously protected with a methoxymethyl group (MOM group) to avoid side reactions (Figure 25). The introduction of the protecting group proceeded with 89% yield. The subsequent Reformatsky reaction progressed with nearly quantitative yield (98%). The desired product **39** was verified by NMR analysis and mass spectrometry.

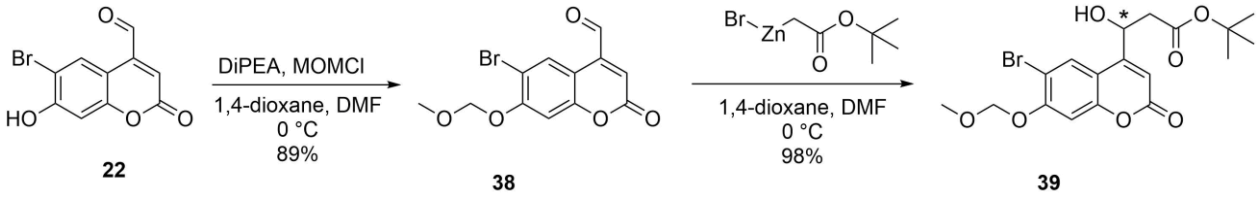

Figure 25: Synthesis of Bhc-based, *tert*-butyl protected ß-hydroxy acid. The hydroxy group in position 7 was methoxymethyl protected to avoid side reactions. Following the Reformatsky reaction with *in-situ* produced 2-(*tert*-butoxy)-2-oxoethyl)zinc bromide was performed. The nucleophilic addition yielded in 98% of the desired product **39**.

The analogous Reformatsky reaction with DEAC carbaldehyde **29** was also successful (Figure 26). The DEAC-based *tert*-butyl ß-hydroxypropanoate **40** was obtained in 75% yield.

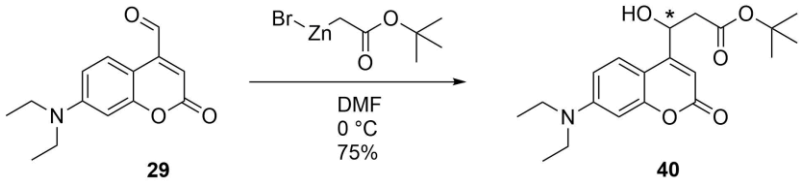

Figure 26: Synthesis of DEAC based *tert*-butyl ß-hydroxypropanoate. DEAC carbaldehyde **29** reacted with *in-situ* produced 2-(*tert*-butoxy)-2-oxoethyl)zinc bromide to the desired product **40** in 75% yield.

The experimental procedure from Seyfried *et al.*[162] foresees DMF as solvent. However, since NDBF carbaldehyde **17** has a very low solubility in DMF, the reaction was carried out in THF (Figure 27). Unfortunately, the reaction did not lead to the desired product. No conversion of the starting material could be detected by TLC. It is assumed that the reaction was unsuccessful because THF instead of DMF was used. Possibly the Reformatsky reagent is not reactive enough in this solvent or the *in-situ* preparation did not occur. However, since NDBF is not soluble in DMF or NMP, their use as solvent for the reaction is not possible.

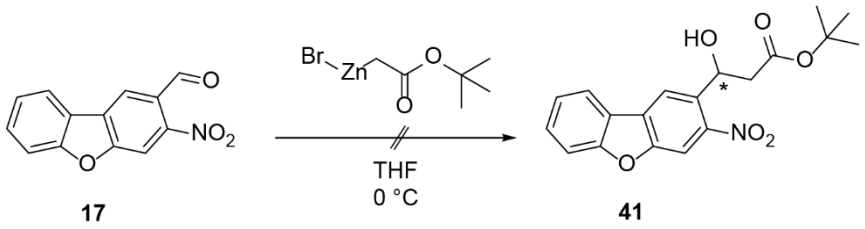

Figure 27: Reformatsky reaction of NDBF carbaldehyde with 2-(*tert*-butoxy)-2-oxoethyl)zinc bromide. The reaction showed no conversion of the starting material. Product **41** could not be obtained.

In summary, the synthesis of the carbaldehydes of all three PPGs (NDBF, Bhc, DEAC) was successful. These building blocks were used as the basis for the preparation of amino acid derivatives and ß-hydroxy acids. The synthesis of amino acid derivatives was not accomplished, whereas the preparation of ß-hydroxy acids of the PPGs DEAC and Bhc were achieved. In particular, the DEAC component was of interest for the construction of TPA-*tris*NTA because of its two-photon absorption ability and the possibility to produce large quantities, which is why this compound was pursued further.

4.4. Two-photon activatable-*tris*NTA

4.4.1. Design and synthesis of two-photon activatable-*tris*NTA

The design of TPA-*tris*NTA aimed to build a small lock-and-key element, which can be activated by light to immobilize peptides and proteins in four dimensions (x/y/z and time) at high precision. The functional mechanism is based on the autoinhibition of the multivalent chelator head *tris*NTA, which is connected through a peptide linker to an intramolecular His_5-tag (Figure 28). In presence of Ni(II)-ions, the *tris*NTA head group is self-inhibited by the intramolecular His-tag (OFF-state). Upon photo-activation, the intramolecular His-tag is cleaved and *tris*NTA is liberated (ON-state). Due to the high affinity of the *tris*NTA towards $His_{6\text{-}10}$-tagged proteins, TPA-*tris*NTA functionalized interfaces are able to immobilize any His-tagged protein of interest (POI) with defined orientation after illumination (TRAPPED-state).

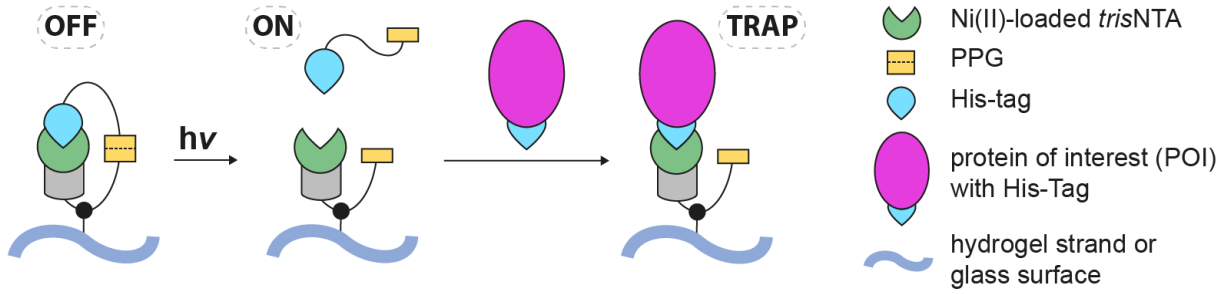

Figure 28: Schematic illustration of operating principle of TPA-*tris*NTA. Autoinhibited (OFF) TPA-*tris*NTA gets activated upon illumination (ON) and is subsequently able to bind His-tagged POIs (TRAP).

The operating principle of autoinhibition and photoactivation was adapted from PA-*tris*NTA, developed by Grunwald *et al.*[72] and Labòria *et al.*[73] but was developed further to improve control in the z-dimension as well as biocompatbility.[73] Therefore, the new interaction molecule should contain a two-photon (2P) activatable group instead of Anp as PPG. Since DEAC has very good two-photon properties as well as very good water solubility, the focus was placed on DEAC as a trigger point for light activation. When incorporating two PPGs, incomplete cleavage could occur, whereby one PPG stays intact. To prevent this, only one DEAC group should be incorporated. Therefore, instead of a His_6-tag a His_5-tag was chosen, since it is known from previous studies that a His_5-tag has a sufficiently high stability against competing His_6-tags of a POI to maintain autoinhibition.[72] The PPG was strategically placed between the His_5-tag and a cysteine, which was used as an anchor for surface immobilizations *via* Michael addition. Upon illumination, the PPG undergoes cleavage, which sets free the His_5-tag to diffuse away while the *tris*NTA headgroup remains anchored to the surface by the cysteine. The chemical structure of TPA-*tris*NTA is shown in Figure 29.

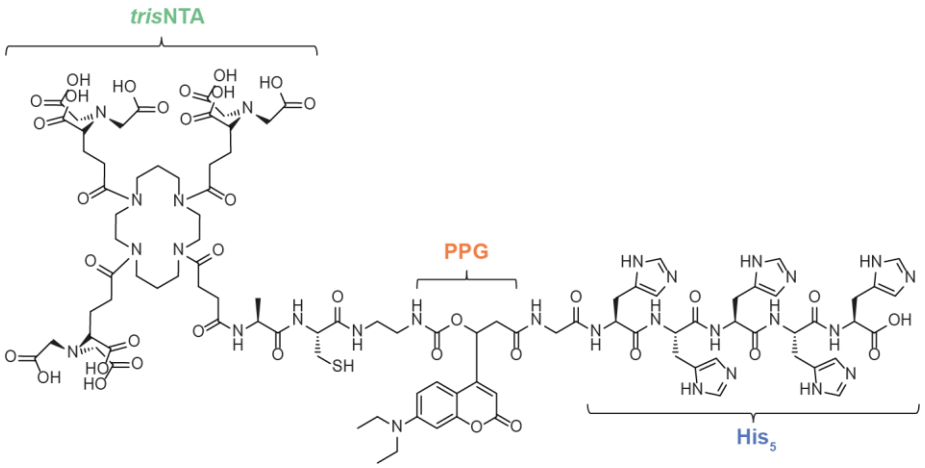

Figure 29: Chemical structure of TPA-*tris*NTA. The interaction molecule consists of the *tris*NTA head group (green) and an intramolecular His_5-tag (blue) at the *C*-terminus. For 2P-cleavage, a DEAC-based β-amino acid (orange) is strategically incorporated within the linker.

For the synthesis of TPA-*tris*NTA, the successfully synthesized photolabile *tert*-butyl ß-hydroxypropanoates should be converted into Fmoc-protected amino acid analogs (Figure 30). This allows incorporation into the peptide backbone of the affinity tool by solid phase peptide synthesis (SPPS). Coumarin PPGs have very poor light-driven C-N bond cleavage efficiency, since the bond-photolysis is very slow and often results in rebinding between the two atoms.[125] Therefore, the DEAC building block was linked *via* a carbamate structure, which lead to the favored O-C bond scission upon irradiation. To establish the carbamate linkage, the hydroxyl group of DEAC ß-hydroxypropanoate **40** was first converted to a chloroformate by reaction with triphosgene. Thin layer chromatography (TLC) confirmed the successful chloroformate formation, which was then used without further analysis or purification to avoid hydrolysis. Subsequently, the carbamate linkage was prepared by nucleophilic substitution by the free primary amine of Fmoc-ethylenediamine (Fmoc-EDA). The *N*- and *C*-terminally protected amino acid analog **42** was obtained with 56% yield. Then, the carboxylic acid was deprotected under acidic conditions (TFA: DCM, 1:1, v/v) and **43** was obtained with 73% yield after column chromatography purification using RP-C_{18} silica (water: MeCN, 1:1, 1% TFA v/v%). The resulting Fmoc-protected amino acid analog **43** was incorporated into the peptide backbone (sequence: H_2N-Ala-Cys-**43**-Gly-His-His-His-His-His-CO_2H) of the interaction molecule by microwave-assisted SPPS. The *tris*NTA headgroup was manually coupled to the peptide. After acidic cleavage (TFA:H_2O:EDT, 95:2.5:2.5, v/v) from the resin and lyophilization the raw product was purified by RP-C_{18}-HPLC. The final product TPA-*tris*NTA was obtained with an overall yield of 10%, which was verified by MALDI-TOF-MS analysis and the purity was confirmed by RP-C_{18}-HPLC (Figure 31).

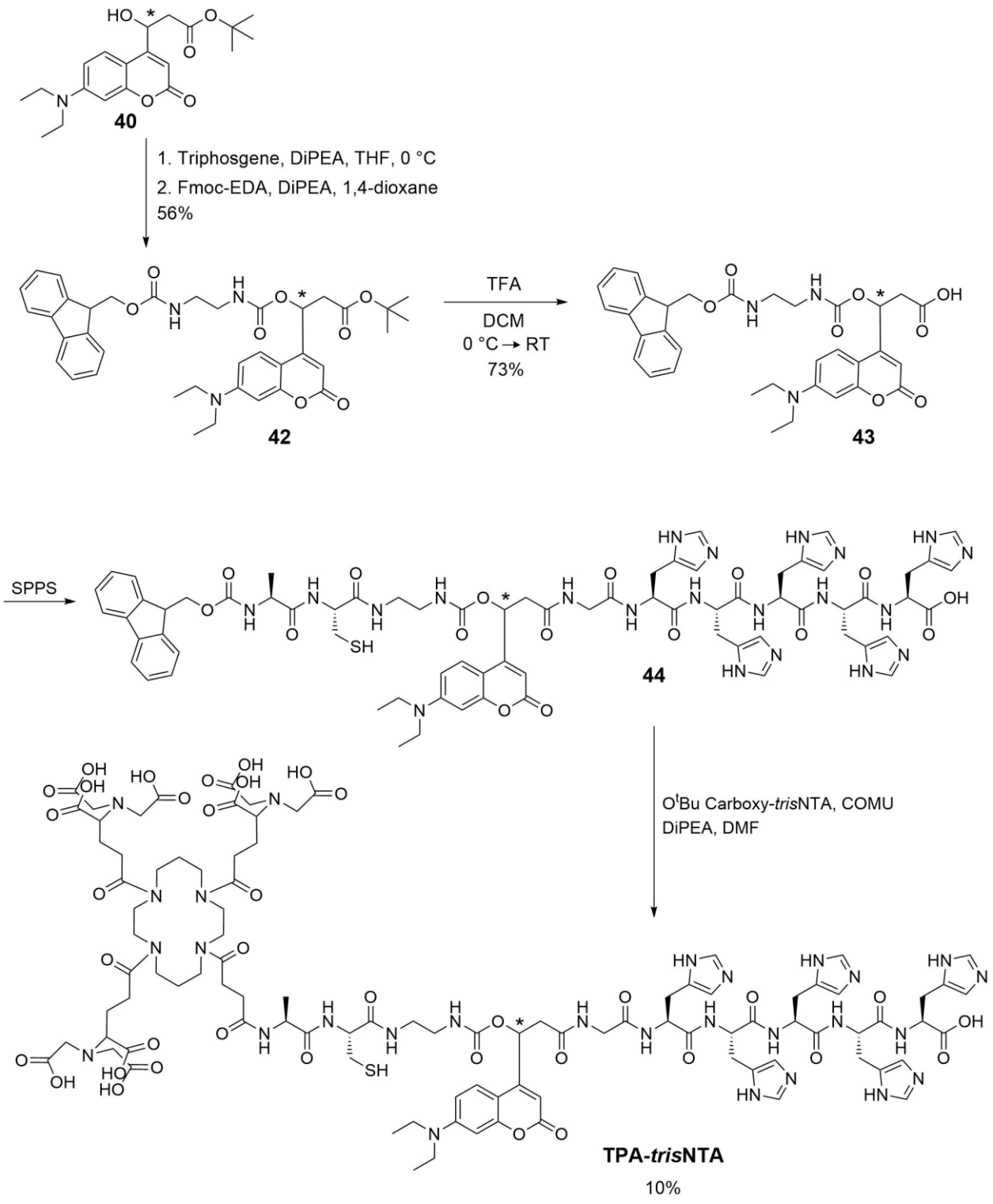

Figure 30: Synthesis of **TPA-*tris*NTA** containing a DEAC PPG. First the DEAC based *tert*-butyl ß-hydroxypropanoate **40** was converted with triphosgene to the respective chloroformate, second Fmoc-ethylenediamine was added and *via* nucleophilic substitution the *C*-and *N*-terminal amino acid analog **42** was obtained. Subsequently, the carboxylic acid was deprotected (**43**) for the incorporation into the peptide backbone *via* SPPS (**44**). Finally, the *tris*NTA headgroup was attached to the peptide backbone by manual coupling to obtain the desired **TPA-*tris*NTA** with an overall yield of 10%.

Having successfully synthesized **TPA-*tris*NTA** with photolabile protection group DEAC incorporated, the focus was on the proof-of-principle, characterization, and application of the interaction molecule (see chapter 4.4.2). Therefore, the development of additional **TPA-*tris*NTA** variants with other PPGs such as NDBF, Bhc, NC, NP, was not pursued further.

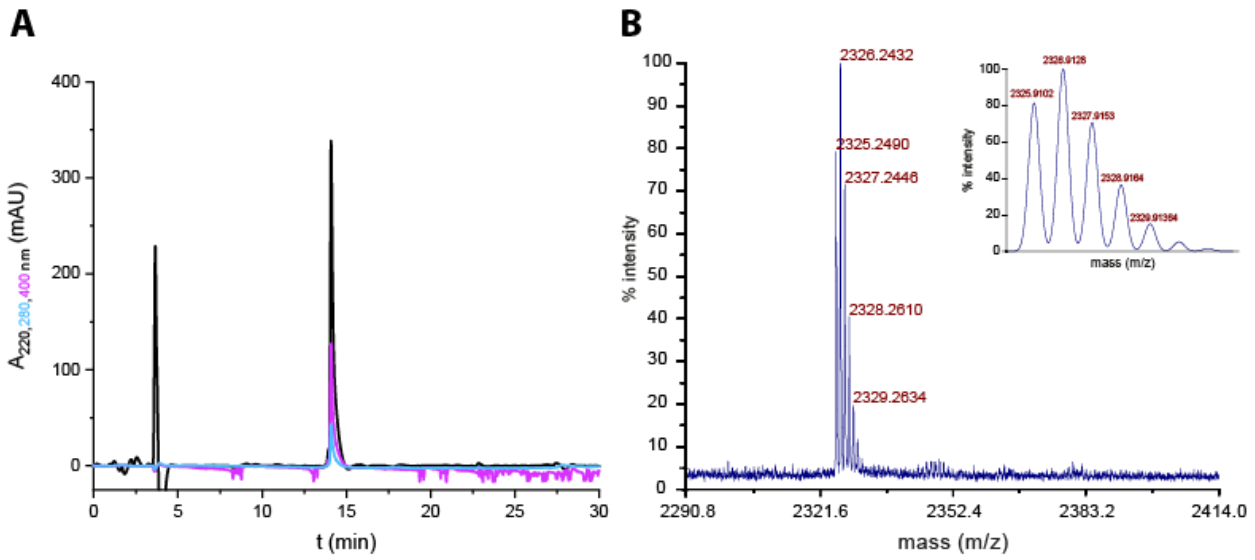

Figure 31: Validation and analysis of TPA-*tris*NTA synthesis. **A**) RP-C_{18}-HPLC chromatogram of purified TPA-*tris*NTA using method 2. Absorbance was detected at 220 nm (black line), 280 nm (blue line), 400 nm (magenta line). Spikes in the 400 nm chromatogram are due to fluctuations of the light source. **B**) MALDI-TOF-MS of purified TPA-*tris*NTA showing a mass of 2326.2432 Da $[M+H]^+$, which was in good agreement to the expected mass of 2326.9126 Da $[M+H]^+$. The isotope pattern observed corresponds to the simulated pattern, which is displayed in the inlay.

4.4.2. Photophysical characterization of TPA-*tris*NTA and its building blocks in solution

To compare the spectroscopic properties of TPA-*tris*NTA with its precursors, one-photon absorption and fluorescence spectra of TPA-*tris*NTA and as a comparison of **2**-**4** were measured (Figure 32). All compounds displayed an intense absorption band located around 390 nm and an intense fluorescence emission with maxima around 480 nm. Only the DEAC-derivative **2** showed a second absorption maximum at 460 nm due to its aldehyde substitution in the 3-position. The unaltered absorption profile of TPA-*tris*NTA compared to the other DEAC derivatives demonstrates that the light absorbing properties are unaffected by the electronical environment of the structure. The fluorescence emission spectra of TPA-*tris*NTA and compounds **2**-**4** were almost the same, this indicated that the structural differences did not influence the fluorescence emission.

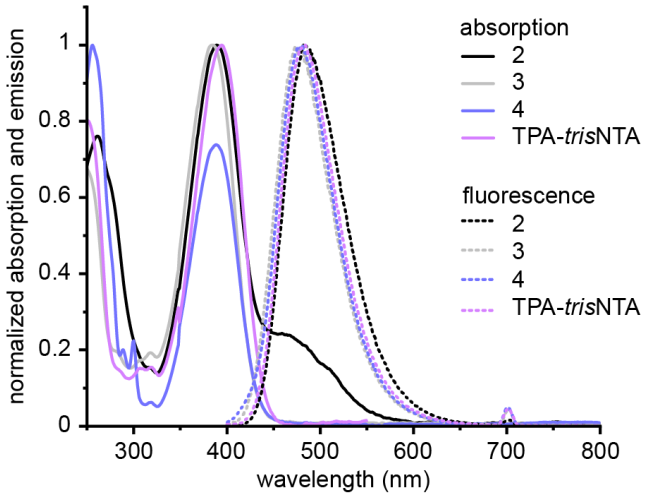

Figure 32: Normalized absorbance and emission spectra of compounds **2**-**4** as well as TPA-*tris*NTA. All compounds exhibit an absorbance maximum around 390 nm and an emission maximum around 480 nm. DEAC-aldehyde **2** also has an absorbance maximum at 460 nm, because of the aldehyde group.

To verify the uncaging efficiency of the newly developed amino acid derivative **4** upon irradiation, the compound was illuminated using a 405 nm LED lamp (185 mW/cm^2) with increasing light doses (5-900 s). Each sample was analyzed by RP-C_{18}-HPLC. Investigation of the HPLC traces showed that the starting peptide peak disappeared as a function of illumination time, concomitant with the formation of a new peak with an earlier retention time. With increasing light exposure, the peak of the starting material (t_R = 17 min) decreased and a peak (t_R = 12 min) most likely of cleavage product increased. Quantification revealed a fast exponential decay curve with a decay kinetic of $t_{1/2}$ = 12 s under one-photon photolysis conditions. Complete cleavage was achieved after 300 s. Notably, no other photo-byproducts were detected during the photolysis studies, indicating a clean photo-fragmentation of the carbamate-linked DEAC.

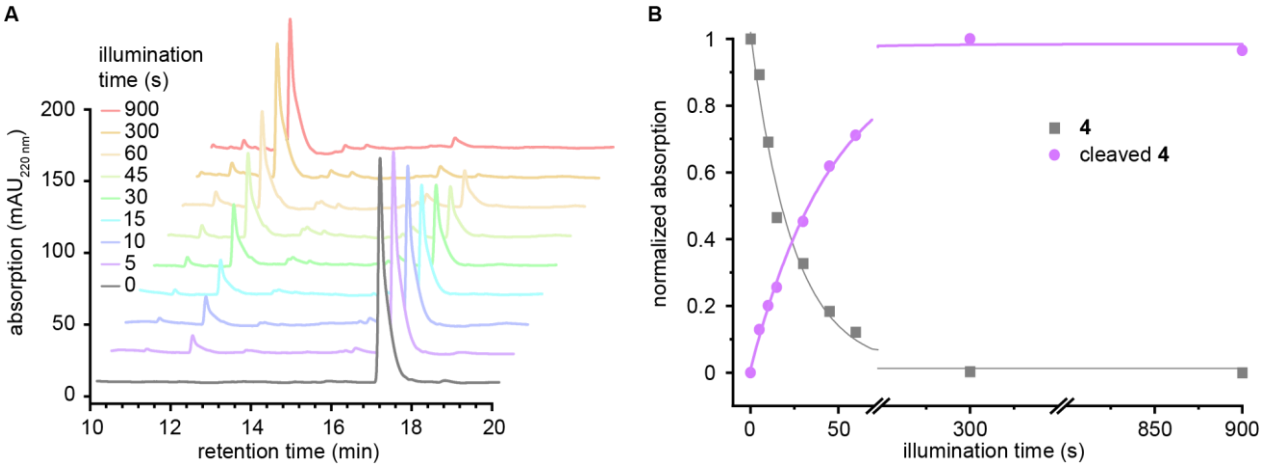

Figure 33: Photocleavage studies of compound **4**. A) RP-C_{18}-HPL-chromatograms of **4** after 0-900 s illumination with 405 nm. Quantification of decreasing peak of starting material and increasing peak of photolysis product revealed a cleavage kinetic of 12 s for 50% of **4**.

To evaluate the photophysical properties of TPA-*tris*NTA, the fluorescence quantum yield (φ_F) and the 2P absorption action cross sections ($\varphi_F\delta_2$) were determined in collaboration with Marvin Asido (Wachtveitl lab). The measurement in an integrative sphere revealed φ_F to be 15% (Figure 34A). $\varphi_F\delta_2$ were assessed by 2P-excited fluorescence (TPEF) and given in units of Goeppert-Mayer (GM). In the excitation range from 770 to 860 nm $\varphi_F\delta_2$ values of 7.1 GM at 800 nm and 7.7 GM at 810 nm for TPA-*tris*NTA were determined (Figure 34B). The $\varphi_F\delta_2$ values of TPA-*tris*NTA are thus more than 7-fold higher than 2,6-dimethylnitrobenzene derivatives ($\varphi_F\delta_2$= ~0.1-1 GM, 720 nm)[182] but well below the values of stilbene derivatives ($\varphi_F\delta_2$= ~20 GM, 800 nm).[183] Nevertheless, the 2P absorption action cross section values of TPA-*tris*NTA are well above 0.1 GM, which is recommended for biological applications.[115,184]

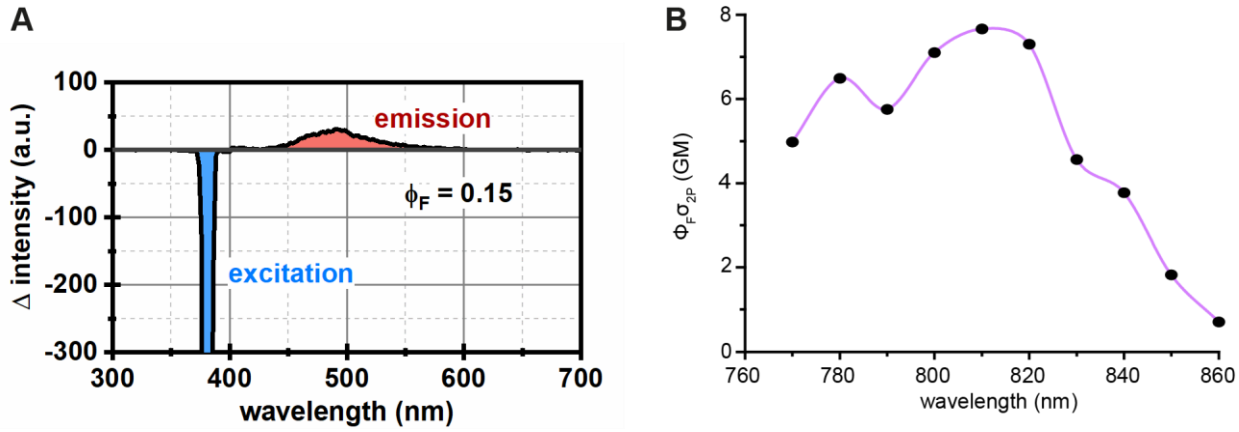

Figure 34: Estimation of fluorescence quantum yield and two-photon absorbance spectrum of TPA-*tris*NTA (performed by Marvin Asido, Wachtveitl lab). A) Fluorescence quantum yield was calculated by the ratio between emission integral and excitation integral. For better illustration the excitation peak (blue) is not shown entirely. B) Two-photon absorption cross section values of GM ($\phi_F\sigma_{2P}$) for TPA-*tris*NTA determined by the method of two-photon excited fluorescence.

To confirm the 2P effect, the power dependent 2P absorption of TPA-*tris*NTA was tested at 800 nm by varying the excitation energies from 20 to 100 mW (Figure 35A) by Marvin Asido (Wachtveitl lab). The double-logarithmical plot of excitation energy *versus* fluorescence intensity reveals a slope of 1.93 ± 0.02, which reflects an almost perfect quadratic power dependency (Figure 35B) and confirms a 2P-activation process. Having validated and characterized 1P and 2P activation of TPA-*tris*NTA, the focus was on the application of TPA-*tris*NTA on 2D surfaces.

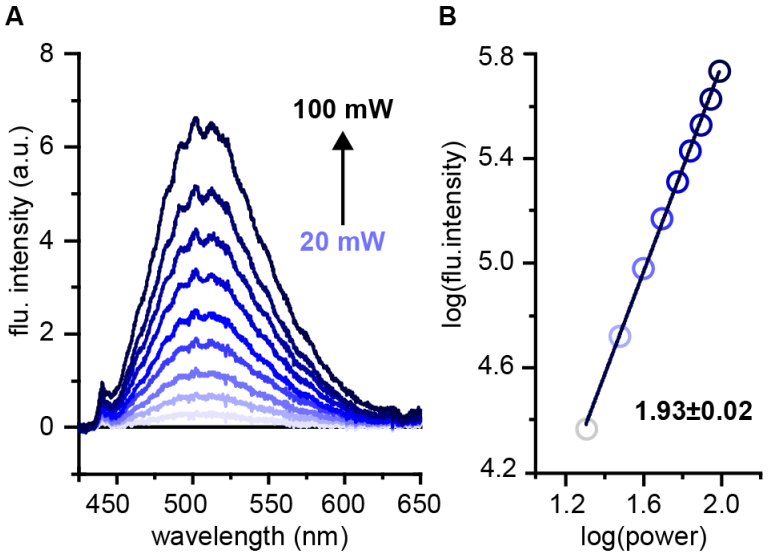

Figure 35: Power dependency of 2P absorption of TPA-*tris*NTA (performed by Marvin Asido, Wachtveitl lab). Intensities of the power dependent fluorescence spectra of TPA-*tris*NTA were logarithmically plotted against the logarithm of the power, where the slope representing the two-photon power dependence was found to be 1.93±0.02, confirming a two-photon process for TPA-*tris*NTA activation at 800 nm.

4.5. 2D protein organization *via* (T)PA-*tris*NTA

Functionalized glass surfaces are useful to study both the proof of principle of the light activatability of PA-*tris*NTA and TPA-*tris*NTA and to evaluate the correlation of activation to applied energy dosage. This requires initially a homogeneous functionalization of the surface. The requirements for a good functionalization for protein immobilization are: I) specific enrichment of the POI only in activated areas II) high signal to noise ratio III) precise activation in x,y- dimension IV) no unspecific binding V) uniform functionalization VI) reversibility. Three different functionalization methods based on 3-glycidyloxypropyl-trimethoxysilane (GOPTS), poly-L-lysine (PLL) or 3-aminopropyl-triethoxysilane (APTES) were tested. The differences, disadvantages and advantages are discussed in the following chapters.

4.5.1. GOPTS-based PA-*tris*NTA functionalized surfaces

PA-*tris*NTA functionalized surfaces based on GOPTS were prepared according to chapter 3.2.1.8.1. Therefore, thoroughly cleaned glass slides were activated by treatment with peroxymonosulfuric acid to generate silanol groups on the surface, before 3-glycidyloxypropyl-trimethoxysilane (GOPTS) was added between two stacked glass slides (Figure 36). Hydrolysis of the trimethoxysilane generates silanol groups, which condensate *in-situ* with silanol groups on the glass slide, forming a covalent siloxane bond. The epoxide moiety is a reactive group which reacts with alcohols, water, amines, and thiols *via* ring opening. This was used to install a polyethylene glycol (PEG) spacer on the surface, by incubating the epoxide modified surface with diamino-PEG (2 kDa). Subsequently, the primary amine of the PEG-spacer was reacted with the active ester of a maleimidopropionic acid *N*-hydroxysuccinimide ester (Mal-NHS) crosslinker to obtain a maleimide functionality on the surface. Finally, the maleimide group was used as an anchor to decorate the surface with PA-*tris*NTA or TPA-*tris*NTA by Micheal addition.

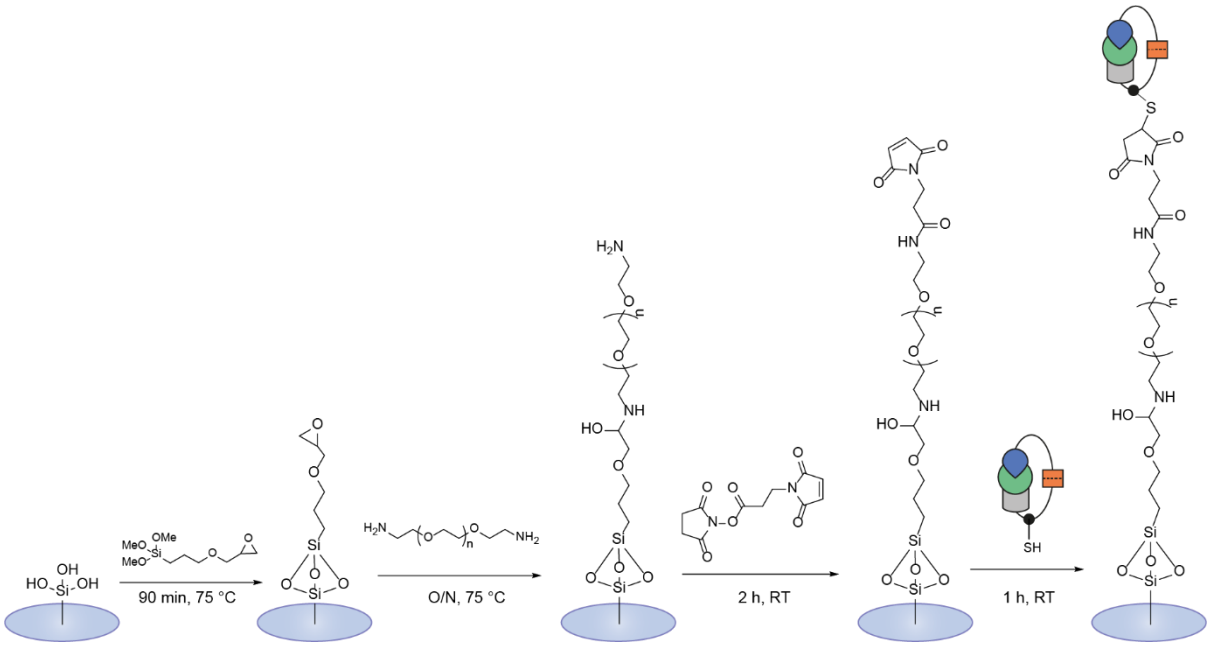

Figure 36: Schematic illustration of GOPTS-based photoactivatable glass surfaces. After plasma cleaning the glass slides were silanized with 3-glycidyloxypropyl-trimethoxysilane (GOPTS) and the epoxy-group of GOPTS was coupled with a diamino-PEG linker (2 kDa). Subsequently the amino-group of the linker was conjugated to an NHS-maleimide linker. PA-*tris*NTA was anchored on top *via* Michael addition.

Mask patterning was performed to illuminate large areas (~1 cm^2). A quartz mask with a regular pattern of circles was placed on top of the glass slide with a drop of MQ water in between. In order to investigate, which exposure time is required for optimal activation of PA-*tris*NTA, the surfaces were exposed for 20-160 s at constant power (185 mW/cm^2) at 365 nm with an LED lamp (CS2010 curing System, Thorlabs). After Ni(II)-loading and incubation with His_{10}-MBP^{OG488} (300 nM in HBS buffer), confocal laser scanning microscopy (CLSM) images were acquired. As seen in Figure 37, functionalization and specific light activation in the circular ROIs of the mask were successful for all probes. It was found that already an exposure time of 20 s is sufficient to write the expected pattern on the surface. It should also be noted that with an 8-fold longer irradiation (160 s) no signs of overexposure like effects of stray light were visible. Since light exposure with these settings for 160 s did not lead to an increase of PA-*tris*NTA activation and protein binding, further increase of activation time was not conducted. However, the fluorescence background signal by unspecifically bound protein was high for all surfaces independent of illumination time.

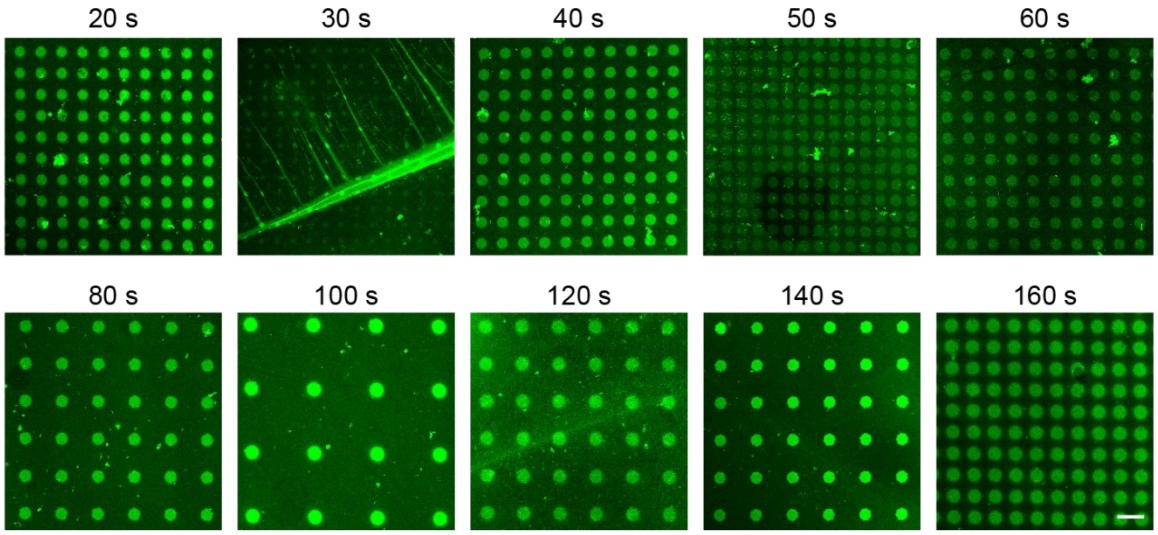

Figure 37: PA-*tris*NTA functionalized surfaces on the basis of GOPTS silanization. The surfaces were mask patterned with varying illumination time (20-160 s) at 365 nm with a LED handlamp before Ni(II)-loading and His_{10}-MBP^{OG488} immobilization. Scale bar, 50 µm.

An analysis of PA-*tris*NTA activation dependent of the light dose by quantitative comparison of protein accumulation was not possible due to inhomogeneities of the surfaces. As can be seen in Figure 38, the functionalization was not homogeneous, resulting in patchy areas of varying fluorescence intensity within the field of view. In addition, layered superimpositions occurred in which the protein bound non-specifically. These unspecific protein immobilizations occurred again when the experiment was repeated (14-times), therefore other methods for glass surface functionalization were investigated.

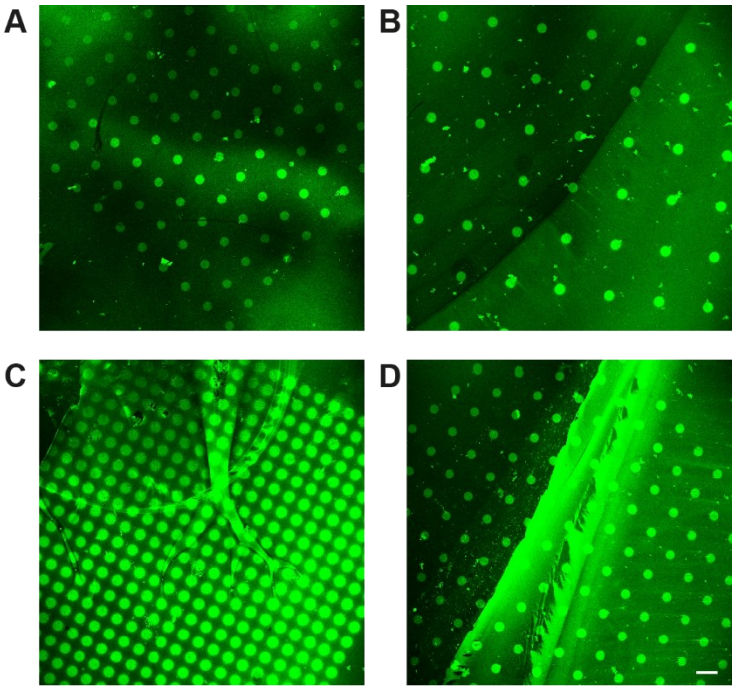

Figure 38: Inhomogeneities of GOPTS functionalized surfaces with immobilized. His_{10}-MBP^{OG488} A) Fluorescence intensity varied in the field of view because of inhomogeneous functionalization. B-D) Layered superimpositions on the glass surfaces resulted in unspecific protein binding. Scale bar, 50 µm.

To test the reversibility of the immobilization, images were taken before and after the addition of imidazole (500 mM in HBS buffer, 1 min). In Figure 39 can be seen that the pattern was based on specific interaction between *tris*NTA and His-tag of the protein, therefore a short imidazole pulse outcompetes the protein from the NTA complex, whereas unspecific bound protein remains stuck to the surface.

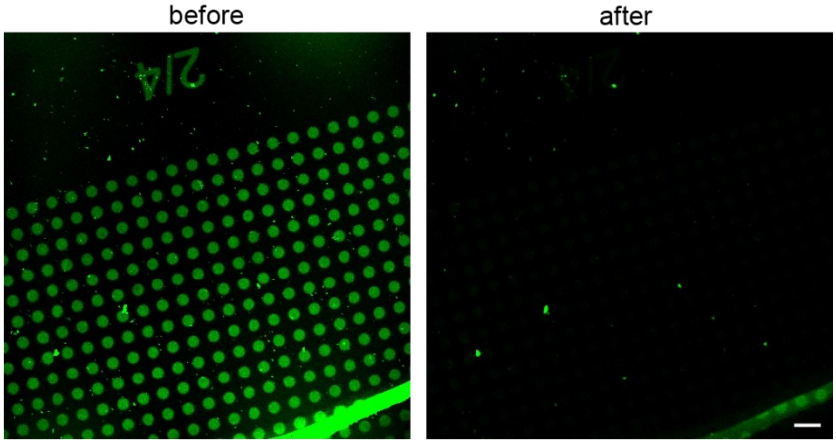

Figure 39: Reversibility test of His_{10}-MBP^{OG488} binding on GOPTS functionalized surfaces. Images before and after the addition of imidazole demonstrate that the specific *tris*NTA His-tag interaction is outcompeted by imidazole (500 mM, 1 min), while unspecific binding remains. Scale bar, 50 µm.

4.5.2. PLL-based PA-*tris*NTA functionalized surfaces

PA-*tris*NTA functionalized surfaces based on poly-L-lysine (PLL) were conducted according to the procedure described in 3.2.1.8.2. First, PA-*tris*NTA was added to a solution of 3-maleimido-PEG-*N*-hydroxysuccinimide ester (Mal-PEG-NHS) to bind *via* Michael addition to the maleimide functionality. In the next step, the primary amine of PLL reacted with the active NHS ester to form a stable amide bond. The preformed functionalization mixture (PLL-PEG-PA-*tris*NTA) was added to the glass surfaces to form a homogenous layer by electrostatic interaction between PLL and the surface.

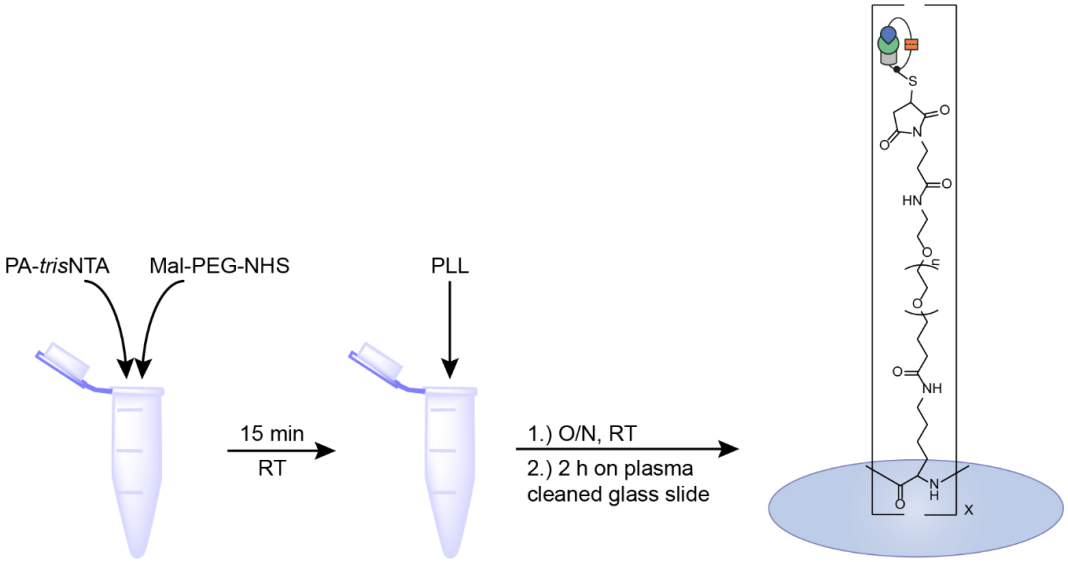

Figure 40: Schematic overview of PLL-based functionalized, photoactivatable glass surfaces. PA-*tris*NTA and a Maleimide-PEG-NHS linker were preincubated and subsequently added to poly-*L*-lysine. Following the mixture was added to the glass slides to form photoactivatable surfaces.

In order to evaluate the homogeneity of the functionalization, large patterns were written onto the surface by mask illumination. Therefore, a quartz mask was put on top of the with HBS buffer moistened surfaces and illuminated for 1 min, since it is known from the illumination studies on GOPTS surfaces that this time period was sufficient for activation of PA-*tris*NTA (365 nm, 185 mW/cm^2) with an LED lamp. After Ni(II)-loading, the surfaces were incubated with different proteins and peptides to compare their binding behavior towards the functionalized surfaces (Figure 41). The glass slides were incubated with either His_{10}-mVenus, His_6-GFP or His_6-AF647 (300 nM in HBS buffer) for 30 min. In all three cases, the pattern of mask illumination was observed, demonstrating successful PLL based functionalization, light activation of PA-*tris*NTA and also protein binding. The CLSM images exhibited uneven exposure of the samples, possibly

due to stresses on the glass surface within the holders. Therefore, the line scans were performed in the image diagonal from top left to bottom right. By comparing the fluorescence profile along the measured line, the signal to noise ratio for His_{10}-mVenus, His_6-GFP or His_6-AF647 was 5-fold, 2.3-fold, and 10-fold, respectively.The intense signal at the surface with immobilized AF647, can be explained on one hand by possibly higher immobilization density, because the small peptide creates less sterically hindrance and on the other hand it can be explained by the higher brightness of the AF647 dye compared to the autofluorescent proteins. The brightness of a chromophore is calculated by the product of its extinction coefficient ε and its fluorescent quantum yield ϕ_F. The brightness of AF647 is 89,100 $M^{-1}cm^{-1}$ (ε=270,000 $M^{-1}cm^{-1}$, ϕ_F= 0.33)[185], of GFP is 45,880 $M^{-1}cm^{-1}$ (ε= 62,000 $M^{-1}cm^{-1}$, ϕ_F= 0.74)[186], and mVenus is 67,200 $M^{-1}cm^{-1}$ (ε= 105,000 $M^{-1}cm^{-1}$, ϕ_F= 0.64).[187] However, differences can also be seen in the background signal, which indicates the level of non-specific binding. Comparison of the surfaces with different immobilized POIs showed, that the fluorescent signal from unspecific binding was the lowest with immobilized His_6-AF647, increased with His_{10}-mVenus and is the highest for His_6-GFP. His_6-AF647 showed the best result in terms of low level of unspecific binding and high-signal-to-noise ratio. mVenus and GFP may also be suitable after improvements to block unspecific binding.

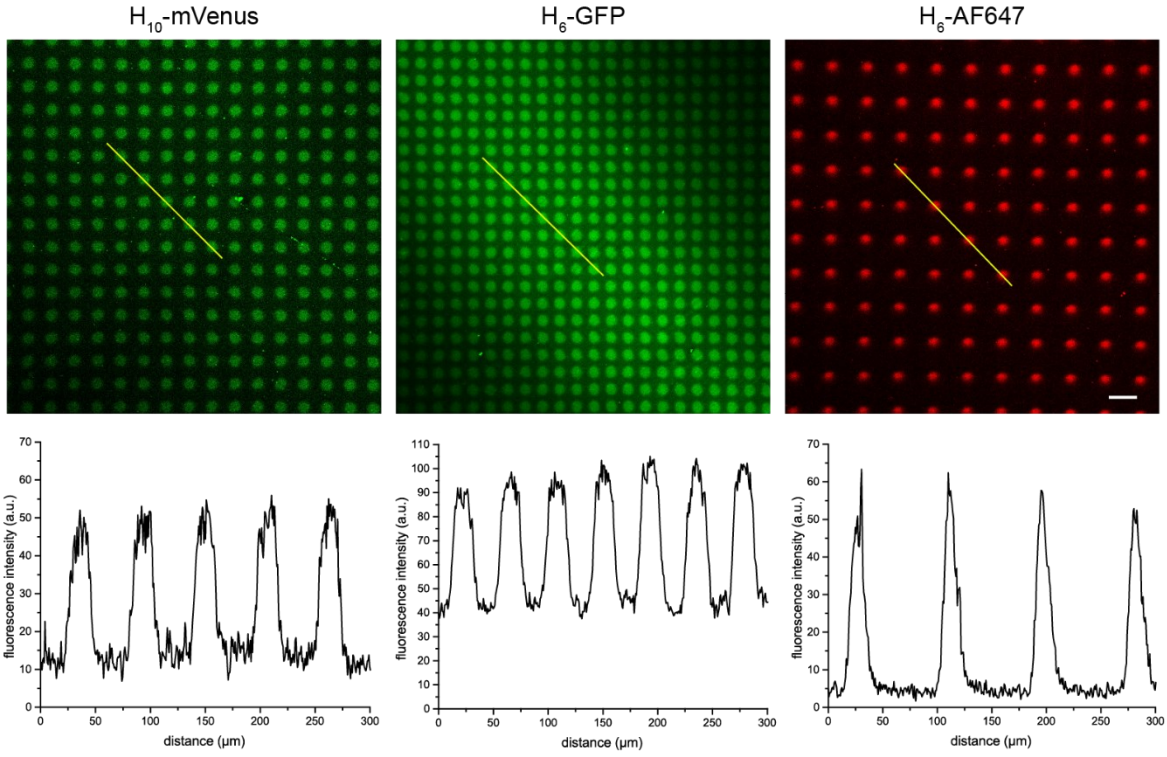

Figure 41: PLL based photoactivatable surfaces. After mask patterning (365 nm, 1 min, 185 mW/cm^2) and Ni(II)-loading either His_{10}-mVenus, His_6-GFP or His_6-AF647 (300 nM in HBS buffer) were immobilized on the interface. Line scans of the CLSM images illustrate the signal to background ratio. The line scan were measured in the diagonal due to uneven surface illumination at the microscope. Scale bar, 50 µm.

To investigate protein binding independent of light activation, one surface was decorated with HS-*tris*NTA and another was functionalized with methoxy-PEG (3 kDa) lacking *tris*NTA (Figure 42). Both surfaces were incubated with His_6-GFP (300 nM in HBS buffer) and the fluorescence intensity was measured in four 66 µm x 66 µm ROIs. The fluorescence signal was on average 300 times higher in the positive control than in the negative control. The controls cannot be compared with the patterned PA-*tris*NTA surfaces because imaging settings differ. This result confirms homogenious functionalization with specific protein immobilization.

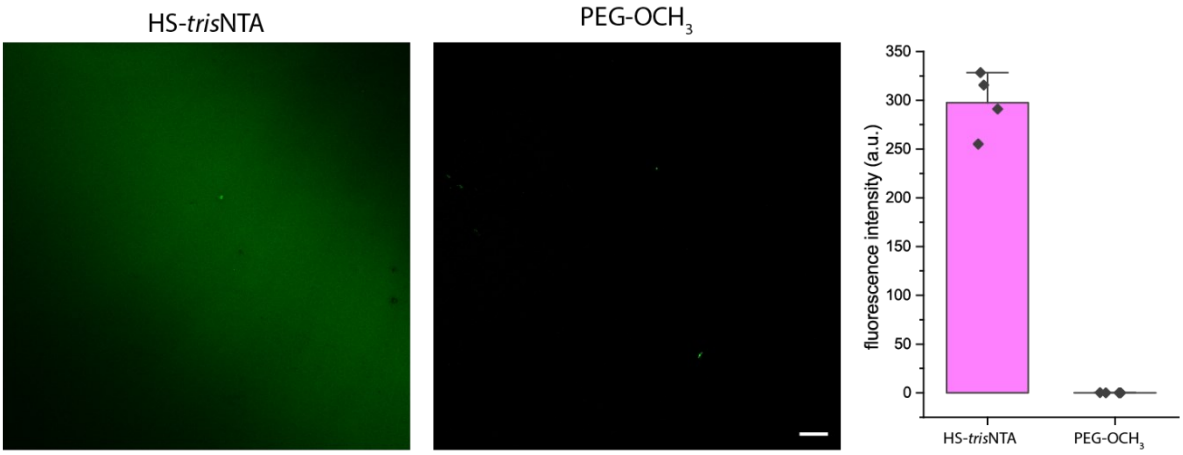

Figure 42: Controls for specificity of protein immobilization on PLL functionalized surfaces. HS-*tris*NTA was used to as a positive control to bind His_6-GFP without light activation, whereas methoxy-PEG decorated surface worked as a negative control. The fluorescence intensity in four 66 µm x 66 µm ROIs was analyzed to compare the amount of specifically bound His_6-GFP to unspecific adherent protein. Scale bar, 50 µm.

To improve the signal-to-noise ratio for protein immobilization, blocking steps were tested after mask pattering to saturate attachment sites for non-specific binding. Short NHS-ester PEG_4 (PEG_4) had been used in literature for passivation of surfaces against unspecific protein binding, hence the small molecule (333 Da) is effective in penetrating into an existing PEG layer, thereby condensing it.[188] Another very frequently used methods is protein blocking of surfaces by adhesion of proteins like bovine serum albumin (BSA), casein, or milk protein.[189] For this purpose, a PLL-PA-*tris*NTA functionalized surface was incubated after mask patterning (365 nm, 185 mW/cm^2) subsequently with a PEG_4 solution (25 mM in 0.1 M $NaHCO_3$ aq., 30 min), and 5% BSA in HBS buffer (v/v) for 10 min. After washing with HBS buffer, His_6-GFP (300 nM in HBS buffer, 30 min) was added to the surface. The excess of protein was washed away with HBS buffer. The line scan of the untreated surfaces showed a signal to noise ratio of 2. Compared to that the line scan of the surface with blocking steps revealed a signal to noise ratio of 8, which demonstrates a significant improvement. This indicated that the PEG layer created during the

functionalization of the surface is not sufficient to avoid unspecific binding. To improve this shortfall, the 3 kDa PEG could be exchanged by a longer PEG *e.g.* 5-10 kDa long. Since, the fluorescence intensity of specifically bound GFP in the activated areas was not significantly decreased by the additional passivation steps, incubation with PEG_4 and BSA solution was included in the standard procedure for PLL surfaces.

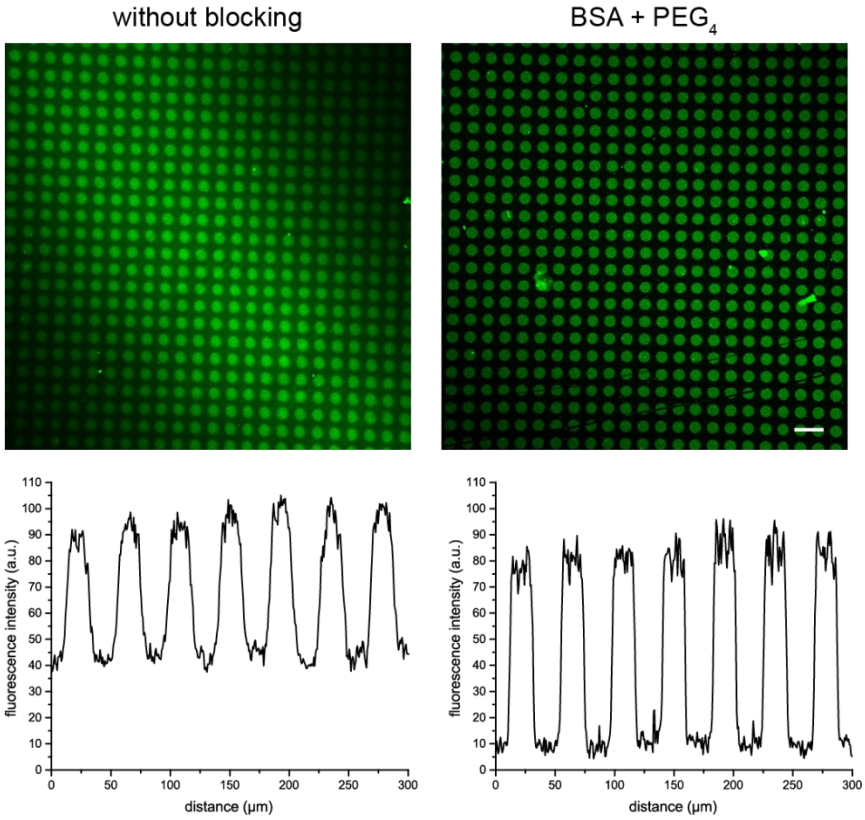

Figure 43: Blocking strategy to avoid unspecific binding to PLL-based photoactivatable surfaces. Without blocking of the mask patterned surface, a high background signal of His_6-GFP is detectable. By incubation with PEG_4-solution after mask patterning and washing with 5% BSA in HBS buffer (v/v) before immobilization of His_6-GFP the signal to noise ratio was improved by a factor of 4. Scale bar, 50 µm.

Precise and specific protein patterns could be obtained on PLL based PA-*tris*NTA functionalized glass surfaces, after blocking of unspecific binding by passivation steps. PLL-modified surfaces are based on electrostatic interaction between the positively charged poly-*L*-lysine and the negatively charged glass surface, therefore they are sensitive to changes in pH, temperature and ionic strength. In order to obtain robust and versatile surfaces, 3-aminopropyl-triethoxysilane (APTES) silanized PA-trisNTA surfaces should be prepared, which are based on covalent functionalization.

4.5.3. APTES-based PA-*tris*NTA functionalized surfaces

As a third functionalization method for PA-*tris*NTA surfaces, 3-aminopropyl-triethoxysilane (APTES) was tested. Therefore, the surface of precleaned glass slides was etched by plasma cleaning with oxygen to activate the surface by generation of silanol groups. Following, a solution consisting of methanol, acetic acid and APTES was added. Thereby, the reactive triethoxysiloxane groups hydrolyze to silanol groups which *in-situ* condense with the silanol groups of the surface. PA-*tris*NTA was coupled to the maleimide functionality of 3-maleimidopropionic acid polyethylene glycol *N*-hydroxysuccinimidyl ester (Mal-PEG-NHS) (3 kDa) *via* Michael addition. Subsequently, the NHS moiety of the bifunctional PEG-linker was used to couple PA-*tris*NTA-PEG-NHS to the APTES silanized surfaces by nucleophilic substitution (S_N2 reaction). The procedure is schematically shown in Figure 44.

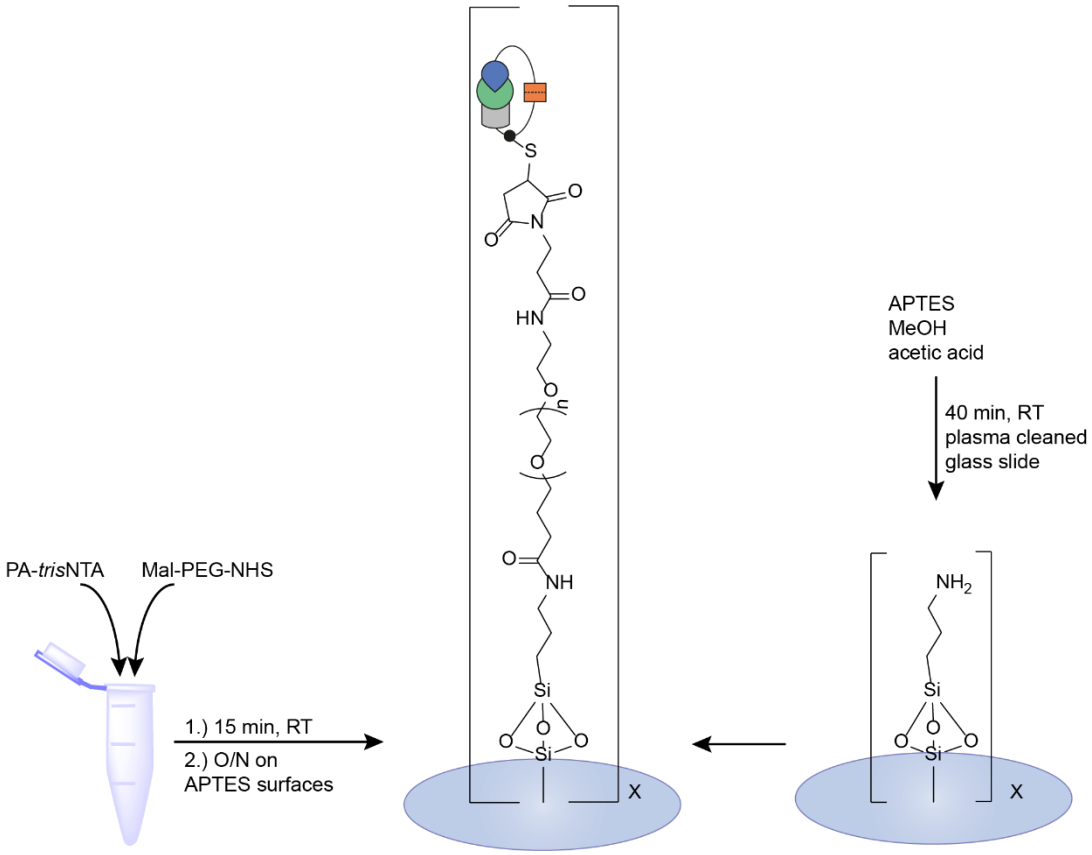

Figure 44: Schematic overview of APTES-based functionalized, photoactivatable glass surfaces. After plasma cleaning the glass slides were silanized with 3-aminopropyl-triethoxysilane (APTES) and subsequently coupled by NHS chemistry to preincubated PA-*tris*NTA-PEG-NHS.

Next the slides were patterned by mask illumination. A quartz mask was placed on top of the with HBS buffer wetted surfaces, following the glass slides were exposed with UV light (365 nm, 1 min, 185 mW/cm^2) with an LED lamp. Then, the *tris*NTA moieties were loaded with Ni(II)-ions to install the intramolecular complex with the $His_{5/6}$-tag for autoinhibition. Thus, the surfaces were first incubated with imidazole to avoid any unspecific bound particles, second they were incubated with EDTA to remove double positively charged ions, and finally they were treated with $NiCl_2$ to install autoinhibition. Before His_6-GFP (300 nM in HBS buffer) was immobilized, the surfaces were split into three groups to investigate the effect of blocking strategies on the signal-to-noise ratio. One group of slides was treated with the short NHS-PEG_4 (PEG_4), the second group was in addition to the incubation with PEG_4, treated with 5% BSA in HBS buffer. As a comparison, the third group had not received any blocking treatment (Figure 45). For quantitative analysis and comparison all surfaces were imaged with the same conditions on the same day. Unfortunately, a small drift of the quartz mask during the illumination process of the untreated surface, caused a shifted pattern.

The intensity profile of each surface showed that all three surfaces had a low background fluorescence. The fluorescence signal for the samples without passivation treatment showed the highest fluorescence signal of GFP, although the activating light dose was distributed in the drifted pattern. Passivation with PEG_4 resulted in a one third lower fluorescence signal of the pattern in comparison to the untreated surface. The combination of PEG_4 and BSA passivation yielded in a two-third lower fluorescence intensity of the protein pattern. This indicated that the treatment with blocking agents may cause an obstruction of binding sites on *tris*NTA. Whereas the combination of PEG_4 and BSA led to an even greater loss of intensity than PEG_4 alone. The best result in terms of GFP intensity inside the activated ROIs and signal-to-noise ratio was achieved without blocking agents. This result differs to the observations of PLL functionalized surfaces, where the usage of PEG_4 and BSA enhanced the signal-to-noise ratio. PEG_4 and BSA reduce unspecific protein binding to the surface, but the APTES functionalized surfaces showed very low background level of unspecific binding, so the potential for improvements were limited. Whereas the PLL functionalized surfaces had more unspecific adhesion of proteins, which could be decreased by blocking treatment.

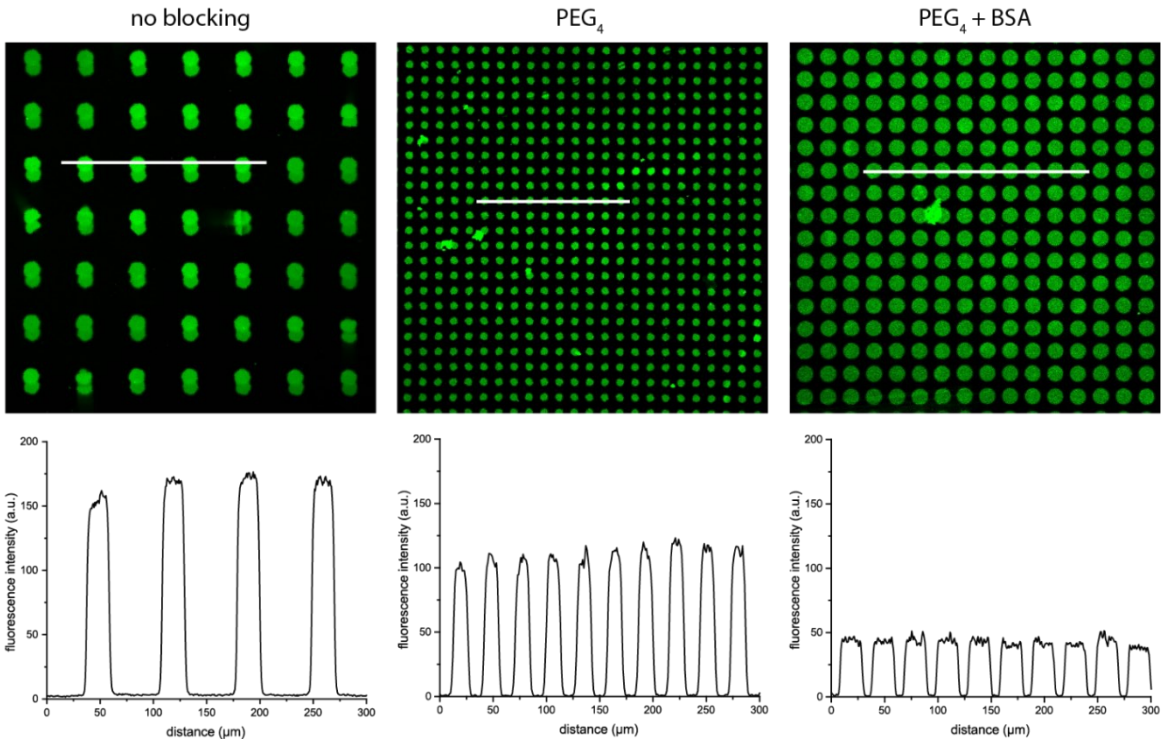

Figure 45: Comparison of passivation strategies to block unspecific binding of His_6-GFP on APTES based PA-*tris*NTA surfaces after mask patterning. The surface was prior to protein binding incubated with a MS-PEG_4-solution (middle) or in addition washed with 5% BSA in HBS buffer (v/v) (right). As a comparison, one surface was not treated with blocking agents (left). Here, the mask shifted during illumination thereby creating doubled circles. Line scans indicate a very good signal to noise ratio for all APTES surfaces, whereas the best ratio was observed without blocking agents. Scale bar, 50 µm.

To demonstrate the specificity of protein binding to the APTES based PA-*tris*NTA surfaces, a positive control was prepared with HS-*tris*NTA and a negative control with methoxy-PEG lacking *tris*NTA moieties (Figure 46). The surfaces of the positive control were coated with NTA groups, which were not blocked by autoinhibition, therefore incubation with His_6-GFP (300 nM in HBS buffer, 30 min) should lead to a homogeneous and complete decoration with GFP. On the contrary, on the surfaces of the negative control, no *tris*NTA groups were present, therefore no His_6-GFP should bind. As expected, the positive control revealed a homogeneous layer of bound GFP. The decreased fluorescence intensity at the image boundaries is due to uneven illumination of the microscope. The surfaces of the negative control displayed no unspecifically bound GFP, which was a very good indication for the repellence of the surface to unspecific binding. The fluorescence intensity signal of the positive control is on average 800-fold higher than that of the negative control, demonstrating the potential to immobilize His-tagged GFP on the surface.

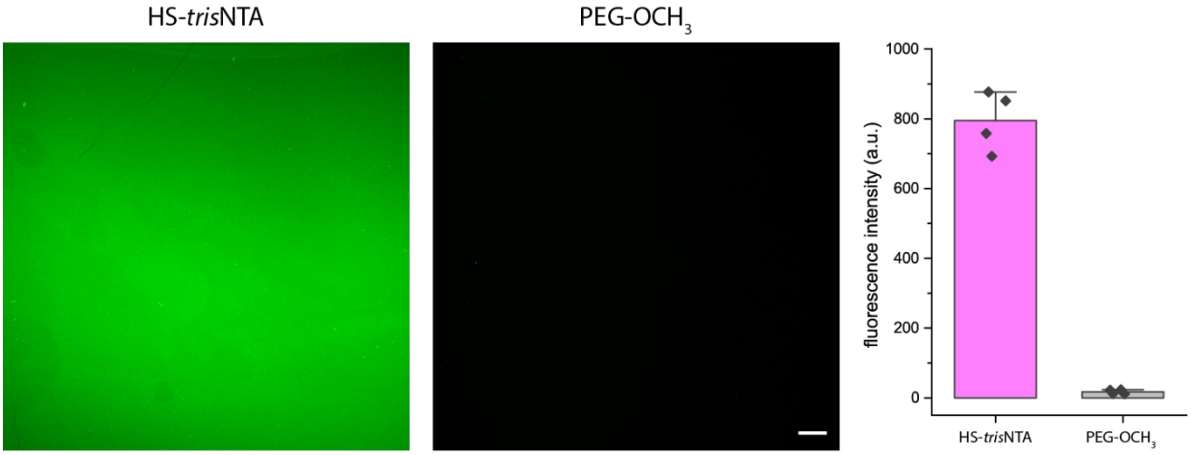

Figure 46: APTES-silanized surfaces modified with HS-*tris*NTA (positive control) or methoxy-PEG (negative control). In the *tris*NTA decorated positive control, His_6-GFP is bound without light activation. The even GFP signal indicated a homogeneous functionalization. The negative control lacking *tris*NTA, should not bind any His_6-GFP. The very low fluorescence signal verifies the repellence of the surface towards unspecific protein binding. Evaluation of four 66 µm x 66 µm ROIs in each image revealed a 800-fold higher fluorescence intensity for the positive control in comparison to the negative control. Scale bar, 50 µm.

In-situ photoactivation is a favorable way to generate different protein densities with high spatiotemporal control. Based on the results, a step further was taken to *in-situ* activations. For this purpose, an APTES silanized surface decorated with PA-*tris*NTA was mask patterned (365 nm, 1 min, 185 mW/cm^2) and treated with His_6-GFP (300 nM in HBS buffer, 30 min). Following, specific ROIs were activated with the 405 nm laser and 63x objective of the CLSM. The influence of laser power (10-100%, max output 4 mW) at constant iterations (500 iterations) (Figure 47A) and the change of iterations (50-500 iterations) at constant laser power (100%, 25 mW) (Figure 47D) was tested. A gradual increase in protein density from 10-80% laser power was observed in the intensity profiles (Figure 47B,C). A further increase of the laser power did not lead to any further protein immobilization. Likewise, a gradual increase in immobilized protein was measured with a stepwise increase of iterations (Figure 47E). An excellent signal-to-noise ratio at full saturation was observed when activating with 500 iterations and 100% laser power, therefore these settings were used for further *in-situ* activations.

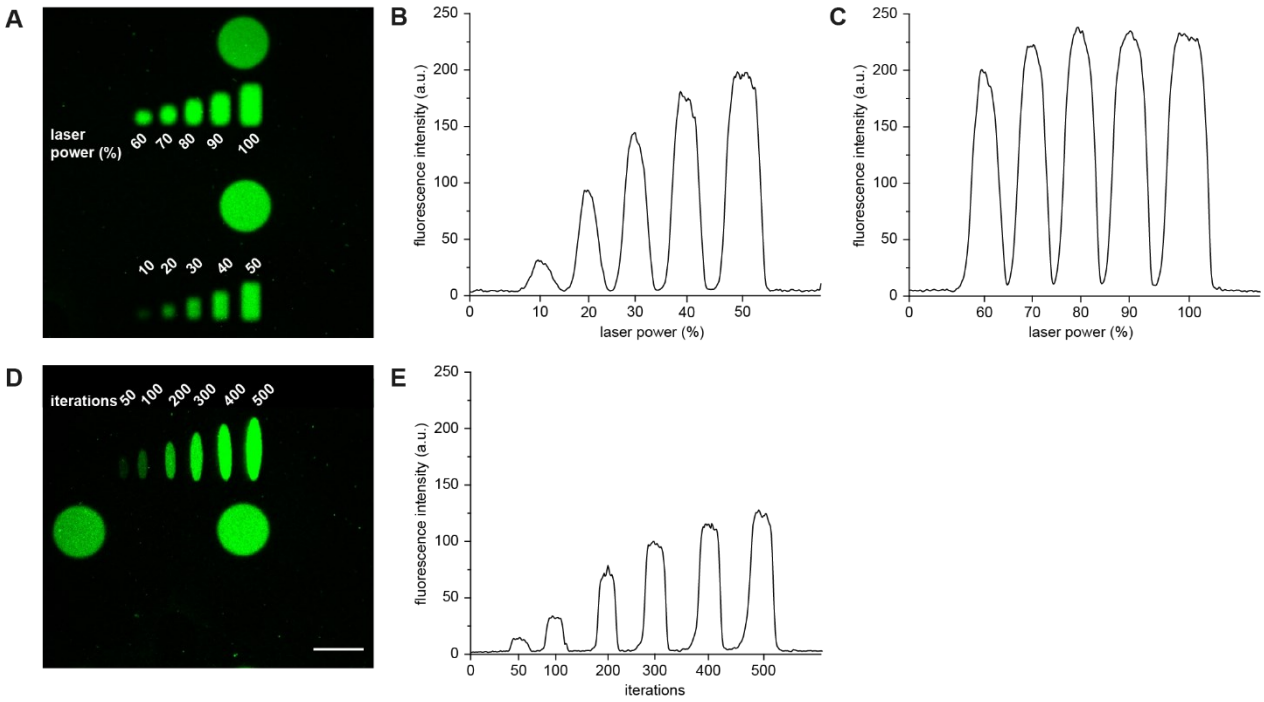

Figure 47: *In-situ* activation of PA-*tris*NTA functionalized surfaces. First, mask patterning (circels) was performed with a 365 nm handlamp (365 nm, 1 min, 185 mW/cm^2), second *in-situ* activation (ovals and rectangles) with the 405 nm laser and the 63x objective was performed. The influence of different laser power (10-100%, max output 4.5 mW) at constant iterations (500 iterations) (A) and the change of iterations (50-500 iterations) at constant laser power (100%, 4.5 mW) (D) were tested. After second incubation with His_6-GFP, photo-patters were visible. Line scans across photo-patterns at 10-50% laser power, 60-100% laser power were shown in (B) and (C) respectively. Intensity profile along ROIs activated with 50-500 iterations, depicted in (E), showed increased protein densities proportional to increased light dosages. Scale bar, 20 µm.

Next, freely designed ROIs were written on the surface with the optimized settings (405 nm, 4.5 mW, 500 iterations) (Figure 48). After His_6-GFP binding, the fluorescence intensity in the *in-situ* patterned ROIs was compared to the mask patterned regions. It can be seen that there are differences of about 20% in fluorescence intensities between the circular ROIs (ROI 1: 56 a.u., ROI 2: 45 a.u.), which is due to uneven illumination of the microscope. Therefore, the ROIs 1 and 2, which were in close proximity to the *in-situ* patterned structures, were used for comparison. The *in-situ* activated ROIs 3 and 4 (average fluorescence intensity: ROI 3 = 40 a.u., ROI 4= 44 a.u.) had similar fluorescence intensity of immobilized GFP in ROI 2. This indicates that the optimized photopatterning conditions for *in-situ* activation were as effective as mask patterning.

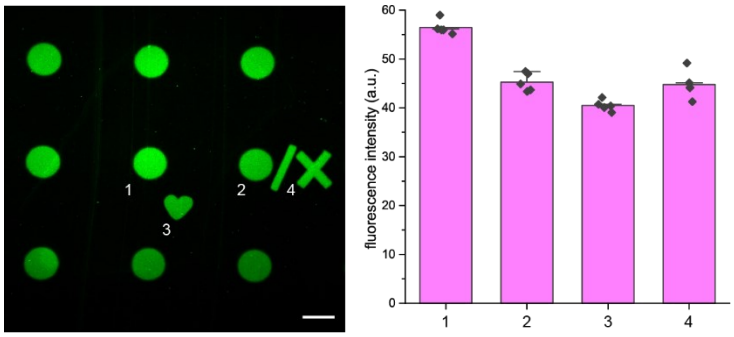

Figure 48: *In-situ* activation of freely designed ROIs on a previously mask patterned PA-*tris*NTA surface. Activation was performed using a 405 nm laser and the 63x objective on a CLSM. Measurement of the fluorescence intensity in two circular mask patterned ROIs (average fluorescence intensity: ROI 1= 56 a.u., ROI 2= 45 a.u.) and two *in-situ* activated ROIs (average fluorescence intensity: ROI 3= 40 a.u., ROI 4= 44 a.u.) revealed that activation by *in-situ* patterning was activating the surface in similar extent (46±6 a.u.) as mask patterning. Scale bar, 20 µm.

Furthermore, the technique of *in-situ* activation was used to perform dual-color lithography with two different POIs. After mask patterning and immobilization of His_6-GFP, freely designed ROIs were again activated with the 405 nm laser (4.5 mW, 100% laser power, 500 iterations) on the surface in the presence of His_6-AF647. Figure 49 showed specifically bound peptide in the activated regions with a good signal to noise ratio and sharp contours. Attachment in the circular ROIs generated by mask lithography, were also visible and are due to the competition of the His_6-tags of the protein and the peptide. Beside that, it is also possible that GFP does not occupy all the binding sites due to steric hindrance and that the smaller peptide binds in the interspace of the proteins.

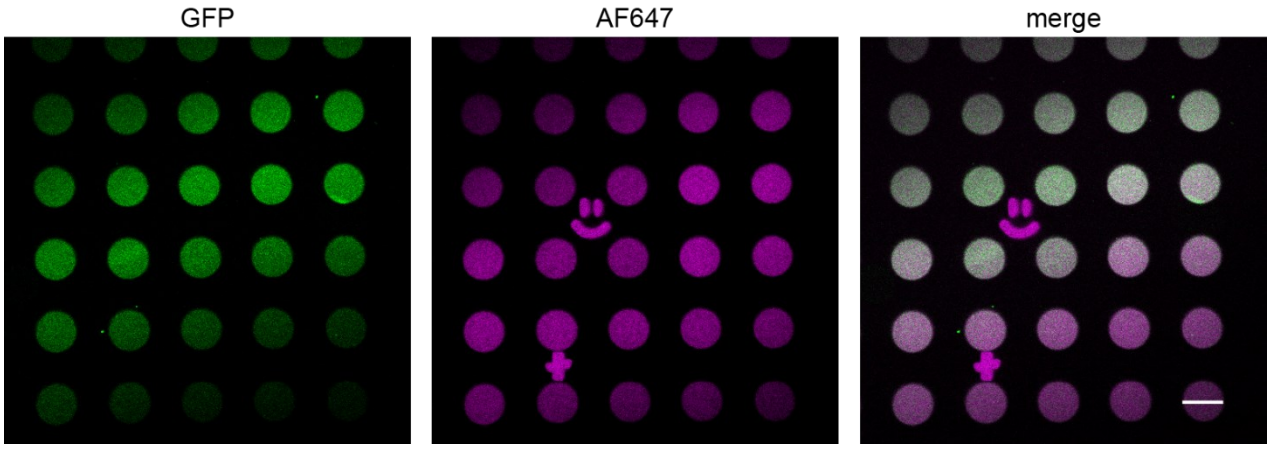

Figure 49: Dual-color lithography on PA-*tris*NTA functionalized surfaces with two different POIs. Between mask patterned areas with bound His_6-GFP freely designed ROIs were activated using a 405 nm laser and a 63x objective on a CLSM. His_6-AF647 bound specifically in written structures but also in the previously activated circles. Since the peptide and the protein are tagged with a His_6-tag, they compete with each other, or the smaller peptide fills up binding sites between the sterically more demanding protein. Scale bar, 20 µm.

4.5.3.1. APTES-based TPA-*tris*NTA functionalized surfaces

By establishing APTES-based PA-*tris*NTA functionalized surfaces, proteins and peptides could be patterned with high precision and very low non-specific adsorption. The tested conditions were next applied to surfaces functionalized with TPA-*tris*NTA as a photoactivatable interaction molecule. To test the autoinhibition of the newly developed TPA-*tris*NTA in the presence of a His_6-tagged protein as well as to verify the remote light-activation, TPA-*tris*NTA functionalized surfaces were prepared. Since the photocleavable amino acid derivative DEAC in TPA-*tris*NTA has an absorption maximum at 390 nm a 405 nm LED was used for TPA-*tris*NTA instead of the 365 nm LED used for mask patterning of PA-*tris*NTA. After mask patterning (405 nm, 1 min 185 mW/cm^2), Ni(II)-loading ($NiCl_2$ 10 mM in MQ water, 5 min), and incubation with His_6-GFP (300 nM in HBS buffer, 30 min), images of the surfaces were acquired on a CLSM (Figure 50). The confocal images as well as the line scan showed an excellent signal to noise ratio and sharp contours of the pattern. The very low background fluorescence of His_6-GFP confirmed the stable autoinhibition of Ni(II)-loaded TPA-*tris*NTA in the presence of His_6-tagged POIs as well as the repellence of the surface for unspecific binding. Upon illumination the interaction molecule became activated and subsequently protein binding took place in the irradiated areas. This is a proof-of-principle for the functionality of TPA-*tris*NTA, which can be used for immobilization of proteins.

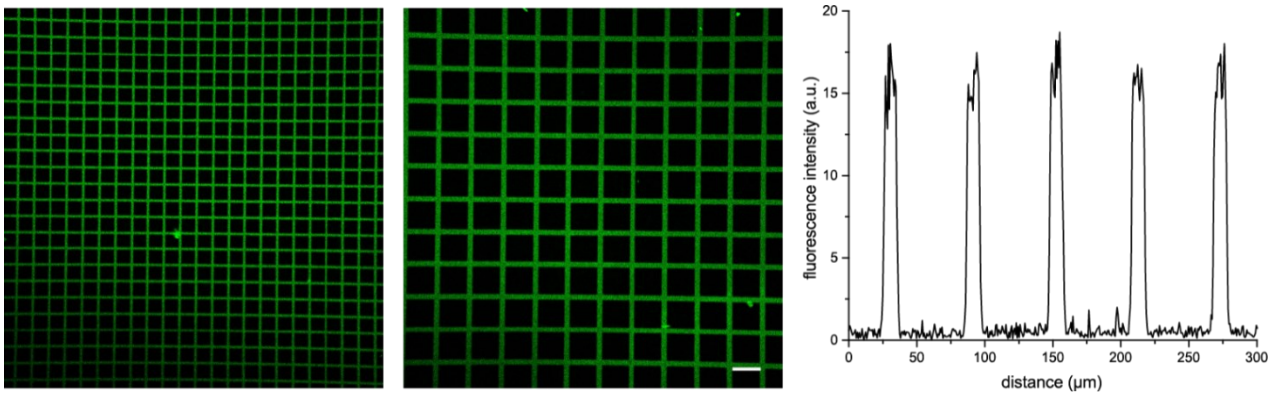

Figure 50: Mask patterned TPA-*tris*NTA functionalized surface. After illumination at 405 nm and Ni(II)-loading , His_6-GFP was immobilized and the surfaces were imaged by CLSM. Images and line scan showed a bright photo-patterning with sharp edges and very good signal to noise ratio. Scale bar, 50 µm.

4.6. TPA-*tris*NTA functionalized hydrogels for protein assembly in three dimensions

Having investigated the photophysical properties of TPA-*tris*NTA in solution, the proof-of-concept of light-driven protein immobilization on two-dimensional (2D) glass surfaces was demonstrated. This opens up the opportunity to advance to more complex three-dimensional (3D) interfaces for protein patterning. When moving to 3D samples, such as hydrogels, aspects like extended diffusion times, sample depth, and possible absorption by the hydrogel must be considered. Therefore, the exposure settings had to be readjusted and optimized for the changed surface. To this aim, TPA-*tris*NTA functionalized hydrogels were engineered for protein assembly in 3D. TPA-*tris*NTA was linked *via* its cysteine to a maleimide polyvinyl alcohol (PVA) precursor and immediately polymerized with a dithiol polyethylenglycol to obtain a photo-instructive hydrogel. First, the TPA-*tris*NTA functionalized hydrogel was mask patterned using a LED-lamp (405 nm,1 min, 185 mW/cm^2) to verify light activation and protein immobilization and to compare them to patterned glass surfaces by generating large circular regions within the biocompatible scaffold (Figure 51A). Visualization of the illuminated areas was realized by binding of His_6-GFP followed by CLSM. Similar to the APTES silanized TPA-*tris*NTA glass surfaces, the hydrogels showed a low background fluorescence of GFP, which indicated a very low non-specific binding of the protein. Therefore, no blocking strategy was used for the hydrogels. In the case of hydrogels, the interface is expanded by a z-dimension in addition to the x/y dimension, which allows conclusions about the hydrogel volume, which became activated by the laser beam. The mask defined geometry showed patterning of GFP with a penetration depth of 100 µm into the biocompatible scaffold. The fluorescence intensity of bound GFP decreased along the z-axis, which indicated that the light intensity faded with increasing hydrogel depth which led to a diminished amount of activated TPA-*tris*NTA.

Although mask patterning offers only limited spatial resolution and no temporal control, the rapid structuring of large areas with well-defined bulk gel properties can be performed. In contrast, *in-situ* laser lithography provides the potential to photo-structure hydrogels with high spatial control for protein assembly. *In-situ* writing was performed using the 405 nm laser (4.5 mW, 1000 iterations) or focused fs-laser pulses at 800 nm (5.5 mW, 1000 iterations), followed by visualization of the regions of interest (ROI) *via* binding of a His_6-AF647 (Figure 51B). For both approaches, a custom-made, spatially defined region (heart) was written in the hydrogel at the same focal plane.

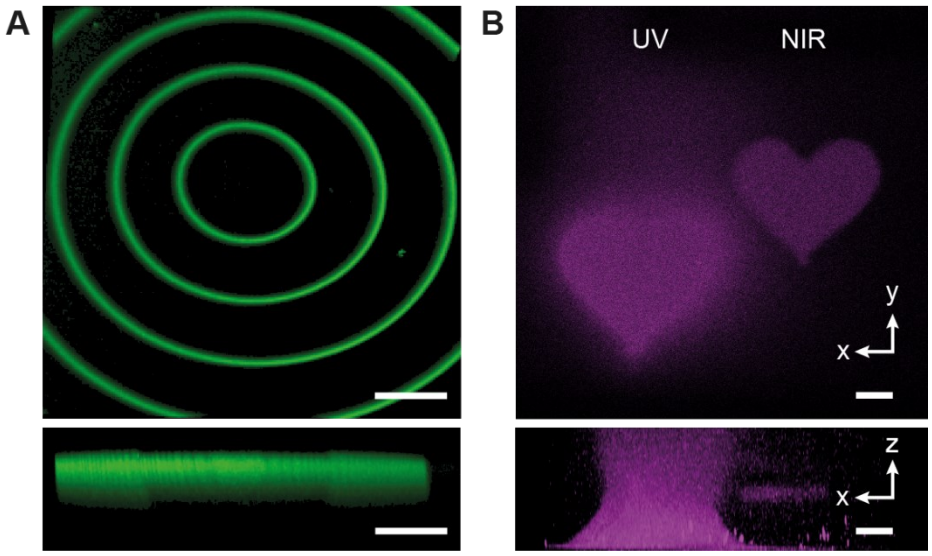

Figure 51: Protein assembly in three dimensions *via* one-and two-photon excitation inside TPA-*tris*NTA functionalized hydrogels. A) Mask lithography of global structure using 405 nm at 185 mW/cm^2 for 1 min. Light-initiated immobilization of His_6-GFP was recorded in x/y- and as well as in a z-stack. The penetration of the mask lithography was observed until a depth of 100 µm into the scaffold. Images from a z-stack series were reconstructed to visualize the sideview of the 3D structure (bottom). Scale bars, 100 µm. B) Laser scanning lithography of TPA-*tris*NTA by one- and two-photon excitation (1P: 405 nm, 4.5 mW, 1500 iterations; 2P: 800 nm, 5.5 mW, 2000 iterations). Heart-shaped ROIs were visualized by immobilization of His_6-AF647. One-photon activation occurred with vicinal photo-activation of TPA-*tris*NTA above and below the focal plane, resulting in a conical shape of POI alignment in the gel. Two-photon excitation of TPA-*tris*NTA led to a sharp and precise POI assembly in x/y-direction and localized activation in z-dimension, accentuating the superior control over photo-activation and subsequently over protein organization. 3D images were reconstructed after collecting a series of z-stacks by CLSM recording. Scale bars: 20 µm.

Comparison of the conventional laser lithography with two-photon patterning in x/y-dimension showed in both cases a localized photoreaction in close proximity to the focal point. However, laser rastering by UV light resulted in a deteriorated x/y-resolution compared to 2P activation by NIR light. For 2P patterning, a sharper photo-activation and thus protein assembly in the focal plane was observed. Comparing the protein patterning in z-direction impressively illustrated the improved 3D resolution for the photoreaction. Whereas conventional laser scanning lithography permitted only a certain degree of 3D pattering (z-resolution > 30 µm), the z-resolution for the 2P patterning was typically 5-10 µm, which is in good agreement with resolution demonstrated in literature (z-resolution 1P: >25 µm, 2P: 2-3 µm).[90] This feature is depicted by the sharp image in the focal plane in x/y and x/z, respectively. The conical shape of protein alignment by one-photon *in-situ* activation is owned to the unavoidable photoreaction initiated above and below the focal plane, resulting in partial and gradual protein assembly throughout the thickness of the hydrogel. For 1P lithography the laser light is focused to a specific ROI, but the light intensity along the beam is high enough to cause photo reactions. In contrast, for 2P patterning the laser power is the highest in the focal plane, therefore TPA-*tris*NTA solely became activated in the distinct layer.

Hence, a localized and precise activation of TPA-*tris*NTA and thus protein alignment in x/y-dimension and z-direction was observed by 2P activation processes. This clearly demonstrated that focused two-photon processes permit the deterioration of neighboring photosensitive TPA-*tris*NTAs within the ROI and allows the modification of specific volumes of the hydrogel with high accuracy in 3D.

A major advantage of the *tris*NTA-His-tag system in comparison to other lithography strategies is its reversibility. Therefore, two freely designed ROIs were written into a hydrogel by laser-assisted lithography (800 nm, 5.5 mW, 1500 iterations) followed by His_6-GFP immobilization (300 nM in HBS buffer, 30 min) and visualization *via* confocal laser scanning microscopy (Figure 52,upper part). POI binding to the photo-structured areas was observed. After incubation with imidazole (500 mM, 5 min), no fluorescence signal for His_6-GFP was detected indicating the displacement of the His-tagged POI by the competitor imidazole. After extensive washing with HBS buffer (6x 5 min) to remove the competitor, a second POI-binding was demonstrated. *Via* incubation with His_6-AF647 (300 nM, 30 min), POI photo-pattern reassembly was realized, indicated by the fluorescence signal emanating from His_6-AF647 (Figure 52, lower part). This verifies the reversibility and regeneration of the photo-patterns in TPA-*tris*NTA functionalized hydrogels, facilitated by the non-covalent *tris*NTA/His_6-tag interaction.

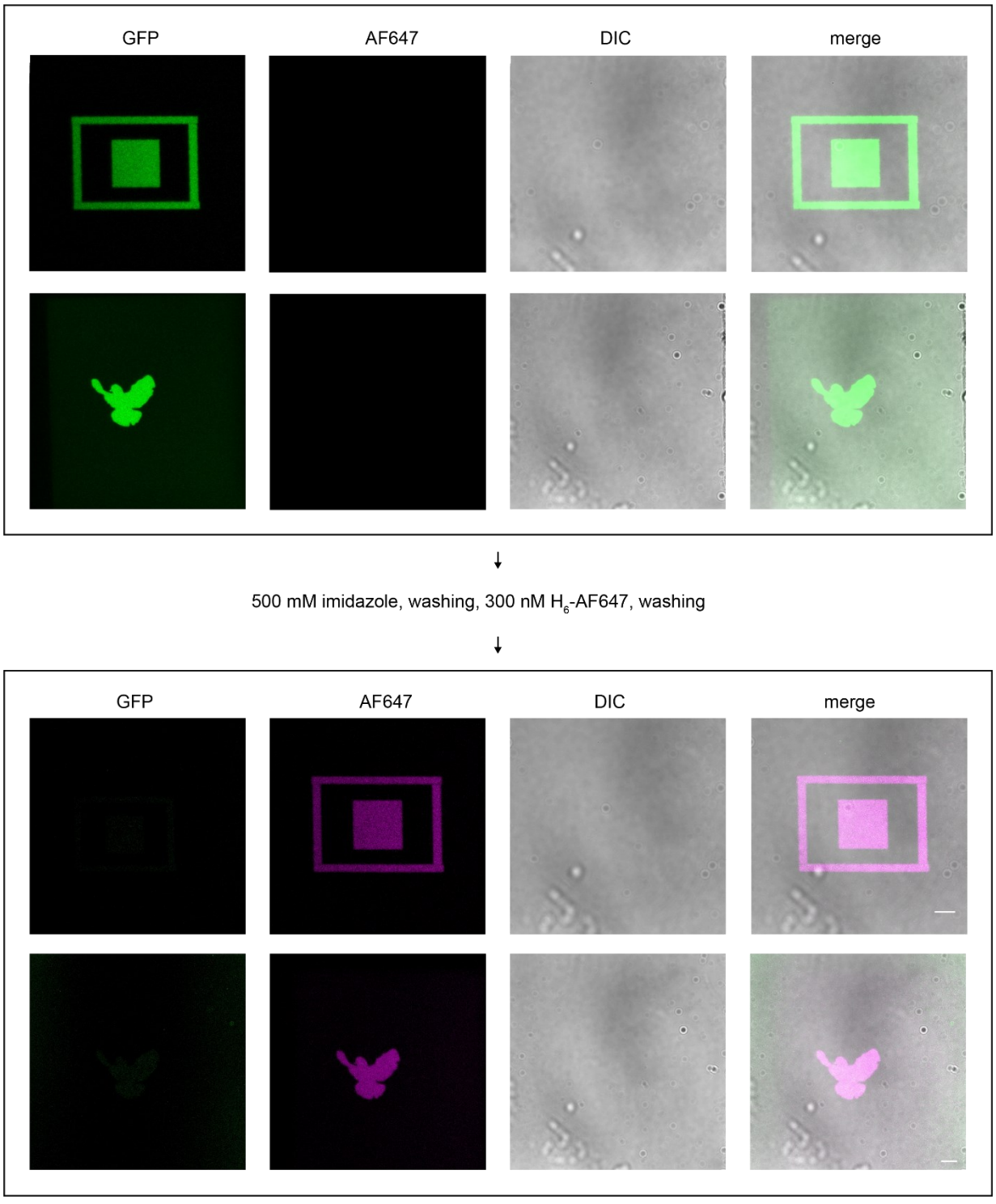

Figure 52: Reversibility of POI-binding in TPA-*tris*NTA hydrogels. Two-photon structuring of freely designed ROIs was performed by laser-assisted lithography followed by His_6-GFP immobilization and visualization *via* confocal laser scanning microscopy. Before imidazole treatment, POI binding to the photo-structured ROIs was observed. After incubation with 500 mM imidazole, no fluorescence signal for His_6-GFP was detected, demonstrating the displacement of the His-tagged POI by the competitor imidazole. By incubation with 300 nM His_6-AF647, POI photo-pattern reassembly was realized, indicated by the fluorescence signal emanating from His_6-AF647. Scale bar, 10 µm.

In addition, the long-term stability and persistence of photo-patterns was analyzed. An arbitrary protein pattern (bird) was generated by laser-assisted two-photon structuring (800 nm) followed by POI tethering of 300 nM His_6-AF647 (Figure 53). A strong fluorescence intensity emanating from His_6-AF647 within the bird shaped ROI was detected at day 0. After a prolonged time (10 days), a diminished fluorescence signal intensity was measured. The bar diagram of the analysis of the fluorescence intensity at day 0 and day 10 showed a 5-fold decreased fluorescence signal. Due to the high-affinity interaction between *tris*NTA and the His_6-tagged POI, 19% of the POI assembly remains tethered to the photo-structured ROI after an extended time period.

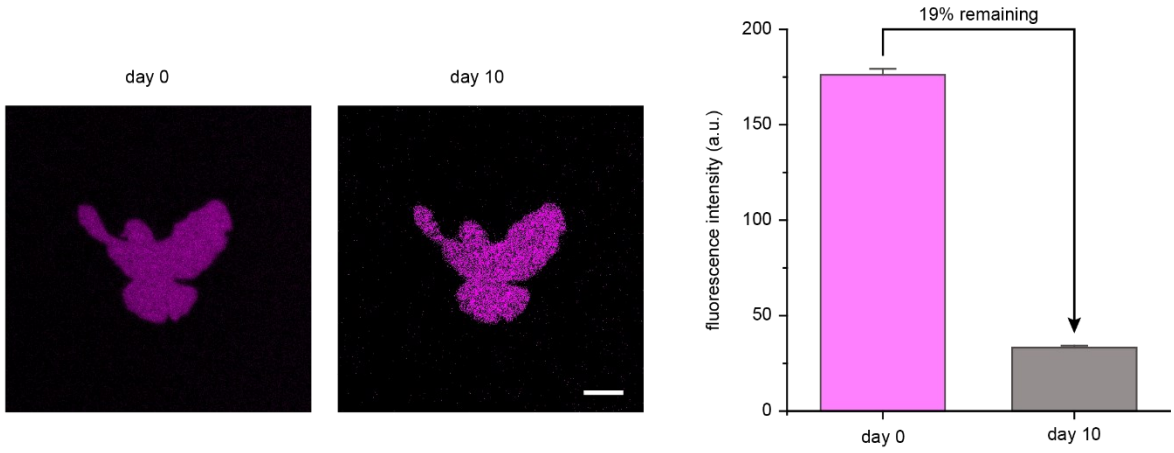

Figure 53: Long-term stability of POI immobilization in photo-structured, TPA-*tris*NTA functionalized hydrogel. Imaging the assembled His_6-AF647 ten days after 2P structuring showed that the gel was still decorated with the POI. After this prolonged time, a 5-fold decreased fluorescence intensity was measured. Scale bar, 10 µm.

The high-resolution 2P patterning of proteins was further explored in terms of wavelength-selective activation within hydrogels as well as improved resolution in x/y/z-direction. To examine the in-gel excitation profile of TPA-*tris*NTA, activation wavelengths ranging from 720 to 800 nm with 20 nm increments were tested at a constant laser power of 5 mW (Figure 54A). Wavelengths above 800 nm were not applicable, because of technical limitations of the microscope setup. After binding of His_6-AF647, the fluorescence intensities of the activated ROIs were determined by CLSM. The intensity profile through the focal plane displays a gradual increase with the strongest TPA-*tris*NTA photo-activation at 800 nm. This result is in good agreement with the 2P-absorption profile determined in solution (Figure 34B), which indicates that the hydrogel did not influence the optimal activation wavelength for TPA-*tris*NTA. So, the determined activation wavelength can be translated from analysis in solution to hydrogels without modulation.

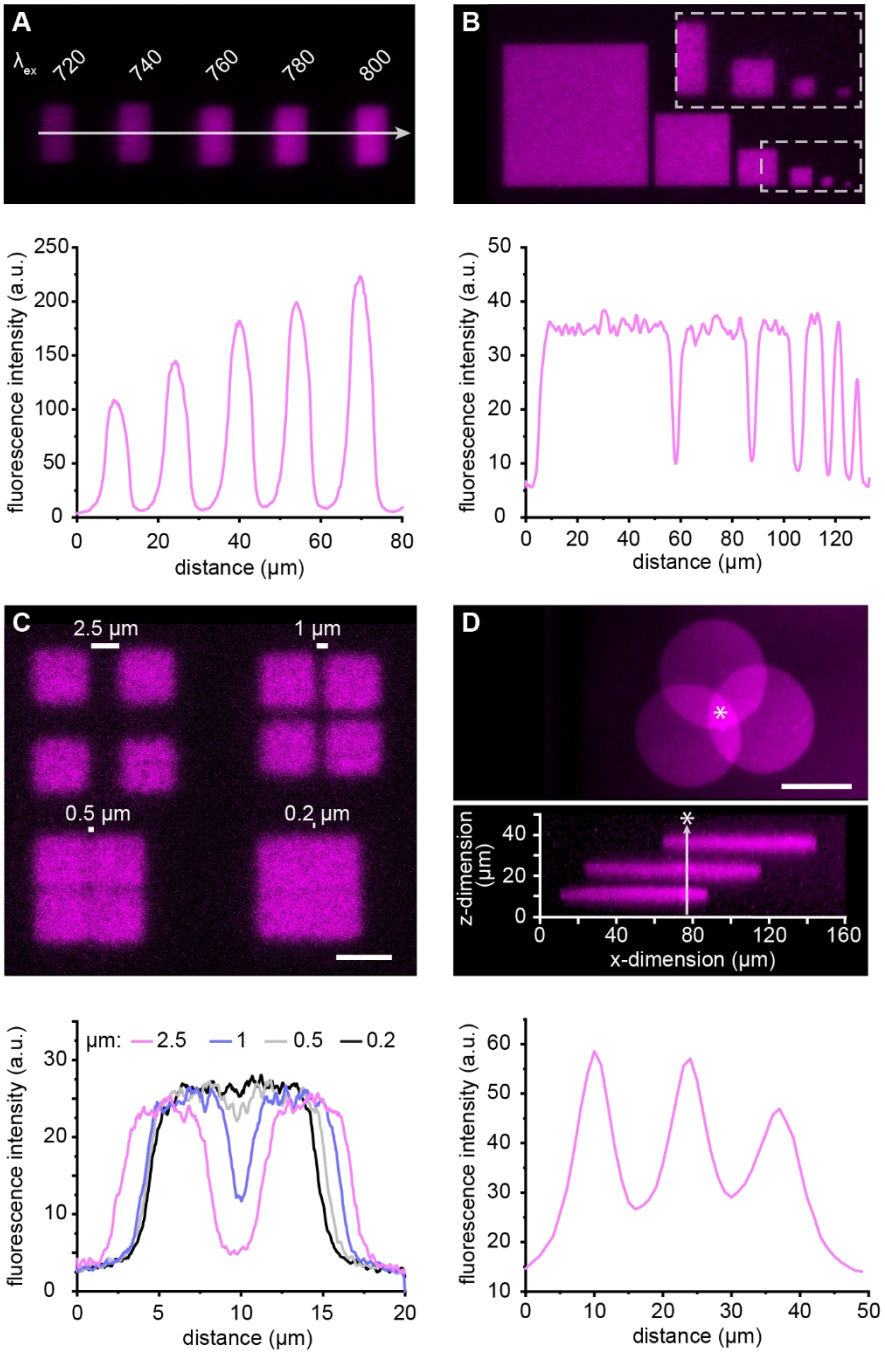

Figure 54: *In-gel* analysis of photoactivation of TPA-*tris*NTA. A) TPA-*tris*NTA functionalized hydrogel was activated with wavelengths from 720 to 800 nm at 5 mW. Intensity profiles of the sum of z-slices of immobilized His_6-AF647 displayed the strongest photo-activation at 800 nm. Wavelengths higher than 800 nm were not applicable due to technical reasons. B) Assignment of the size limit for photo-structuring in x/y-dimension by writing six quadratic ROIs of decreasing size (50, 25, 12, 6, 3, and 2 µm) into the hydrogel. Intensity profiles of the ROIs demonstrated constant fluorescence intensities in all ROIs except for the 2 µm ROI. C) Determination of the resolution limit *via* two-photon structuring of 4 individual diffraction-limited squares in x/y-direction. Spots separated by 1 µm or larger can be clearly distinguished by CLSM imaging, which is also reflected in the intensity profile. Scale bar, 5 µm. D) 3D POI network constructed by two-photon activation of TPA-*tris*NTA. Three circular spots were written in different z-layers to investigate the z-resolution. Intensity profiles of His_6-AF647 in z-direction showed spatially localized photo-activation with clearly distinguishable edges of the three written ROIs. Scale bar, 50 µm.

The lower limit for the dimension of ROIs is determined by the precision of the laser scanning process. To determine the minimal possible patterning area in x/y-dimension, six quadratic ROIs of decreasing size (50, 25, 12, 6, 3, and 2 µm) were written into the hydrogel utilizing 800 nm (3 mW/µm^2) for the photo-activation of TPA-*tris*NTA (Figure 54B). Following the photo-patterns were visualized by immobilization of fluorescently labeled POI imaged by CLSM. Remarkably, even the 2 µm ROI could be precisely written into the gel with clearly distinguished edges. However, the line scan profile of the ROIs revealed a diminished fluorescence intensity of the 2 µm ROI compared to the 3 µm or bigger ROIs, respectively. This indicates that the minimal ROI size for 2P patterning in TPA-*tris*NTA functionalized hydrogels without detraction of protein assembly is between 2-3 µm. Important, the fluorescence intensity emanating from the POI in the written ROIs gained equal levels in all other ROIs, showing that the photo-activation efficiency is uniform and most likely determined by the TPA-*tris*NTA density within the gel. Since, TPA-*tris*NTA is immobilized *via* random Michael addition to maleimide groups on PVA strains, the TPA-*tris*NTA distribution can vary within the hydrogel and from sample to sample. Determination of the density of TPA-*tris*NTA within the hydrogels was not possible. Worth to mention, the accuracy of photo-pattering is determined by the point spread function during writing and thus by the numerical aperture of the system. Collectively, *via* 2P activation processes of TPA-*tris*NTA ROI sizes of 2-3 µM can be locally specified with single micrometer-scale precision in the gel without decrease of POI density.

In addition, the x/y-resolution of the writing process and thus the ability of the microscope system to discern individual diffraction-limited spots was analyzed. Therefore, varying sets of four adjacent quadratic ROIs (20 µm) were written into the hydrogel with successively decreased spacing between the squares (2, 1, 0.5, 0.2 µm) (Figure 54C). Whereas photo-patterns with an inter-ROI distance of 1 µm or larger were clearly distinguishable, shorter ROI-spacing resulted in fuzzy and barely discriminable photo-patterned areas. The designed ROIs could no longer be spatially classified into individual protein patterns, demonstrating that structures with an inter-ROI distance of 1 µm or larger can be 2P patterned in x/y-dimension. Noteworthy, the resolution received by 2P laser scanning lithography is a convolution of the writing as well as the imaging process. The resolution of the writing procedure is expected to be more precise than the imaging process, which depends on the point-spread function of the imaging wavelength.[190,191]

The main asset of 2P excitation is the precise control of activation in z-dimension. To verify a defined protein organization in 3D, circular ROIs at different z-locations with 10 µm distance to each other were photo-structured into the TPA-*tris*NTA functionalized hydrogel (Figure 54D). In x/y- as well as in z-dimension a homogenous and spatially defined protein organization was

detected by CLSM, demonstrated by the uniform and high fluorescence intensity emanating from the labeled POI within the photo-patterned areas. The z-axis profile emphasized the 3D precision of the 2P writing process, showing visibly resolved and distinct protein alignment along the z-coordinate. A z-resolution of 5 ± 1 µm (FWHM) was determined for the two-photon activation process, which is in good agreement with typically observed z-resolutions for protein patterns (8 µm FWHM).[192]

4.7. Photo-sensitizer enhancement of two-photon scission of TPA-*tris*NTA

Encouraged by the precise 3D spatial protein arrangement within hydrogels, the next aim was to improve the photo-activation efficacy of TPA-*tris*NTA under 2P excitation. In many applications very high light intensities or prolonged illumination time is necessary for 2P excitation that can lead to photo-thermal destruction of the hydrogel or the embedded material (*e.g.* cells) by local combustion or overheating, respectively. To avoid these artifacts, laser power and illumination time should be reduced to the minimum. By acting as auxiliary chromophore, 2P active fluorophores efficiently absorb NIR light and transfer the absorbed energy to the acceptor photo-cage such as DEAC to enhance photo-scission. To this end, the presence of 2P active fluorophores ATTO390 and rhodamine B (RB) in various concentrations during the two-photon patterning process was systematically studied. Specifically, ATTO390 and rhodamine B were chosen as these fluorophores have large two-photon absorption cross sections (ATTO390: 14 GM; Rhodamine B: 150 GM) and are biocompatible[168,193], which is important for cell applications. As the photo-scission of TPA-*tris*NTA is dependent on the intensity of the 800 nm laser and the activation time, a matrix consisting of 20 light-induced quadratic ROIs was written into the hydrogel with increased light dosage (laser power *versus* time matrix: 0.5-5.5 mW and 6-30 s) (Figure A1, Figure A2). For quantification, the fluorescence intensities emanating from the entire activated volume (voxel) of each ROI were measured and analyzed (Figure 55,Figure 56). The matrix approach was applied to TPA-*tris*NTA functionalized hydrogels exposed to distinct concentrations of ATTO390 (50, 100 and 500 µM) and rhodamine B (50 and 100 µM) or buffer. In total, 120 conditions were screened to systematically optimize the two-photon accessibility of the optochemical nanotool as well as to establish robust protocols for arbitrary two-photon patterning.

As expected, for all hydrogels higher laser intensities as well as extended activation times accelerated the photo-activation and thus increased protein recruitment to the specific ROI. For hydrogels immersed to just buffer, POI patterns were incipiently visible with 3.1 mW laser power for 18 s as well as 1.5 mW for 24 s. However, the photo-patterned structures generally depicted

weak fluorescence intensities at activating laser powers below 1.5 mW, inferring that the photo-scission of TPA-*tris*NTA occurred only to a minor degree.

In contrast, hydrogels exposed to 100 µM ATTO390 and subjected to 2P patterning showed a globally enhanced POI recruitment and thus 2P-activation of the optochemical tool (Figure 55). Here, the onset of visibly detectable protein tethering was at a laser power of 1.5 mW and already 6 s. Notably, photo-structuring in presence of 50 µM ATTO390 did not show a significant increase of fluorescently labeled POI recruitment compared to the buffer-exposed hydrogels. 500 µM ATTO390 in comparison to 100 µM resulted in no further increase of photo-patterned POI tethering and thus photo-activation of TPA-*tris*NTA. Quenching effects of the auxiliary chromophore need to be considered at higher concentration and thus can stall an efficient energy transfer to the acceptor TPA-*tris*NTA. Here 100 µM of ATTO390 is optimal to act as two-photon sensitizer *via* diffusive encounter.

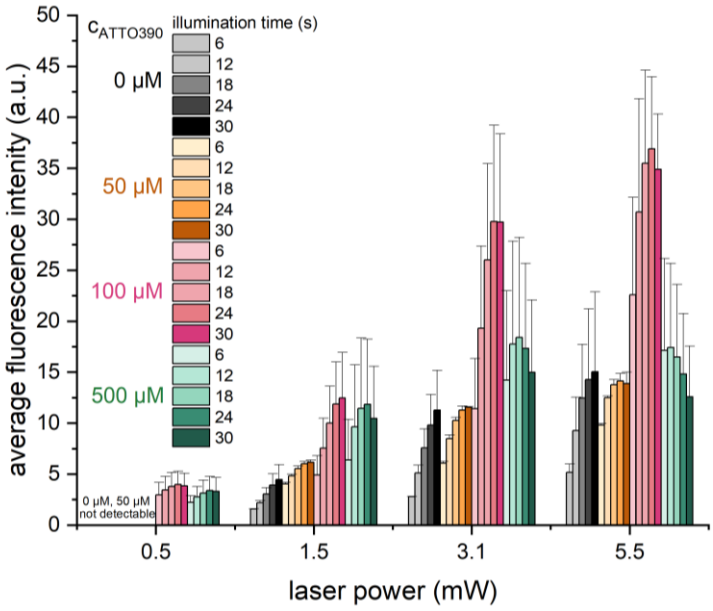

Figure 55: Quantification of ATTO390 sensitized two-photon patterned hydrogels (see Figure A1). TPA-*tris*NTA functionalized hydrogels were patterned at 800 nm in presence of 0, 50, 100 or 500 µM ATTO390. Binding of His_6-AF647 was visualized *via* z-stacks of the ROI over the full range of the photo-activated area. After background correction, the integrated fluorescence density within each ROI was quantified as the sum over all z-slices. Values obtained under equal conditions (illumination time, laser power, sensitizer concentration) were averaged and presented in the bar diagram. Error bars indicate the s.d.

Although an increased protein alignment at higher light-dosages was detected in x/y-dimension, investigation of the protein organization in z-direction depicted a deteriorated, out of focus alignment at elevated laser powers or iterations, respectively. The threshold for this phenomenon

was dependent on the respective photo-patterning conditions. In the presence of 100 µM ATTO390, the extended z-depth of the activated area set in at 12 s and a laser power of 5.5 mW, resulting in out of focus and diffuse protein tethering in z-direction. Most likely, the diminished z-resolution is a result of plasma-mediated ablation in the focal area[194,195], yielding a disproportional POI recruitment in z-direction as well as decreased fluorescence intensity measured in the focal pane (Figure 57A,C).

An even more efficient 3D protein pattering was realized by two-photon structuring in the presence of rhodamine B (Figure 56). Hydrogels exposed to 50 µM rhodamine B showed an already weak fluorescence signal emanating from the immobilized POI in areas illuminated with 0.5 mW for 18 s. Enhanced photo-scission of TPA-*tris*NTA is expressed by the very good POI enrichment as well as signal-to-noise ratio and was effectually obtained at 1.5 mW for 12 s. Even with the minimal applied laser power of 0.5 mW pattering was effectually realized. In contrast, at the highest applied light-dosage (5.5 mW; 30 s), a halo-effect exceeding the ROI boundary was observed, concomitant with a diminished fluorescence intensity compared to surrounding ROIs. This observation already implicates a destruction of the hydrogel in the focal plane.

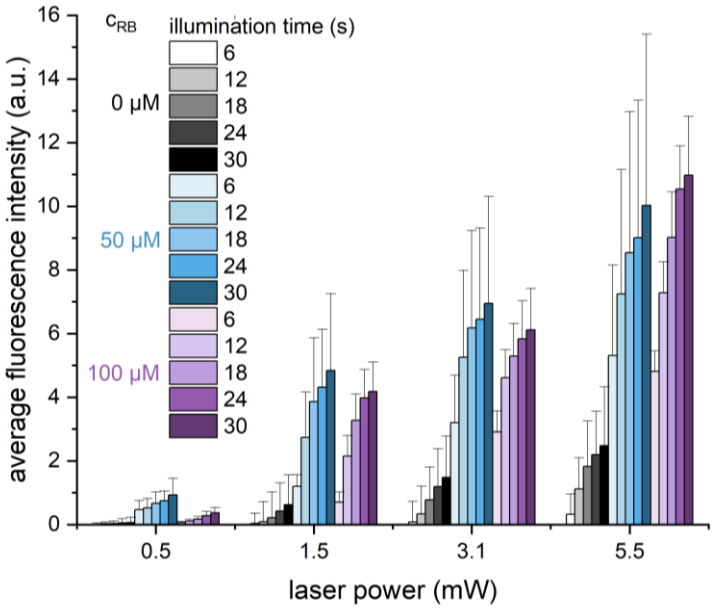

Figure 56: Quantification of rhodamine B sensitized two-photon patterned hydrogels (see Figure A2). TPA-*tris*NTA functionalized hydrogels were patterned at 800 nm in presence of 0, 50, or 100 µM rhodamine B. Binding of His_6-AF647 was visualized *via* z-stacks of the ROI over the full range of the photo-activated area. After background correction, the integrated fluorescence density within each ROI was quantified as the sum over all z-slices. Values obtained under equal conditions (illumination time, laser power, sensitizer concentration) were averaged and presented in the bar diagram. Error bars indicate the s.d.

Indeed, a dumbbell-shaped pattern was visibly in the z-stack of the CLSM image with the focal plane devoid of the POI (Figure 57B,D). A combustion process in combination with enhanced light scattering most likely caused these photo-pattern artifacts. Destructive effects were increased to a greater extent in two-photon patterned hydrogels immersed to 100 µM rhodamine B. Since this concentration already led to massive photo-destruction during two-photon writing, higher concentrations were not tested. To advance 3D protein tethering *via* a two-photon writing process, both the outcome of the TPA-*tris*NTA photo-activation determined by fluorescence intensity of the POI as well as the obtained resolution in x/y- and particular z-direction were taken into consideration for optimal photo-patterning. In this regard, hydrogels photo-structured in the presence of 100 µM ATTO390 and 50 µM rhodamine B under 3.1 mW laser power and 12 s iterations showed the best results without photo-destruction. With these settings, the enhancement effect of TPA-*tris*NTA activation by two-photon processes was 3.8-fold for ATTO390 and 15.6-fold for rhodamine B (Figure 57E) compared to untreated gels. As a result, the laser power can be reduced up to 10-fold (5.5 mW to 0.5 mW) during protein alignment, yielding similar protein densities as received for buffer-treated hydrogels. As two-photon lithography can be time consuming, an acceleration of the process by decreasing the illumination time from 30 s to 6-12 s is likewise crucial for real-time cell experiments.

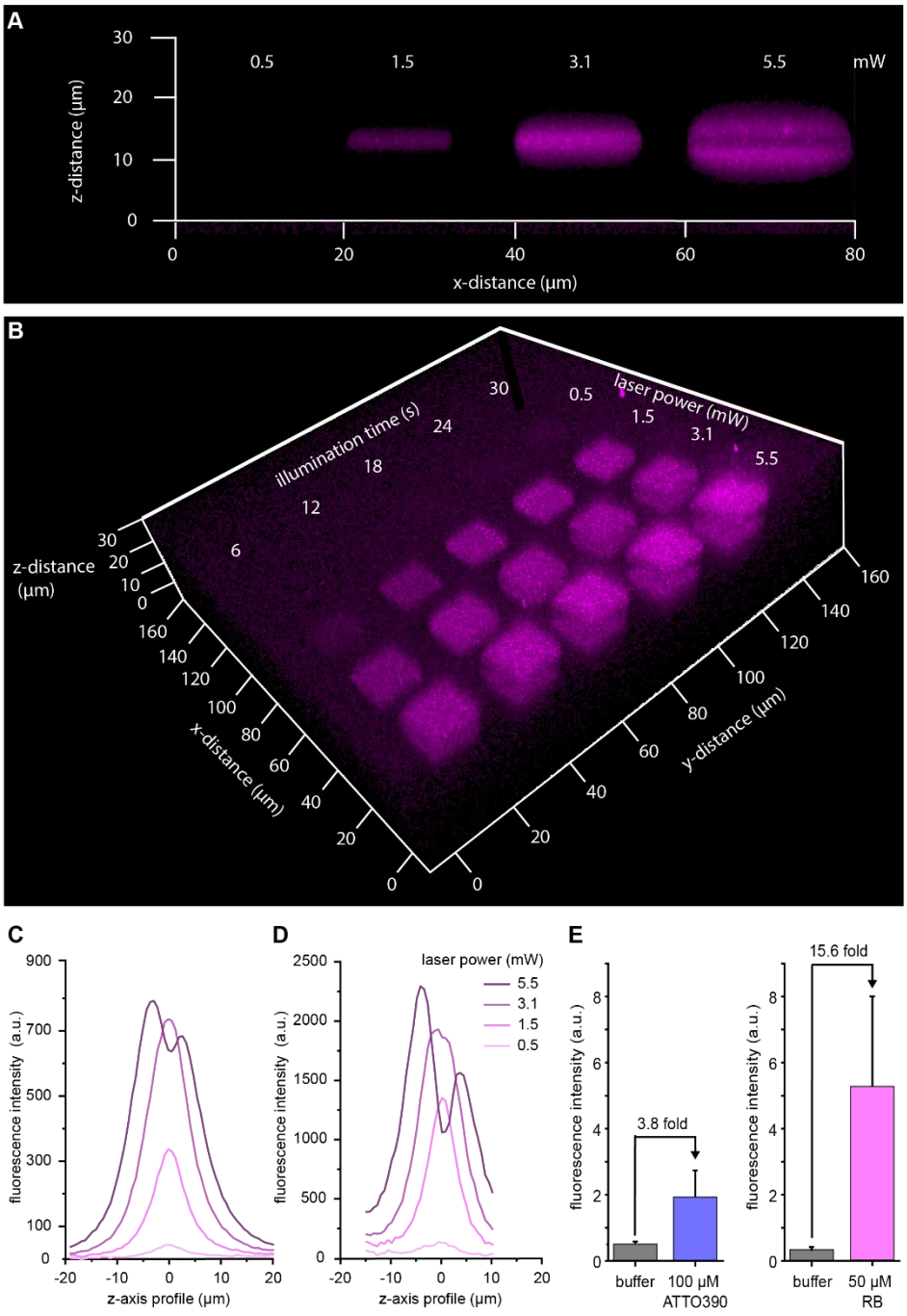

Figure 57: Enhanced two-photon laser lithography of TPA-*tris*NTA functionalized matrices. Hydrogels were activated at 800 nm in presence of buffer, 100 µM ATTO390 or 50 µM rhodamine B (RB) with varying laser power and illumination time. With increased light dosage, an accelerated binding of His_6-AF647 was observed in the illuminated regions, displaying an improved photo-activation of TPA-*tris*NTA. The presence of photo-sensitizers ATTO390 and RB have stimulated an enhanced photo-cleavage and consequently enriched POI binding. A) Hydrogel activated in presence of 100 µM Atto390. The matrix was imaged row by row *via* z-stacks. Displayed is the reconstruction of the row with 12 s illumination time and increasing laser power. The sideview of the written patterns revealed that with 5.5 mW plasma mediated ablation occurs in the focal plane. B) Hydrogel activated in the presence of 50 µM rhodamine B. The pattern written into the hydrogel was recorded *via* a z-stack of the complete matrix. Depicted is the tilted reconstruction of the z-stack. It is visible that prolonged illumination time and or higher laser power leads to ablation of the hydrogel in the focal point. C) Intensity profile of ROIs activated for 12 s with 0.5-5.5 mW in the presence of 100 µM ATTO390. The intensity line scan is measured along the z-coordinate. For comparison the maximum was centered at 0 µm. D) Intensity profile of ROIs activated for 12 s with 0.5-5.5 mW in the presence of 50 µM rhodamine B. The intensity line scan is measured along the z-coordinate. For comparison the maximum was centered at 0 µm. E) Comparison the fluorescence intensity of ROIs illuminated with 3.1 mW and 12 s demonstrated enhanced photo-activation of the gels exposed to photo-sensitizers. For 100 µM ATTO390, a 3.8-fold higher fluorescence intensity was detected compared to HBS buffer, and for a hydrogel photo-patterned in presence of 50 µM RB, a 15.6-fold increased fluorescence intensity was determined.

4.7.1. Two-photon activation of TPA-*tris*NTA with single digit micrometer precision

The optimized writing conditions were transferred to POI alignment in very small-scale in different loci in the hydrogel to demonstrate the precision of the lithography process, which is possible with this system. Two-photon lithography is often applied to write 3D patterns on the order of tens of microns (> 100 µm). While this scale is powerful for manipulating the behavior of larger cell networks or multicellular clusters for cell spreading or invasion studies, the ability of two-photon processes to modify the environment with single micrometer-scale precision is underrepresented.

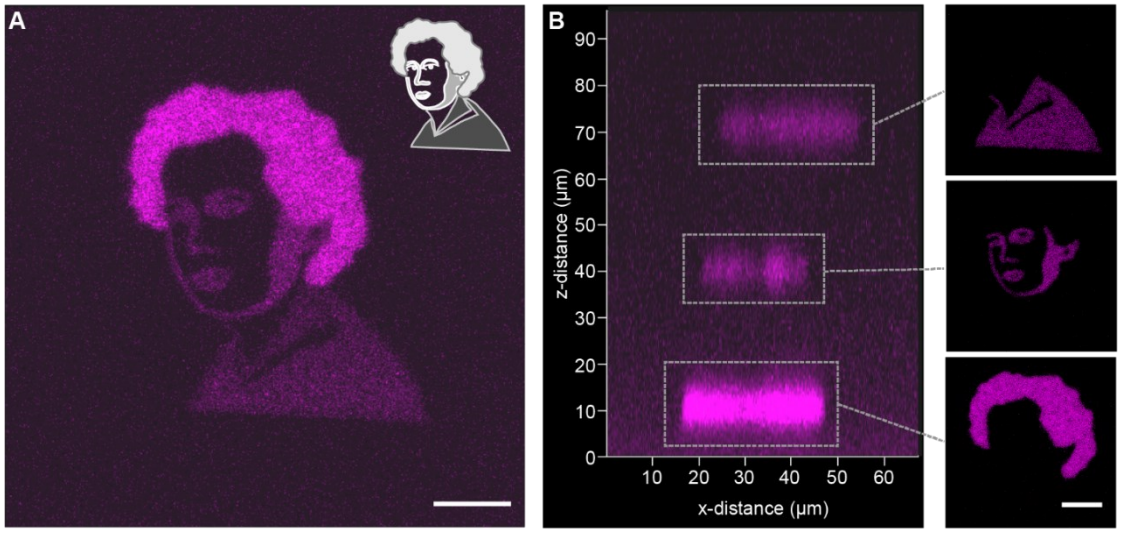

Figure 58: Two-photon induced 3D arbitrary patterns in a photo-instructive TPA-*tris*NTA matrix. A) The portrait of Maria Goeppert-Mayer was printed by two-photon excitation (800 nm, 3.1 mW, 12 s, 50 µM rhodamine B) in three different z-layers. Structures were visualized by assembly of His_6-AF647. B) Sideview of z-stack reconstruction of the two-photon patterned ROIs imaged by CLSM. Images displayed a spatially localized activation of TPA-*tris*NTA within the different z-layers, reflected by the confined immobilization of His_6-AF647 in z-direction. CLSM images of the respective focal plane (x/y-dimension) are shown on the right side. Scale bars: 10 µm.

To modify TPA-*tris*NTA functionalized hydrogels on the order of a few microns in 3D, custom-made, spatially defined ROIs were created by NIR laser illumination. Upon locally defined photo-activation the portrait of Maria Goeppert-Mayer was written in three distinct z-planes. Patterning was performed in the presence of 50 µM rhodamine B at 800 nm (3.1 mW, 12 s). His_6-AF647 was site-selectively immobilized within the hydrogel (Figure 58). The difference between patterned and unpatterned areas is a result of the improved 2P lithography as well as high-affinity, site-selective binding of His-tagged proteins to photo-liberated *tris*NTA. CLSM imaging of the spatially controlled POI distribution in z-dimension revealed a continuous decrease of the POI intensity with increasing z-depth to approximately 70-80 µm. This is in line with the Lambert-Beer law, in which the amount

of applied laser attenuation decays at greater depth. Important to mention, the penetration depth is dependent on the laser intensity as well as wavelength. Here, structuring was performed with low laser intensity compared to other two-photon laser lithography approaches.[191,196,197] If required, additional depth can be received by increasing the laser power. The 3D POI network of Maria Goeppert-Mayer clearly shows the power of two-photon lithography to pattern freely designed structures at micrometer precision (approx. 1.5 µm) (Figure 59) in 3D and the increased resolution in z-direction.

The precision of the lithography of biomolecules in 3D matrices has not been demonstrated with comparable systems yet. The smallest written protein pattern in PA-*tris*NTA functionalized hydrogels by Labòria *et al.*[73] has a line thickness of ~10 µm in the x/y-dimension. In comparison, the portrait of Maria Goeppert-Mayer written in the TPA-*tris*NTA modified hydrogel harbors lines up to 10 times narrower. The difference and advantages of the newly developed TPA-*tris*NTA become even more pronounced when the fineness of the pattern in the z-dimension is compared. PA-*tris*NTA hydrogels showed a depth of activation of ~130 µm in the z-dimension due to the 1P lithography, whereas TPA-*tris*NTA hydrogels can be written with a spatial resolution of up to 5 µm in the z-dimension.[198] These findings demonstrate the superior properties of TPA-*tris*NTA, which will be useful for patterning membrane proteins of single cells.

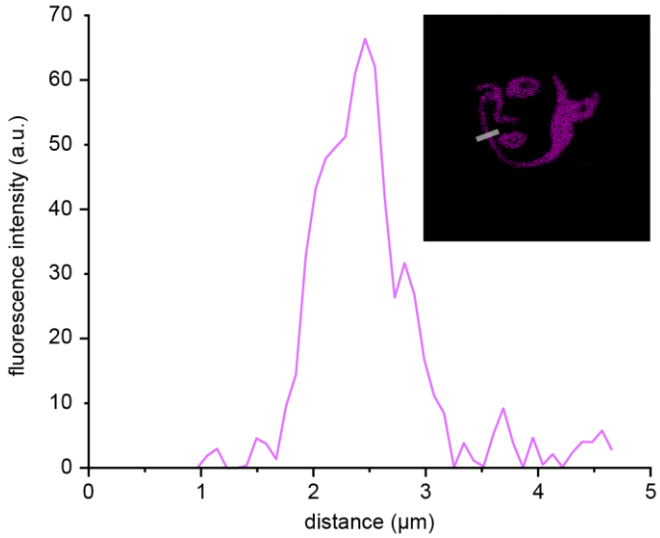

Figure 59: Two-photon activation of TPA-*tris*NTA in photo-instructive hydrogels with micrometer precision. A 3D arbitrary POI-pattern (portrait of Maria Goeppert-Mayer) was generated by two-photon excitation (800 nm, 3.1 mW, 12 s illumination; 50 µM rhodamine B) and visualized *via* tethering of 300 nM His_6-AF647. After recording a z-stack through the corresponding focal plane, an intensity line scan (gray line) in x/y-dimension along the cheek of Maria Goeppert-Mayer was performed. Micrometer precise (~1.5 µm) peptide pattern could be written with 70-fold signal-to-background ratio between patterned and non-patterned areas. The result is a combination of the improved two-photon lithography as well as high-affinity, site-selective binding of the photo-liberated *tris*NTA to the His-tagged POI.

4.8. Functionalized hydrogels as 3D cell matrix

For an application as 3D cell culture platform, the compatibility of (T)PA-*tris*NTA functionalized hydrogels were tested. To test the cell viability within hydrogels, living HeLa cells were homogenized with a solution containing TPA-*tris*NTA functionalized polymers and cross-linked to form a cell-laden hydrogel. After gel formation was finished, the encapsulated cells were stained with annexin V AF647 conjugate to report on apoptotic cells. To visualize the total amount of cells, the cells were also stained with the nuclei marker Hoechst33342. For analysis 708 x 708 µm images (n=3) were taken by CLSM (Figure 60). The quantity of cells indicated by the Hoechst33342 signal and the number of AF647-stained cells were counted with Fiji multipoint tool.[169] The ratio between Hoechst33342 and AF647 counts revealed that 91±1% of the encapsulated cells were vital, indicating that the encapsulation into the hydrogel was not harmful for cell viability.

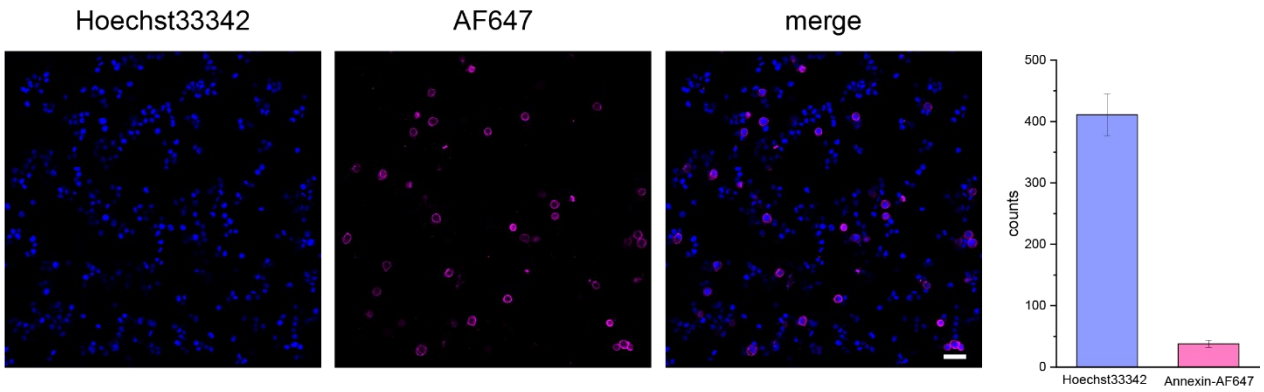

Figure 60: Cell viability test in cell-laden hydrogels. Living HeLa cells were added to TPA-*tris*NTA functionalized PVA-polymers and subsequently crosslinked for hydrogel formation. The embedded cells were stained with annexin V AF647 conjugate to indicate cells in an apoptotic state. In addition, they were stained with Hoechst33342 for visualization of the total cell number. The ratio of Hoechst- and AF647-stained cells showed that 91±1% of the cells are vital and the incorporation into the hydrogel was not harmful for cell viability. The experiment was conducted in triplicates and error bars indicate the s.d. Scale bar, 50 µm.

To assess the cytotoxicity of the two-photon sensitizers under illumination conditions, HeLa cells were exposed to increasing concentrations of either ATTO390 or rhodamine B and analyzed *via* the 3-(4,5-dimethylthiazol-2yl)-2,5-dipehnyltetrazolium bromide (MTT) assay. Both enhancers showed no dark toxicity up to 100 µM (ATTO390: > 70% cell viability; rhodamine B: > 90% cell viability) (Figure 61). However, cell vitality was severely affected when cells were incubated with 500 µM of ATTO390 whether illuminated or not. On the opposite, 500 µM rhodamine B hardly

affected the cells at all (>70% of viable cells). Importantly for cell experiments, both sensitizers were cytocompatible at the optimized concentrations for laser scanning lithography in the dark as well as under light actuation. Therefore, ATTO390 (100 µM) and RB (50 µM) are suited for cell application.

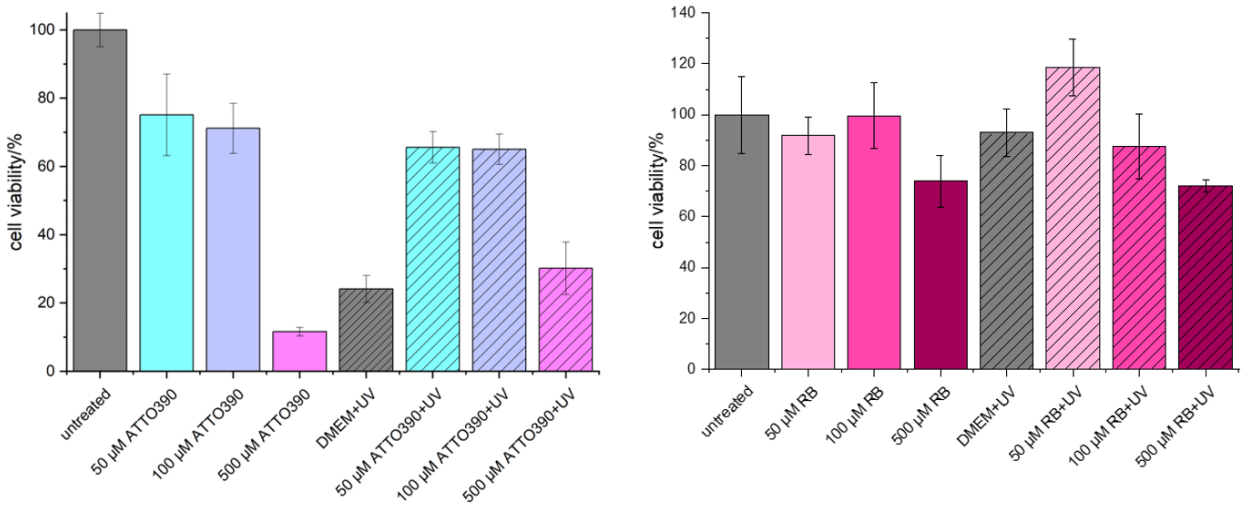

Figure 61: HeLa cells (1x10^6 cells/well) were seeded in 96-well plates and exposed to increasing concentrations of either ATTO390 (0, 50, 100, 500 µM) or rhodamine B (0, 50, 100 µM). Cells were illuminated for 1 min at 365 nm with 185 mW/cm^2 with a custom-made 96-well LED setup and incubated for 2 h. Thereafter, the medium was replaced, and cells cultivated for 24 h. Cytotoxicity was assessed *via* the MTT assay. Untreated cells served as reference. Both compounds showed the absence of dark toxicity up to 100 µM of the photo-sensitizer (ATTO390: > 70% cell viability; rhodamine B: > 70% cell viability). At 500 µM ATTO390, a cytotoxic effect was detected, both in the illuminated and non-illuminated state. In contrast, 500 µM rhodamine B had no cytotoxic effect at all (>70% of viable cells). Collectively, both sensitizers showed cytocompatibility at the applied concentrations (100 µM ATTO390; 50 µM rhodamine B) in the dark as well as under light actuation.

4.8.1. Transmembrane receptor labeling with *tris*NTA inside hydrogels

Having demonstrated the vitality of cells embedded in functionalized hydrogels, these cell matrices were used to organize His-tagged membrane proteins of encapsulated cells. HeLa cells stable transfected with the His_6-Y_2R^{mEGFP} plasmid were provided by Dr. Florencia Sanchez (Tampé lab). Expression of His_6-Y_2R^{mEGFP} was induced by supplementing the cells with tetracycline 16 h before the cells were embedded in the hydrogels. The chosen model receptor Y_2R belongs to the guanine nucleotide-binding protein (G-protein)-coupled receptors (GPCR) which are connected to multiple physiological and pathological pathways.[170,199] The Y_2 receptor is not evenly distributed in neurons and locally restricted ligand-receptor interactions have been observed *in vivo*. In addition, Y_2 confinement seems impact signal transduction and cell morphology.[170,200,201]

To validate the accessibility of the His-tag from the receptor after the cells are incorporated in a hydrogel, a soluble fluorescently labeled *tris*NTA was utilized for His-tag/NTA-interaction. Therefore, HeLa cells expressing His_6-Y_2R^{mEGFP} were homogenized with thioglycerol functionalized PVA and crosslinked with dithiol-PEG to form a hydrogel around the cells. Hence, no light activability of the hydrogel was needed, Thioglycerol was used as a substitute for (T)PA-*tris*NTA. Thioglycerol was used in the same concentration as TPA-*tris*NTA (20 mM) to maintain the crosslinking strength of the hydrogel. After incubation with *tris*NTA^{AF647} (100 nM in LCIS supplemented with 10 mM $NiCl_2$) for 30 min at 37 °C, confocal images (Figure 62) of the His_6-Y_2R^{mEGFP} signal (green channel) and *tris*NTA^{AF647} signal (magenta channel) were taken. The high Pearson coefficient (R=0.87) of the GFP and the AF647 channel displayed colocalization of the His_6-Y_2R^{mEGFP} and the *tris*NTA^{AF647}, which is also confirmed by the fluorescence intensity profiles. To exclude unspecific interaction of *tris*NTA^{AF647} and the cell membrane, HeLa cells without induction of the expression of His_6-Y_2R^{mEGFP} were used as a negative control. Indeed, nearly no binding was exhibited, confirming the specificity of the interaction pair.

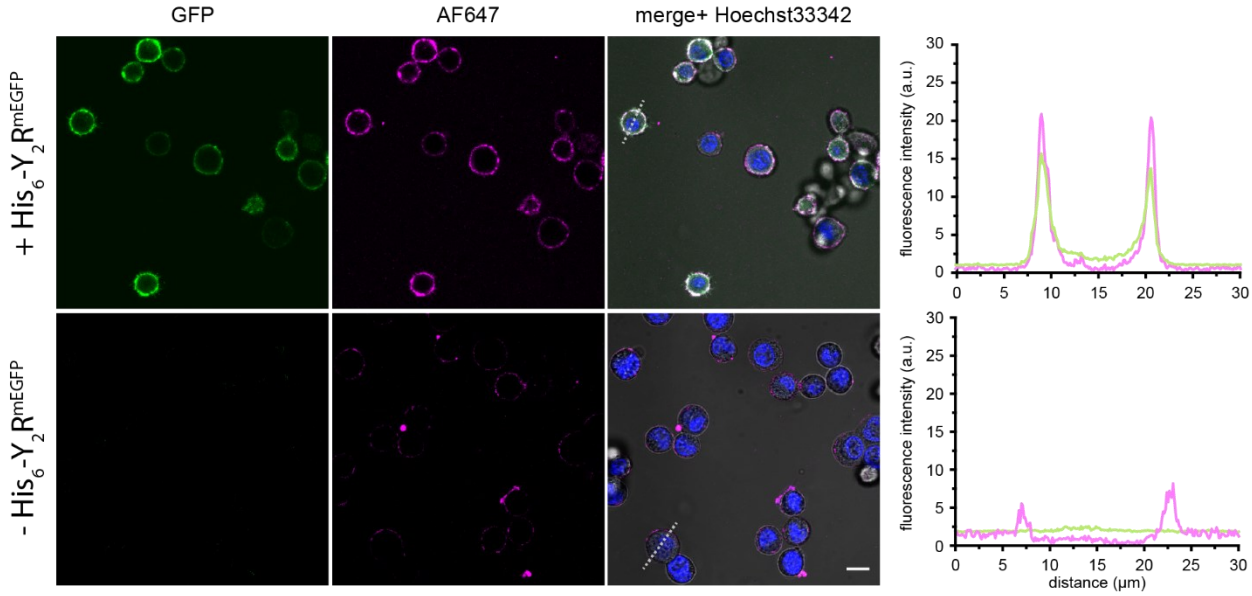

Figure 62: Analysis of His-tag accessibility of membrane receptor from cells embedded inside thioglycerol functionalized hydrogels. The hydrogels were incubated for 30 min at 37 °C with soluble *tris*NTA^{AF647}. HeLa cells expressing His_6-Y_2R^{mEGFP} displayed colocalization of the fluorescence signals of GFP and AF647 and in the intensity profile (ROI: grey dashed line, GFP: green line, AF647: magenta line), indicating successful His-tag/*tris*NTA interaction. HeLa cells without induction of the expression of His_6-Y_2R^{mEGFP} showed nearly no *tris*NTA^{AF647} binding to the cell membrane, however some unspecific binding to the cell surface was observed. Scale bar, 10 µm.

4.8.2. Photo-induced receptor confinement in PA-*tris*NTA functionalized hydrogels

After confirming biocompatibility of (T)PA-*tris*NTA functionalized hydrogels and His-tag accessibility of membrane receptors of cells within a hydrogel, light-induced membrane protein assembly was tested. The ultimate goal was the organization of receptors in a defined area at single cell level, therefore high spatiotemporal control is needed. PA-*tris*NTA functionalized hydrogels were prepared as a cell matrix for light-induced receptor enrichment to obtain spatial and temporal resolution of activation. PA-*tris*NTA instead of TPA-*tris*NTA was chosen as light activatable interaction tool to establish the proof of principle. HeLa cells expressing His_6-Y_2R^{mEGFP} were embedded in PA-*tris*NTA functionalized hydrogels, incubated with $NiCl_2$ (10 mM in life cell imaging solution, 30 min) and subsequently washed with life cell imaging solution (LCIS). An ROI covering one hemisphere of a cell was exposed by on-demand photoactivation of PA-*tris*NTA *via in-situ* laser scanning microscopy with the 405 nm laser (4.5 mW, 600 iterations). After 20 min, confocal images were taken using the same imaging conditions before and after photoactivation (see Figure 63). An intensity profile through the photoactivated cell displayed an asymmetric distribution of the receptor in the cell membrane. An increased GFP intensity in the illuminated area after light exposure (Figure 63B left) was visible, indicating an enrichment of the receptor.

In order to confirm activation of PA-*tris*NTA, the hydrogel was incubated with His_6-AF647 (300 nM in HBS buffer pH 7.2, 30 min) and re-imaged after washing. An increased accumulation of the peptide was seen at the photoactivated cell side (Figure 63 bottom row), which was also illustrated in the intensity profile (Figure 63B right). However, peptide binding was expected evenly throughout the ROI, instead the peptide was mainly observed at the illuminated area of the cell membrane.

To investigate receptor assembly as well as activation of the hydrogel and subsequent binding of the peptide in the ROI, a z-stack was generated across the entire volume of the cell. The side view of the reconstruction of the z-stack (Figure 64) showed in the GFP channel and in the merge channel enrichment of His_6-Y_2R^{mEGFP} at the illuminated region of the cell. Remarkably, a cone-shaped immobilization of the peptide was also seen in the AF647 channel and in the merge channel. Presumably, the hydrogel got activated along the beam path of the 405 nm laser. An accumulation of His_6-AF647 in the shape of the ROI in the focal plane was not visible. In order to investigate why the peptide did not bind in the photoactivated ROI, further experiments were conducted.

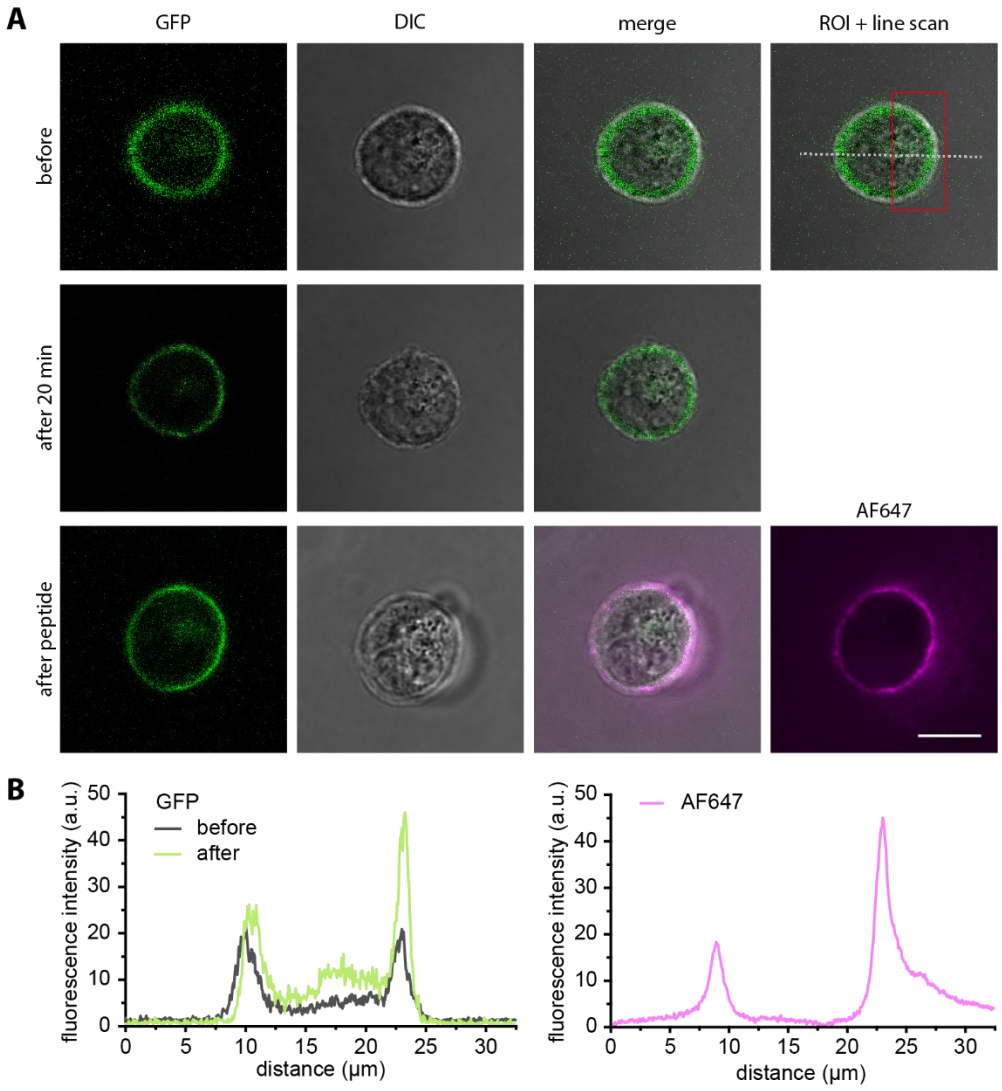

Figure 63: *In-situ* activation of cell-laden PA-*tris*NTA functionalized hydrogel for receptor enrichement. The ROI located at the cell membrane (red box) was illuminated using the 405 nm laser (4.5 mW, 600 iterations) at 37 °C. After 20 min, receptor enrichment in the activated area was visible. This finding was confirmed by the intensity profile (B left) across the cell (grey dashed line). To visualize the entire activated ROI the hydrogel was incubated with 100 nM His_6-AF647 and re-imaged after washing steps. In the AF647 channel binding of His_6-AF647 to the cell membrane especially in the illuminated ROI was visible. The intensity profile of the AF647 signal confirmed increased binding of His_6-AF647 to the ROI. Scale bar, 10 µm.

Light-induced membrane protein/*tris*NTA interactions inside 3D cell matrices are a challenging task within a complex system. So far, the reproducibility of the reorganization of receptors inside PA-*tris*NTA functionalized hydrogels was not consistent. In order to develop a standard procedure for PA-*tris*NTA mediated receptor enrichment, the effects of the light dose, addition of protease inhibitor and the temperature were studied.

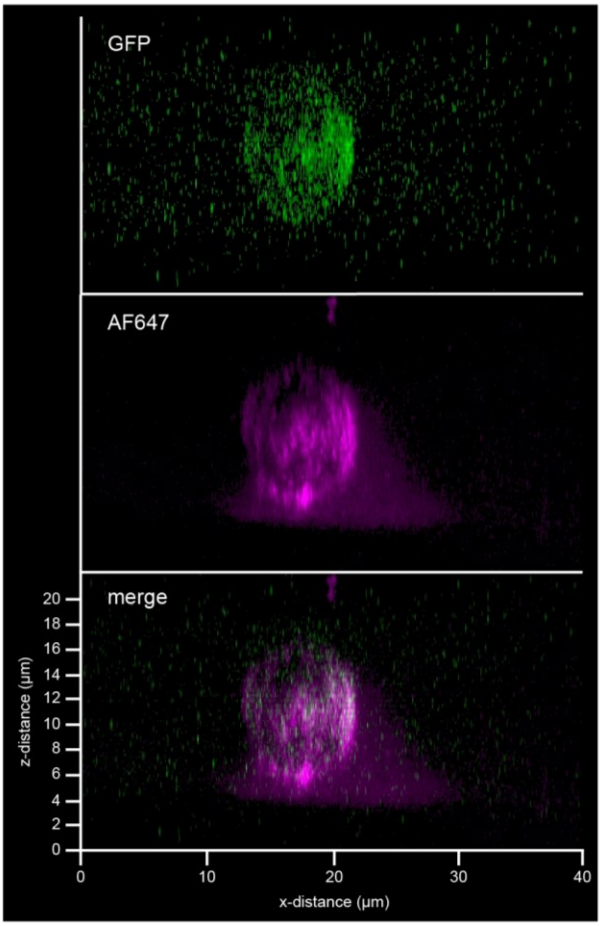

Figure 64: Reconstruction of the optical sectioning of the cell shown in Figure 63 displayed in x/z-direction. The GFP and AF647 signal was recorded through the entire cell volume (z-stack). In the GFP channel and the merge channel receptor enrichment in the illuminated area was visible. The AF647 channel displayed binding of His_6-AF647 on the cell membrane especially in the illuminated ROI. Furthermore, a conical shaped His_6-AF647 pattern was visible in the hydrogel surrounding the cell. Most likely this was due to activation along the laser beam path.

First, the influence of an increased activation energy was investigated. Since, the laser power of the 405 nm laser (100%= 4.5 mW) could not be increased further the number of scans in the ROI was increased from 600 to 1000 iterations (Figure 65, upper row, representative cell). In the intensity profile before and after the illumination no receptor enrichment was observed in the photoactivated region of the membrane (red box). On the contrary, the fluorescence intensity of the GFP signal has decreased compared to before the photopatterning. This was an indication that photobleaching of GFP occurred due to high light intensity.

Next, the impact of the temperature was studied. In previous experiments *in-situ* activation of the hydrogels with embedded living cells was performed at physiological temperature (37 °C), whereas hydrogels without cells were activated at RT. To exclude that the increased temperature

has an effect on the function of the hydrogel or PA-*tris*NTA, cells were embedded in PA-*tris*NTA functionalized hydrogel and activated *in-situ* by CLSM at RT (Figure 65 middle row, representative cell). The distribution of the receptor after exposure was unchanged, suggesting that the decreased temperature had not improved the light induced receptor enrichment.

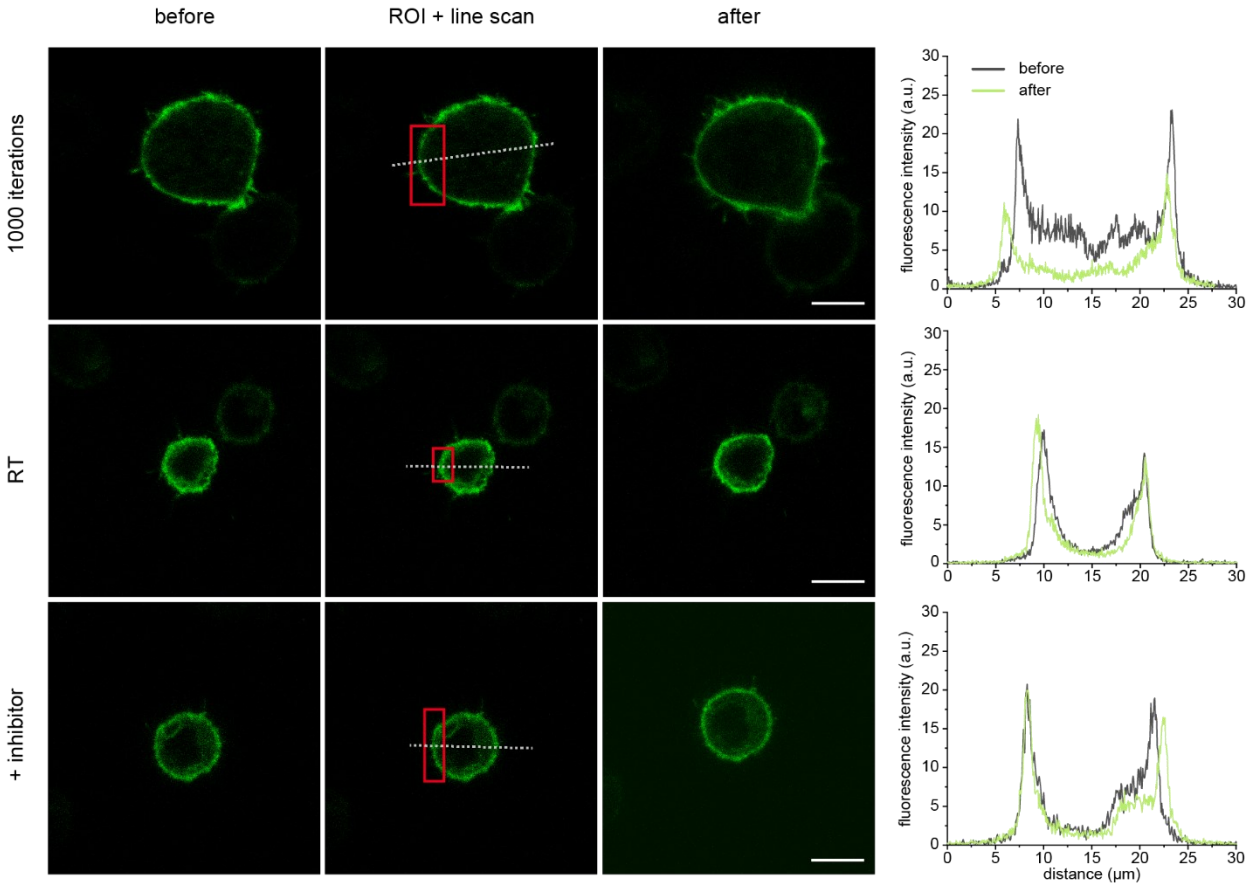

Figure 65: Optimization approaches for *in-situ* activation of PA-*tris*NTA functionalized hydrogels with embedded HeLa cells expressing His_6-Y_2R^{mEGFP}. ROIs indicated by the red box were illuminated using the 405 nm laser. Before and 20 min after illumination, the respective areas were imaged, and intensity profiles were measured (grey dashed lines). Upper row: the light dosage for photo-patterning was increased to 1000 iteration. The intensity profile before and after illumination indicated photobleaching of GFP instead of receptor enrichment. Middle row: *in-situ* activation was conducted at RT to investigate the influence of temperature for PA-*tris*NTA function. 20 min after light activation, the homogeneous distribution of His_6-Y_2R^{mEGFP} revealed no protein enrichment in the illuminated areas. Lower row: to exclude degradation of the PA-*tris*NTA peptide backbone by proteases, protease inhibitor was added to the imaging buffer. Also, in this case illumination of membrane located ROIs did not lead to receptor recruitment. Scale bars, 10 µm.

Within the cytotoxicity assay (section 3.2.3.3), 91±1% of the cells embedded in the hydrogel were found to be viable. However, ~10% of cells are in an apoptotic state and could secrete proteases, which could degrade the peptide backbone or His_5-tag of PA-*tris*NTA, thereby rendering

PA-*tris*NTA dysfunctional. To avoid this, the cell matrix was covered with LCIS supplemented with EDTA-free Halt Protease Inhibitor Cocktail immediately after gelation (Figure 65, bottom row). Addition of the protease inhibitor made proteolytic degradation unlikely, however no membrane receptor enrichment was achieved after light activation.

The *in-situ* protein patterning inside PA-*tris*NTA functionalized hydrogels without cells was consistently successful, whereas the on-demand assembly of membrane proteins within cell-laden PA-*tris*NTA hydrogel was not consistently reproducible yet. Therefore, it was tested whether photoactivation of the hydrogel surrounding the cells was possible. For this purpose, HeLa cells expressing His_6-Y_2R^{mEGFP} were embedded in PA-*tris*NTA functionalized hydrogels and after Ni(II)-loading exposed at specific sites *via* CLSM (Figure 66). ROIs were illuminated at the cell membrane (red box: 4.5 mW, 600 iterations) to trigger receptor enrichment as well as ROIs between the cells.

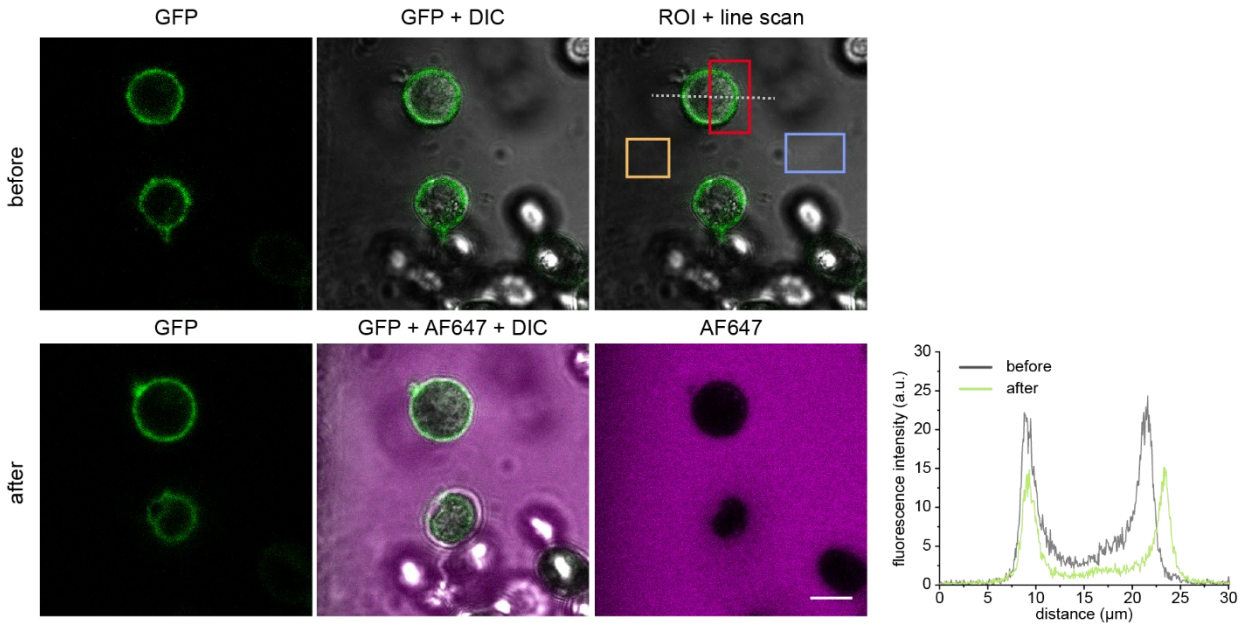

Figure 66: *In-situ* activation of cell-laden PA-*tris*NTA functionalized hydrogel. The hydrogel around HeLa cells expressing His_6-Y_2R^{mEGFP} were illuminated (red box) using the 405 nm laser (4.5 mW, 600 iterations). In addition, the hydrogel between the cells were exposed with different laser intensities (4.5 mW, orange box: 600 iterations, blue bow: 1000 iterations). To visualize the activated areas the hydrogel was incubated with 100 nM His_6-AF647 and re-imaged after washing. The intensity profile through the cell before and after illumination indicated that no receptor assembly in the exposed area took place. In the AF647 channel no His_6-AF647 assembly in the illuminated areas could be observed even after signal amplification. Scale bar, 10 µm.

As can be seen in the GFP channel as well as in the intensity profile, the receptor was homogeneously distributed in the membrane before and after the illumination. This finding

suggests that no light-driven receptor confinement occurred. As a positive control for PA-*tris*NTA activation two additional ROIs between the cells were irradiated (4.5 mW, orange box: 600 iteration, blue box: 1000 iterations) and the hydrogel was subsequently incubated with 100 nM His_6-AF647. Re-imaging of the hydrogel after washing showed no binding of the peptide in the illuminated areas, even after strong signal amplification.

The quality and functionality of PA-*tris*NTA was regularly checked and confirmed by RP-C_{18}-HPLC, MALDI-TOF analysis and photoactivation in cell-free hydrogels. So far, the cause of the low reproducibility of the membrane protein enrichment by photoactivation of PA-*tris*NTA could not been identified yet.

4.8.3. Cells in TPA-*tris*NTA functionalized hydrogels for 3D structuring

The PA-*tris*NTA/His-Tag interaction with cells embedded in the hydrogel gave promising results, although it was not yet consistently reproducible. The use of TPA-*tris*NTA in hydrogels allows the use of near-infrared (NIR) light. Radiation with a wavelength between 650-950 nm (therapeutic window) can penetrate deeper into tissue than shorter wavelength light, and it also causes less photodamage along the illumination path than UV-light.[202] The DEAC group incorporated in TPA-*tris*NTA also enables precise activation in 3D by using fs-pulsed lasers by quasi-simultaneous absorption of two photons. These advantages were exploited to organize His-tagged membrane receptors in hydrogels. HeLa cells expressing His_6-Y_2R^{mEGFP} were entrapped in TPA-*tris*NTA functionalized hydrogels and regions of interest (ROIs) located at the cell membrane (ROI 1,2) as well as in the hydrogel only (ROI 3) were activated by 2P illumination (800 nm, 3.1 mW, 1500 iterations) (Figure 67A). Comparison of the fluorescence intensity of GFP inside ROI 1,2 (Figure 67B) revealed that the fluorescence signal decreased instead of the expected intensification. This is likely due to bleaching of the GFP chromophore, making it impossible to draw conclusions about successful enrichment of the receptor within the ROI. To verify whether the hydrogel had been activated within the ROI, the sample was incubated with His_6-mCherry (Figure 67C). Subsequently, the immobilized protein within the irradiated areas could be detected by confocal laser scanning microscopy (CLSM), confirming the immobilization at the photoactivated area.

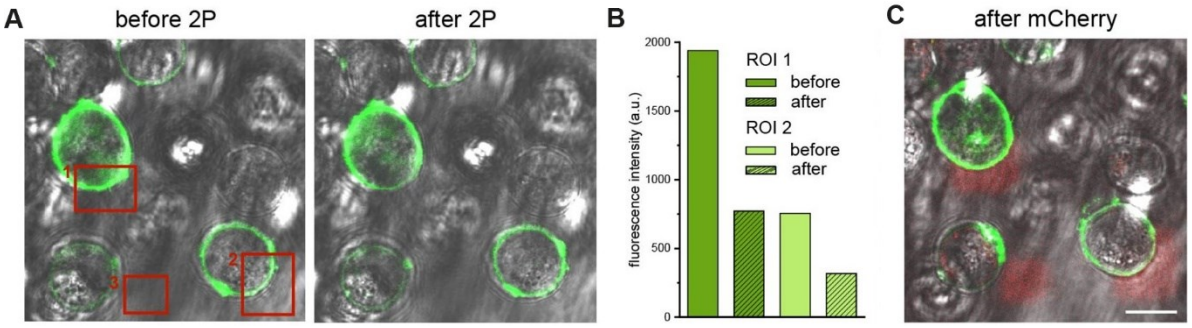

Figure 67: 2P-activation of TPA-*tris*NTA functionalized hydrogel with embedded HeLa cells expressing His_6-Y_2R^{mEGFP}. ROIs located at the cell membrane (ROI 1,2) as well as in the hydrogel only (ROI 3) were activated by 2P illumination (800 nm, 3.1 mW, 1500 iterations). The fluorescence intensity of GFP inside ROI 1,2 was compared before and after the illumination. The intensity decrease indicated photobleaching of GFP. The successful activation of TPA-*tris*NTA was verified by binding of His_6-mCherry inside the illuminated regions. Scale bar, 10 µm.

To avoid photobleaching, the sensitizing agents ATTO390 and rhodamine B (RB) were used in the next step to reduce the light dose required for activation. HeLa cells expressing His_6-Y_2R^{mEGFP} showed a significant change in receptor localization after addition of RB (50 µM). In Figure 68 it can be seen that before the addition of RB the receptor was localized at the membrane. Afterwards, however, the GFP signal was distributed throughout the cell. It was assumed that RB interacts with the receptor, resulting in internalization. It is unclear how the His_6-Y_2R^{mEGFP} uptake is triggered. However, RB was thereby not useful as sensitizing agent for the intended application.

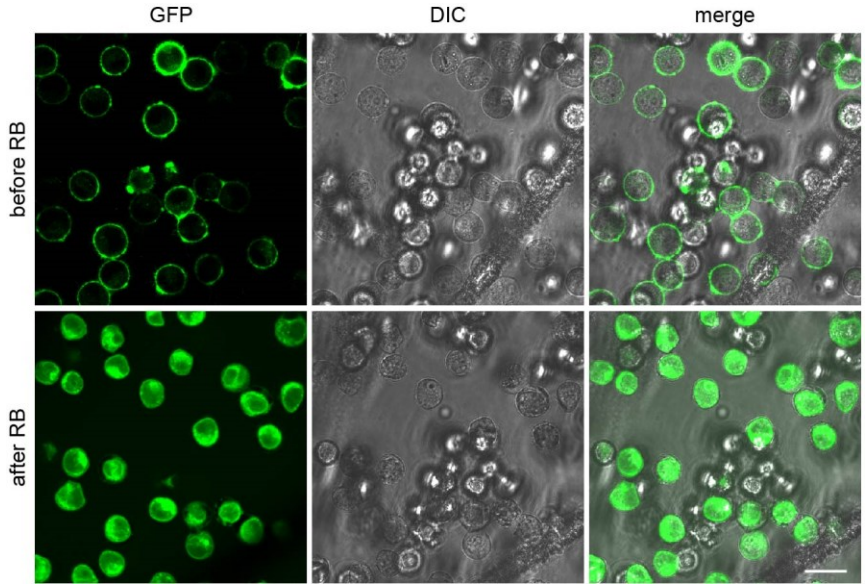

Figure 68: HeLa cells expressing His_6-Y_2R^{mEGFP} inside TPA-*tris*NTA functionalized hydrogels before and after addition of Rhodamine B (RB) (50 µM). Before the sensitizer was added, the receptor was located at the membrane, whereas after the addition the receptor is distributed within the cell. This side effect made RB for the intended application unsuitable. Scale bar, 20 µm.

In contrast, cells from the same batch embedded in TPA-*tris*NTA hydrogel showed no change in His_6-Y_2R^{mEGFP} localization in the presence of ATTO390 (100 µM). Therefore, ROIs located at the membrane of the cells were irradiated with 800 nm using the conditions optimized for TPA-*tris*NTA (3.1 mW, 1500 iterations) (Figure 69). After illumination, a homogeneous GFP signal was observed in the activated area in the exact shape and location of the ROI, indicating His_6-Y_2R^{mEGFP} distribution within the ROI. The intensity profile of GFP before and after exposure confirms the dislocation of the receptor in the activated area. Significant changes in receptor localization also occurred in the part of the ROI that was inside the cell. Inside the cell, an accumulation of His_6-Y_2R^{mEGFP} was observed in the rectangular shape of the exposed region (white arrow in Figure 69). This could indicate a specific light-driven response of the cell to the activation of TPA-*tris*NTA in the ROI. This knowledge was subsequently used to specifically manipulate the shape of the membrane of embedded HeLa cells expressing His_6-Y_2R^{mEGFP} in a TPA-*tris*NTA functionalized hydrogel and in the presence of ATTO390.

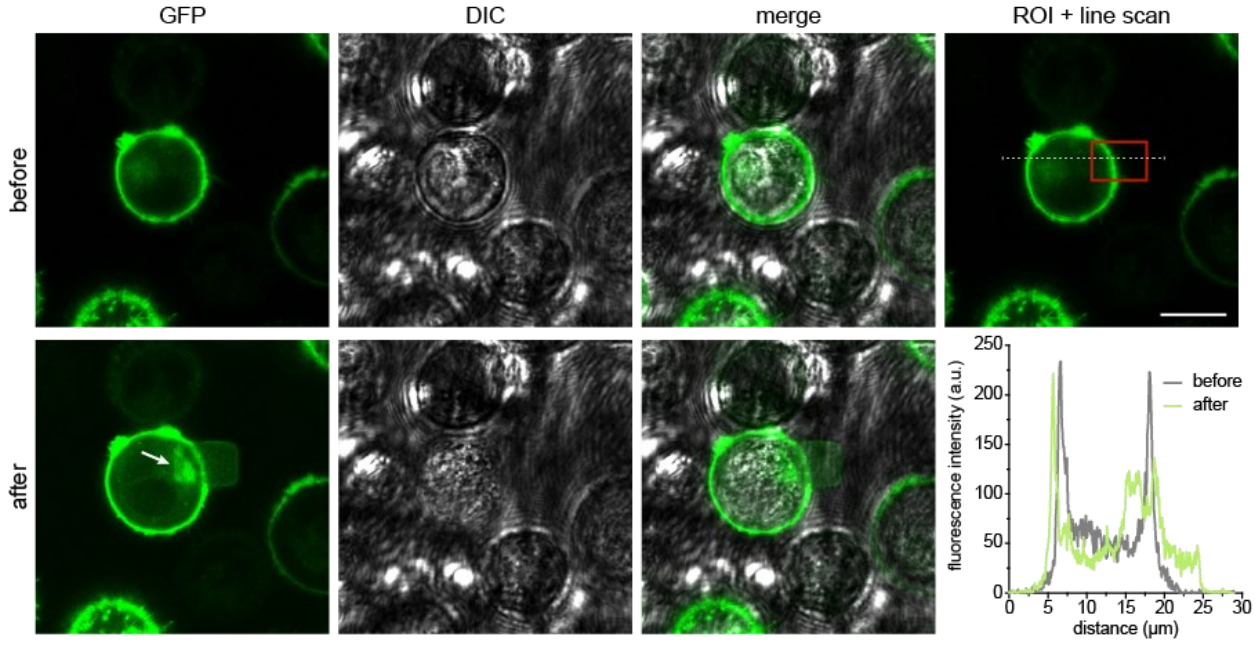

Figure 69: 2P illumination of membrane located ROIs at HeLa Cells expressing His_6-Y_2R^{mEGFP} embedded in TPA-*tris*NTA functionalized hydrogels in presence of ATTO390 (100 µM). The intensity profile across the membrane (grey dashed line) shows after exposure a decreased GFP fluorescence in the ROI. However, in the exposed region a membrane protrusion in the shape of the ROI was visible. In addition, inside the cell an accumulation of His_6-Y_2R^{mEGFP} (white arrow) could be seen. Scale bar: 20 µm.

To examine, whether more than one protrusion on a cell can be triggered, two opposite areas were sequentially illuminated with 800 nm light (Figure 70A). In both cases, a protrusion of the membrane filling the ROI was observed in the CLSM image. Again, in both exposure steps, an

accumulation of the receptor inside the cell was observed in the irradiated areas. Subsequently, z-stacks were taken along the cell z-axis and processed into a spatial representation using microscope software (ZEN Blue, Zeiss) (Figure 70B). The induced protrusions at cell surface can be seen on both sides. The experiment showed that the deformation of the membrane was possible at several locations and that accumulations of Y_2R occurred inside the cells.

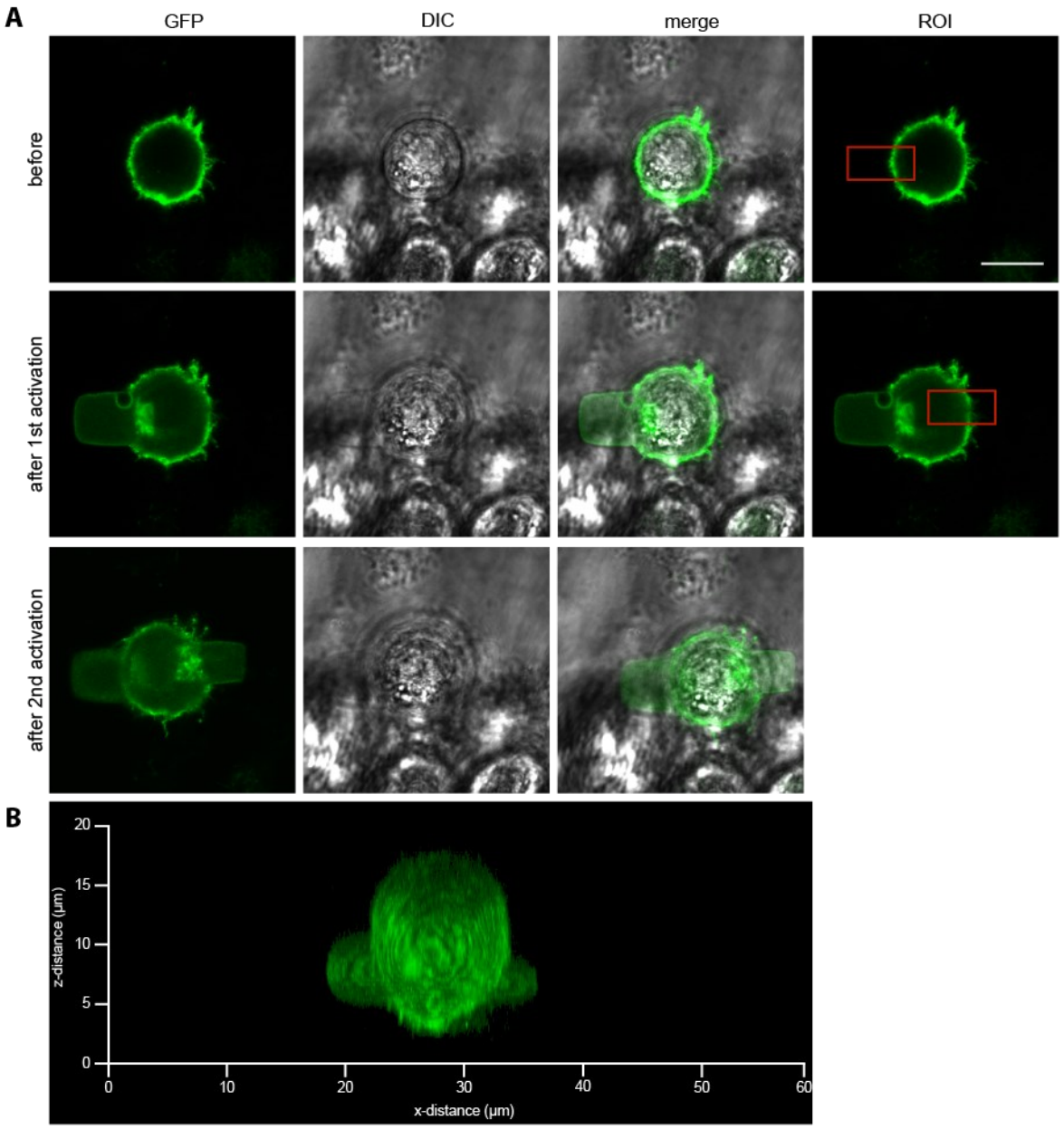

Figure 70: Sequential 2P illumination of two opposite directed ROIs at a HeLa Cell expressing His_6-Y_2R^{mEGFP} embedded in TPA-*tris*NTA functionalized hydrogels. In order to investigate if more than one protrusion can be triggered, two ROIs in opposite directions of a cell were illuminated in presence of ATTO390 (100 µM). A) After light exposure the activated regions were filled with His_6-Y_2R^{mEGFP}, indicating a light-triggered manipulation of the membrane shape. Scale bar, 10 µm. B) In the reconstituted z-stack the protrusion on both sides of the cell was visible.

Next, it was tested if a stepwise expansion of the membrane was possible by sequential irradiation. The same settings (800 nm, 3.1 mW, 1500 iterations) were used for all studies of cell-loaded hydrogels and an image was taken by CLSM between each step. As can be seen in Figure 71, the membrane successfully expanded after each illumination. The generated protrusion of the cell membrane showed a homogeneous distribution of His_6-Y_2R^{mEGFP}, as well as in the regions where the ROIs overlapped.

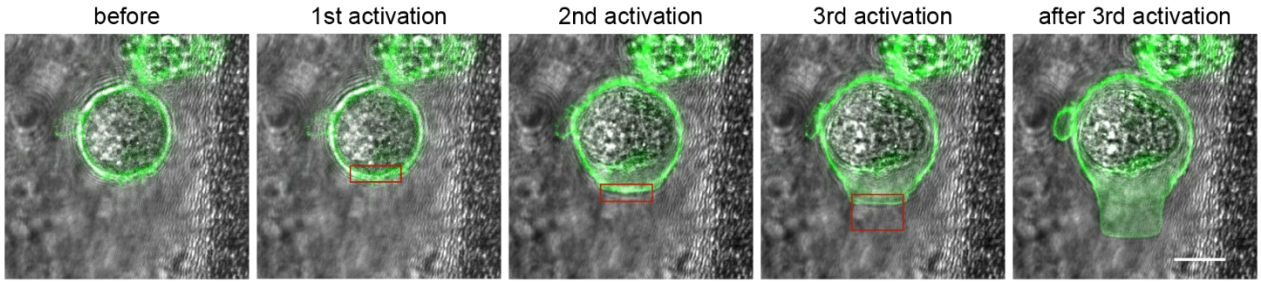

Figure 71: Directed expansion of the cell membrane by sequential 2P illumination. The cell membrane of HeLa cells expressing His_6-Y_2R^{mEGFP} could be stepwise extended by three illumination steps in the presence of ATTO390 (100 µM). After each step the protrusion was enlarged by the size of the ROI. Scale bar, 10 µm.

In this way, the membrane of the cell was extended by photoactivation of a ROI with the sizes of about 10x7 µm. In addition, it was also observed that the cell diameter increased during the experiment. The untreated cell had a radius of 9 µm, which results in an area of 254 µm^2 in the confocal plane using equation 5.

$$A = \pi \cdot r^2 \qquad \text{Equation 5}$$

After the sequential illuminated a radius of approx. 12 µm (A=452 µm^2) was measured. Summing up the cell as well as the membrane protrusion area, the total cell area in the confocal plane increased from 254 µm^2 to 522 µm^2. This means that the cell dimension in the focal plane increased more than twice during the experiment. This already appeared to be a large expansion. However, in order to test which extensions of the membrane are possible with this technique and where the limit is, a 50 µm long and 5 µm wide ROI on a cell membrane was illuminated with the previously used parameters (800 nm, 3.1 mW, 1500 iterations). After irradiation of the hydrogel, the cell already filled most of the ROI. Within the ROI, the signal of His_6-Y_2R^{mEGFP} was homogeneously distributed (Figure 72A). Again, a rectangular region where the receptor was assembled was seen within the cell. This light-driven manipulation of the cell shape is astonishing,

because the membrane was elongated by 44 µm *via* the illumination of the hydrogel, which meant a significant increase in cell surface area. Additionally, the speed of the process was analyzed. The exposure of the ROI lasted 2 min. The image taken immediately afterwards showed that the protrusion had already grown 36 µm into the ROI, which meant a speed of membrane movement of 18 µm/s. The remaining 8 µm of the ROI took another 25 s until the GFP signal emanating from the transmembrane receptor filled up the defined area, which meant a significant slowing down of the process to 0.32 µm/s. Along the z-axis, z-stacks were acquired of the cell (Figure 72B) and again processed into a spatial representation. In the side view, the 44 µm extension of the cell membrane can be clearly seen in the exact shape of the drawn ROI. The thickness of the protrusion in the z-direction corresponds to approx. 5 µm, which is in very good agreement with the determined half-width of 2P-activation of TPA-*tris*NTA (5 ± 1 µm FWHM).

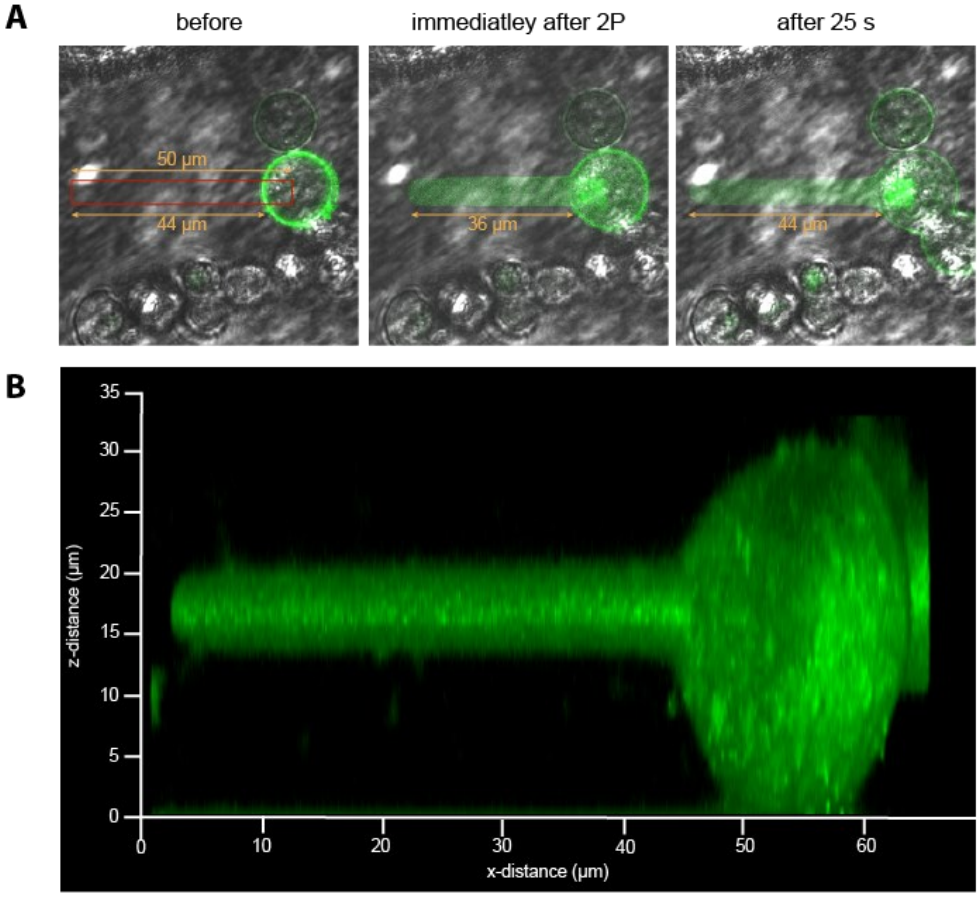

Figure 72: Directed expansion of the cell membrane by 2P illumination. The light-triggered expansion of the cell membrane was tested in regard of speed and maximum length of the ROI. Therefore a 50 µm long ROI was illuminated in presence of ATTO390. A) Immediately after the exposure the ROI was already filled with His_6-Y_2R^{mEGFP} up to a length of 36 µm. After 25 s the complete ROI showed a homogenous GFP signal. B) The sideview of the reconstruction of the z-stack illustrated the 44 µm long membrane expansion.

To address whether cell-cell contacts could be induced by this manipulation of the cell membrane, a rectangular ROI connecting two adjacent cells at the same x/y plane was illuminated (800 nm, 3.1 mW, 1500 iterations). After CLSM imaging, the illuminated ROI between the cells showed a connection of the two cells (Figure 73A). In addition, the previously observed His_6-Y_2R^{mEGFP} accumulations within the two cells were also visible. The cell junction was also clearly visible in the side view of the z-stack reconstruction (Figure 73B). The observation raises the question of whether the cell junction was originating from both cells or whether it grew from one cell to the other.

The membrane of cell 2 seems to be in a roundish shape as before the illumination. In contrast, the cell membrane of cell 1 appeared to have adopted the shape of the ROI. From the confocal images no conclusions about the contribution of membrane parts of the two cells could be drawn. The direction of the development of the linkage could not be clearly determined in the confocal images. For this purpose, in addition to cells expressing His_6-Y_2R^{mEGFP}, cells expressing the receptor with a different colored fusion proteins would have to be embedded. Triggered cell junction of membranes with different colored fluorescence signals could be used to investigate whether membrane fusion is taking place or not. These would be an insightful experiment, when an appropriate second cell line is available.

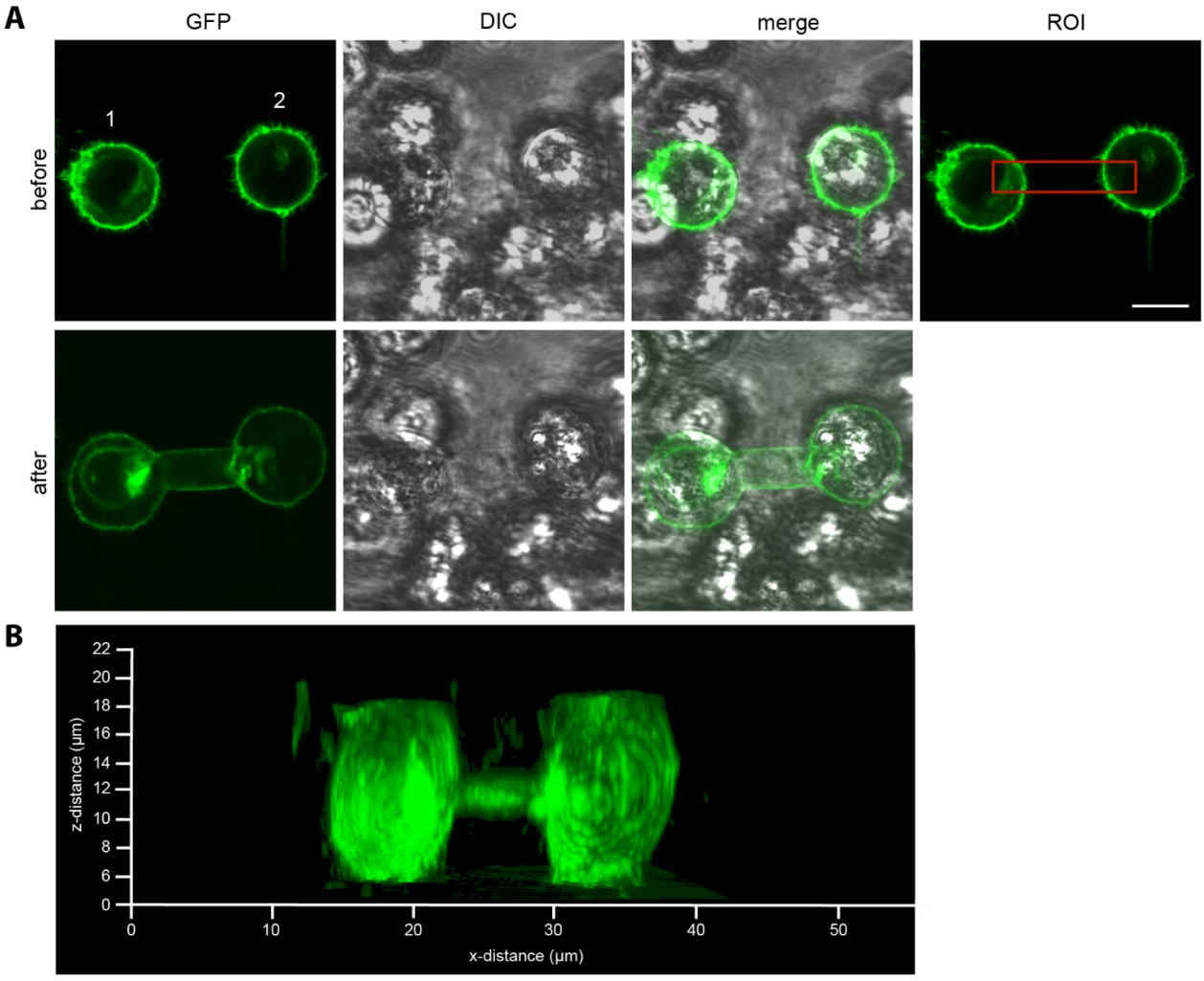

Figure 73: Light-triggered membrane manipulation for cell-cell contacts. A) A ROI connecting two HeLa cells expressing His_6-Y_2R^{mEGFP} was 2P illuminated in presence of ATTO390 to investigate cell manipulation. After the exposure a connection of the cells was visible. Scale bar, 10 µm. B) The sideview of the z-stack reconstruction visualized the joint of the two cells.

To demonstrate that the light-triggered manipulation of the cell membrane was based on an interaction of the immobilized *tris*NTA and the His-tag of Y_2R^{mEGFP}, control experiments were performed. His-tagged proteins of interest (POIs) bound by *tris*NTA can be released from the complex by imidazole due to competition. The reversibility of POI structuring can be used as evidence for immobilization by *tris*NTA. To this end, cells expressing His_6-Y_2R^{mEGFP} embedded in TPA-*tris*NTA functionalized hydrogel were imaged, then cell membrane protrusions were induced by two-photon exposure (800 nm, 3.1 mW, 1500 iterations) in the presence of ATTO390 (100 µM) (Figure 74A). Next, imidazole (500 mM) was added to outcompete the affinity binding of the receptor. Contrary to the possibility that the protrusion would retract, no change in membrane

protrusion was observed after addition of the histidine competitor. One hypothesis was that the His-tag of the receptor was released by the addition of imidazole, but the membrane remains in its shape. To test this theory, cells were encapsulated in hydrogels functionalized with thioglycerol instead of TPA-*tris*NTA in the presence of ATTO390 (100 µM).

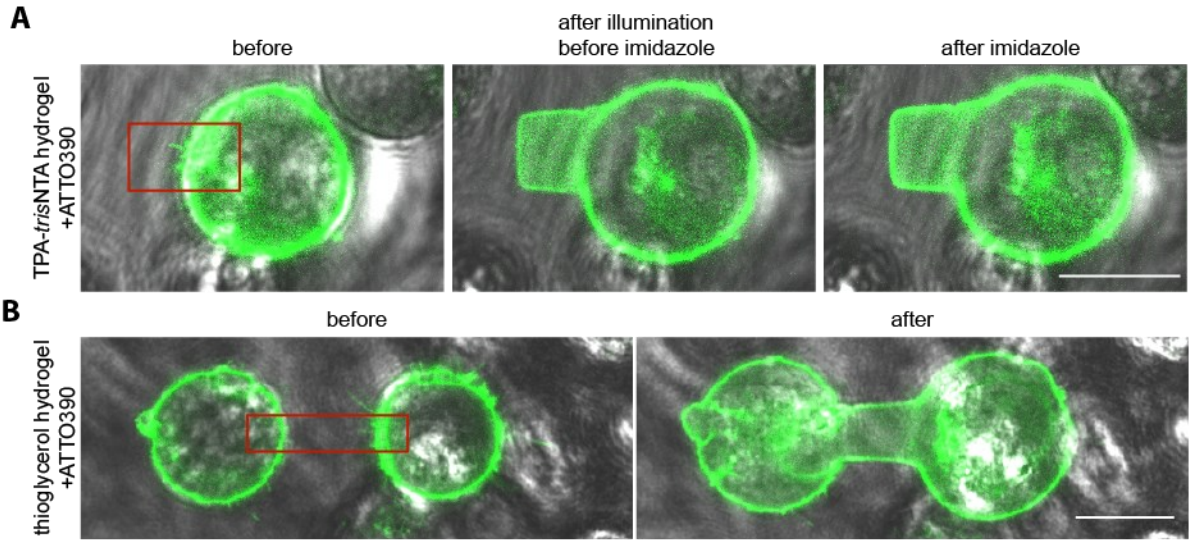

Figure 74: Specificity experiments to demonstrate that the protrusion was triggered by *tris*NTA/His-tag interaction between activated TPA-*tris*NTA and His_6-Y_2R^{mEGFP}. A) Inside a TPA-*tris*NTA functionalized hydrogel a protrusion of the cell membrane was triggered by 2P illumination in the presence of ATTO390. Subsequently, imidazole was added to outcompete the *tris*NTA/His-tag interaction. The competitor did not cause any visible changes in His_6-Y_2R^{mEGFP} location. Scale bar, 10 µm. B) HeLa cells expressing His_6-Y_2R^{mEGFP} were embedded in thioglycerol functionalized hydrogels and a ROI connecting two cells was illuminated in the presence of ATTO390. The membrane connection was again visible, indicating that the membrane manipulation is not *tris*NTA dependent. Scale bar, 10 µm.

Thioglycerol has no active function in the hydrogel, but serves as a substitute for TPA-*tris*NTA to maintain the crosslinking strength of the hydrogel. Without TPA-*tris*NTA, no protrusion of the cell membrane should occur after 2P activation. Nevertheless, after irradiation of a cell connecting ROI, cell-cell contact was observed as before *via* CLSM (Figure 74B). Thus, the negative control showed that the effect was not *tris*NTA dependent. It is hypothesized that 2P radiation causes deformation of the hydrogel possibly by depolymerization, creating cavities into which the spatially confined cells crawled.

The cellular processes that caused the cells to spread into the illuminated regions of the hydrogel are unknown so far. Furthermore, the reason and formation of the His_6-Y_2R^{mEGFP} accumulations within the cells is not clear. Investigation of the effects of the formed cell-cell contacts is of great

interest for preparation of artificial cell networks. It is possible that signaling pathways are activated that affect cell morphology and viability. The observations and investigations from these experiments require a long-term and more detailed study of the cellular processes. These findings open up a new research project which will explore these cellular networks.

5. Summary

The specific and precise arrangement of proteins and biomolecules in 3D is an important prerequisite for the study of cell migration, cellular signal transduction and the production of artificial tissue. In a variety of research approaches, proteins have been immobilized on rigid surfaces such as glass or gold to observe protein-protein or protein-cell interactions. While these commonly used analytical platforms offer advantages such as rapid washing steps and easy use, due to their rigidity and two-dimensionality, they cannot replicate the extracellular matrix (ECM) the native environment of cells. This severe deviation from the natural environment results in significant changes in cell structure and cellular processes such as the polarization of the cell, its morphology, and signal transduction. In order to maintain the functionality of the immobilized proteins, it is also enormously important that the proteins are oriented and anchored in the material under mild conditions.

An immobilization strategy that makes this possible is bioaffinity. For this, the specific interaction of a biomolecule with an interaction partner anchored on a surface is used to immobilize the biomolecule. Such an interaction is for example the nitrilotriacetic acid (NTA)/His-tag binding. NTA is a chelator molecule that, when bound to divalent metal ions such as Ni(II), forms an octahedral complex with oligohistidines. The oligo histidine-tag can be competed out of the complex by free histidine or imidazole due to structural similarity. This is exploited in immobilized metal affinity chromatography (IMAC). The binding of a *mono*NTA/His-tag complex (K_D=10 µM) is not stable enough to be used for immobilizations. Therefore, multivalent variants of the chelator were developed, like *tris*NTA which has a high affinity for His_6-tagged proteins (K_D= 10 nM). The PA-*tris*NTA developed in a preliminary work was the first light-activatable system based on the *tris*NTA chelator head.[73]

The aim of this work was to synthesize a new two-photon (2P) activatable *tris*NTA (TPA-*tris*NTA) interaction molecule, to analyze its photophysical characteristics and to apply it for two- and three-dimensional (2D/3D) biomolecule patterning. The final goal was to use TPA-*tris*NTA for cellular applications in order to manipulate membrane protein organization. Therefore,

TPA-*tris*NTA was designed to maintain a stable autoinhibition enabling the immobilization of proteins under physiological conditions with high precision in the x/y, as well as z dimension only upon light activation. 2P activation brings some outstanding advantages: i) the use of near-infrared (NIR) light is less harmful to cells compared to ultraviolet (UV) light, ii) the longer wavelength allows the radiation to penetrate deeper into tissues, iii) the precision of focal irradiation is more accurate because only a focal volume (about 1 fL) is excited and, unlike UV light, scattered light does not lead to activation.

Several backbones for TPA-*tris*NTA were considered as 2P cleavable groups due to their 2P absorption ability and small size: 3-nitrodibenzofuran (NDBF), 6-bromo-7-hydroxycoumarin (Bhc), and 7-diethylaminocoumarin (DEAC). Initially, suitable synthetic routes were developed for the respective carbaldehydes, since these represented an important intermediate for both the construction of amino acid (aa) derivatives as well as ß-hydroxy acids. ß-Hydroxy acids were important intermediates because their photocleavage differs from aa derivatives. To establish the conversion from carbaldehydes to hydroxy acids *via* Reformatsky reaction, commercially available carbaldehydes of the nitroveratral (NV) or nitropiperonal (NP) group were used in addition. The conversion of NDBF, NV, NP proved to be difficult, whereas the ß-hydroxy acid was successfully synthesized from Bhc as well as from DEAC.

Starting from DEAC ß-hydroxy acid, a Fmoc-protected amino acid derivative was synthesized. To ensure high cleavage efficiency, the DEAC ß-hydroxy acid was linked to *mono*Fmoc-ethylenediamine through a carbamate linker. Subsequently, the photocleavable group was successfully incorporated into the linker of TPA-*tris*NTA by solid-phase peptide synthesis (SPPS).

The functional principle of TPA-*tris*NTA, similar to PA-*tris*NTA, is based on the autoinhibition of the multivalent chelator head *tris*NTA, which is linked to an intramolecular oligohistidine sequence by a peptide linker. In presence of Ni(II)-ions, *tris*NTA forms a metal ion-mediated complex with histidine, causing TPA-*tris*NTA to self-inactivate. The cleavage site is the DEAC based photocleavable amino acid. In contrast to PA-*tris*NTA, the incorporation of two photocleavable amino acids was omitted. Instead, only one photocleavable DEAC was incorporated in front of the His-tag. To avoid a second DEAC group within the His-tag, a His_5-tag was used instead of an His_6-tag. It is known from preliminary work that a His_5-tag is sufficient to maintain autoinhibition in the presence of His_6-tagged proteins of interest (POIs), but can be displaced from the complex after light-driven cleavage of the peptide backbone.[72] Placement of a cysteine in the peptide linker

between the *tris*NTA and the DEAC group allowed for permanent surface anchoring after photocleavage of the linker.

After the target compound was successfully synthesized, TPA-*tris*NTA was examined for its photophysical properties. The UV/Vis spectra of TPA-*tris*NTA (in HBS buffer:MeCN, 1:1) showed an absorption/emission maximum at 390 nm and 480 nm respectively, indicating an optimal one-photon (1P) activation with light sources of about 400 nm. Subsequently, the cleavage kinetics of the incorporated DEAC amino acid were investigated. Irradiation of the Fmoc-protected amino acid with 405 nm for 5-900 s resulted in a cleavage kinetic of 12 s for 50% of compound. Furthermore, a fluorescence quantum yield φ_F of 15% for TPA-*tris*NTA was determined by two-photon excited fluorescence (TPEF) measurements. In general, the absorption maximum for 2P excitations is about twice the wavelength for single-photon irradiation. To determine the exact value experimentally, the two-photon absorption cross section $\varphi_F\delta_2$ at 770-860 nm was determined by TPEF measurements. At 810 nm, 7.7 GM and at 800 nm, 7.1 GM were obtained. To prove that this was a 2P process, the two-photon excitation was measured as a function of increasing laser power. The count rate of the fluorescence response was logarithmically plotted against the logarithm of the excitation energy. The obtained slope of 1.93± 0.02 is close to the perfect square dependence and confirmed TPA-*tris*NTA as a two-photon excitable molecule.

Next, the organization of biomolecules on two-dimensional glass surfaces was tested before more complex 3D biomaterials were used. For this purpose, different surface functionalization strategies were tested. 3-Glycidyloxypropyl-trimethoxysilanes (GOPTS), poly-*L*-lysine (PLL) and 3-aminopropyl-triethoxysilane (APTES) were used as functionalization agents, which were linked to PEG to passivate the glass surface against non-specific adsorption. Subsequently, PA-*tris*NTA or TPA-*tris*NTA were immobilized on the surface *via* maleimide-cysteine linkage.

For activation, surfaces were exposed to 365 nm light through quartz masks or irradiated with a 405 nm laser on a confocal laser scanning microscope (CLSM). For protein patterning, $His_{6\text{-}10}$-tagged mVenus, mCherry, MBP^{OG488}, or GFP were used as model proteins. In addition, a short Alexa647-tagged His_6-peptide (His_6-AF647) was used, because it is much smaller compared to the bulky proteins, allowing higher immobilization densities. To visualize the immobilized proteins and peptides, the fluorescence of the proteins or fluorophores was detected by CLSM. For evaluation of the different functionalized surfaces, particular focus was placed on reproducibility, specificity, and accuracy of the protein structure. With respect to all these points, GOPTS surfaces gave the least good result and APTES functionalized glass slides gave the best result. APTES

functionalized surfaces showed superior repellence to non-specific binding and allowed for homogeneous protein patterning compared to GOPTS and PLL.

Protein patterns with high signal-to-noise ratio and very good reproducibility could be obtained on PLL and APTES surfaces, whereas the use of blocking agents to increase specificity could be omitted for APTES surfaces. Therefore, APTES PA-*tris*NTA functionalized surfaces were used to realize *in-situ* patterning, laser power dependent protein densities and multiprotein/peptide patterns.

The knowledge gained from patterning the two-dimensional (2D) glass surfaces was then used to immobilize biomolecules in three-dimensional (3D) networks of hydrogels. Hydrogels are a class of biomaterials that serves as tissue replicate or 3D cell culture platform depending on their composition and modifications.[90] To form functionalized hydrogels, TPA-*tris*NTA was bound onto maleimide-polyvinylalcohol strands and cross-linked with dithiol-polyethyleneglycol. First, the mask exposure and also the single-photon activation with the 405 nm laser was performed. The written patterns were visualized by immobilizing His_6-GFP or His_6-AF647. Although 1P exposure allowed precise activation of TPA-*tris*NTA in the focal x/y-plane, the hydrogel was activated up to 100 µm in the z-plane by scattered light. This was observed by the accumulation of His_6-GFP/His_6-AF647 along the light beam.

Subsequently, the 2P activation of TPA-*tris*NTA in hydrogels was investigated. To evaluate the optimal exposure parameters in 3D, the wavelength dependence of activation was examined in the range of 720 to 800 nm and visualized by binding of His_6-AF647. This revealed an optimal activation wavelength of 800 nm, which was in very good agreement with the absorbance values obtained in solution. Therefore, 800 nm was used for 2P activation of TPA-*tris*NTA. Due to technical limitations of the microscope used, wavelengths longer than 800 nm could not be used for patterning. The characteristics of 2P patterning were investigated in terms of precision in x/y-dimension as well as the full width at half maximum (FWHM) along z-axis. It was possible to selectively enrich His_6-AF647 in a region of interest (ROI) as small as 2x2 µm, whereas the fluorescence intensity was diminished compared to 3x3 µm ROIs, the ROI size for optimal activation should be ranked between 2-3 µm.

Since the activation of TPA-*tris*NTA in the hydrogel is indirectly visualized by the binding of the His-tagged biomolecule, the 2P writing process cannot be evaluated separately from the confocal recording of the fluorescence signal. By patterning ROIs with successively reduced inter-ROI distance, a resolution limit for the overall process of 1 µm in the x/y-axis was obtained. The precision of patterning in the z-plane was analyzed by imaging and reconstructing z-stacks. 2P

illumination made it possible to write patterns with an offset in the z-plane, which were sharply distinguishable from each other (5 ± 1 µm FWHM).

The reversibility of biomolecule immobilization by affinity binding represents a major advantage over systems based on covalent bond. To demonstrate that proteins bound in a pattern can be removed and exchanged to other biomolecules, His_6-GFP was competed out with imidazole and replaced by His_6-AF647. Although protein structures in TPA-*tris*NTA functionalized hydrogels are fully reversible, long-term binding of biomolecules was observed. This was shown by an analysis of a 2P patterned hydrogel, where 19% of His_6-AF647 was still immobilized after 10 days in the pattern.

Effective light patterning of biomolecules at the lowest possible laser power is particularly important for a cellular application. To achieve this, the use of rhodamine B (RB) and ATTO390 as 2P sensitizing agents was tested, which have high 2P absorption cross sections. In the presence of different ATTO390 (0, 50, 100 and 500 µM) or RB (0, 50 and 100 µM) concentrations, ROIs were activated by systematically increasing the light dose. Laser power was varied from 0.5-5.5 mW and exposure time from 6-30 s, so that a total of 120 conditions were tested. Activation of TPA-*tris*NTA was read out by binding of His_6-AF647. Without sensitizing agent, weak POI immobilization was detected from 3.1 mW and 18 s and 1.5 mW and 24 s, respectively. In contrast, the activation threshold could be lowered to 0.5 mW and 18 s by using 50 µM RB and to 1.5 mW and 6 s for 100 µM ATTO390. To determine the optimal exposure parameters for single cell applications, precision in the z-plane and immobilization density of the POI were taken into account in addition to the lowest light dose possible. Considering these aspects, 2P activation in the presence of 100 µM ATTO390 or 50 µM RB at 3.1 mW and 12 s provided the best results. A 3.8-fold and 15.6-fold enhancement of TPA-*tris*NTA activation was observed for ATTO390 and RB, respectively, compared to samples without sensitizing agents. Optimized illumination settings (1.5 mW, 1500 iterations) using RB allowed complex structures to be written in 3D with high precision. The portrait of Maria Goeppert-Mayer could be written into the hydrogel with a precision in x/y dimension of about 1 µm.

The mild activation conditions and the possibility of precise immobilization of biomolecules made TPA-*tris*NTA functionalized hydrogels suitable for cell studies. To verify biocompatibility, living HeLa cells embedded in functionalized hydrogels were incubated with Annexin-V AF647 conjugate. The apoptosis marker confirmed a high cell viability of (91± 1%) of the embedded cells. In addition, possible cytotoxicity of the sensitizing agents was checked with and without light exposure. In the 3-(4,5-dimethylthiazol-2yl)-2,5-dipehnyltetrazolium bromide (MTT) assay, no

significant toxicity was detected up to a concentration of 100 µM for none of the sensitizing agents (cell viability for ATTO390: >70%, RB: >90%). Thus, 100 µM ATTO390 and 50 µM RB were suitable for cell experiments.

Subsequently, the established photostructuring conditions were applied to living cells. For this purpose, experiments were performed with HeLa cells stably expressing His_6-tagged Y_2 receptor. First, it was important to verify whether the His_6-tag of the membrane receptor is accessible for *tris*NTA interaction when the cells are incorporated in the hydrogel. To this end, His_6-Y_2R^{mEGFP} expressing cells were incubated in the hydrogel with free *tris*NTA^{AF647} dissolved in buffer. Colocalization of GFP and AF647 signal confirmed the accessibility of the receptor to the His-tag/*tris*NTA interaction. HeLa cells without induction of the expression of His_6-Y_2R^{mEGFP} were treated with *tris*NTA^{AF647} and used as a negative control to investigate unspecific binding. These exhibited a low unspecific *tris*NTA^{AF647} binding.

Next, light-induced patterning of membrane receptors was tested at the single cell level. Since transferring *in vitro* experiments to living cells involved increased complexity, the single-photon activatable PA-*tris*NTA was first used to induce *tris*NTA/His-tag binding under UV exposure. For this purpose, HeLa cells expressing the His_6-Y_2R^{mEGFP} were embedded in PA-*tris*NTA functionalized hydrogels and rectangular ROIs covering one hemisphere of the cell were irradiated at 405 nm. The comparison of the GFP intensity profiles before and after irradiation showed significant enrichment in the exposed half of the cell, which was indicative of *tris*NTA-mediated enrichment. To verify the activation of PA-*tris*NTA in the hydrogel and to visualize any unsaturated binding sites, the small His_6-AF647 peptide was added. Accumulation of the peptide at the exposed membrane side of the cell was observed. However, the peptide did not bind in the entire activated ROI. To address this question, further experiments were performed. Since replication of the result was difficult, the influence of temperature, light dose, and possibly proteases secreted by dead cells was investigated. Even by lowering the temperature, increasing the exposure time, or using a protease inhibitor, the PA-*tris*NTA-induced receptor enrichment could not be consistently reproduced.

Since the *tris*NTA/His-tag interaction with hydrogel-embedded cells showed promising results, the system was switched to TPA-*tris*NTA functionalized hydrogels. This allowed the use of longer wavelengths and precise photoactivation in the z dimension in addition to x/y-plane. For this purpose, ROIs at the plasma membrane of HeLa cells expressing His_6-Y_2R^{mEGFP} were exposed to 800 nm in the hydrogels. Subsequently, the hydrogel was incubated with His_6-mCherry to control the activation of TPA-*tris*NTA in the hydrogel. The intensity of the GFP signal was slightly

decreased after exposure, indicating bleaching of the chromophore, hence no further conclusions could be drawn for enrichment of the receptor. However, successful activation of the TPA-*tris*NTA within the ROI was demonstrated by specific binding of His_6-mCherry. Because chromophore bleaching occurred, the next step was to perform 2P activation in the presence of the 2P sensitizing agent ATTO390 in the cell-loaded hydrogel to reduce the light dose. RB was unsuitable for this purpose, as receptor internalization was observed upon addition of RB to His_6-Y_2R^{mEGFP} expressing HeLa cells. Cells embedded in a hydrogel showed an extremely interesting behavior. The area of the ROI was occupied after irradiation, by a protrusion of the cell membrane. The shape of the protrusion corresponded exactly to the written ROI. This observation could be used to specifically manipulate the shape of cells. First, two opposing directional protrusions could be created on a single cell, and second, the cell membrane could be gradually expanded by sequential exposure. To explore, which expansions were possible, a 44 µm long ROI was irradiated on the membrane of a cell. Surprisingly, the GFP signal emanating from the membrane protein could be detected throughout the entire ROI after activation. Directed manipulation of the cell membrane was also used to trigger cell-cell contacts. For this purpose, a square ROI was exposed between two adjacent cells. Images of the z-stacks confirmed bridging of the cells.

To demonstrate that the change in cell shape was due to an interaction of the immobilized *tris*NTA and the His-tag of the Y_2 receptor, imidazole was added after deformation to release the binding. However, no change was observed. As a control, cells in hydrogels containing no TPA-*tris*NTA were exposed in the same manner in the presence of ATTO390. This also resulted in the controlled deformations of the cell membrane. The negative control showed that the effect was not *tris*NTA dependent. It is hypothesized that the 2P radiation causes deformation of the hydrogel possibly by depolymerization, creating cavities into which the spatially confined cells crawl. However, this hypothesis was outside the focus of this work.

Within this thesis, TPA-*tris*NTA was synthesized as a new two-photon activatable interaction molecule, characterized chemically and photophysically, and successfully used for light-guided immobilization of proteins and peptides. Improved functionalization strategies for glass surfaces were developed using PA-*tris*NTA/TPA-*tris*NTA for specific, reversible, and long-lasting patterning of proteins and peptides. These properties could be transferred to photostructuring of proteins into three-dimensional hydrogels. The use of sensitizing agents enabled POI-enrichment with micrometer-precise accuracy in x/y and z dimensions with very low light doses. 2P-initiated manipulation of cell shape was observed, which allowed to structure cell membranes as well as to induce cell-cell contacts.

5.1. Zusammenfassung

Die spezifische und präzise Anordnung von Proteinen und Biomolekülen in 3D ist eine wichtige Voraussetzung für die Erforschung der Zellmigration, zellulärer Signaltransduktion und der Herstellung von künstlichem Gewebe. In einer Vielzahl an Forschungsansätzen wurden Proteine auf rigiden Oberflächen wie Glas oder Gold immobilisiert, um die Protein-Protein oder Protein-Zell Interaktionen zu beobachten. Diese häufig verwendete Analyseplattformen bieten zwar Vorteile wie schnelle Waschschritte und einfache Handhabung, aber sie können aufgrund ihrer Festigkeit und Zweidimensionalität nicht die Extrazelluläre Matrix (ECM), die native Umgebung der Zellen nachbilden. Durch diese starke Abweichung von der natürlichen Umgebung ergeben sich erhebliche Veränderungen der Zellstruktur und zellulärer Prozesse wie die Polarisierung der Zelle, deren Morphologie und die Signaltransduktion. Um die Funktionalität der immobilisierten Proteine zu erhalten ist es außerdem enorm wichtig, dass die Proteine orientiert und unter milden Bedingungen im Material verankert werden.

Eine Immobiliserungsstrategie die dies ermöglicht, ist die Bioaffinität. Hierfür wird die spezifische Wechselwirkung eines Biomoleküls mit einem auf einer Oberfläche verankertem Interaktionspartner genutzt, um das Biomolekül zu immobilisieren. Eine solche Interaktion ist die NTA/His-Tag Bindung. *N*-Nitriloessigsäure (NTA) ist ein Chelatormolekül, das wenn es bivalente Metallionen wie Ni(II) gebunden hat, einen oktaedrischen Komplex mit Oligo-Histidinen eingeht. Der Oligohistidin-Tag kann aufgrund der strukturellen Ähnlichkeit aus dem Komplex durch freies Histidin oder Imidazol kompetitiert werden. Dies macht man sich bei Metallchelatorchromatographie (IMAC) zunutze. Die Bindung eines *mono*NTA/His-Tag Komplexes (K_D=10 µM) ist nicht stabil genug, um für Immobilisierungen genutzt werden zu können. Daher wurden multivalente Varianten des Chelators entwickelt, wie bsw. *tris*NTA welches eine hohe Affinität für His_6-Tags besitzt (K_D= 10 nM). Das in einer Vorarbeit entwickelte PA-*tris*NTA war das erste Licht-aktivierbare System auf Basis des *tris*NTA Chelatorkopfes.

Ziel dieser Arbeit war es ein neues Zwei-Photonen (2P) aktivierbares *tris*NTA (TPA-*tris*NTA) Interaktionsmolekül zu synthetisieren, seine photophysikalischen Eigenschaften zu analysisieren und es für die zwei-und dreidimensionale (2/3D) Strukturierung von Biomolekülen einzusetzen. Ultimativ wurde die Verwendung von TPA-*tris*NTA für die zelluläre Anwendung angestrebt, um die Organisation von Membranproteinen zu beeinflussen. Daher wurde TPA-*tris*NTA so designt um eine stabile Autoinhibition zu besitzen, aber bei Lichtaktivierung die Immobilisation von Proteinen unter physiologischen Bedingungen mit hoher Präzision in der x,y, als auch z-Dimension zu erlauben. 2P Aktivierung bringt einige Vorteile: i) der Einsatz von nah-infrarotem (NIR) Licht ist

weniger zellschädlich als ultraviolettes (UV) Licht, ii) durch die längere Wellenlänge kann die Strahlung tiefer in Gewebe eindringen, iii) die Präzision der fokalen Bestrahlung ist deutlich besser, da nur ein fokales Volumen (ca. 1 fL) angeregt wird und im Gegensatz zu UV-Licht das Streulicht zu keiner Aktivierung führt.

Als 2P spaltbare Gruppen kamen aufgrund ihrer 2P-Absorbtion und kleinen Größe mehrere Grundgerüste für TPA-*tris*NTA in Frage: 3-Nitrodibenzofuran (NDBF), 6-Bromo-7-hydroxycumarin (Bhc) und 7-Diethylaminocumarin (DEAC). Zunächst wurden geeignete Synthesewege zur Herstellung des jeweiligen Aldehyds entwickelt, da diese ein wichtiges Intermediat sowohl für den Aufbau von Aminosäurederivaten als auch für ß-Hydroxysäuren darstellten. ß-Hydroxysäuren waren wichtige Zwischenprodukte, da sich ihre Photospaltung von den aa Derivaten unterscheidet. Um die Umwandlung von Carbaldehyden in Hydroxysäuren über die Reformatsky-Reaktion zu etablieren, wurden zusätzlich kommerziell erhältliche Carbaldehyde der Nitroveratral- (NV) und Nitropiperonal-Gruppe (NP) verwendet. Hierbei stellte sich die Umsetzung von NDBF, NV, NP als herausfordernd da, wohingegen von Bhc als auch von DEAC die ß-Hydroxysäure erfolgreich synthetisiert wurden.

Ausgehend von der DEAC ß-Hydroxysäure wurde ein Fmoc geschütztes Aminosäurederivat synthetisiert. Um eine gute Spaltungseffizienz zu gewährleisten, wurde die DEAC ß-Hydroxysäure durch einen Carbamatlinker an *mono*Fmoc-Ethylendiamin geknüpft. Anschließend konnte die photospaltbare Gruppe erfolgreich per Festphasen-Peptid-Synthese (SPPS) in den Linker von TPA-*tris*NTA eingebaut werden.

Das Funktionsprinzip von TPA-*tris*NTA beruhte, ähnlich wie PA-*tris*NTA, auf der Autoinhibition des multivalenten Chelatorkopfes *tris*NTA, welcher durch einen Peptidlinker mit einer intramolekularen Oligohistidin-Sequenz verknüpft ist. In Gegenwart von Ni(II)-Ionen geht *tris*NTA mit Histidinen eine Metallionen vermittelte Komplexbindung ein, wodurch TPA-*tris*NTA selbstinaktiviert wird. Die Spaltungsstelle ist die DEAC basierte photospaltbare Aminosäure. Im Gegensatz zu PA-*tris*NTA wurde auf den Einbau von zwei photospaltaren Aminosäuren verzichtet, sondern nur eine vor dem His-Tag eingebaut, um die Lichtaktivierung des neuartigen Aminosäurederivats zu verifizieren. Um nur eine DEAC Gruppe innerhalb des His-Tags verwenden zu können, wurde ein His_5-Tag anstelle eines His_6-Tags verwendet. Aus Vorarbeiten ist bekannt, dass ein His_5-Tag als Oligohistidinsequenz ausreichend ist, um die Autoinhibition in Gegenwart von His_6-getaggten Proteinen von Interesse (POIs) aufrecht zu erhalten, aber nach Licht-getriebener Spaltung des Peptidrückgrads aus dem Komplex verdrängt werden kann.[72] Die Platzierung eines Cysteins im

Peptidlinker zwischen dem *tris*NTA und der DEAC Gruppe erlaubt eine dauerhafte Oberflächenverankerung auch nach Photospaltung des Linkers.

Nachdem die Zielverbindung erfolgreich hergestellte wurde, wurde diese auf ihre photophysikalischen Eigenschaften untersucht. Die UV/Vis-Spektren von TPA-*tris*NTA (in HBS Puffer:MeCN, 1:1) zeigten ein Absorptions-/Emissionsmaximum bei 390 nm bzw. 480 nm, weshalb für die 1P Aktivierung Lichtquellen mit 400 nm besonders geeignet sind. Daraufhin wurde die Spaltungskinetik der eingebauten DEAC Aminosäure untersucht. Die Bestrahlung der Fmoc-geschützten Aminosäure mit 405 nm für 5-900 s ergab eine Spaltungskinetik von 12 s für 50% der Verbindung. Desweitern wurde eine Fluoreszenzquantenausbeute φ_F für TPA-*tris*NTA von 15% ermittelt. Das Absorptionsmaximum für Zweiphotonenanregungen beträgt im Allgemeinen ungefähr das Doppelte der Wellenlänge für die Einphotonenbestrahlung. Um den genauen Wert experimentell zu bestimmen, wurde der Zwei-Photonen Absorptionsquerschnitt $\varphi_F\delta_2$ von 770-860 nm durch Zweiphotonen-angeregte Fluoreszenz (TPEF) Messungen bestimmt. Bei 810 nm wurden 7.7 GM und bei 800 nm 7.1 GM gemessen. Um zu belegen, dass es sich um einen 2P Prozess handelte, wurde die Zweiphotonenanregung in Abhängigkeit einer steigenden Laserleistung gemessen. Der erhaltene Wert von 1.93± 0.02 liegt nahe an der perfekten quadratischen Abhängigkeit der Anregung von DEAC von der Laser Leistung und bestätigt TPA-*tris*NTA als Zweiphotonen anregbares Molekül.

Nachfolgend wurde die Organisation von Biomolekülen auf zweidimensionalen (2D) Glasoberflächen getestet, bevor komplexere, drei-dimensionale (3D) Biomaterialien verwendet wurden. Hierfür wurden verschiedene Oberflächenfunktionalisierungsstrategien getestet. Neben 3-Glycidyloxypropyl-trimethoxysilane (GOPTS) wurden Poly-*L*-Lysin (PLL) und 3-Aminopropyl-triethoxysilan (APTES) als Funktionalisierungsmittel verwendet, welche mit PEG verknüpft wurden, um die Glasoberfläche gegen unspezifische Adsorptionen zu passivieren. Anschließend wurde PA-*tris*NTA oder TPA-*tris*NTA über eine Maleimid-Cystein Verknüpfung auf der Oberfläche immobilisiert.

Zur Aktivierung wurden die Oberflächen mit 365 nm Licht durch Quarzmasken hindurch bestrahlt oder mit einem 405 nm Laser am konfokalen Laser-Scanning-Mikroskop (CLSM) bestrahlt. Für die Proteinstrukturen wurden $His_{6\text{-}10}$-getaggtes mVenus, mCherry, MBP^{OG488}, oder GFP als Modelproteine verwendet. Außerdem wurde ein kurzes Alexa647-markiertes His_6-Peptid (His_6-AF647) eingesetzt, da es im Vergleich zu den voluminösen Proteinen deutlich kleiner ist und so höhere Immobilisierungsdichten ermöglicht. Zur Visualisierung der gebundenen Proteine und des Peptids wurde die Fluoreszenz der Proteine und der Fluorophore mittels CLSM detektiert. Bei

der Evaluierung der verschieden funktionalisierten Oberflächen wurde der Fokus insbesondere auf Reproduzierbarkeit, Spezifität und Genauigkeit der Proteinstruktur gelegt. In Bezug auf alle diese Punkte haben die GOPTS Oberflächen das schlechteste und APTES funktionalisierten Glasträger das beste Ergebnis geliefert. Mit APTES funktionalisierte Oberflächen wiesen im Vergleich zu GOPTS und PLL eine deutlich bessere Passivierung gegen unspezifische Bindung und eine homogenere Funktionalisierung auf. Auf PLL und APTES Oberflächen konnten Proteinmuster mit hohem Signal-zu-Rausch Verhältnis mit sehr guter Reproduzierbarkeit erhalten werden, wobei bei APTES Flächen auf den Einsatz von Blockierungsmitteln zur Erhöhung der Spezifität verzichtet werden konnte. Daher wurden APTES, PA-*tris*NTA funktionalisierte Oberflächen verwendet um *in-situ* Strukturierungen und Laserstärke-abhängige Proteindichten und Multiprotein/-peptide Muster zu realisieren.

Die durch die Strukturierung der Glasoberflächen gewonnenen Erkenntnisse wurden anschließend für die Immobilisierung von Biomolekülen in dreidimensionalen (3D) Netzwerken von Hydrogelen genutzt. Hydrogele sind eine Klasse von Biomaterialien, die abhängig von ihrer Zusammensetzung und Modifizierung als Gewebenachbildung oder 3D Zellkulturplattform dienen.[90] Zur Ausbildung des funktionalisierten Hydrogels wurde TPA-*tris*NTA auf Maleimid-Polyvinylalkoholstränge gebunden und mit Dithiol-polyethylenglycol quervernetzt. Zunächst wurde die auf den Glasoberflächen optimierte Maskenbelichtung und auch die Einphotonenaktivierung mit dem 405 nm Laser reproduziert. Die geschriebenen Muster wurden durch die Immobilisierung von His_6-GFP oder His_6-AF647 visualisiert. Zwar war bei der Einphotonenbelichtung eine präzise Aktivierung von TPA-*tris*NTA in der fokalen x/y-Achse möglich, jedoch war das Hydrogel bis zu 100 µm in der z-Ebene durch Streulicht ebenfalls aktiviert. Dies konnte durch die Anreicherung von His_6-GFP/His_6-AF647 entlang des Lichtstrahls beobachtet werden.

Daraufhin wurde die Zwei-Photonen Aktivierung von TPA-*tris*NTA in Hydrogelen untersucht. Zur Evaluierung der optimalen Belichtungsparameter in 3D wurde die Wellenlängenabhängigkeit der Aktivierung im Bereich 720 bis 800 nm überprüft und mit der Bindung von His_6-AF647 sichtbar gemacht. Hierbei ergab sich eine optimale Aktivierungswellenlänge von 800 nm, was in sehr guter Übereinstimmung mit den in Lösung erhaltenen Absorptionswerten war. 800 nm wurde fortan zur 2P Aktivierung von TPA-*tris*NTA genutzt. Aufgrund technischer Limitierungen des verwendeten Mikroskops konnten Wellenlängen über 800 nm nicht verwendet werden. Desweitern wurden die Charakteristika der 2P Strukturierung im Hinblick auf die Präzision in x/y-Dimension wie auch die Halbwertsbreite entlang der z-Achse (FWHM) untersucht. Es war möglich His_6-AF647 in einer Region von Interesse (ROI) von 2x2 µm gezielt anzureichern, wobei die Intensität der

Anreicherung etwas schwächer war als bei 3x3 µm großen ROIs, weswegen die ROI-Größe für eine optimale Aktivierung zwischen 2-3 µm einzuordnen ist.

Da die Aktivierung von TPA-*tris*NTA im Hydrogel indirekt durch die Bindung des His-getaggten Biomoleküls visualisiert wird, kann der 2P Schreibprozess nicht getrennt von der konfokalen Aufnahme des Fluoreszenzsignals ausgewertet werden. Durch die Strukturierung von ROIs mit sukzessiv verringerter Inter-ROI Distanz, ergab sich eine Auflösungsgrenze für den Gesamtprozess von 1 µm in der x/y-Achse. Die Präzision der Strukturierung in der z-Ebene wurde durch die Aufnahme und Rekonstruktion von z-Stapeln analysiert. Bei der 2P Belichtung kommt es zu einer minimierten Aktivierung durch Streulicht, wodurch es möglich war in der z-Ebene versetzte Muster zu schreiben die scharf voneinander abgrenzbar waren (5 ± 1 µm Halbwertsbreite).

Die Reversibilität der Biomolekülimmobilisierung durch Affinitätsbindung stellt einen großen Vorteil gegenüber anderen Systemen dar, die auf kovalenten Bindungen beruhen. Zur Demonstration, dass in einem Muster gebundene Proteine entfernt und gegen andere Biomoleküle ausgetauscht werden können, wurde His_6-GFP mit Imidazol herauskompetitiert und durch His_6-AF647 ersetzt. Obwohl Proteinstrukturen in TPA-*tris*NTA funktionalisierten Hydrogelen vollständig reversibel sind, zeigte eine Langzeituntersuchung das Biomoleküle ohne Kompetitor für mehrere Tage gebunden bleiben. Dies wurde durch die Untersuchung einer 2P Strukturierung beobachtet bei der nach 10 Tagen im Muster immer noch 19% des His_6-AF647 immobilisierten waren.

Eine effektive Lichtstrukturierung von Biomolekülen bei möglichst geringer Laserpower ist insbesondere für eine zelluläre Anwendung von großer Wichtigkeit. Um dies zu erreichen wurde der Einsatz von Rhodamin B (RB) und ATTO390 als 2P Sensibilisierungsmittel getestet, welche hohe 2P Einfangquerschnitte besitzen. In Anwesenheit verschiedener ATTO390 (0, 50, 100 and 500 µM) oder RB (0, 50 and 100 µM) Konzentrationen wurden ROIs mit systematisch ansteigender Lichtdosis aktiviert. Die Laserleistung wurde von 0.5-5.5 mW und die Belichtungsdauer von 6-30 s variiert, sodass insgesamt 120 Bedingungen untersucht wurden. Die Aktivierung von TPA-*tris*NTA wurde durch die Bindung von His_6-AF647 ausgelesen. Ohne Sensibilisierungsmittel wurde eine schwache Aktivierung von TPA-*tris*NTA mit nachfolgender Peptidimmobilisierung ab 3.1 mW und 18 s bzw. 1.5 mW und 24 s festgestellt. Die Aktivierungsschwelle konnte durch den Einsatz von 50 µM RB auf 0.5 mW und 18 s herabgesenkt werden und für 100 µM ATTO390 auf 1.5 mW und 6 s. Zur Bestimmung der besten Belichtungsparameter für Anwendungen auf Einzelzellebene, wurde neben einer möglichst

geringen Lichtdosis, die Präzision in der z-Ebene und Immobilisierungsdichte des POIs beachtet. Unter Berücksichtigung dieser Aspekte lieferte die 2P Aktivierung in Gegenwart von 100 µM ATTO390 oder 50 µM RB mit 3.1 mW und 12 s die besten Ergebnisse. Dafür wurde eine 3,8-fache und 15,6-fache Verstärkung der Aktivierung von TPA-*tris*NTA für ATTO390 bzw. RB gegenüber Proben ohne Sensibilisierungsmittel festgestellt. Durch die optimierte Belichtung (1.5 mW, 1500 iterations) unter Verwendung von RB konnten komplexe Strukturen mit hoher Präzision in 3D geschrieben werden. Das stilisierte Portrait von Maria Goeppert-Mayer konnte mit einer Präzision der Linien von ca. 1 µm in das Hydrogel geschrieben werden.

Durch die milden Aktivierungsbedingungen und die Möglichkeit der präzisen Immobilisierung von Biomolekülen eigneten sich TPA-*tris*NTA-funktionalisierte Hydrogele für Zellstudien. Um die Biokompatibilität zu überprüfen, wurden lebende HeLa Zellen in funktionalisierte Hydrogele mit Annexin-V AF647 Konjugat inkubiert. Der Apoptose-Marker bestätigte eine hohe Zellvitalität von (91± 1%) der eingeschlossenen Zellen. Außerdem wurde eine mögliche Cytotoxizität der Sensibilisierungsmittel mit und ohne Belichtung überprüft. In dem dafür durchgeführten 3-(4,5-Dimethylthiazol-2yl)-2,5-dipehnyltetrazolium Bromid (MTT) Test wurde bis zu einer Konzentration von 100 µM für keine der beiden Sensibilisierungsmittel eine signifikanten Toxizität festgestellt (Zellvitalität für ATTO390: >70%, RB: >90%). Somit war sowohl ATTO390 als auch 50 µM RB für Zellversuche geeignet.

Anschließend sollten die etablierten Photostrukturierungsbedingungen auf lebende Zellen angewendet werden. Dazu wurden Experimente mit HeLa Zellen welche His_6-Y_2R^{mEGFP} exprimierten durchgeführt. Zunächst war es wichtig zu verifizieren, ob der His_6-Tag des Membranrezeptors für eine *tris*NTA-Interaktion erreichbar ist, wenn die Zellen im Hydrogel eingebettet sind. Dazu wurden His_6-Y_2R^{mEGFP} exprimierende Zellen im Hydrogel mit freiem, in Puffer gelöstem *tris*NTA^{AF647} inkubiert. Die Kolokalisation des GFP- und des AF647-Signals bestätigte die Zugänglichkeit des Rezeptors für die His-Tag/*tris*NTA-Interaktion. Die Spezifität der Bindung wurde durch die Negativkontrolle bestätigt bei der HeLa Zellen ohne His_6-Y_2R^{mEGFP} mit *tris*NTA^{AF647} versetzt wurden. Diese zeigten nur eine sehr geringe unspezfische *tris*NTA^{AF647} Bindung.

Als nächstes wurde die Licht-induzierte Strukturierung von Membranrezeptoren auf Einzelzellebene getestet. Da die Übertragung von *in vitro* Experimenten auf *in vivo* eine erhöhte Komplexität mit sich bringt, wurde zunächst das Einphotonen aktivierbare PA-*tris*NTA genutzt, um eine *tris*NTA/His-Tag-Bindung unter UV-Belichtung auszulösen. Dazu wurden HeLa Zellen, welche den His_6-Y_2R^{mEGFP} exprimierten in PA-*tris*NTA funktionalisierte Hydrogele eingebettet und

rechteckige ROIs, die eine Zellhälfte bedeckten, mit 405 nm bestrahlt. Ein Vergleich des GFP-Intensitätsprofils vor und nach der Bestrahlung zeigte eine deutliche Anreicherung in der belichteten Zellhälfte, was für eine *tris*NTA-vermittelte Anreicherung sprach. Um die Aktivierung von PA-*tris*NTA im Hydrogel zu verifizieren und eventuell nicht abgesättigte Bindungsstellen zu visualisieren wurde mit His_6-AF647 Peptid inkubiert. Es konnte eine Anreicherung des Peptids an der belichteten Membranseite der Zelle festgestellt werden, allerdings hatte das Peptid nicht im gesamten ROI gebunden. Um zu untersuchen warum das Peptid im belichteten Hydrogel nicht gebunden hat, wurde das Experiment mehrfach wiederholt. Da die Reproduktion des Ergebnisses noch nicht konsistent war, wurde der Einfluss der Temperatur, der Lichtdosis und eventuell von toten Zellen sekretierte Proteasen untersucht. Auch durch Erniedrigung der Temperatur, Erhöhung der Belichtungszeit oder den Einsatz eines Protease-Inhibitors, konnte die PA-*tris*NTA induzierte Rezeptoranreicherung nicht reproduziert werden.

Da die *tris*NTA/His-Tag Interaktion mit im Hydrogel eingebetteten Zellen grundsätzlich funktionierte, wurde das System auf TPA-*tris*NTA funktionalisierte Hydrogele umgestellt. Dies ermöglicht die Verwendung deutlich langwelligeren Lichts und eine zusätzlich zur x/y- auch in der z-Dimension fokussierte Aktivierung von TPA-*tris*NTA. Hierfür wurden in den Hydrogelen ROIs an der Membran von HeLa Zellen die His_6-Y_2R^{mEGFP} exprimieren mit 800 nm belichtet. Anschließend wurde das Hydrogel mit His_6-mCherry inkubiert um die Aktivierung des TPA-*tris*NTA im Hydrogel zu kontrollieren. Die Intensität des GFP-Signals war nach der Belichtung innerhalb des ROIs leicht verringert, was auf Bleichen des Chromophors hindeutete und keine weiteren Rückschlüsse für eine Anreicherung des Rezeptors zuließ. Allerdings konnte die erfolgreiche Aktivierung des TPA-*tris*NTAs innerhalb des ROIs durch die spezifische Bindung von His_6-mCherry gezeigt werden. Wegen des aufgetretenen Chromophorbleichens wurde im nächsten Schritt, um die Lichtdosis verringern zu können, die 2P Aktivierung in Gegenwart des 2P Sensitivierungsmittels ATTO390 (100 µM) im Zell-beladenen Hydrogel durchgeführt. RB war hierfür ungeeignet, da bei Zugabe von RB zu His_6-Y_2R^{mEGFP} exprimierenden HeLa Zellen eine Rezeptorinternalisierung beobachtet wurde. Zellen, die in Hydrogel umgeben von ATTO390 Lösung belichtet wurden, zeigten ein interessantes Verhalten. Die Fläche des ROIs war nach der Bestrahlung, durch eine Ausstülpung der Zellmembran gefüllt. Die Form der Ausstülpung entsprach exakt dem geschriebenen ROI. Diese Beobachtung konnte genutzt werden um die Form von Zellen gezielt zu manipulieren. Zum einen konnten zwei entgegengesetzte gerichtete Ausstülpungen an einer Zelle erzeugt werden, zum anderen konnte die Zellmembran durch sequenzielle Belichtung schrittweise erweitert werden. Um zu erkunden welche Ausdehnungen möglich waren, wurde ein 44 µm langes, von der Zellmembran ausgehendes ROI bestrahlt.

Erstaunlicherweise konnte nach der Aktivierung auch in diesem Fall im gesamten ROI das GFP Signal des Membranproteins detektiert werden. Die gerichtete Manipulation der Zellmembran wurde außerdem verwendet, um Zell-Zell-Kontakte zu auszulösen. Dazu wurde ein quadratisches ROI zwischen zwei benachbarten Zellen belichtet. Die Aufnahmen der z-Stapel bestätigten eine Verbrückung der Zellen.

Zum Nachweis dass die Veränderung der Zellformen auf einer Interaktion des immobilisierten *tris*NTAs und dem His-Tag des Y_2R^{mEGFP} Rezeptors beruhten, wurde nach erfolgter Deformierung Imidazol hinzugegeben, um die Bindung zu lösen. Allerdings konnte keine Veränderung bei der Ausstülpung beobachtet werden. Als Kontrolle wurden Zellen in Gegenwart von 100 µM ATTO390 in Hydrogele welche kein TPA-*tris*NTA enthielten auf die gleiche Weise belichtet. Hierbei kam es ebenfalls zu den zuvor beschriebenen gezielt hervorgerufenen Verformungen der Zellmembran. Die Negativkontrolle zeigte, dass der Effekt nicht *tris*NTA abhängig ist. Es wurde vermutet, dass die 2P Strahlung eine Deformierung des Hydrogels evtl. durch Depolymerisation verursacht, wodurch Hohlräume entstehen, in die die räumlich beengten Zellen hineinkriechen. Um diese These zu überprüfen, wären experimentelle Untersuchungen notwendig, die außerhalb des Fokus dieser Arbeit lagen.

Innerhalb der vorliegenden Arbeit wurde TPA-*tris*NTA als neues Zwei-Photonen aktivierbares Interaktionsmolekül synthetisiert, chemisch und photophysikalisch charakterisiert und erfolgreich für die Immobilisierung von Proteinen und Peptiden eingesetzt. Es wurden verbesserte Funktionalisierungsstrategien für Glasoberflächen entwickelt, die durch PA-*tris*NTA/TPA-*tris*NTA eine spezifische, reversible und langanhaltende Strukturierung von Proteinen und Peptiden ermöglichen. Diese Eigenschaften konnten auf die Photostrukturierung von Proteinen in dreidimensionale Hydrogele übertragen werden. Durch den Einsatz von Sensibilisierungsmitteln war eine POI-Anreicherung mit Mikrometer-präziser Genauigkeit in x/y und z-Dimension mit geringer Lichtdosis möglich. Es wurde eine durch 2P Belichtung initiierte Manipulation der Zellform beobachtet, die sowohl die Strukturierung von Zellmembranen ermöglicht als auch Zell-Zell-Kontakte.

6. Appendix

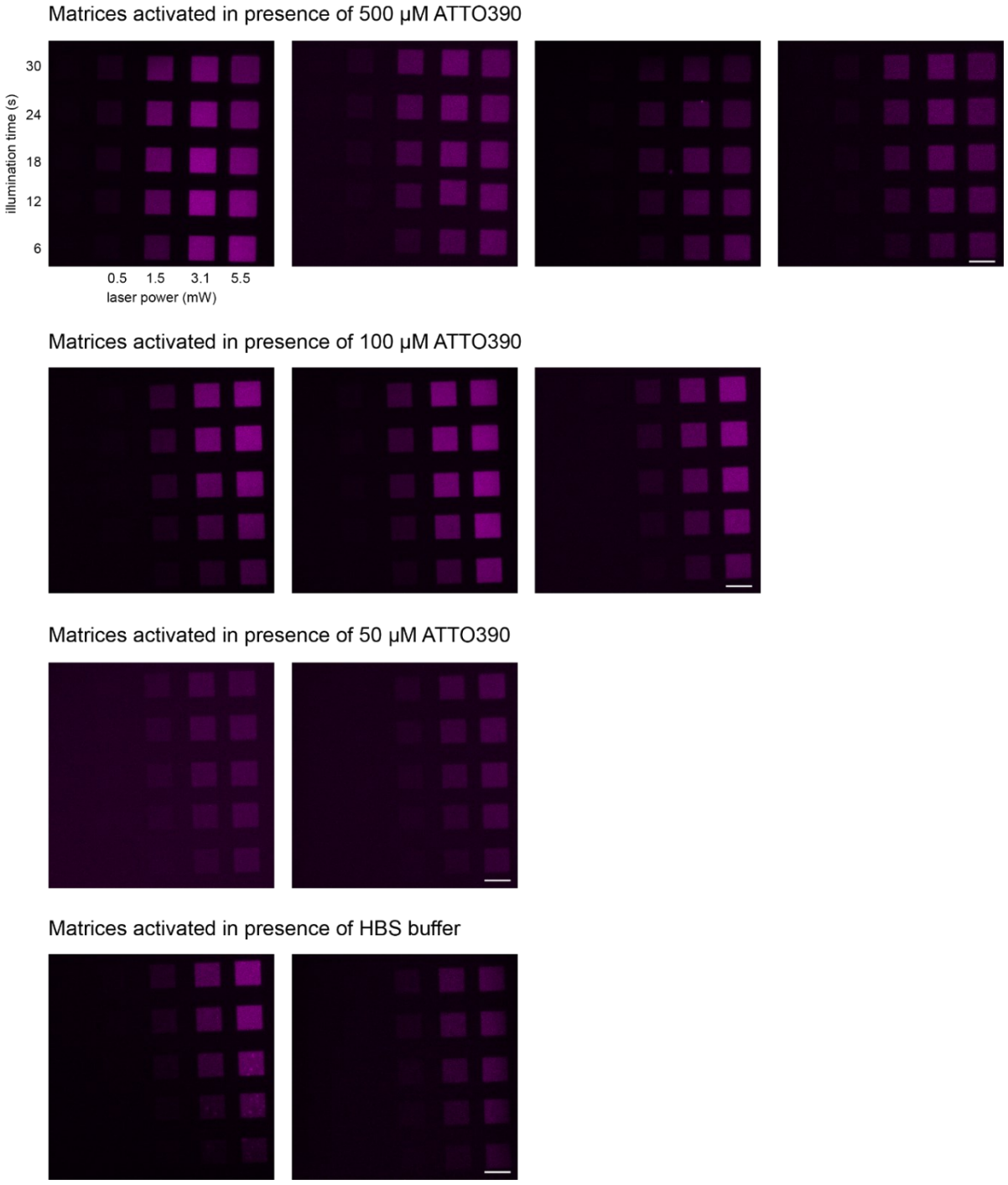

Figure A1: ATTO390-sensitized two-photon laser lithography in photo-instructive matrices. TPA-*tris*NTA functionalized hydrogels were photo-activated at 800 nm in the presence of 0, 50, 100 or 500 µM ATTO390 with varying laser power (0.5, 1.5, 3.1 or 5.5 mW) and illumination time (6-30 s). With increased laser power or illumination time, an enhanced tethering of His_6-AF647 was observed, implicating an improved photo-activation of TPA-*tris*NTA. Overall, the presence of 100 µM ATTO390 induced an intensified photo-scission and consequently enriched POI binding. Images were obtained by confocal laser scanning microscopy and the shown images were not background-corrected. Scale bar, 15 µm.

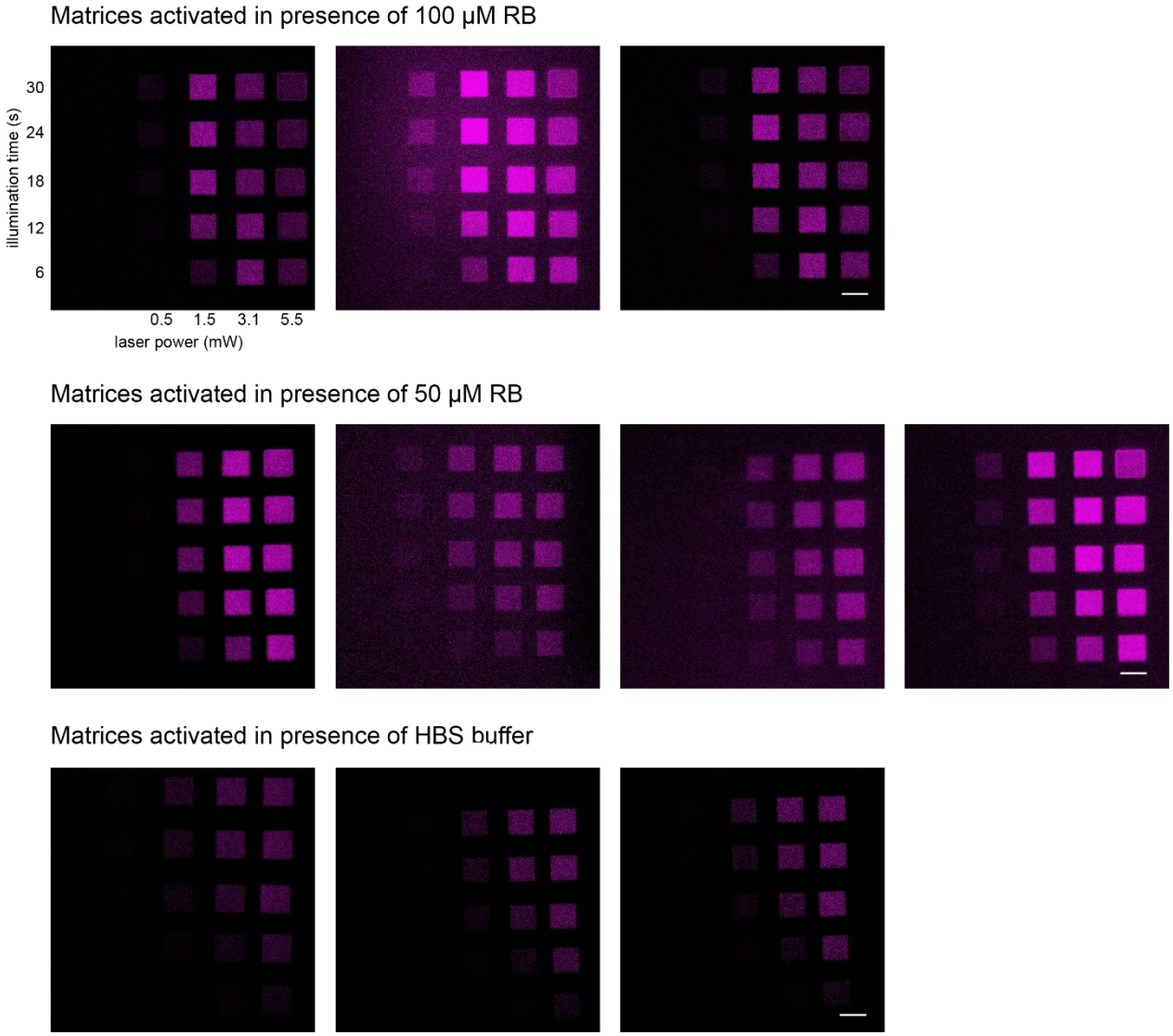

Figure A2: Rhodamine B sensitized two-photon laser lithography in photo-instructive matrices. Two-photon excitation of TPA-*tris*NTA functionalized hydrogels was performed at 800 nm in the presence of 0, 50 or 100 µM rhodamine B and increasing both laser power (0.5, 1.5, 3.1 or 5.5 mW) and illumination time (6-30 s). An enhanced binding of His_6-AF647 in response to elevated laser power and illumination time indicates an improved photo-activation of TPA-*tris*NTA. At 100 µM rhodamine B, destructive photo-artifacts induced by plasma-mediated ablation occurred more frequently (top row). A halo-effect in the focal plane was already observed with 50 µM rhodamine B plus increased laser power and extended illumination time (middle row, rightmost top). Collectively, the presence of 50 µM rhodamine B induced an intensified photo-scission and thus enriched POI binding. CLSM was employed to visualize the gels and images were not background corrected. Scale bar, 15 µm.

7. References

[1] M. Chalfie, Y. Tu, G. Euskirchen, W. W. Ward, D. C. Prasher, *Science* **1994**, *263*, 802.

[2] G.-J. Kremers, S. G. Gilbert, P. J. Cranfill, M. W. Davidson, D. W. Piston, *J Cell Sci* **2011**, *124*, 157.

[3] R. Y. Tsien, *Annu Rev Biochem* **1998**, *67*, 509.

[4] D. M. Chudakov, M. V. Matz, S. Lukyanov, K. A. Lukyanov, *Physiol Rev.* **2010**, *90*, 1103.

[5] L. Wang, P. G. Schultz, *Chem Biol.* **2001**, *8*, 883.

[6] L. Wang, A. Brock, B. Herberich, P. G. Schultz, *Science* **2001**, *292*, 498.

[7] C. C. Liu, P. G. Schultz, *Annu Rev Biochem* **2010**, *79*, 413.

[8] J. W. Chin, *Nature* **2017**, *550*, 53.

[9] B. J. Des Soye, V. R. Gerbasi, P. M. Thomas, N. L. Kelleher, M. C. Jewett, *Cell Chem Biol.* **2019**, *26*, 1743-1754.e9.

[10] E. Seki, T. Yanagisawa, M. Kuratani, K. Sakamoto, S. Yokoyama, *ACS Synth Biol.* **2020**, *9*, 718.

[11] G. T. Debelouchina, T. W. Muir, *Q Rev Biophys.* **2017**, *50*, e7.

[12] J. W. Chin, *Annu Rev Biochem.* **2014**, *83*, 379.

[13] W. Brown, J. Liu, A. Deiters, *ACS Chem Biol.* **2018**, *13*, 2375.

[14] E. Michel, F. H.-T. Allain, *Methods Enzymol.* **2015**, *565*, 389.

[15] N. Broguiere, I. Lüchtefeld, L. Trachsel, D. Mazunin, R. Rizzo, J. W. Bode, M. P. Lutolf, M. Zenobi-Wong, *Adv Mater.* **2020**, *32*, e1908299.

[16] J. A. Shadish, G. M. Benuska, C. A. DeForest, *Nat Mater.* **2019**, *18*, 1005.

[17] C. P. Guimaraes, M. D. Witte, C. S. Theile, G. Bozkurt, L. Kundrat, A. E. M. Blom, H. L. Ploegh, *Nat Protoc* **2013**, *8*, 1787.

[18] X. Dai, A. Böker, U. Glebe, *RSC Adv.* **2019**, *9*, 4700.

[19] Y. Yamamura, H. Hirakawa, S. Yamaguchi, T. Nagamune, *Chem Commun.* **2011**, *47*, 4742.

[20] L. Chen, J. Cohen, X. Song, A. Zhao, Z. Ye, C. J. Feulner, P. Doonan, W. Somers, L. Lin, P. R. Chen, *Sci Rep* **2016**, *6*, 31899.

[21] K. Piotukh, B. Geltinger, N. Heinrich, F. Gerth, M. Beyermann, C. Freund, D. Schwarzer, *JACS* **2011**, *133*, 17536.

[22] K. D. Nikghalb, N. M. Horvath, J. L. Prelesnik, O. G. B. Banks, P. A. Filipov, R. D. Row, T. J. Roark, J. M. Antos, *ChemBioChem* **2018**, *19*, 185.

[23] A. Keppler, S. Gendreizig, T. Gronemeyer, H. Pick, H. Vogel, K. Johnsson, *Nat Biotechnol* **2003**, *21*, 86.

[24] A. Keppler, H. Pick, C. Arrivoli, H. Vogel, K. Johnsson, *PNAS* **2004**, *101*, 9955.

[25] A. Juillerat, C. Heinis, I. Sielaff, J. Barnikow, H. Jaccard, B. Kunz, A. Terskikh, K. Johnsson, *ChemBioChem* **2005**, *6*, 1263.

[26] M. Xu-Welliver, J. Leitão, S. Kanugula, W. J. Meehan, A. E. Pegg, *Biochem Pharmacol.* **1999**, *58*, 1279.

[27] X. Sun, A. Zhang, B. Baker, L. Sun, A. Howard, J. Buswell, D. Maurel, A. Masharina, K. Johnsson, C. J. Noren et al., *ChemBioChem* **2011**, *12*, 2217.

[28] S. Banala, D. Maurel, S. Manley, K. Johnsson, *ACS Chem Biol.* **2012**, *7*, 289.

[29] M. Kamiya, K. Johnsson, *Anal Chem.* **2010**, *82*, 6472.

[30] A. Gautier, A. Juillerat, C. Heinis, I. R. Corrêa, M. Kindermann, F. Beaufils, K. Johnsson, *Chem Biol.* **2008**, *15*, 128.

[31] F. Stagge, G. Y. Mitronova, V. N. Belov, C. A. Wurm, S. Jakobs, *PLOS ONE* **2013**, *8*, e78745.

[32] G. V. Los, L. P. Encell, M. G. McDougall, D. D. Hartzell, N. Karassina, C. Zimprich, M. G. Wood, R. Learish, R. F. Ohana, M. Urh et al., *ACS Chem Biol.* **2008**, *3*, 373.

[33] G. V. Los, K. Wood, *Methods Mol Biol.* **2007**, *356*, 195.

[34] Y. Zhang, M.-K. So, A. M. Loening, H. Yao, S. S. Gambhir, J. Rao, *Angew. Chem. Int. Ed.* **2006**, *45*, 4936.

[35] E. M. Sletten, C. R. Bertozzi, *Angew. Chem. Int. Ed.* **2009**, *48*, 6974.

[36] C. D. Spicer, B. G. Davis, *Nat Commun* **2014**, *5*, 4740.

[37] F. C. Neidhardt, J. L. Ingraham, M. Schaechter, *Physiology of the bacterial cell*. *A molecular approach / Frederick C. Neidhardt, John L. Ingraham, Moselio Schaechter*, Sinauer Associates, Sunderland, Mass., U.S.A., **1990**.

[38] S. Kalkhof, A. Sinz, *Anal Bioanal Chem.* **2008**, *392*, 305.

[39] T. Nakamura, Y. Kawai, N. Kitamoto, T. Osawa, Y. Kato, *Chem Res Toxicol.* **2009**, *22*, 536.

[40] G. T. Hermanson, *Bioconjugate techniques*, Elsevier Academic Press, Amsterdam, Boston, **2008**.

[41] J. I. MacDonald, H. K. Munch, T. Moore, M. B. Francis, *Nat Chem Biol* **2015**, *11*, 326.

[42] J. M. Chalker, G. J. L. Bernardes, Y. A. Lin, B. G. Davis, *Chem Asian J.* **2009**, *4*, 630.

[43] B. A. Griffin, S. R. Adams, R. Y. Tsien, *Science* **1998**, *281*, 269.

[44] S. R. Adams, R. E. Campbell, L. A. Gross, B. R. Martin, G. K. Walkup, Y. Yao, J. Llopis, R. Y. Tsien, *JACS* **2002**, *124*, 6063.

[45] S. R. Adams, R. Y. Tsien, *Nat Protoc* **2008**, *3*, 1527.

[46] B. R. Martin, B. N. G. Giepmans, S. R. Adams, R. Y. Tsien, *Nat Biotechnol* **2005**, *23*, 1308.

[47] G. Gaietta, T. J. Deerinck, S. R. Adams, J. Bouwer, O. Tour, D. W. Laird, G. E. Sosinsky, R. Y. Tsien, M. H. Ellisman, *Science* **2002**, *296*, 503.

[48] C. Hoffmann, G. Gaietta, M. Bünemann, S. R. Adams, S. Oberdorff-Maass, B. Behr, J.-P. Vilardaga, R. Y. Tsien, M. H. Ellisman, M. J. Lohse, *Nat Methods* **2005**, *2*, 171.

[49] O. Tour, R. M. Meijer, D. A. Zacharias, S. R. Adams, R. Y. Tsien, *Nat Biotechnol* **2003**, *21*, 1505.

[50] E. Hochuli, H. Döbeli, A. Schacher, *J Chromatogr.* **1987**, *411*, 177.

[51] J. Porath, *Protein Expr Purif* **1992**, *3*, 263.

[52] A. N. Kapanidis, Y. W. Ebright, R. H. Ebright, *JACS* **2001**, *123*, 12123.

[53] M.-K. Yu, S.-H. Lee, S.-H. Chang, S.-Y. Jon, *Bull. Korean Chem. Soc.* **2010**, *31*, 1474.

[54] P. D. Gershon, S. Khilko, *J Immunol Methods.* **1995**, *183*, 65.

[55] L. Nieba, S. E. Nieba-Axmann, A. Persson, M. Hämäläinen, F. Edebratt, A. Hansson, J. Lidholm, K. Magnusson, A. F. Karlsson, A. Plückthun, *Anal Biochem.* **1997**, *252*, 217.

[56] George B. Sigal, Cynthia Bamdad, Alcide Barberis, Jack Strominger, and George M. Whitesides, *Anal Chem.* **1996**, *3*, 490.

[57] E. L. Schmid, T. A. Keller, Z. Dienes, H. Vogel, *Anal Chem.* **1997**, *69*, 1979.

[58] L. Schmitt, M. Ludwig, H. E. Gaub, R. Tampé, *Biophys J.* **2000**, *78*, 3275.

[59] G. D. Meredith, H. Y. Wu, N. L. Allbritton, *Bioconjug Chem.* **2004**, *15*, 969.

[60] B. Krishnan, A. Szymanska, L. M. Gierasch, *Chem Biol Drug Des.* **2007**, *69*, 31.

[61] S. Lata, A. Reichel, R. Brock, R. Tampé, J. Piehler, *JACS* **2005**, *127*, 10205.

[62] S. Lata, J. Piehler, *Anal Chem.* **2005**, *77*, 1096.

[63] S. Lata, M. Gavutis, R. Tampé, J. Piehler, *JACS* **2006**, *128*, 2365.

[64] A. Tinazli, J. Tang, R. Valiokas, S. Picuric, S. Lata, J. Piehler, B. Liedberg, R. Tampé, *Chemistry* **2005**, *11*, 5249.

[65] V. Platt, Z. Huang, L. Cao, M. Tiffany, K. Riviere, F. C. Szoka, *Bioconjug Chem.* **2010**, *21*, 892.

[66] T. Rakickas, M. Gavutis, A. Reichel, J. Piehler, B. Liedberg, R. Valiokas, *Nano Letters* **2008**, *8*, 3369.

[67] C. Grunwald, K. Schulze, G. Giannone, L. Cognet, B. Lounis, D. Choquet, R. Tampé, *JACS* **2011**, *133*, 8090.

[68] C. You, S. Wilmes, O. Beutel, S. Löchte, Y. Podoplelowa, F. Roder, C. Richter, T. Seine, D. Schaible, G. Uzé et al., *Angew. Chem. Int. Ed.* **2010**, *49*, 4108.

[69] V. Roullier, S. Clarke, C. You, F. Pinaud, G. G. Gouzer, D. Schaible, V. Marchi-Artzner, J. Piehler, M. Dahan, *Nano Letters* **2009**, *9*, 1228.

[70] C. Baldauf, K. Schulze, P. Lueders, E. Bordignon, R. Tampé, *Chemistry* **2013**, *19*, 13714.
[71] A. Reichel, D. Schaible, N. Al Furoukh, M. Cohen, G. Schreiber, J. Piehler, *Anal Chem.* **2007**, *79*, 8590.
[72] C. Grunwald, K. Schulze, A. Reichel, V. U. Weiss, D. Blaas, J. Piehler, K.-H. Wiesmüller, R. Tampé, *PNAS* **2010**, *107*, 6146.
[73] N. Labòria, R. Wieneke, R. Tampé, *Angew. Chem. Int. Ed.* **2013**, *52*, 848.
[74] A. Kollmannsperger, A. Sharei, A. Raulf, M. Heilemann, R. Langer, K. F. Jensen, R. Wieneke, R. Tampé, *Nat Commun* **2016**, *7*, 10372.
[75] A. S. Blawas, W. M. Reichert, *Biomaterials* **1998**, *19*, 595.
[76] S. Fruncillo, X. Su, H. Liu, L. S. Wong, *ACS Sensors* **2021**, *6*, 2002.
[77] S. Piletsky, E. Piletska, A. Bossi, N. Turner, A. Turner, *Biotechnol. Bioeng.* **2003**, *82*, 86.
[78] M. Fuentes, B. C. C. Pessela, J. V. Maquiese, C. Ortiz, R. L. Segura, J. M. Palomo, O. Abian, R. Torres, C. Mateo, R. Fernández-Lafuente et al., *Biotechnol. Prog.* **2004**, *20*, 1134.
[79] F. Rusmini, Z. Zhong, J. Feijen, *Biomacromolecules* **2007**, *8*, 1775.
[80] G. S. Makowski (Ed.) *Advances in Clinical Chemistry*, Elsevier, **2015**.
[81] B. M. Lowe, K. Sun, I. Zeimpekis, C.-K. Skylaris, N. G. Green, *Analyst* **2017**, *142*, 4173.
[82] D. Gerhold, T. Rushmore, C. Caskey, *Trends Biochem Sci.* **1999**, *24*, 168.
[83] M. Bednár, *Med Sci Monit* **2000**, *6*, 796.
[84] J. K. West, R. Latour, L. L. Hench, *J. Biomed. Mater. Res.* **1997**, *37*, 585.
[85] J. B. Delehanty, K. M. Shaffer, B. Lin, *Biosens Bioelectron.* **2004**, *20*, 773.
[86] C. am Hong, H. Y. Son, Y. S. Nam, *Sci Rep* **2018**, *8*, 7738.
[87] S. Mao, Q. Zhang, H. Li, Q. Huang, M. Khan, K. Uchiyama, J.-M. Lin, *Anal Chem.* **2018**, *90*, 9637.
[88] R. A. Quirk, W. C. Chan, M. C. Davies, S. J. Tendler, K. M. Shakesheff, *Biomaterials* **2001**, *22*, 865.
[89] R. Marie, J. P. Beech, J. Vörös, J. O. Tegenfeldt, F. Höök, *Langmuir* **2006**, *22*, 10103.
[90] E. R. Ruskowitz, C. A. DeForest, *Nat Rev Mater* **2018**, *3*.
[91] L. Klouda, A. G. Mikos, *Eur J Pharm Biopharm.* **2008**, *68*, 34.
[92] M. Rizwan, R. Yahya, A. Hassan, M. Yar, A. D. Azzahari, V. Selvanathan, F. Sonsudin, C. N. Abouloula, *Polymers* **2017**, *9*, 137.
[93] J. C. Athas, C. P. Nguyen, B. C. Zarket, A. Gargava, Z. Nie, S. R. Raghavan, *ACS Applied Materials & Interfaces* **2016**, *8*, 19066.
[94] X. Qin, W. Xie, S. Tian, J. Cai, H. Yuan, Z. Yu, G. L. Butterfoss, A. C. Khuong, R. A. Gross, *Chem. Commun.* **2013**, *49*, 4839.

[95] I. Tomatsu, K. Peng, A. Kros, *Adv Drug Deliv Rev.* **2011**, *63*, 1257.
[96] L. Li, J. M. Scheiger, P. A. Levkin, *Adv Mater.* **2019**, *31*, e1807333.
[97] S. Murdan, *J Control Release* **2003**, *92*, 1.
[98] Q. Shi, H. Liu, D. Tang, Y. Li, X. Li, F. Xu, *NPG Asia Mater* **2019**, *11*, 1.
[99] B. P. Nowak, M. Niehues, B. J. Ravoo, *Soft Matter* **2021**, *17*, 2857.
[100] P. Ilg, *Soft Matter* **2013**, *9*, 3465.
[101] E. Lih, J. S. Lee, K. M. Park, K. D. Park, *Acta Biomater.* **2012**, *8*, 3261.
[102] A. S. Hoffman, *Adc. Drug Deliv. Rev.* **2012**, *64*, 18.
[103] C. A. DeForest, K. S. Anseth, *Angew. Chem. Int. Ed.* **2012**, *51*, 1816.
[104] S. K. Seidlits, C. E. Schmidt, J. B. Shear, *Adv. Funct. Mater.* **2009**, *19*, 3543.
[105] W. Ji, Q. Wu, X. Han, W. Zhang, W. Wei, L. Chen, L. Li, W. Huang, *Sci China Life Sci.* **2020**, *63*, 1813.
[106] S. Kampaengsri, B. Wanno, T. Tuntulani, B. Pulpoka, C. Kaewtong, *Environ. Technol.* **2020**, *41*, 3016.
[107] J. Li, X. Yu, A. Herberg, D. Kuckling, *Macromol. Rapid Commun.* **2019**, *40*, e1800674.
[108] K. Shi, Z. Liu, Y.-Y. Wei, W. Wang, X.-J. Ju, R. Xie, L.-Y. Chu, *ACS Appl. Mater. Interfaces* **2015**, *7*, 27289.
[109] Jennifer Patterson, Mikaël M. Martino, Jeffrey A. Hubbell, *Materials Today* **2010**, 14.
[110] B. G. Munoz-Robles, I. Kopyeva, C. A. DeForest, *Adv. Mater. Interfaces* **2020**, *7*, 2001198.
[111] M. Lee, R. Rizzo, F. Surman, M. Zenobi-Wong, *Chemical Reviews* **2020**, *120*, 10950.
[112] H. K. Kleinman, D. Philp, M. P. Hoffman, *Curr Opin Biotechnol.* **2003**, *14*, 526.
[113] M. Vázquez-González, I. Willner, *Angew. Chem. Int. Ed.* **2020**, *59*, 15342.
[114] C. Brieke, F. Rohrbach, A. Gottschalk, G. Mayer, A. Heckel, *Angew. Chem. Int. Ed.* **2012**, *51*, 8446.
[115] R. Weinstain, T. Slanina, D. Kand, P. Klán, *Chem Rev.* **2020**, *120*, 13135-1372.
[116] J. H. Kaplan, B. Forbush, J. F. Hoffman, *Biochemistry* **1978**, *17*, 1929.
[117] J. A. Barltrop, P. Schofield, *Tetrahedron Letters* **1962**, *3*, 697.
[118] H.-M. Lee, W. Xu, D. S. Lawrence, *JACS* **2011**, *133*, 2331.
[119] X. Tang, J. Swaminathan, A. M. Gewirtz, I. J. Dmochowski, *Nucleic Acids Res* **2008**, *36*, 559.
[120] M. A. Priestman, L. Sun, D. S. Lawrence, *ACS chemical biology* **2011**, *6*, 377.
[121] S. Kantevari, M. Matsuzaki, Y. Kanemoto, H. Kasai, G. C. R. Ellis-Davies, *Nat Methods* **2010**, *7*, 123.
[122] S. Banala, D. Maurel, S. Manley, K. Johnsson, *ACS Chem Biol.* **2012**, *7*, 289.
[123] A. P. Gorka, R. R. Nani, J. Zhu, S. Mackem, M. J. Schnermann, *JACS* **2014**, *136*, 14153.

[124] B. R. Sarode, K. Kover, P. Y. Tong, C. Zhang, S. H. Friedman, *Molecular Pharmaceutics* **2016**, *13*, 3835.
[125] P. Klán, T. Šolomek, C. G. Bochet, A. Blanc, R. Givens, M. Rubina, V. Popik, A. Kostikov, J. Wirz, *Chem. Rev.* **2013**, *113*, 119.
[126] R. S. Givens, B. Matuszewski, *JACS* **1984**, *106*, 6860.
[127] Abraham. Patchornik/B. Amit/R. B. Woodward, *JACS* **1970**, *92*, 6333.
[128] J. E. T. Corrie, A. Barth, V. R. N. Munasinghe, D. R. Trentham, M. C. Hutter, *JACS* **2003**, *125*, 8546.
[129] I. R. Dunkin, J. Gębicki, M. Kiszka, D. Sanín-Leira, *J. Chem. Soc., Perkin Trans. 2* **2001**, 1414.
[130] A. K. Singh, P. K. Khade, *Tetrahedron* **2005**, *61*, 10007.
[131] A. Momotake, N. Lindegger, E. Niggli, R. J. Barsotti, G. C. R. Ellis-Davies, *Nat Methods* **2006**, *3*, 35.
[132] A. Hasan, K.-P. Stengele, H. Giegrich, P. Cornwell, K. R. Isham, R. A. Sachleben, W. Pfleiderer, R. S. Foote, *Tetrahedron* **1997**, *53*, 4247.
[133] K. Takaoka, Y. Tatsu, N. Yumoto, T. Nakajima, K. Shimamoto, *Bioorg Med Chem Lett.* **2003**, *13*, 965.
[134] P. Berroy, M. L. Viriot, M. C. Carre, *Sens Actuators B Chem.* **2001**, *74*, 186.
[135] B. Schade, V. Hagen, R. Schmidt, R. Herbrich, E. Krause, T. Eckardt, J. Bendig, *J. Org. Chem.* **1999**, *64*, 9109.
[136] V. Hagen, J. Bendig, S. Frings, T. Eckardt, S. Helm, D. Reuter, U. B. Kaupp, *Angew. Chem. Int. Ed.* **2001**, *40*, 1045.
[137] T. H. MAIMAN, *Nature* **1960**, *187*, 493.
[138] W. Kaiser and C. G. B. Garrett, *Phys. Rev. Lett.* **1961**, *7*, 229.
[139] W. Denk, J. H. Strickler, W. W. Webb, *Science* **1990**, *248*, 73.
[140] F. Helmchen, W. Denk, *Nat Methods* **2005**, *2*, 932.
[141] W. R. Zipfel, R. M. Williams, W. W. Webb, *Nat Biotechnol* **2003**, *21*, 1369.
[142] C. N. LaFratta, J. T. Fourkas, T. Baldacchini, R. A. Farrer, *Angew. Chem. Int. Ed.* **2007**, *46*, 6238.
[143] W. G. Fisher, W. P. Partridge, C. Dees, E. A. Wachter, *Photochem Photobiol.* **1997**, *66*, 141.
[144] O. Hernandez, E. Papagiakoumou, D. Tanese, K. Fidelin, C. Wyart, V. Emiliani, *Nat Commun* **2016**, *7*, 11928.
[145] S. Kawata, Y. Kawata, *Chem Rev.* **2000**, *100*, 1777.
[146] D. A. Parthenopoulos, P. M. Rentzepis, *Science* **1989**, *245*, 843.

[147] E. B. Brown, J. B. Shear, S. R. Adams, R. Y. Tsien, W. W. Webb, *Biophysical Journal* **1999**, *76*, 489.

[148] G. Bort, T. Gallavardin, D. Ogden, P. I. Dalko, *Angew. Chem. Int. Ed.* **2013**, *52*, 4526.

[149] D. Kim, H. G. Ryu, K. H. Ahn, *Org. Biomol. Chem.* **2014**, *12*, 4550.

[150] F. Terenziani, C. Katan, E. Badaeva, S. Tretiak, M. Blanchard-Desce, *Adv. Mater.* **2008**, *20*, 4641.

[151] M. Pawlicki, H. A. Collins, R. G. Denning, H. L. Anderson, *Angew. Chem. Int. Ed.* **2009**, *48*, 3244.

[152] P. Klán, J. Wirz, *Photochemistry of organic compounds*. *From concepts to practice / Petr Klán, Jakob Wirz*, Wiley, Oxford, **2009**.

[153] M. Bixon, J. Jortner, J. Cortes, H. Heitele, M. E. Michel-Beyerle, *J. Phys. Chem.* **1994**, *98*, 7289.

[154] G. Papageorgiou, J. E. Corrie, *Tetrahedron* **2000**, *56*, 8197.

[155] I. Aujard, C. Benbrahim, M. Gouget, O. Ruel, J.-B. Baudin, P. Neveu, L. Jullien, *Chemistry* **2006**, *12*, 6865.

[156] J. P. Olson, H.-B. Kwon, K. T. Takasaki, C. Q. Chiu, M. J. Higley, B. L. Sabatini, G. C. R. Ellis-Davies, *JACS* **2013**, *135*, 5954.

[157] L. Fournier, I. Aujard, T. Le Saux, S. Maurin, S. Beaupierre, J.-B. Baudin, L. Jullien, *Chemistry* **2013**, *19*, 17494.

[158] Y. Zhao, Q. Zheng, K. Dakin, K. Xu, M. L. Martinez, W.-H. Li, *JACS* **2004**, *126*, 4653.

[159] G. Papageorgiou, D. Ogden, J. E. T. Corrie, *Photochem Photobiol Sci* **2008**, *7*, 423.

[160] D. Wöll, S. Walbert, K.-P. Stengele, T. J. Albert, T. Richmond, J. Norton, M. Singer, R. D. Green, W. Pfleiderer, U. E. Steiner, *HCA* **2004**, *87*, 28.

[161] E. J. Cueto Díaz, S. Picard, V. Chevasson, J. Daniel, V. Hugues, O. Mongin, E. Genin, M. Blanchard-Desce, *Organic Letters* **2015**, *17*, 102.

[162] P. Seyfried, L. Eiden, N. Grebenovsky, G. Mayer, A. Heckel, *Angew. Chem. Int. Ed.* **2017**, *56*, 359.

[163] F. Friedrich, K. Klehs, M. A. H. Fichte, S. Junek, M. Heilemann, A. Heckel, *Chem. Commun.* **2015**, *51*, 15382.

[164] V. Hagen, F. Kilic, J. Schaal, B. Dekowski, R. Schmidt, N. Kotzur, *J. Org. Chem.* **2010**, *75*, 2790.

[165] K. Ito, J. MARUYAMA, *Chem. Pharm. Bull.* **1983**, *31*, 3014.

[166] G. Liu, D. A. Cogan, T. D. Owens, T. P. Tang, J. A. Ellman, *J. Org. Chem.* **1999**, *64*, 1278.

[167] V. Hagen, J. Bendig, S. Frings, T. Eckardt, S. Helm, D. Reuter, U. B. Kaupp, *Angew. Chem. Int. Ed.* **2001**, *40*, 1045.

[168] C. Xu, W. W. Webb, *J. Opt. Soc. Am. B, JOSAB* **1996**, *13*, 481.
[169] J. Schindelin, I. Arganda-Carreras, E. Frise, V. Kaynig, M. Longair, T. Pietzsch, S. Preibisch, C. Rueden, S. Saalfeld, B. Schmid et al., *Nat Methods* **2012**, *9*, 676.
[170] M. F. Sánchez, S. Els-Heindl, A. G. Beck-Sickinger, R. Wieneke, R. Tampé, *Science* **2021**, *26*, 6536.
[171] C. C. Uphoff, H. G. Drexler, *Current Protocols in Molecular Biology* **2014**, *106*, 28.4.1-14.
[172] J. Zhao, T. D. Gover, S. Muralidharan, D. A. Auston, D. Weinreich, J. P. Y. Kao, *Biochemistry* **2006**, *45*, 4915.
[173] P. Neveu, I. Aujard, C. Benbrahim, T. Le Saux, J.-F. Allemand, S. Vriz, D. Bensimon, L. Jullien, *Angew. Chem. Int. Ed.* **2008**, *47*, 3744.
[174] T. Furuta, S. S. Wang, J. L. Dantzker, T. M. Dore, W. J. Bybee, E. M. Callaway, W. Denk, R. Y. Tsien, *PNAS* **1999**, *96*, 1193.
[175] W. Lin, D. S. Lawrence, *J. Org. Chem.* **2002**, *67*, 2723.
[176] K. Kitamura, N. Ieda, K. Hishikawa, T. Suzuki, N. Miyata, K. Fukuhara, H. Nakagawa, *Bioorg Med Chem Lett.* **2014**, *24*, 5660.
[177] T. Weinrich, M. Gränz, C. Grünewald, T. F. Prisner, M. W. Göbel, *Eur. J. Org. Chem.* **2017**, *2017*, 491.
[178] K. Brinner, B. Doughan, D. Poon, *Synlett* **2009**, *2009*, 991.
[179] E. Nakamura, S. Aoki, K. Sekiya, H. Oshino, I. Kuwajima, *JACS* **1987**, *109*, 8056.
[180] A. Z. Suzuki, T. Watanabe, M. Kawamoto, K. Nishiyama, H. Yamashita, M. Ishii, M. Iwamura, T. Furuta, *Organic Letters* **2003**, *5*, 4867.
[181] R. Subramaniam, Y. Xiao, Y. Li, S. Y. Qian, W. Sun, S. Mallik, *Tetrahedron Letters* **2010**, *51*, 529.
[182] K. Hishikawa, H. Nakagawa, T. Furuta, K. Fukuhara, H. Tsumoto, T. Suzuki, N. Miyata, *JACS* **2009**, *131*, 7488.
[183] C. Bao, M. Jin, B. Li, Y. Xu, J. Jin, L. Zhu, *Org. Biomol. Chem.* **2012**, *10*, 5238.
[184] M. Goeldner, R. Givens, *Dynamic studies in biology*, Wiley-VCH, Weinheim, **2005**.
[185] L. D. Hughes, R. J. Rawle, S. G. Boxer, *PLOS ONE* **2014**, *9*, e87649.
[186] J. W. Lichtman, J.-A. Conchello, *Nat Methods* **2005**, *2*, 910.
[187] T. Nagai, K. Ibata, E. S. Park, M. Kubota, K. Mikoshiba, A. Miyawaki, *Nat Biotechnol* **2002**, *20*, 87.
[188] S. D. Chandradoss, A. C. Haagsma, Y. K. Lee, J.-H. Hwang, J.-M. Nam, C. Joo, *J Vis Exp.* **2014**, e50549.
[189] Y. L. Jeyachandran, J. A. Mielczarski, E. Mielczarski, B. Rai, *J Colloid Interface Sci.* **2010**, *341*, 136.

[190] A. M. Kasko, D. Y. Wong, *Future Med Chem.* **2010**, *2*, 1669.

[191] C. D. McNitt, H. Cheng, S. Ullrich, V. V. Popik, M. Bjerknes, *JACS* **2017**, *139*, 14029.

[192] V. Gatterdam, R. Ramadass, T. Stoess, M. A. H. Fichte, J. Wachtveitl, A. Heckel, R. Tampé, *Angew. Chem. Int. Ed.* **2014**, *53*, 5680.

[193] C. A. Hammer, K. Falahati, A. Jakob, R. Klimek, I. Burghardt, A. Heckel, J. Wachtveitl, *J. Phys. Chem. Lett.* **2018**, *9*, 1448.

[194] S. Pradhan, K. A. Keller, J. L. Sperduto, J. H. Slater, *Adv. Healthc. Mater.* **2017**, *6*, 1700681.

[195] P. S. Tsai, P. Blinder, B. J. Migliori, J. Neev, Y. Jin, J. A. Squier, D. Kleinfeld, *Curr. Opin. Biotechnol.* **2009**, *20*, 90.

[196] Y. Becker, E. Unger, M. A. H. Fichte, D. A. Gacek, A. Dreuw, J. Wachtveitl, P. J. Walla, A. Heckel, *Chem. Sci.* **2018**, *9*, 2797.

[197] M. A. H. Fichte, X. M. M. Weyel, S. Junek, F. Schäfer, C. Herbivo, M. Goeldner, A. Specht, J. Wachtveitl, A. Heckel, *Angew. Chem. Int. Ed.* **2016**, *55*, 8948.

[198] Noemie Laboria Vinuelas, *Dissertation*, Johann Wolfgang Goethe-University, Frankfurt am Main, **2014**.

[199] S. L. Parker, A. Balasubramaniam, *Br. J. Pharmacol.* **2008**, *153*, 420.

[200] J. P. Mackay, M. Bompolaki, M. R. DeJoseph, S. D. Michaelson, J. H. Urban, W. F. Colmers, *J. Neurosci.* **2019**, *39*, 4909.

[201] S. J. Smith, U. Sümbül, L. T. Graybuck, F. Collman, S. Seshamani, R. Gala, O. Gliko, L. Elabbady, J. A. Miller, T. E. Bakken et al., *eLife* **2019**, *8*, e47889.

[202] A. M. Smith, M. C. Mancini, S. Nie, *Nat. Nanotechnol.* **2009**, *4*, 710.

8. Abbreviations

a.u.	Arbitrary unit
aa	Amino acid
Ac_2O	Acetic anhydride
AF647	Alexa Fluor647
Ala	Alanine
Anp	3-Amino-3-3(2-nitrophenyl)-propionic acid
APTES	3-Aminopropyl-triethoxysilane
AU	Absorption units
Boc	*tert*-Butoxycarbonyl
BSA	Bovine serum albumin
CLSM	Confocal laser scanning microscopy
COMU	(1-Cyano-2-ethoxy-2-oxoethylidenaminooxy) dimethylamino morpholinocarbenium hexafluorophosphate
CuAAC	Cu(I)-assisted azide-alkyne cycloaddition
Cys	Cysteine
Da	Dalton
DCM	Dichlormethane
DIPEA	*N*,*N*-diisopropylethylamine
DMEM	Dulbecco's modified eagle medium
DMF	*N*,*N*-Dimethylformamide
DMSO	Dimethylsulfoxide
EA	Ethyl acetate
EDT	1,2-Ethanedithiol
EDTA	Ethylenediaminetetraacetic acid
em	Emission
ESI-MS	Electrospray ionization mass spectrometry
Et_2O	Diethyl ether
EtOH	Ethanol
ex	Excitation

FCS	Fetal calf serum
Fmoc	Fluorenylmethoxycarbonyl
FP	Fluorescent protein
FRET	Förster resonance energy transfer
GFP	Green fluorescent protein
Glu	Glutamic acid
Gly	Glycine
GOPTS	3-Glycidyloxypropyl-trimethoxysilane
GSH	Glutathion
HEPES	4-(2-Hydroxyethyl)-1-piperazineethanesulfonic acid
His	Histidine
His_{10}	Decahistindine tag
His_6	Hexahistindinde tag
HOBt · H_2O	Hydroxybenzotriazole monohydrate
HPLC	High performance liquid chromatography
*i*PrOH	Isopropanol
IR	Infrared
LED	Light emitting diode
Lys	Lysine
MALDI-TOF-MS	Matrix-assisted laser desorption/ionization-time of flight mass spectrometry
MBP	Maltose binding protein
MCH	Multivalent chelator head
MeCN	Acetonitrile
MeOH	Methanol
MS	Mass spectrometry
MW	Molecular weight
MW_{calc}	Calculated molecular weight
MW_{obs}	Observed molecular weight
NHS	*N*-hydroxy succinimide

NMM	*N*-methylmorpholine
NMP	*N*-methyl-2-pyrrolidon
NMR	Nuclear magnetic resonance
NTA	*N*-nitrilotriacetic acid
O/N	Overnight
PA-*tris*NTA	Photo-activatable *tris*-*N*-nitrilotriacetic acid
PBS	Phosphate buffered saline
PEG	Polyethylene glycol
PG	Protecting group
PLL	Poly-*L*-Lysine
POI	Protein or peptide of interest
PPG	Photolabile protecting group
RP	Reverse phase
RT	Room temperature
s.d.	Standard deviation
sCy5	sulfo-Cyanine 5
SD	Standard deviation
Ser	Serine
SPPS	Solid-phase peptide synthesis
SPR	Surface plasmon resonance
^{t}Bu	*tert*-Butyl
TCA	Trichloracetic acid
TCEP	*Tris*(2-carboxyethyl)-phosphine
TFA	Trifluoracetic acid
TIPS	Triisopropylsilane
TLC	Thin-layer chromatography
TPA-*tris*NTA	Two-photon-activatable *tris*-*N*-nitrilotriacetic acid
UAA	Unnatural amino acid
w/o	Without
Y_2R	Y_2 receptor

9. Declaration

The work presented in this thesis was generated by myself under supervision of my advisor during my doctoral studies. Exceptions were stated otherwise by reference or acknowledgement. All contributions from colleagues were referred.

The fluorescent protein His_6-mCherry was generated and purified by Dr. Simon Trowitzsch at the Goethe-University Frankfurt, Institute of Biochemistry, Trowitzsch lab, Frankfurt, Germany.

Fluorescently labeled *tris*NTA^{AF647}, the short fluorescently labeled peptide His_6-SGGGSGGG-C^{AF647}-A-NH_2 was synthesized and purified by Dr. Ralph Wieneke, at the Goethe-University Frankfurt, Institute of Biochemistry, Wieneke lab, Frankfurt, Germany.

His-tagged proteins His_{10}-MBP^{OG488}, His_6-GFP were generated and purified by Dr. Karl Gatterdam at the Goethe-University Frankfurt, Institute of Biochemistry, Tampé lab, Frankfurt, Germany.

The His-tagged protein His_{10}-mVenus was generated and purified by Dr. Valentina Herbring at the Goethe-University Frankfurt, Institute of Biochemistry, Tampé lab, Frankfurt, Germany.

The *tris*NTA headgroup as well as thio-*tris*NTA was synthesized and purified by Katrin Schanner at the Goethe-University Frankfurt, Institute of Biochemistry, Tampé lab, Frankfurt, Germany.

The cell line HeLa Flp-In T-Rex cells stably containing His_6-Y_2R^{mEGFP} were produced and provided by Dr. Florencia Maria Sanchez at the Goethe-University Frankfurt, Institute of Biochemistry, Tampé lab, Frankfurt, Germany.

The measurement of the fluorescence quantum yield of TPA-*tris*NTA, the two-photon excited fluorescence (TPEF) measurements for the two-photon absorption spectrum and for the power dependency of TPA-*tris*NTA were performed by Marvin Asido, at the Goethe-University Frankfurt, Institute of Physical and Theoretical Chemistry, Wachtveitl lab, Frankfurt, Germany.

The material listed below as obtained in the context of collaborative research:

Fig. 34 and Fig. 35 were created by Marvin Asido (at the Goethe-University Frankfurt, Institute of Physical and Theoretical Chemistry, Wachtveitl lab, Frankfurt, Germany) and modified by Heike Krüger.

10. Eidesstattliche Erklärung

Erklärung

Ich erkläre hiermit, dass ich mich bisher keiner Doktorprüfung im Mathematisch-Naturwissenschaftlichen Bereich unterzogen habe.

Frankfurt am Main, den ……

Unterschrift

Versicherung

Ich erkläre hiermit, dass ich die vorgelegte Dissertation über

“ High-precision nanotools for *in-situ* photopatterning of biomolecules in 2D and 3D”

selbstständig angefertigt und mich anderer Hilfsmittel als der in ihr angegebenen nicht bedient habe, insbesondere, das alle Entlehnungen aus anderen Schriften mit Angaben der betreffenden Schriften gekennzeichnet sind.

Ich versichere, die Grundsätze der guten wissenschaftlichen Praxis beachtet, und nicht die Hilfe einer kommerziellen Promotionsvermittlung in Anspruch genommen habe.

Frankfurt am Main, den ……

Unterschrift